U.S. DEPARTMENT OF COMMERCE

National Oceanic and Atmospheric Administration
Atlantic Oceanographic and Meteorological Laboratory

SEDIMENT CAP STABILITY STUDY

NEW YORK DREDGED MATERIAL DUMPSITE

by

George L. Freeland
Robert A. Young
Georges Drapeau
Thomas L. Clarke
Bradford L. Benggio

Final Report under Support Agreement No. NYD 80-124(C),
New York District Corps of Engineers

1983

SEDIMENT CAP STABILITY STUDY

NEW YORK DREDGED MATERIAL DUMPSITE

A report prepared for the Department of the Army,
New York District Corps of Engineers, and the
Office of Marine Pollution Assessment, NOAA

by

George L. Freeland
Robert A. Young
Georges Drapeau
Thomas L. Clarke
Bradford L. Benggio

National Oceanic and Atmospheric Administration
Atlantic Oceanographic and Meteorological Laboratories
4301 Rickenbacker Causeway
Miami, Florida 33149

February 15, 1983

Final Report Under Support Agreement No. NYD 80-124(C),
New York District Corps of Engineers

EXECUTIVE SUMMARY

The project objective is to study the frequency and capability of sea-bottom currents to erode surficial sediment in a portion of the southeast quadrant of the New York dredged material dumpsite. The area under study had dredged material dumped which was determined, after the dumping occurred, to be unsuitable for unrestricted ocean disposal under the ocean dumping pollution criteria; this material was subsequently capped by clean dredged material. This study measured sea-bottom conditions on the surface of the cap from November 1980 to June 1981. It also attempts to reconstruct, through hindcasting and mathematical modelling techniques, what conditions might be expected at the site over a much longer period of time.

Both actual and predictive analysis indicate a slight amount of erosion occurs during a 'normal' year. The bottom is particularly susceptable to erosion during the winter season when the water column is unstratified. Especially important for bottom sediment transport are storm conditions when the wind blows from directions of open water fetch: from east-northeast to south-southwest. Sea swell coming from these directions may also cause some transport. Severe conditions did not occur during the measurement period, nevertheless, some sediment transport, primarily to the south, did occur.

Since the present surface of the cap contains high percentages of easily-transported fine sand, it is recommended that additional material be added to the cap, and that this material be clean sand as coarse as is economically available, but not finer than 0.25 mm in grain size.

TABLE OF CONTENTS

Introduction

This project was initiated by a proposal dated August 25, 1980, to the Corps of Engineers, New York District, and the NOAA Office of Marine Pollution Assessment. Funds have been provided by both agencies. The project objective is to study the environmental conditions existing at the southeast quadrant of the New York dredged material dumpsite. This site received 510,565 yd^3 of dredged material in 1980, which was considered unsuitable under the ocean dumping pollution criteria. Subsequently, also in 1980, 119,536 yd^3 of fine-grained material and 1,226,737 yd^3 of sand-sized material were dumped at the same site to form an environmentally acceptable sediment cap over the previously dumped material. This study will examine the surface of the cap and related meteorological and oceanographic conditions to attempt to determine the erosive capabilities of bottom currents at the cap site. The results will indicate the relative stability of the cap.

Location

The area examined is in the southeast quadrant of the designated dredged material dumpsite (Figs. 1 and 2). It is about one nautical mile square lying between 40°21.7'N and 40°22.8'N, and 73°39.7'W and 73°51.2'W, approximately 6 n. mi. east of the New Jersey shoreline. Water depths are between 75 and 85 feet (23 to 26 m).

Background

Energy to transport bottom sediment comes from bottom currents. These are in the form of (a) unidirectional currents caused, in this area, by tides and regional continental shelf circulation, and (b) oscillatory currents caused by waves. In order to transport sediment, the bottom current must exceed a threshold which is sensitive to the nature of the sediment: grain

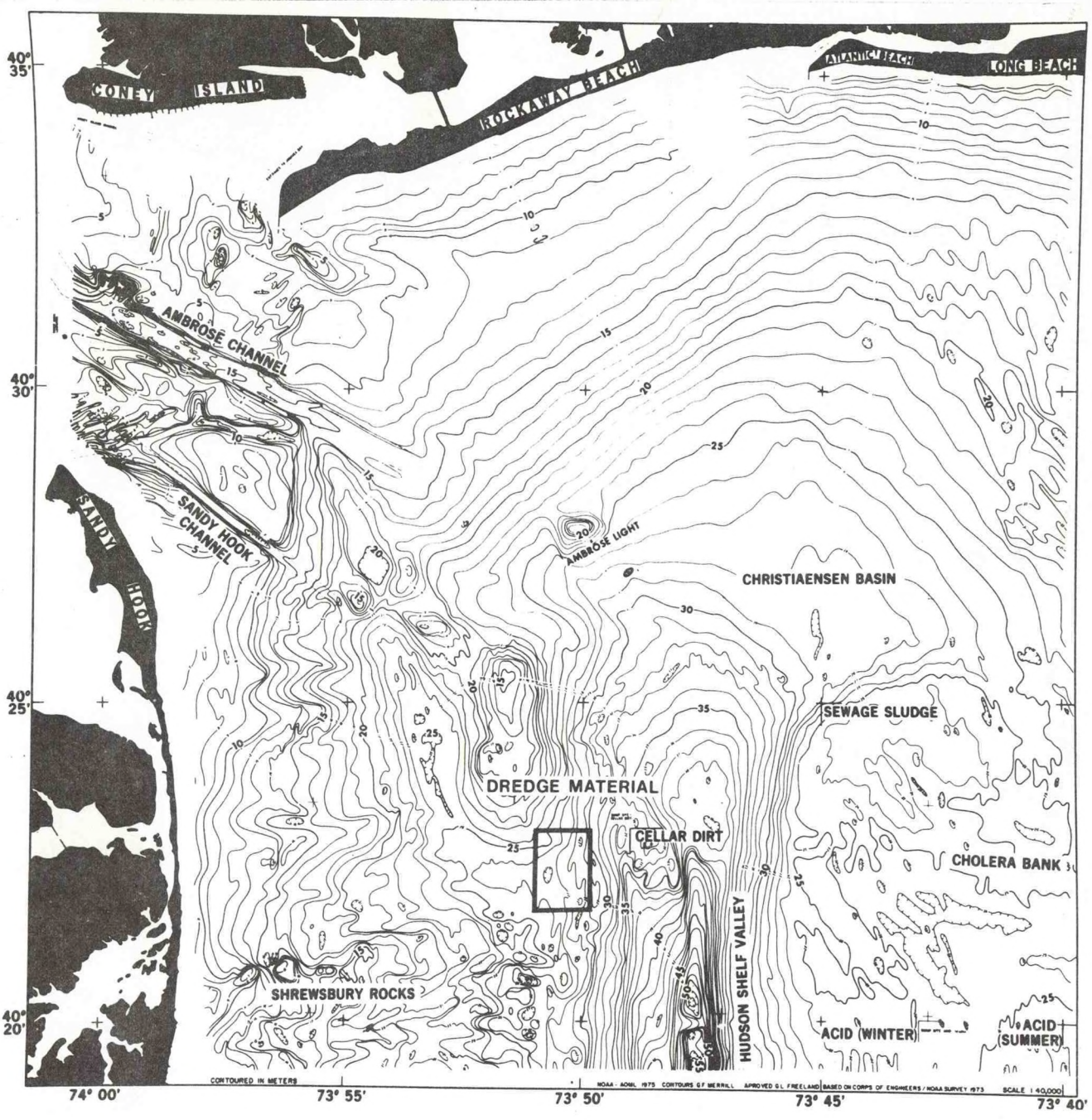

Figure 1. Location of the New York dredged material dumpsite. Bathymetry is in meters from a 1973 COE/NOAA survey. Other dumpsites are for sewage sludge, cellar dirt (construction rubble), and acid waste.

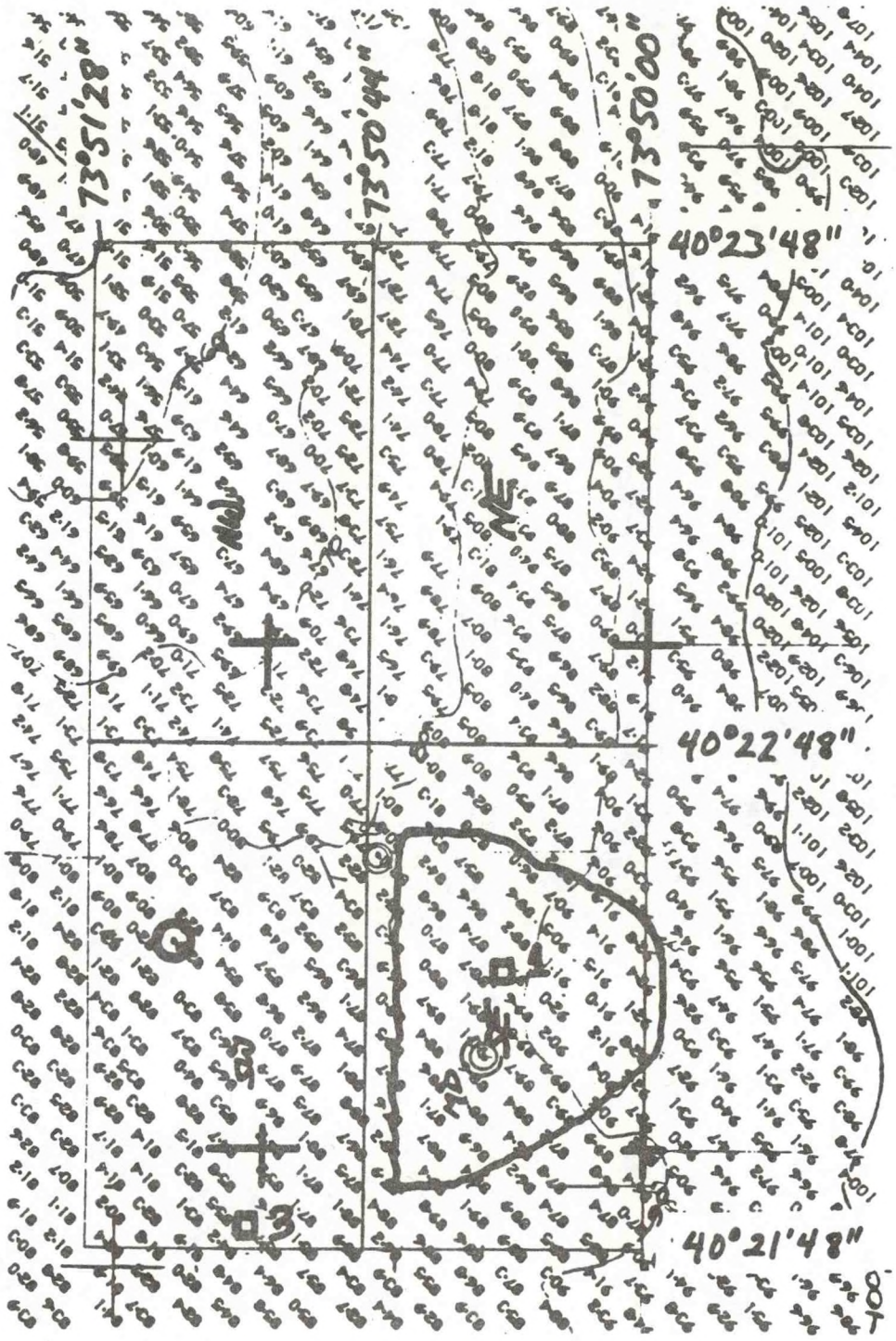

Figure 2. Detail of the dredged material dumpsite. The cap studied is outlined in the southeast quadrant. "MD" is the temporary buoy used to guide dump barges. Depths, in feet and tenths of feet, are from a COE survey completed in October 1978.

size and density, and water and organic content. Normal shelf circulation causes currents usually insufficient to erode bottom sediment, but may transport fine-grained particles once they are in suspension. Tidal currents may be strong enough to erode only the most easily resuspended sediment, fine sand. The strength of wave-generated bottom currents is dependent on water depth and wave height and period; these currents are also too weak to transport sediment during non-storm periods. The result is that bottom transport occurs only when a combination of conditions occur to produce bottom currents exceeding the threshold value for the sediment under study.

There are several site characteristics of the dumpsite which affect the generation of bottom currents. The New York Bight is a broad continental shelf with open fetch from east-northeast to south-southwest. When low-pressure storm cells traverse the eastern U.S. seaboard offshore, their counterclockwise circulation generates east to northeast winds over the Bight resulting in large seas, and a strong unidirection circulation westward along the Long Island shelf and southward along the New Jersey shelf. They occur much less frequently than onshore storms which create westerly winds, but their effect is much more pronounced. There are also seasonal considerations. During summer, the surface water is warmed, creating a two-layer water column with a density interface. This inhibits transfer of surface energy from waves and unidirectional storm-generated current to the bottom. Consequently, winter storms are much more effective as agents of bottom sediment transport. The local bathymetry of the dumpsite area is also important. Water depths to the northeast, east, and southeast drop sharply into the Christiaensen basin and the Hudson Shelf Valley. Therefore, the site is more susceptable to waves and currents from these directions. In addition, the Hudson Shelf Valley, traversing the shelf from the apex to near shelf-edge,

acts as a conduct for cross-shelf water movement during both offshore and onshore storms, the Valley bottom water moving landward during westerly winds, and seaward during easterly winds. Much of the sediment resuspended during storms is transported either towards the harbor mouth or the shelf edge by Valley currents, or settles into the Valley bottom.

The site is close enough to the New York harbor entrance to have tidal currents stronger than on the open shelf, occasionally exceeding threshold values. However, as will be seen in Section D, there does not seem to be a concurrent increase of turbidity when these tidal currents are not coupled with increased wave energy.

Organization

Various environmental factors affecting the site were studied. These are reported as sections herein as follows: (A) The surficial sediments and bottom microtopography of the cap were examined in November 1980 and again in June 1981. (B) Experiments were conducted in both November and June on the cap to determine threshold bottom current velocities necessary to initiate sediment transport. (C) A study was made of long-term meteorological conditions in the Bight apex, how wind-forcing energy is translated into wave energy, and the effect these waves have on the bottom. (D) Estimates were made of the resultant sediment transport from long-term current flow and bottom turbidity measurements. (E) A mathematical study of the combined effects of unidirectional currents and oscillatory waves currents. (F) Summary.

SURFICIAL SEDIMENTS OF A DREDGED MATERIAL CAP IN THE NEW YORK BIGHT APEX

by

George L. Freeland

National Oceanic and Atmospheric Administration
Atlantic Oceanographic and Meteorological Laboratories
4301 Rickenbacker Causeway
Miami, Florida 33149

Methods

The initial operations of the study took place on a cruise in November 1980. Bottom grab samples were taken by Shipek sampler on a 1/8 nmi spacing; sidescan sonar recordings (sonographs) of bottom microtopography were taken on east-west tracklines spaced 400 ft apart using a recording range of 250 ft on both sides of the trackline in an attempt to record 100% bottom coverage; and 12 deployments were made with the SEAFLUME, a device emplaced on the bottom which induces a gradually increasing current over the sediment surface to record photographically the threshold of sediment transport (see Section B). In addition, two graduated steel rods were emplaced into the bottom to measure erosion or deposition, and two bottom-mounted concentration-velocity (CV) probes were emplaced to measure currents and suspended-sediment concentration (see Section D). Both rods and probes remained on the bottom until June 1981. The CV probes were serviced in February and April 1981.

The second cruise took place in June 1981 when the sampling, sidescan sonar recordings, and SEAFLUME data collection were repeated. The graduated steel rods could not be found.

Navigation for both cruises was by a Cubic Autotape system supplied by COE with range towers on the New Jersey and Long Island shores. Station locations and tracklines were plotted before each cruise on 1:3000 scale mylar plotting sheets which contained Autotape ranges. These were furnished by the NOAA Atlantic Marine Center, Norfolk, Virginia. Loran C readings were taken of the CV probe sites and used for recovery and replacement operations in February and April.

Sediment Analysis

Sediment samples were stored refrigerated in Whirl-pac plastic bags. An analysis aliquot was freeze-dried, weighed, and seived on a 2 mm screen to

separate gravel, then weighed and washed on a 62.5 um screen to separate fines (mud fraction = silt + clay). The sand fraction was analysed by running a 5 to 7 gm aliquot through an automated rapid sediment analyser (settling tube) which calculated mean grain size for the sand fraction. Data for gravel, sand, and fines percent were mapped for both November 1980 and June 1981 cruises. Sand percentage maps for both cruises were overlain on each other and a map of the differences (net change) between them was drawn. On this map, areas within each contour were measured by planimeter and multiplied by the contour values (in decimal fractions) to calculate a weighted measure of sand change on the sediment surface over the seven months.

Results

Gravel Percentage: Maps for both November and June (Figs. 3 and 4) show mostly less than 5% gravel with the following exceptions: in the northwest corner, a November maximum of 45% was reduced to 1% by June. In the northeast corner, a 64% maximum in November shifted somewhat southeast and increased to 66% in June. In the southeast corner, an 18% maximum in November increased to 35% to 86%. In general, coarser sediment (higher gravel percentage) lie along the eastern edge of the dumpsite where it was about 15% in November and increased only slightly by June. Composition of the gravel fraction is primarily (30-95%) construction rubble consisting of brick, concrete, rock, and slag fragments, with rounded quartz and feldspar fragments and shell particles intermixed. This is the case particularly in the high-gravel areas along the eastern part of the area which border the cellar dirt (construction rubble) dumpsite. To the west, the gravel fraction consists of larger percentages of shell and rounded particles, except the area of over 30% gravel in the northwest corner of the November 1980 cruise which consists of about 60% construction rubble. Although the areas of high gravel content had

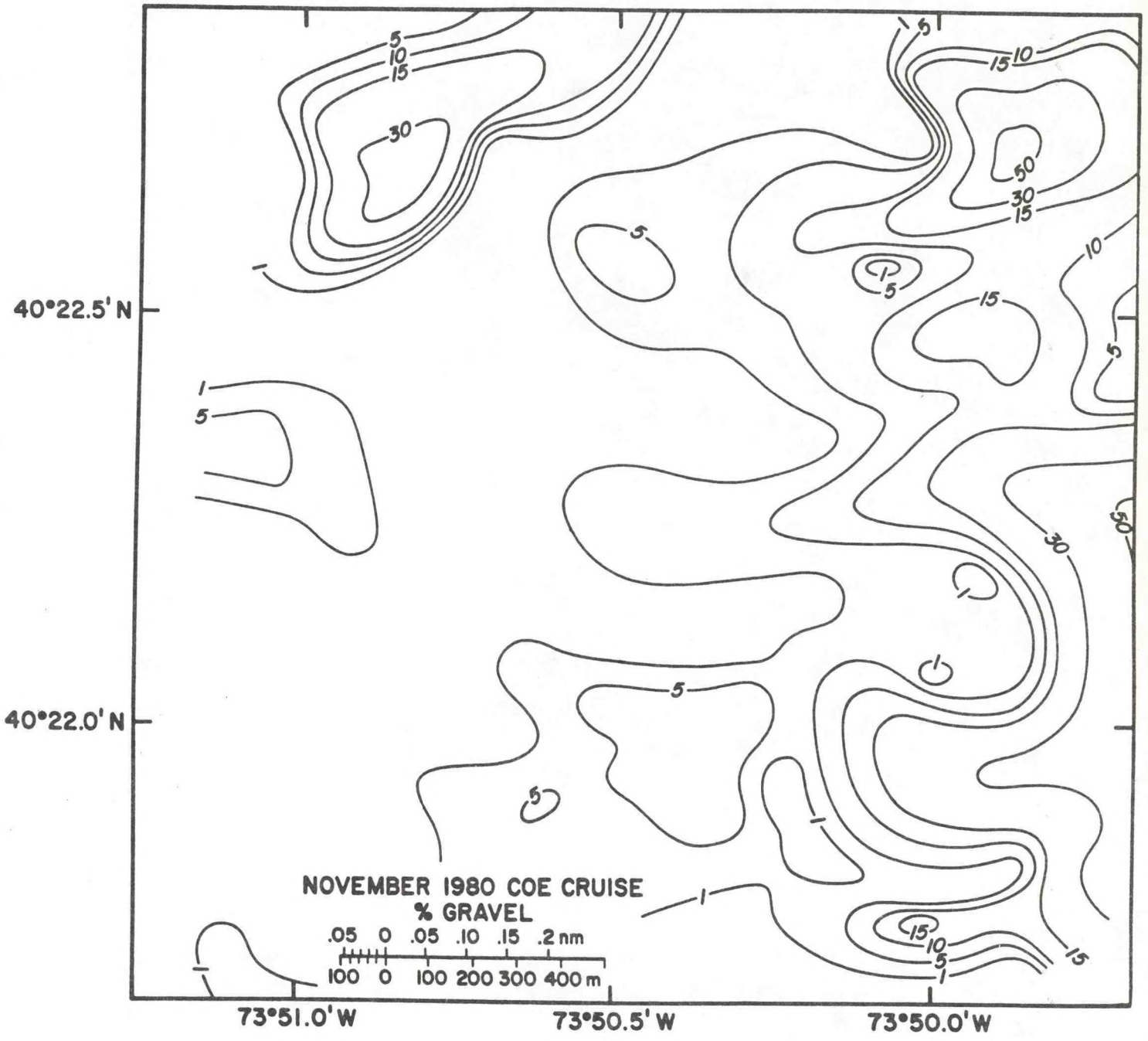

Figure 3. Percent gravel in the surficial sediment, November 1980.

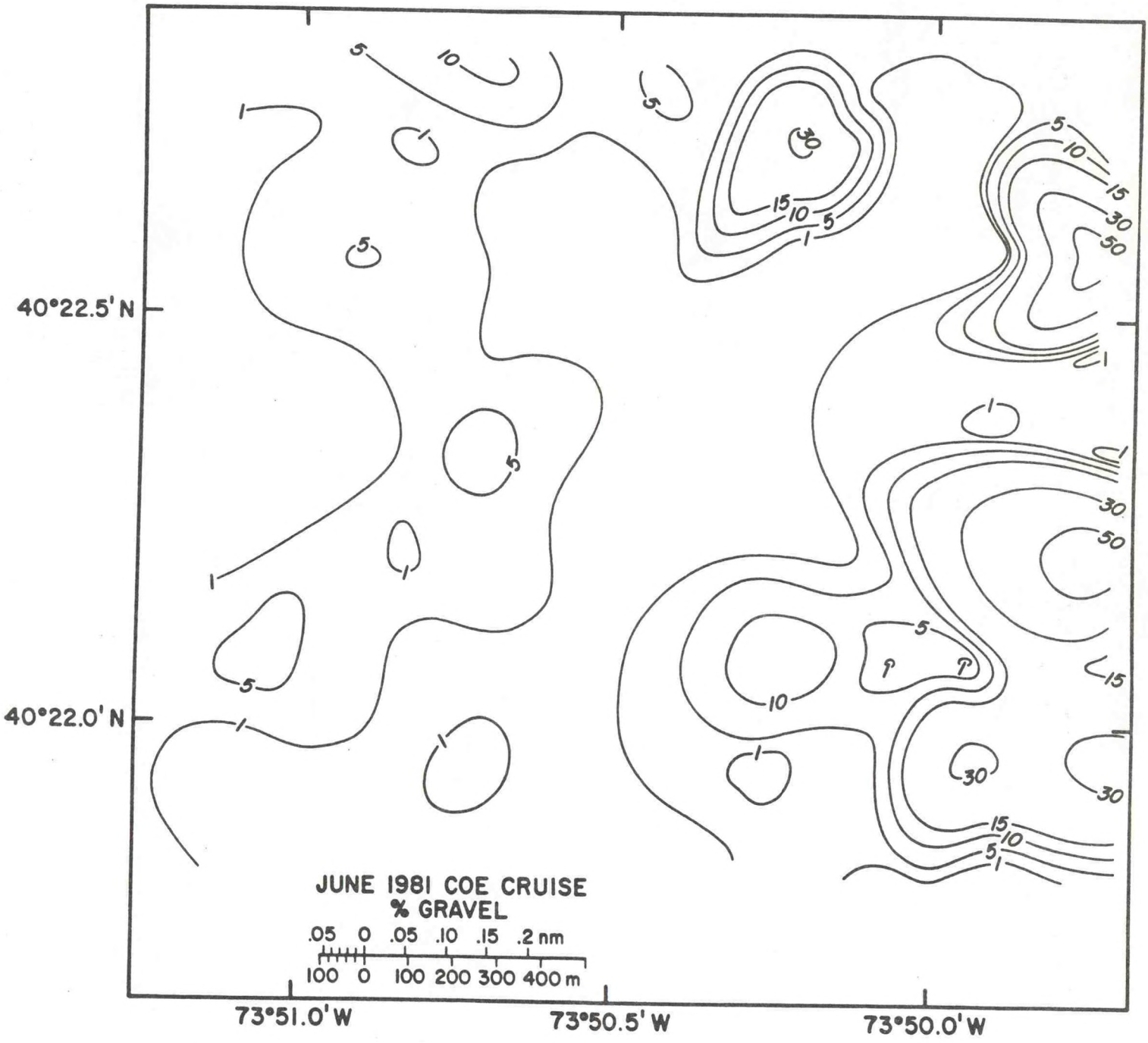

Figure 4. Percent gravel in the surficial sediment, June 1981.

shifted from November to June, the high construction rubble content remains consistently high along the eastern edge of the study site.

Sand Percentage: Both November and June maps (Figs. 5 and 6) show mostly greater than 90% sand (cap material), with areas of less than 50% in the northwest corner, northeast and southeast corners (minimum 32%), and southwest corner (one sample 5%; others 50% - 80%). Along the eastern edge, values varied between 32% and 80%.

Data calculated from the sand percentage net change map (Fig. 7) shows that the northeast quarter of the sampled area lost 6% sand, the southeast quarter gained 2%, and the southwest and northwest quarters each lost 2% and 9% respectively. The total dumpsite lost a weighted average of only 3.1% sand. Most of these changes, however, were around the periphery of the area along the edge of the cap. A large south-central area (the center and highest point of the cap) showed little change. These calculations represent a change in the composition of the surface layer only, and cannot discern whether sand was removed, or was diluted with the addition of fines.

Fines Percentage: The November map (Fig. 8) shows a large central area of less than 5% fines; by June (Fig. 9), this area was somewhat smaller and shifted slightly to the southeast. In the northwest corner, there are several areas on the November map of over 40% fines with one sample of 88%. There, areas had slightly higher fines content in June. Along the northern edge, fines content was about 30% in both November and June. In the northeast corner, fines varied between 5% and 30% in November and increased only slightly in June. In the southeast parts of both maps are areas of between 30% and 60% fines. These values did not change from November to June, but the areas of high and low values shifted. In the southwest corner an area of 30% did not change, but one sample with 99% mud in November was reduced to 67% in June. In general, fines did not change much, but some areas shifted.

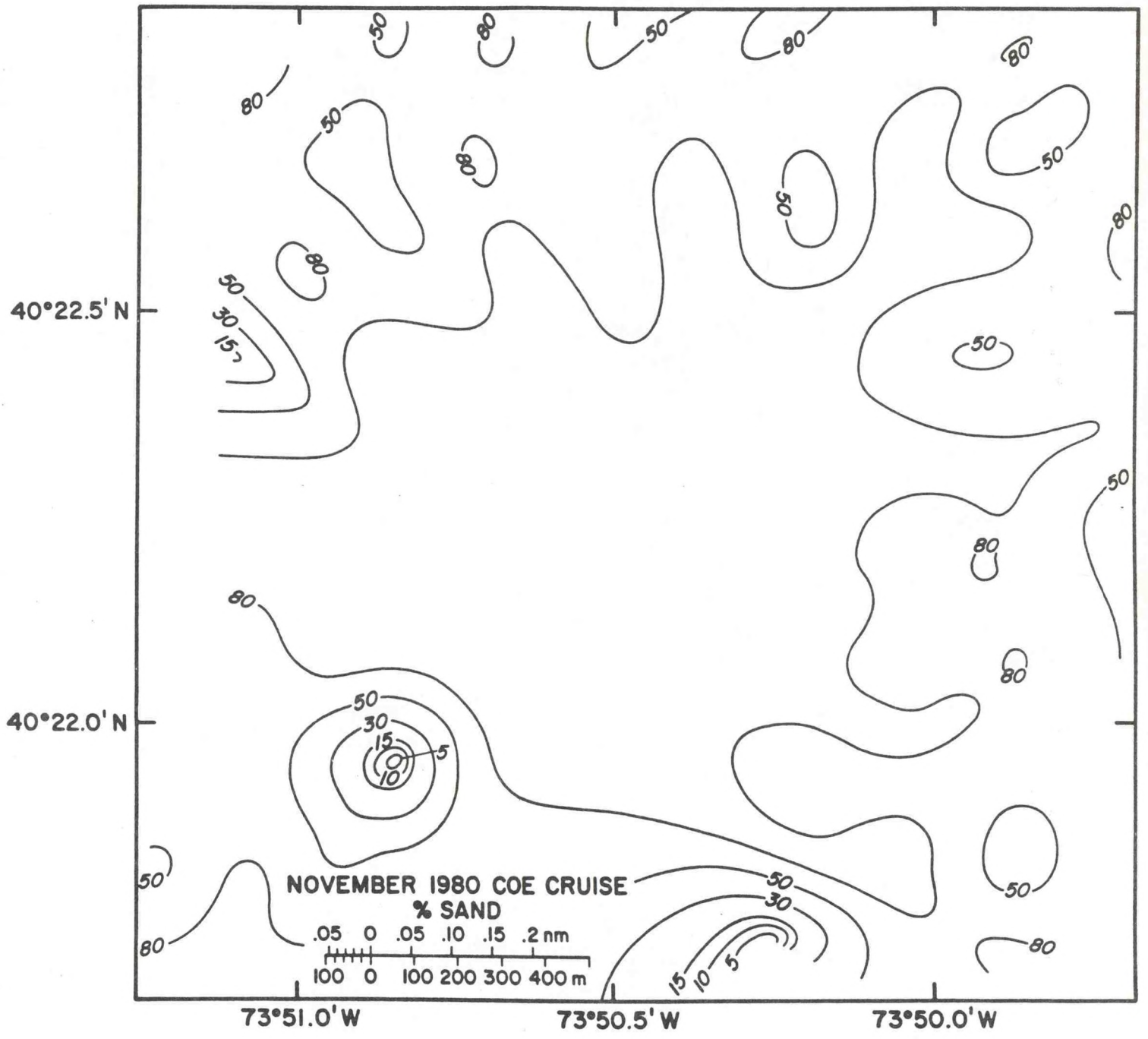

Figure 5. Percent sand in the surficial sediment, November 1980.

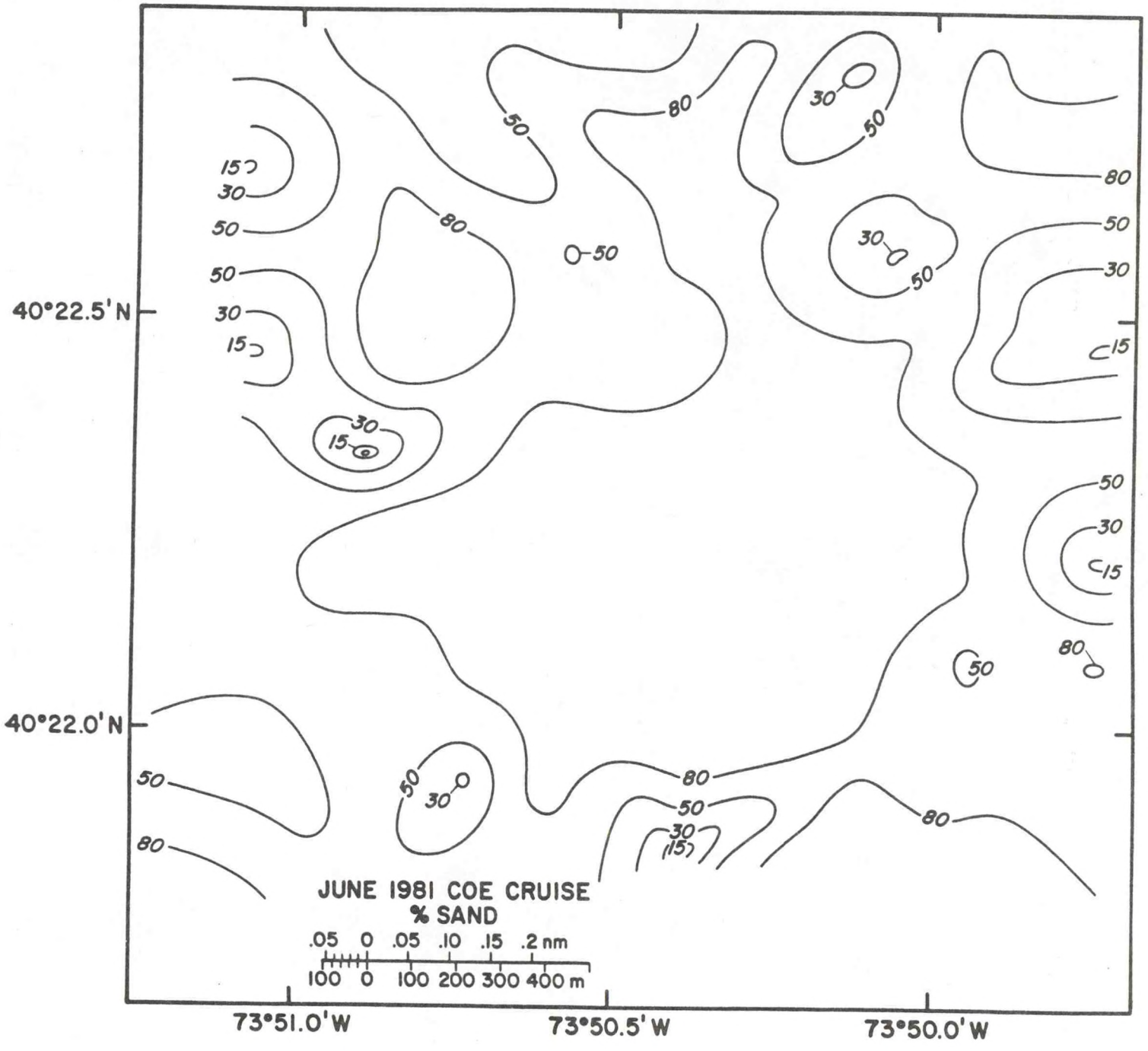

Figure 6. Percent sand in the surficial sediment, June 1981.

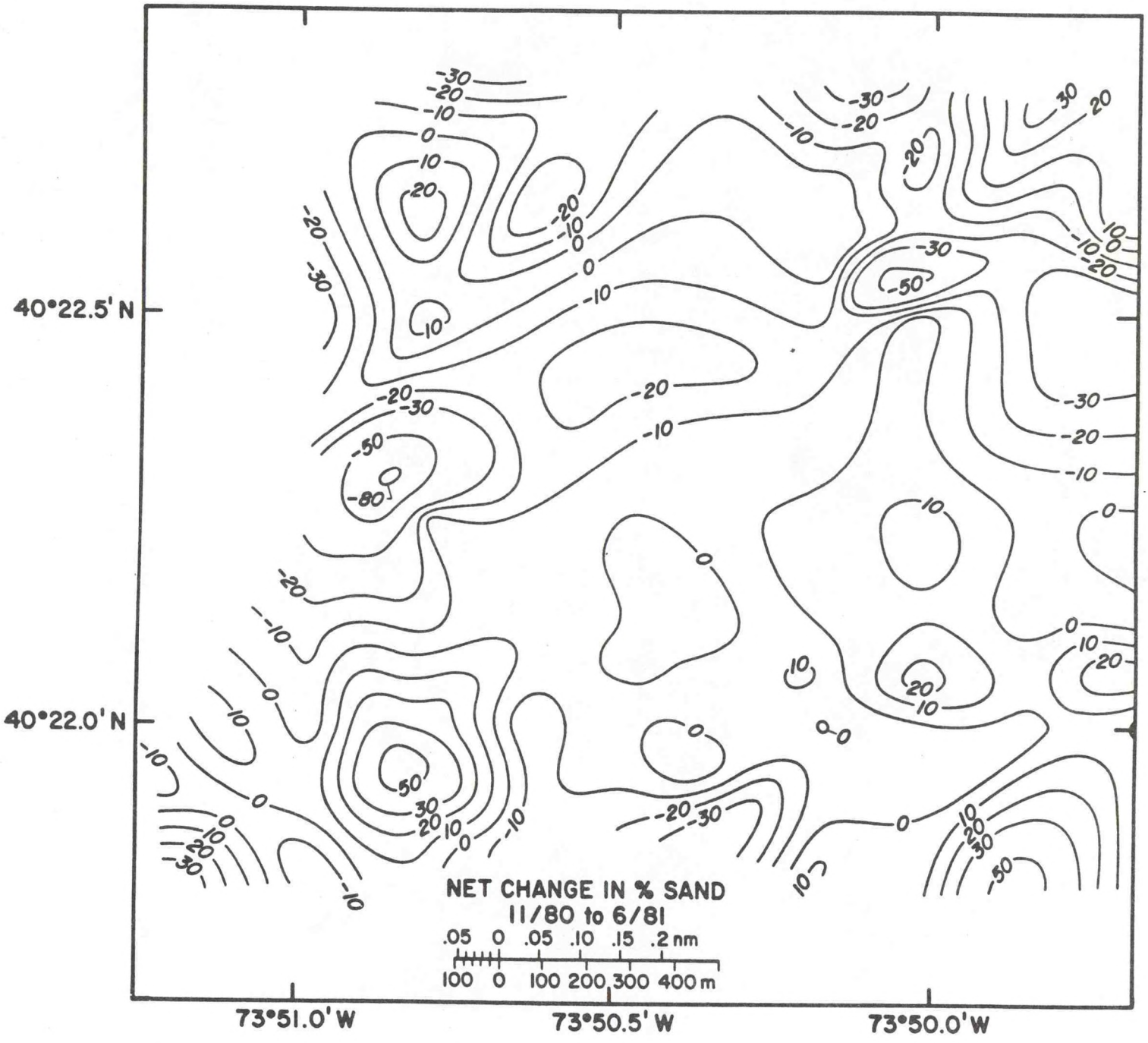

Figure 7. Net change in percent sand, November 1980 to June 1981.

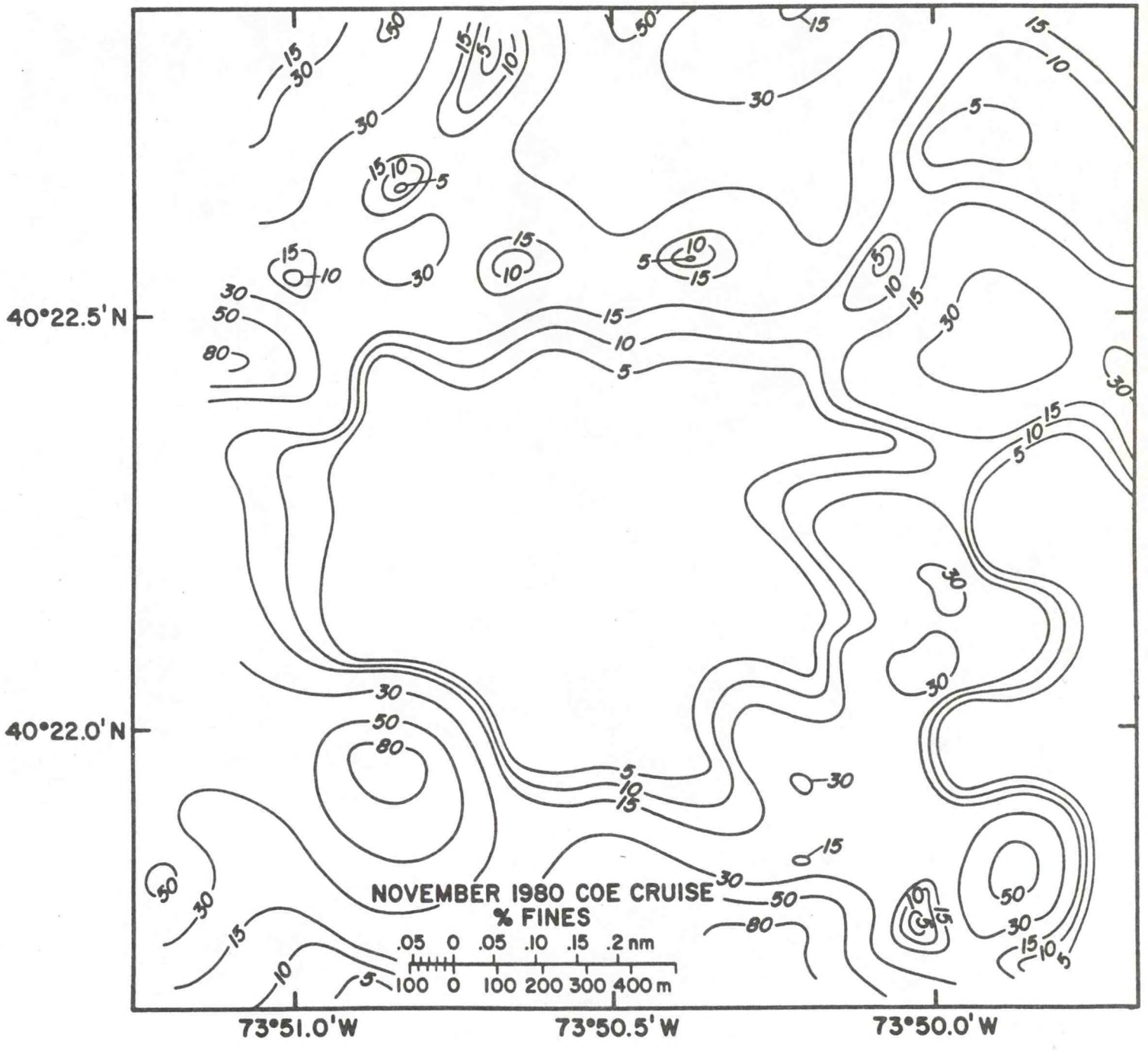

Figure 8. Percent fines (mud) in the surficial sediment, November 1980.

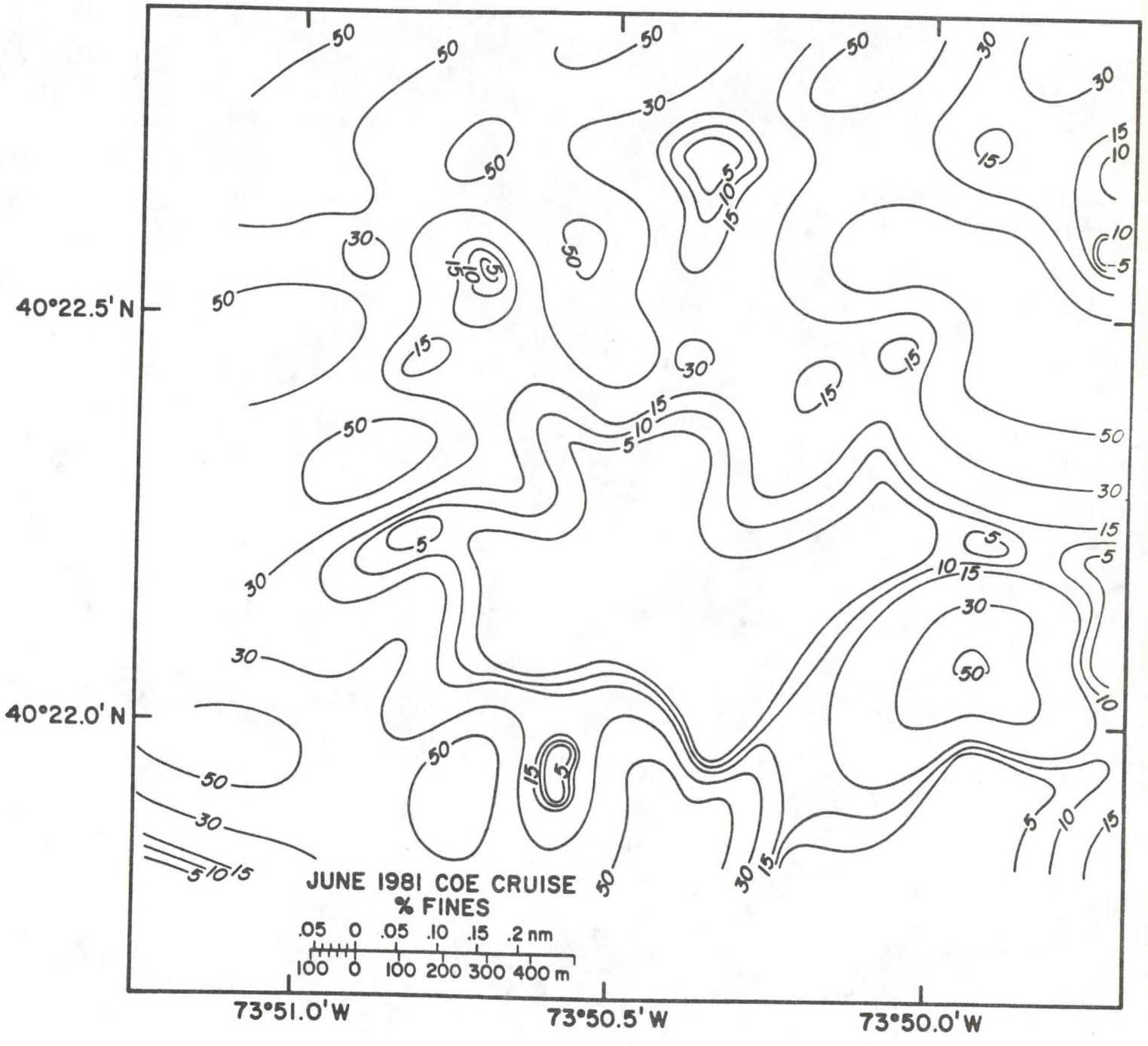

Figure 9. Percent fines (mud) in the surficial sediment, June 1981.

Phi-mean grain size: The mean grain size of the sand-sized fraction is reported in phi units (ϕ = -3.32 log [grain size in mm]) (Figs. 10 and 11). A large central area on both November and June maps is between 2.00 and 2.50 ϕ (fine sand). North of this are samples of 1.25 ϕ (medium sand) to the northwest and northeast, and a sample of 0.00 ϕ (coarse sand) near the north-central edge. Sand in these northern areas became finer by June, varying between 1.75 ϕ (medium sand) and 2.5 ϕ. South of the central area, similar 'fining' occurred: in the southwest one sample with 0.00 ϕ mean in November was 2.57 ϕ in June.

Cap Thickness

The cap proper is defined by the net change (COE 'differences') map drawn by the Corps from the March 1980 and July 1980 surveys (done before and after the cap material was dumped). This area is roughly an isosceles triangle with the base to the west and the apex to the east, covering approximately 6,900,000 ft^2. The cap is mostly 3 to 4 ft thick, with an area 5 to 9 ft thick just west of where the "MD" marker buoy was deployed during the dumping of the cap material. Volumes of material dumped for the cap are reported (by COE) as 119,536 yd^3 of fines [(166,400 + 127,300 bin yardage) x .407 (bin to in-place compaction)], and 1,226,737 yd^3 of sand (1,533,421 bin yardage x .8). This material would average 6 ft thick over the cap area. This discrepancy in thickness between calculated in-place material and survey volumes is likely to be the result of survey errors of up to one foot in each survey.

The COE net change map for the period between July 1980 and March 1982 shows erosion over the two winters of generally less than one foot (maximum of 1.7 ft within the cap area), about the error inherent in the data.

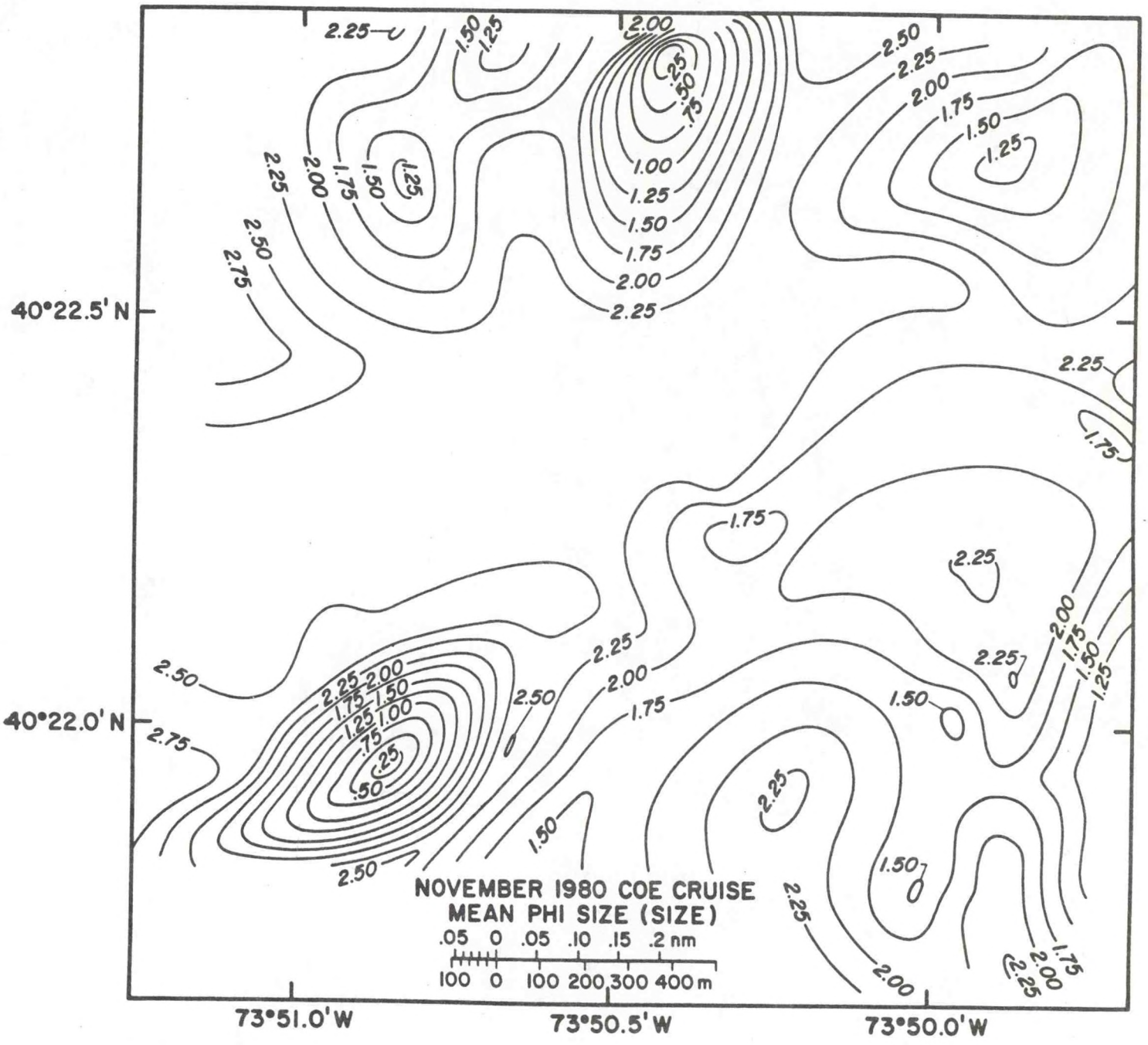

Figure 10. Mean grain size in phi units, sand-sized fraction, November 1980.

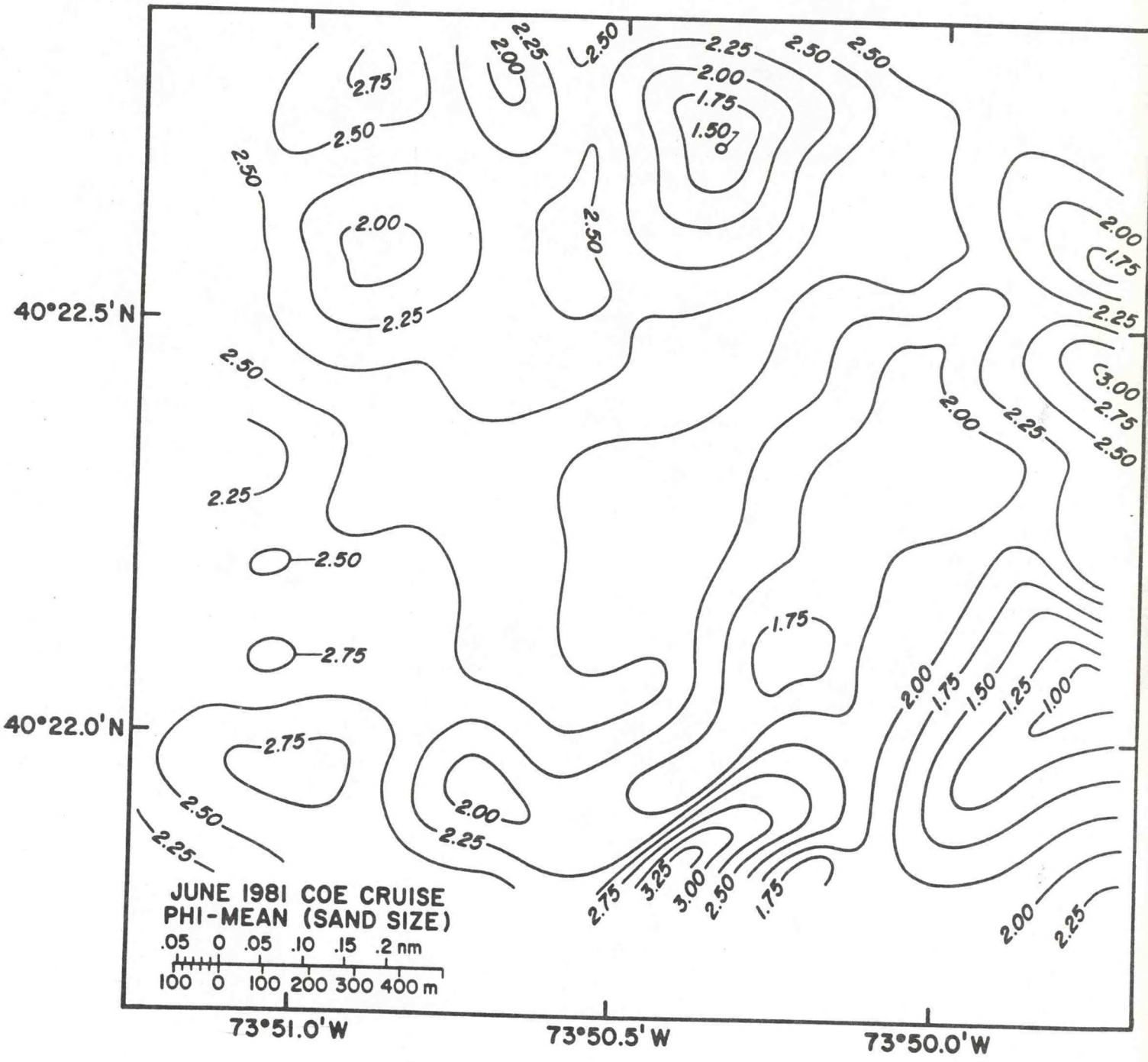

Figure 11. Mean grain size in phi units, sand-sized fraction, June 1981.

Bottom Roughness

A qualitative estimate of bottom roughness was made by examination of sidescan sonar records (sonographs). These were plotted on maps at the same scale as the sediment parameters using nomographs to correct for analog record distortion according to ships' speed (Figs. 12 and 13). The map made for the November 1980 data shows the cap area relatively smooth with occasional dump craters and lineations aligned just west of north. Along the northern edge there is considerably more bottom roughness and lineations with the same orientation. In the eastern third of the area there is irregular roughness probably due to the muddy bottom east of the cap. In the southeast corner several areas of roughness also have ripple marks which indicate relatively high percentages of sand. A total of 29 lineations were measured for azimuth: the mean is 166° (346°) with a standard deviation of 22.5°.

The June 1981 map, compared with the November map, shows the central cap area still relatively smooth. Sonograph images of dump craters and lineations have been modified so that they are smaller but are more numerous. The northern area so disturbed in November is smoother. Areas of intense roughness were smoothed to moderate roughness, but the area of moderate roughness was extended southward (from 1600 ft from the northern edge to 2500 ft). The eastern area of roughness is smaller and has more areas of relative smoothness. The number of measureable lineations was reduced from 29 in November to 10 in June: the latter had a mean direction of 178° (358°) with a standard deviation of 32°.

Conclusion

The sediment sampling data indicates that there was a general decrease in grain size over the winter from November 1980 to June 1981, but most of the

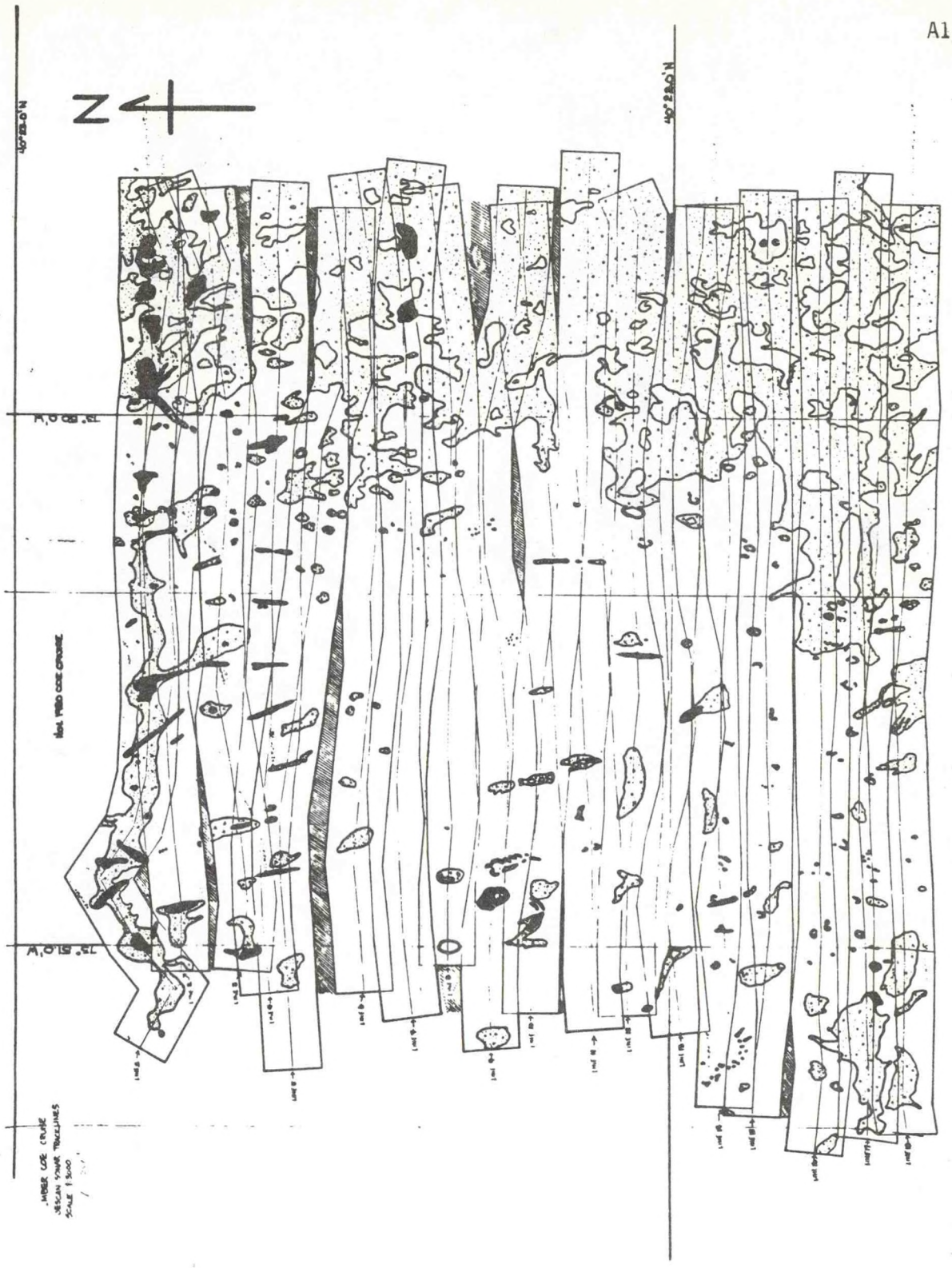

Figure 12. Map of bottom roughness drawn from sidescan sonar analog records, November 1980. Black areas are very rough; dotted areas are moderately rough; clear areas are smooth. Diagonal lines are areas of no bottom coverage.

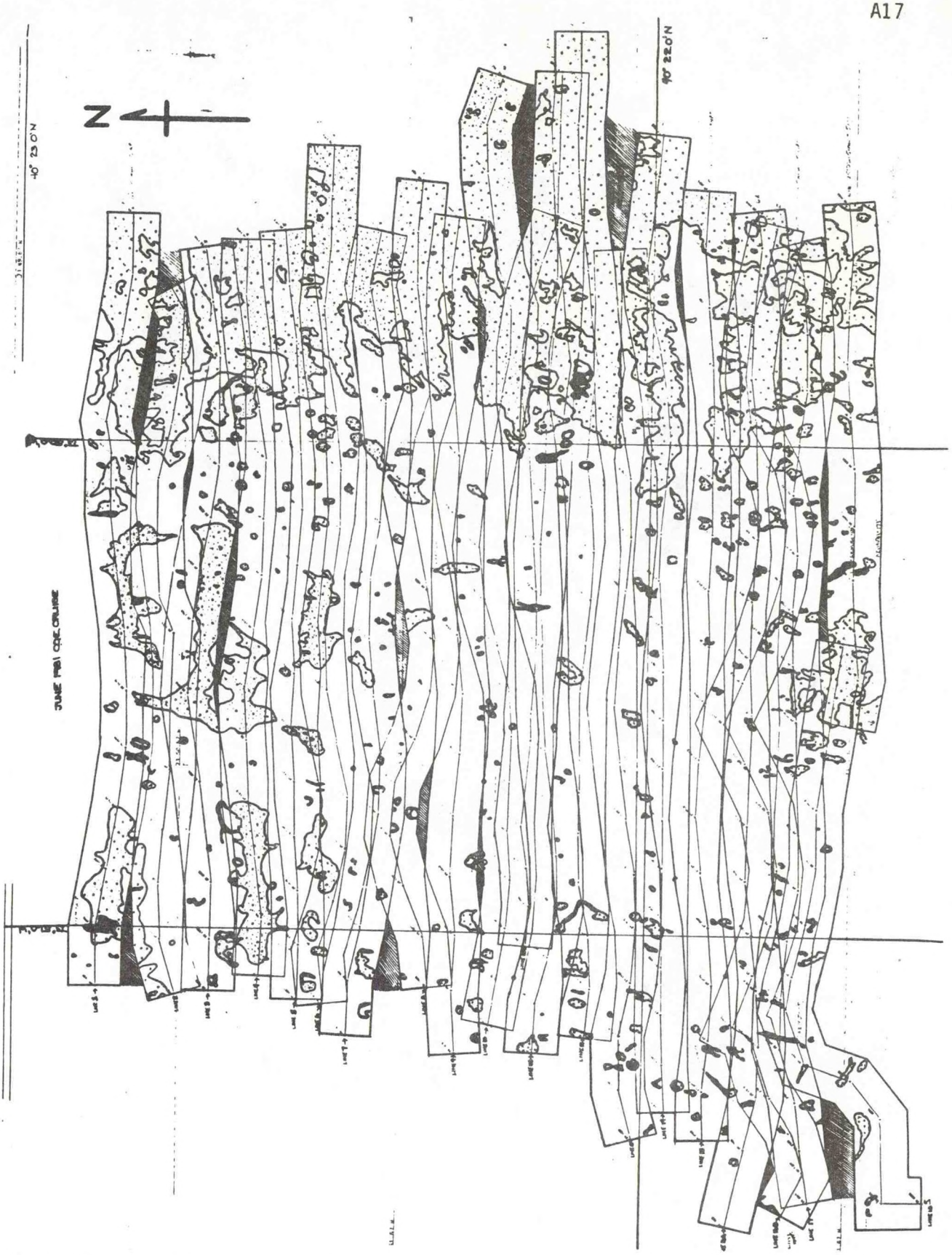

Figure 13. Map of bottom roughness, June 1981. Symbols are the same as in Fig. 12.

changes occurred around the periphery of the cap. The cap itself appears to have undergone little change in grain-size characteristics, with a slight decrease in grain size. Bottom roughness maps drawn from sonograph data support this by showing a smoother bottom in June, indicative of sediment transport which would fill in small-scale depressions. Both the leveling out of bottom roughness and decrease in grain size results in smoother sonographs. It is likely that some of the sand cap was removed, fine sand being the easiest grain size to erode, but silt- and clay-sized sediment eroded from around the cap and muddy bottoms elsewhere was deposited on the cap sand. Thus, there was intermixing of grain sizes resulting in poorer sorting and a reduction of mean size. We would recommend that if additional cap material is desired, the coarsest clean sand available should be used, with an attempt to keep grain size larger than 0.25 mm.

The changes over the seven month winter period reported herein must be viewed as tentative indications of long term phenominon. Most of the changes are within the scope of errors inherent in the data. Longer term analysis will be necessary to reach firm conclusions as to the life of the cap based on this data set.

THRESHOLD EROSION VELOCITIES OF POORLY SORTED SEDIMENTS, DREDGE MATERIAL DUMPSITE, NEW YORK BIGHT APEX

Robert A. Young
Giselher Gust*
Bradford L. Benggio

National Oceanic and Atmospheric Administration
Atlantic Oceanographic and Meteorological Laboratories
4301 Rickenbacker Causeway
Miami, Florida 33149

*Department of Marine Sciences
University of South Florida
St. Petersburg, Florida

ABSTRACT

Field studies have been carried out during two cruises to determine the threshold flow conditions for erosion of sediments emplaced over a fine-grained dredge material deposit. The deposits are located in the apex of the New York Bight. A sea-going flume (SEAFLUME) was used to create the erosional currents under experimental control. Sediments ranged in texture from muddy sands to sandy muds. The in-situ measurements indicate that SEAFLUME measurements yield the best possible field measurements of erosion conditions when suitably treated. The data agree reasonably well with the Shields and Yalin threshold curves usually used to predict threshold flow conditions. Some scatter is observed, but is attributed to poor sorting of the sediments and thus to grain size or roughness features of the sediment beds which are not accounted for by existing flow models.

Threshold shear velocity (U_*) values range between 0.6 to 1.4 cm/sec. The estimated erosional velocities at one meter above bottom (U_{100}) corresponding to the U_* values ranged from 14 to 31 cm/sec. Values of U_* and U_{100} averaged for each cruise are 1.04 and 23 cm/sec, respectively, for the November cruise, and 1.00 and 21 cm/sec, respectively, for the June cruise. These values are thought to be reasonable estimates of threshold U_* and U_{100} to be used in calculations of rates of transport and erosion.

1. INTRODUCTION

A field measurement program has been undertaken to determine the threshold erosion velocity for surficial sediments which are the cap material dumped as part of the COE capping project at the New York dredged material dumpsite.

Only the erosion experiments which were part of a more comprehensive field program are reported in this section.

1.1 Definitions and Objectives

The threshold for erosion may be defined by that value of bed shear stress or near-bed velocity just sufficient to cause particles on the bed surface to move. Suspension is not necessary after initial movement; neither is continuous movement.

Objective definitions or measurements of threshold conditions on even the simplest flat, smooth bed of well-sorted spherical sand grains are rare and not universally agreed upon. When one is possible it is only under laboratory conditions (see Yalin, 1972, for a detailed discussion). Seafloor sediments are rarely smooth, level or mono-sized. Therefore, other, perhaps subjective definitions of threshold conditions creep in where more objective ones fear to

tread. This is certainly the case in the present study where close-up photography of the eroding bed, capable of resolving features of .05 cm or larger, was the only measurement of bed conditions during erosion. Since the diameter of the bed sediments was around .01 cm, it is apparent that individual grain movement is not resolved and threshold conditions are defined on the basis of changes in bed microtopography. This may lead to overestimation of the threshold shear stresses, but hopefully not by a significant amount. Field methods used in this study were designed to minimize disturbance of natural bed conditions before erosion. Therefore, we assume that natural currents will erode the seafloor in about the same way and at about the same bed shear stress as we have observed here under experimental control.

Our objective is to measure the critical shear stress necessary to initiate erosion of the sand capping material. To do this requires measurements and observations of both fluid and sediment properties. We compare these measurements to the existing body of laboratory data on the erosional threshold of similar sediments. Finally, we will assess the factors which influenced field measurements of threshold shear stress and determine how they differ from laboratory conditions.

2. METHODS

2.1 Field

The primary tool used in this study was the SEAFLUME II, a device for in-situ studies of threshold erosion velocities and the resulting erosional behavior of undisturbed marine sediment. This instrument is a modified version of the original model described by Young (1977) and Young and Southard (1978) and is shown in Figure 1. The SEAFLUME photographically records bottom

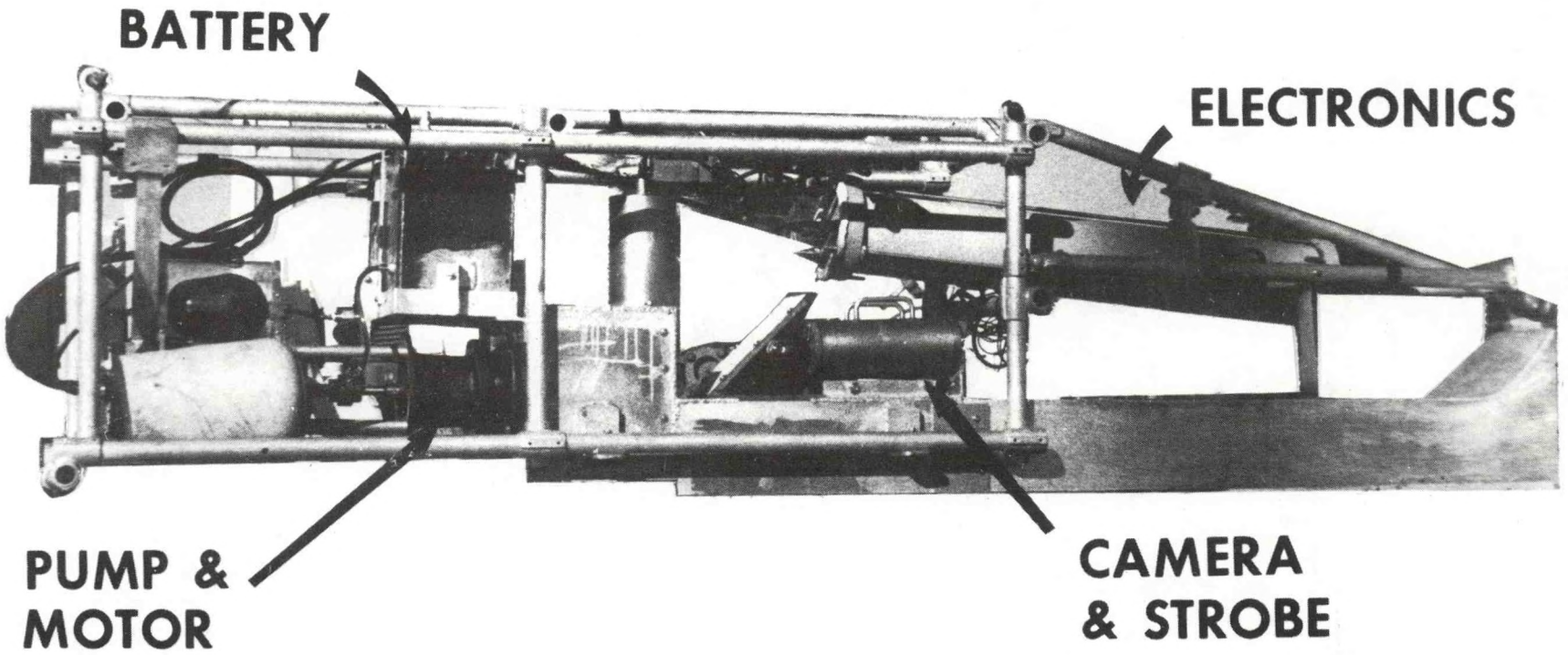

Figure 1: SEAFLUME used in this study. This version is similar to one described by Young (1977) and nearly identical to the one described in Young and Mann (1982).

sediment response to a systematic increase in flow velocity. The 35 mm camera is enclosed in a hood and the optical path includes a 45° mirror (Figure 1). Low angle side-lighting is provided by a synchronized strobe. Photos are taken at the rate of one approximately every three minutes, and about 17 photos were obtained per 45-55 minute flume run. Flow is produced by water being drawn through the three sided, aluminum-walled channel via a submersible pump and motor assembly mounted at the down-stream end. The working part of the flume channel measures about 2.3 m in length, .47 m across and .15 m in height. The bottom of the channel is formed by the seafloor. SEAFLUME is self-contained and can be operated automatically by means of a bottom contact switch. During this study divers accompanied the flume to the bottom to insure that the sediment formed a proper seal around the edges of the channel.

SEAFLUME sites were selected at current-meter deployment sites and other sites on the sandcap and dredge material dump areas shown in Figure 2. Three sites (SF8, SF9, and SF10) were chosen at other locations on the dumpsite just outside of the sandcap for comparison. Sampling took place during two separate cruises from 14 November to 20 November 1980, and 26 June to 30 June 1981, on the NOAA ship GEORGE B. KELEZ. Sea and weather conditions were good during both cruises.

Flow velocity in the channel of SEAFLUME was measured by several different sensors. A propellor flow meter mounted along the flow axis (General Oceanics, Model 2031) measured the mean flow through the channel core at the measurement section about 1.8 m from the entrance. A frequency-to-voltage converter changes the switch closure frequency, induced by propellor rotation, to a voltage which is recorded on a strip chart. An event marker on the strip chart recorded the times when photos were taken. The flow-meter signal is converted to flow velocity by the equation:

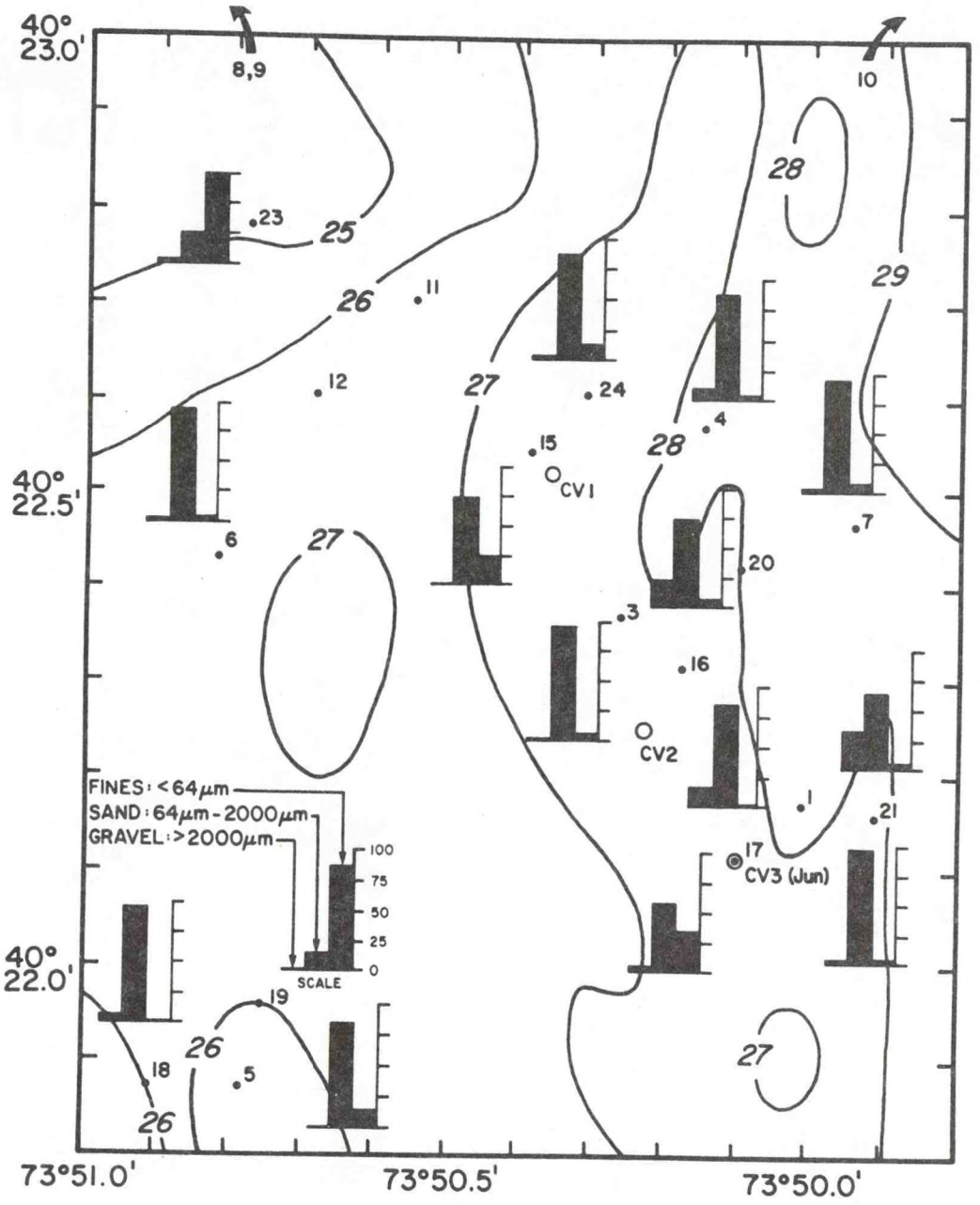

Figure 2: Location map for SEAFLUME sites on the sand cap area. Numbered dots are stations. Circles are sites of long-term current meter/transimissometer deployments. Histograms are explained in text (section 3).

$$V = 5.3 + .156\ (mv) \qquad (1)$$

where V is velocity of current in the channel in cm/sec, and mv the recorded millivolts from the strip chart (Figure 3). Because of propellor size (10 cm) and temporal filtering of the propellor output, propellor velocities are considered to have a 10 sec time constant. The values 5.3 and .156 are constants derived from laboratory calibration of the flow meter in a circular tow tank. This calibration plot is shown in Figure 3. It is estimated that V values calculated from the strip chart records are within ± 10% of actual values.

For the second (June 1981) cruise, an additional group of velocity sensors were added. Three small hot-wire velocity probes mounted on a vertical axis and a hot-film sensor (Gust and Patrick, 1981; Gust, 1982) mounted on an articulated plate below the lowest hot-wire probe were attached to a movable cage assembly (Figure 4). The cage was released after the flume contacted the bottom and was lowered by gravity along guide rails such that when the hot-film plate contacted the bed surface, downward movement ceased. This arrangement was only partially successful due to the unexpectedly low bearing strength of the sediment which allowed the hot-film sensor plate to bury itself in the mud in most deployments. In addition, hot-film sensors were installed inside the channel, on the top and on one side wall (Figure 4). Comparisons between wall stress calculated from the propellor flow meter and observed by the stress sensors are described later in the RESULTS section. Data from all hot-film and wire sensors were sampled and recorded digitally at 1 Hz on magnetic cassette tapes in a pressure housing mounted on the flume frame. Start and stop times on this recorder were electronically synchronized with the propellor flow meter recorder.

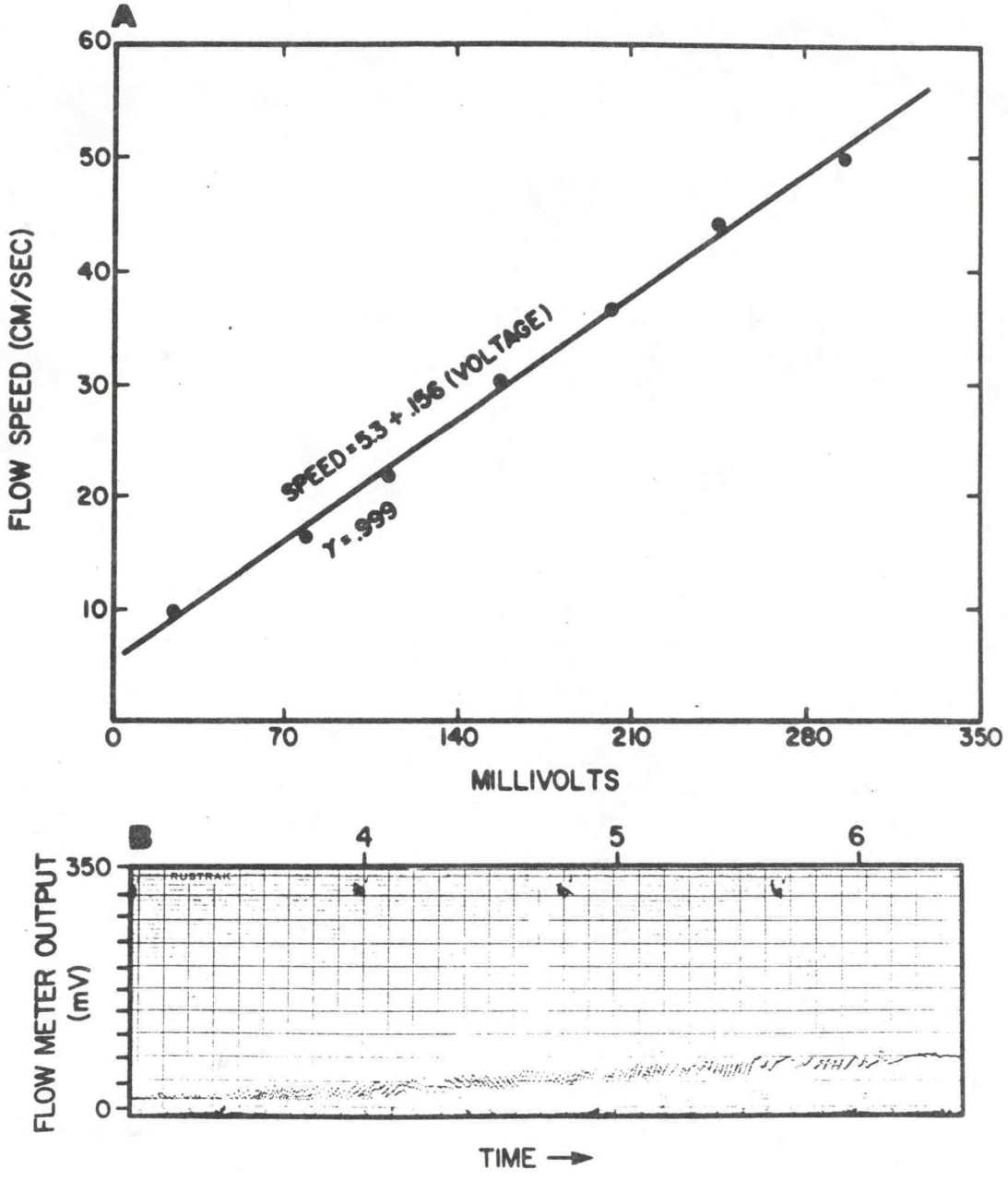

Figure 3: Calibration of propellor flow meter (lower) and example of propellor output to chart recorder (upper).

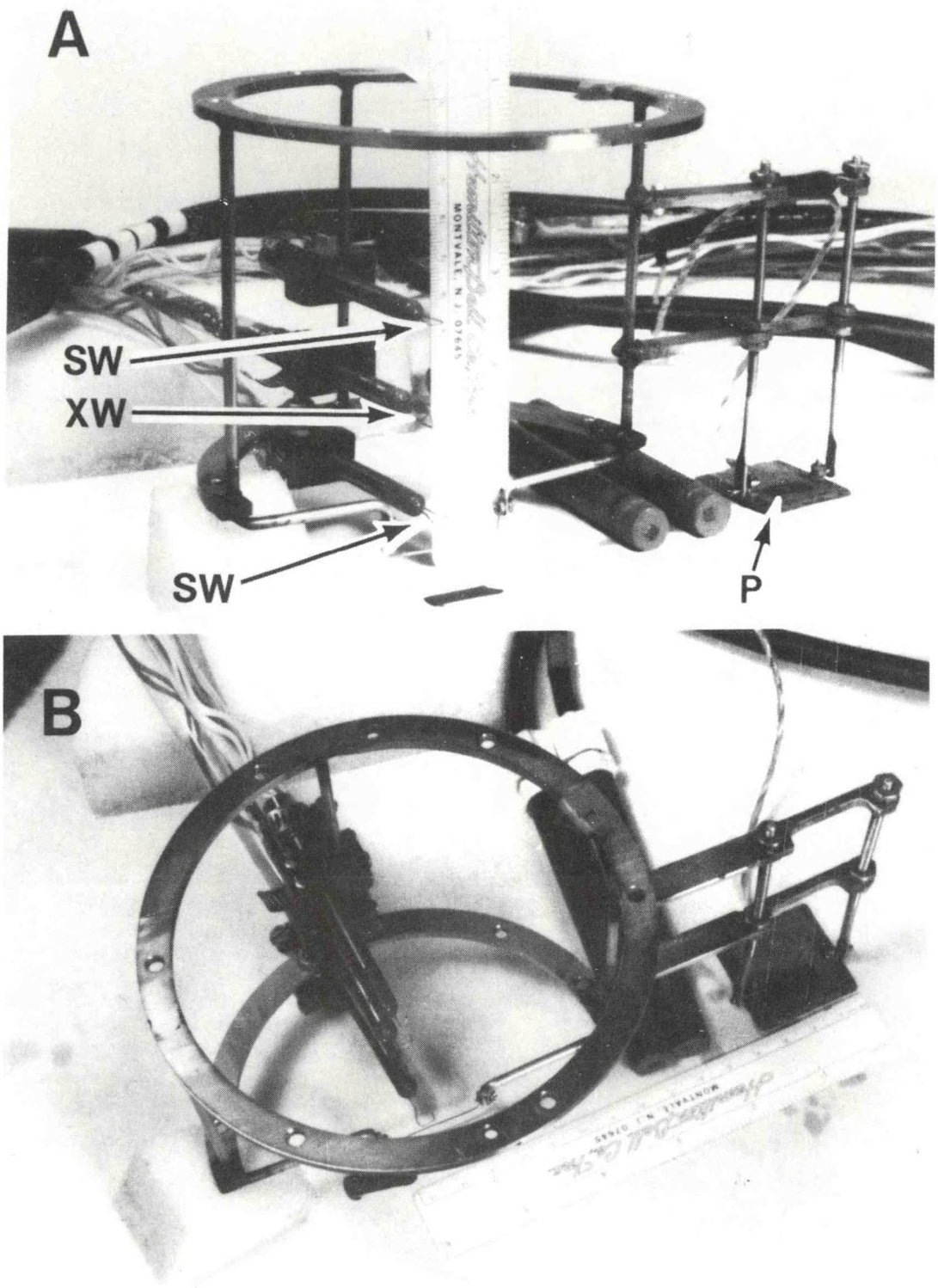

Figure 4: Support system for hot film drag plate and hot-wire flow sensors. SW: single hot-wire probes. XW: crossed-wire probe. P: hot-film plate.

A total of 25 SEAFLUME runs were attempted for this study. Bottom core samples were taken next to the SEAFLUME at each site by SCUBA divers. Cores were taken by shoving PVC pipe 6.25 cm in diameter vertically 12 to 38 cm into the sediment. Both ends of the pipe were then capped and the retrieved cores frozen until analysis could be performed at the laboratory.

2.2 Experimental Conditions

Bottom conditions were highly variable in the sand cap study area. While some sites were fairly smooth, many were covered with irregular mounds and pits ranging in size from centimeters to meters in horizontal or vertical scale. This was also observed on side-scan records, described elsewhere. During several deployments divers found the flume had been placed over large gullies or on dumped debris. The flume was retrieved and relocated by the ship in those instances. Later it will be shown that the seafloor enclosed by the flume was often irregular, certainly not the flat, smooth conditions desired for maximum confidence in the measurement of critical erosion velocity.

Visibility at the bottom was 0.-1.0 meters and the water was usually turbid. This prevented photography of bed features of scales between flume-size and those resolved by side-scan. We are, therefore, unable to comment on the exact nature of bed roughness outside the flume, except to cite divers' reports that no ripples were encountered at any flume site.

2.3 Laboratory Analysis

Positive prints were made for each run and examined in sequence for changes in the bedforms and features. Evidence of movement could be detected, for example, by appearance or disappearance of embedded shell material,

changes in the shape of mounds or ridges, filling of depressions, and in some cases the changes of appearance to shadows. The photo which indicated incipient motion of the bed was correlated with velocities from flow meter, hot-film and hot-wire recordings. Notes for each run indicating features chosen to characterize threshold are given in Appendix A.

Runs for which partial or no propellor flow meter data was obtained (due to malfunction of the recorder or the flow meter) required extrapolation or interpolation from known data. For such cases, flow velocities were taken from the hot film sensors, or flow meter records from several other runs were averaged and a linear first-order curve was fitted to the average velocity and elapsed time data (See RESULTS).

Grain size analysis of core samples from SEAFLUME sites were perfomed to relate the estimated threshold velocity for each run with the particular type of sediment present. Cores were first examined visually for evidence of vertical size fractionation and the length of the core sample was recorded. The cores were then prepared for a standard sieve analysis. When more than one core had been taken from the same site, the samples were combined and homogenized to produce one representative sample. SF1, SF3, SF4, SF6, and SF7 were dried in an oven at 100°C. The remainder of the samples were freeze dried. The sieve analysis yielded percent by weight of fines (< 64 μm), sand (64-2000 μm), and gravel (> 2000 μm) in the sample. When the fine fraction was relatively large, pipette analysis was performed to separate the fines into < 4 μm, 4-16 μm, 16-32 μm and > 64 μm fractions. Further analysis of the sand fractions were performed for all samples by using an automated settling tube (Nelsen, 1976).

2.4 Threshold Calculations

Several velocity profile equations were tested and evaluated for determination of threshold values of shear stress at initiation of erosion. The rough-walled form of the law-of-the-wall equation describing velocity profiles in turbulent boundary layers is given by

$$\frac{U}{U_*} = \frac{2.3}{k} \log\left(\frac{Z}{Z_o}\right) + C. \qquad (2)$$

Here $U_* = (\tau_T/\rho)^{1/2}$ is the friction or shear velocity, U is velocity at height Z above bottom. k is Von Karman's Constant ($\simeq 0.4$), C is a constant dependent on from the nature of the channel, and Z_o is a measure of bed roughness often taken to be the representative grain diameter/30 for uniform sediments.

To apply law-of-the-wall equations, the flume boundary layer must be fully developed at the measurement point, and the flow steady and uniform. Changes in velocity develop slowly during the experiment ($dU/dt \simeq 0.89$ cm/sec/min) so that the flow is considered quasi-steady. In the center of the channel the side-wall boundary layers are assumed to have little affect on the vertical velocity distribution because of the 4:1 width to height aspect of the channel, and the channel water properties (ρ, ν) are assumed unchanged from the ambient exterior conditions; hence, the flow is assumed to be uniform.

To determine if the velocity profile is fully developed at the measurement section, we use the equation given by Schlichting (1968, Chap. 2) for estimating turbulent boundary layer thickness δ at distance x along a flat smooth plate. This gives, for velocity V = 15 cm/sec and distance x = 200 cm, $\delta = 0.37\ (Vx/\nu)^{1/5} \simeq 6.0$ cm, assuming that development of the boundary layer begins at the entrance.

Since smooth flow conditions were assumed, the thickness estimated for δ is conservative, because rough walls cause more rapid growth and greater thickness of the boundary layer, all other factors being equal. This assumption is critical to developments which follow and will be evaluated in light of the experimental results later in this work.

The Shields curve, derived through dimensional analysis, is probably the best recognized of all threshold curves. The ordinate of the curve represents the Reynold's number (Re_*) and is given by:

$$Re_* = \frac{U_* d}{\nu} \tag{3}$$

and the abscissa represents the Shields threshold criterion given by:

$$\theta_t = \frac{\tau_T}{(\rho_s - \rho)\, gd} = \frac{\rho\, U_*^2}{(\rho_s - \rho)\, gd} \tag{4}$$

where d is a representative mean diameter of the bed sediment, ν is the kinematic viscosity, τ is bed shear stress, ρ is the fluid density, ρ_s is sediment density, and g the gravitational constant.

The Yalin curve is very similar to Shields' (cf., Figure 10). The abscissa remains exactly the same. The ordinate in Yalin's curve, $\sqrt{\Xi} = Re_*/\sqrt{\theta_t}$, differs from Shields' in that it combines θ_t and Re_* in such a manner as to eliminate dependence on shear velocity. For this reason the Yalin curve is probably the most useful one available for determination of sediment incipient motion (Miller et al., 1980). Yalin also claims that his curve is more sensitive for grain sizes at small values of Re_*.

3. RESULTS

Figure 6 presents a key to aid in identification of the features seen in the SEAFLUME photos. Photographs in Figure 6 a-t show the initial condition of the seabed and the threshold for motion for each SEAFLUME run. Comments are included in Appendix A to aid the reader in understanding the criteria used for the selection of a given threshold photograph.

Determining the threshold for some runs, as in run SF1 (Figure 6a) was straightforward in that initial changes to the bed were easily seen. Other runs, such as SF6, (Figure 6f) were difficult to judge and required a more subjective approach. During the November experiments (SF1-7) the camera-mirror system was not well sealed and particles often settled out onto the window on the flume top, partially obscuring the bed. A new mirror-window assembly, sealed and filled with clear water was installed for the June cruise and picture clarity was much improved.

For SF17 and SF24 the photographs showing incipient motion could not be identified. This was due to poor picture quality as a result of insufficient lighting (SF17) and the presence of suspended material between the camera lens and the bottom (SF24). Also, flow during SF24 was altered due to a foreign object becoming lodged in the channel. This affected the results of this run and hence no threshold photograph was selected. Where photographs from a SEAFLUME deployment are missing in whole or in part, either an aborted run occurred or mechanical difficulties prematurely terminated the run.

When flow meter data were incomplete or missing but sediment and photographic data were of good quality, velocities were interpolated from other runs or from partial data. Examples are shown in Figures 7 and 8 of curves for SF5 and SF20 from which the threshold velocities were picked.

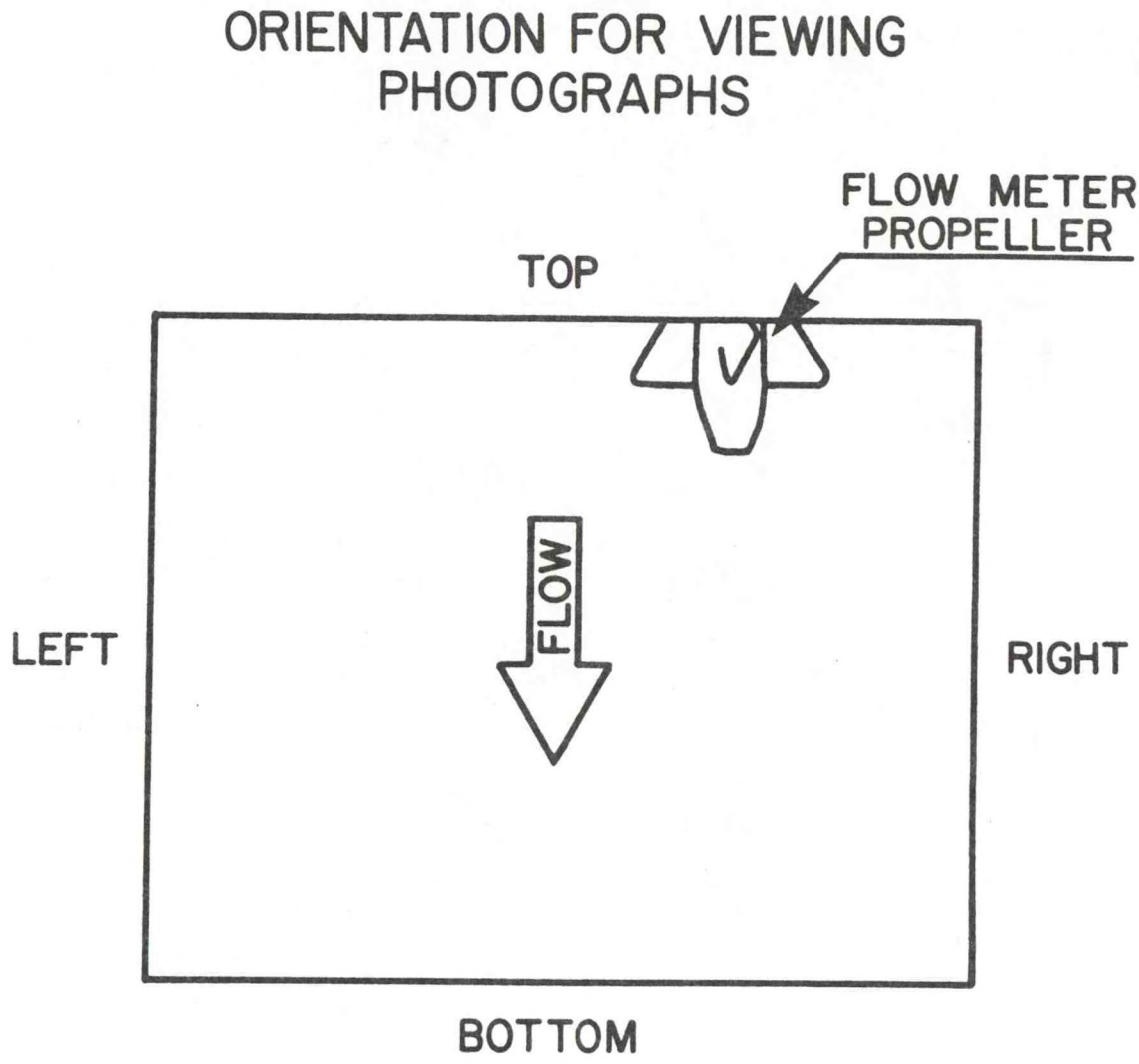

Figure 5: Schematic drawing of a typical seafloor photo taken by the SEAFLUME camera. The directions left and right, and flow direction, are referred to in Appendix A in descriptions of the bed surface during erosion.

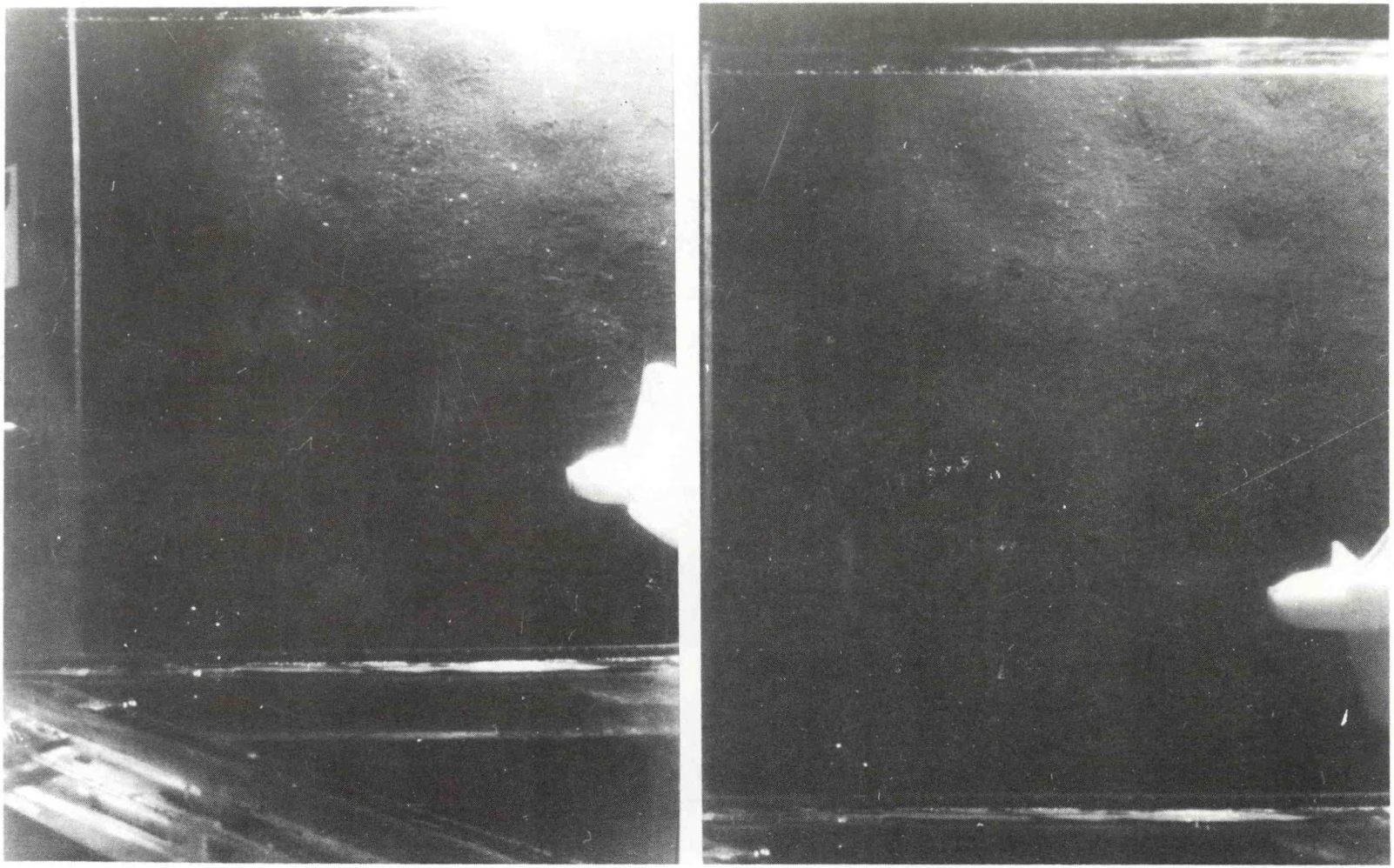

Figure 6a-t: Photos showing bed surfaces before erosion and immediately after implacement of SEAFLUME (upper) and at the threshold condition (lower). Refer to Appendix A for guidance in interpreting features used to estimate threshold.

SF-2

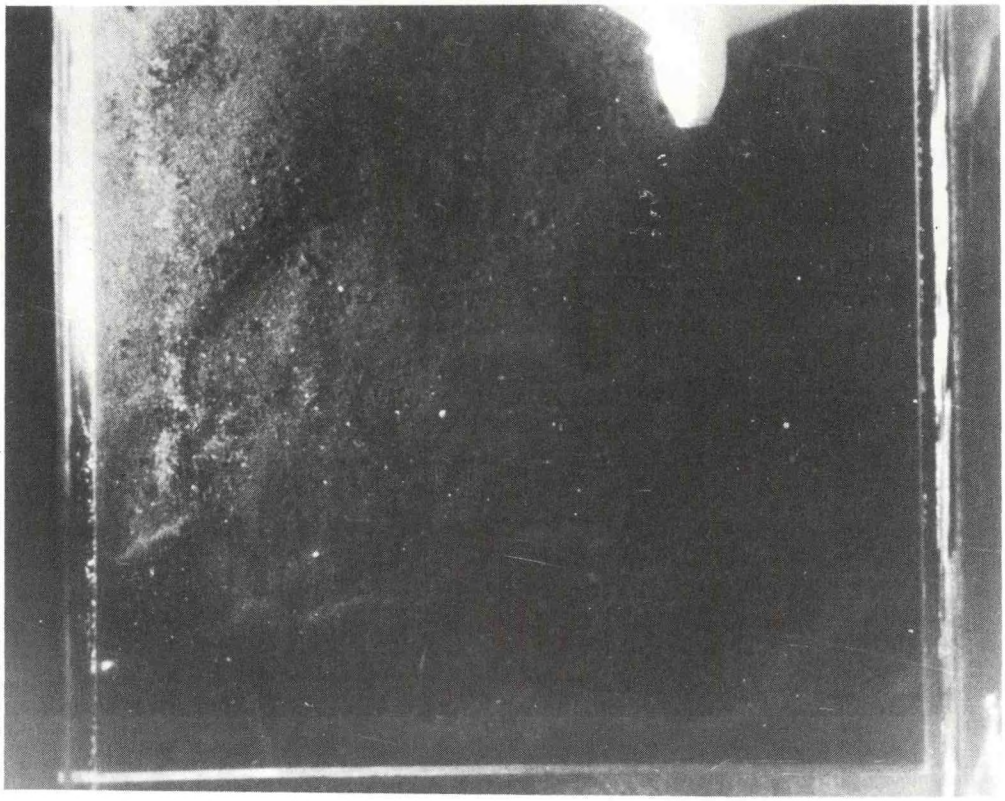

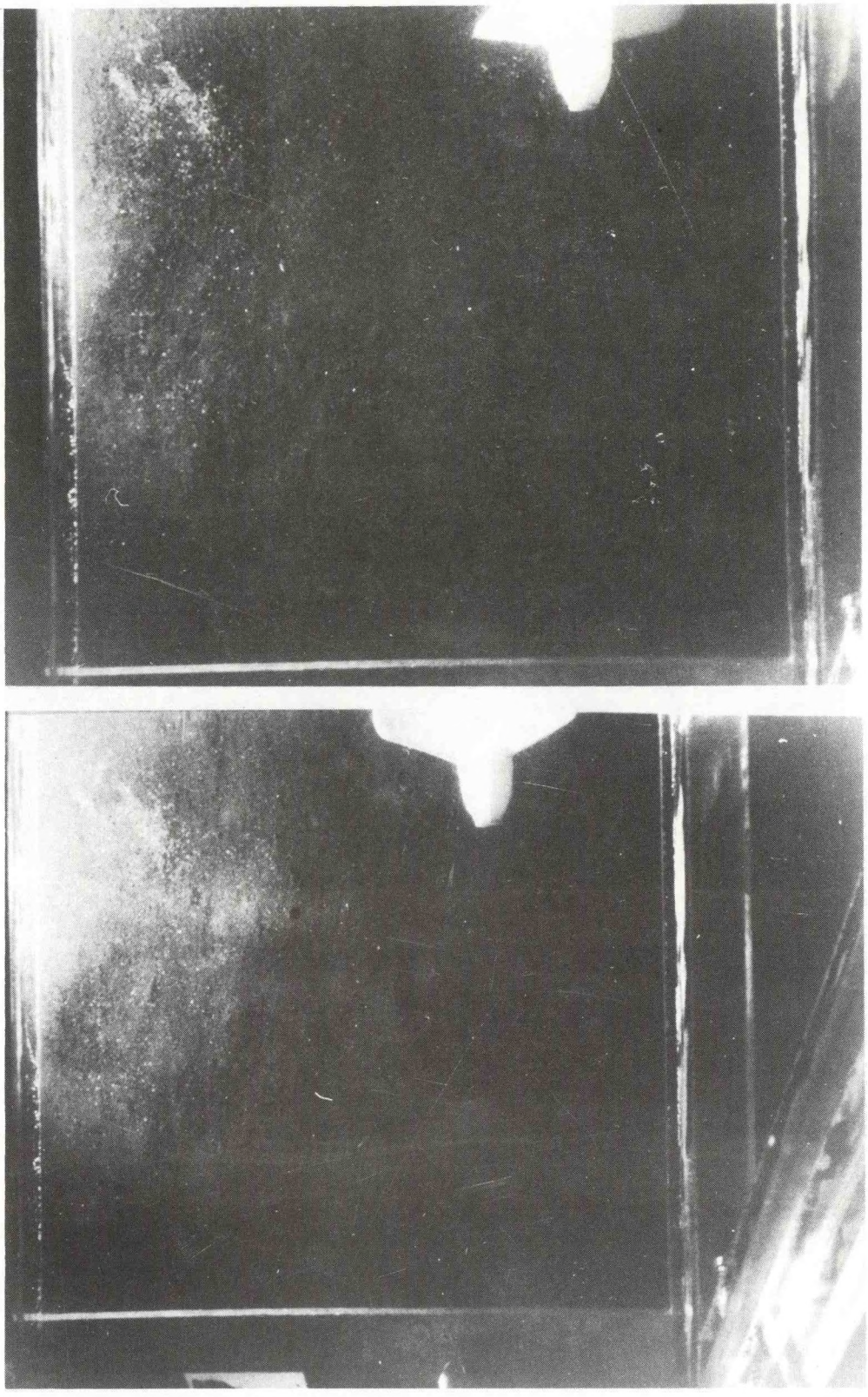

Figure 6c

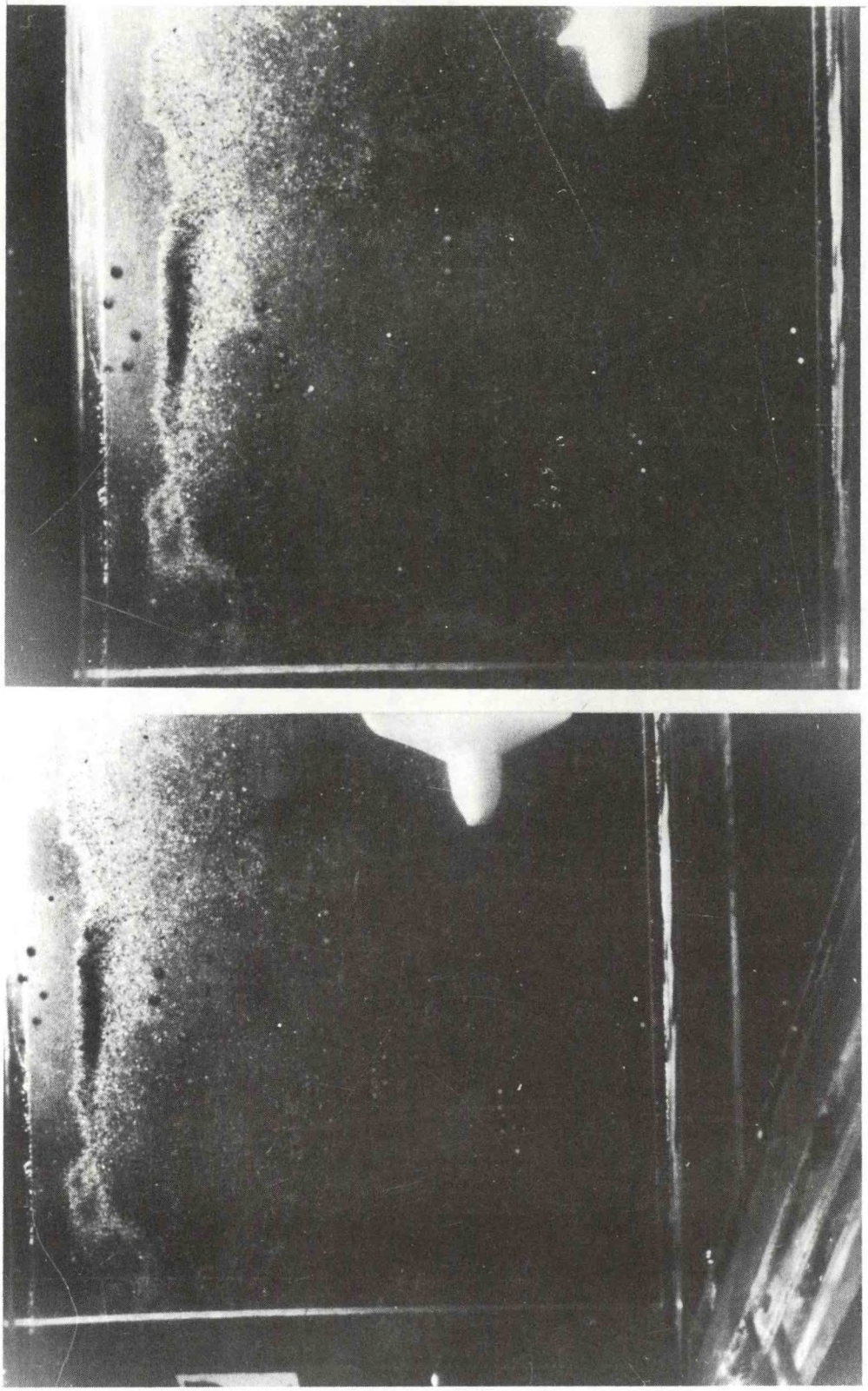

Figure 6d

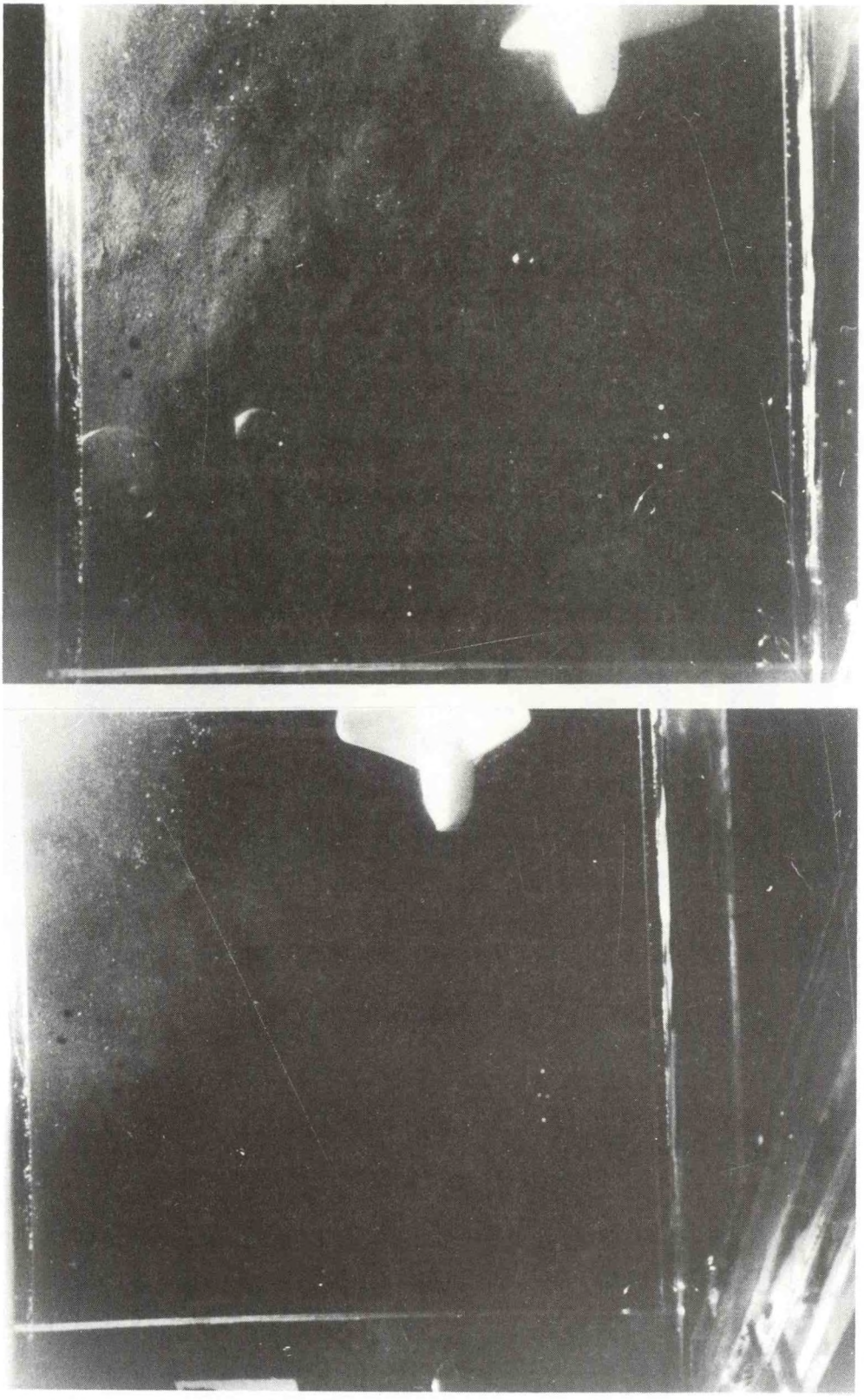

Figure 6e

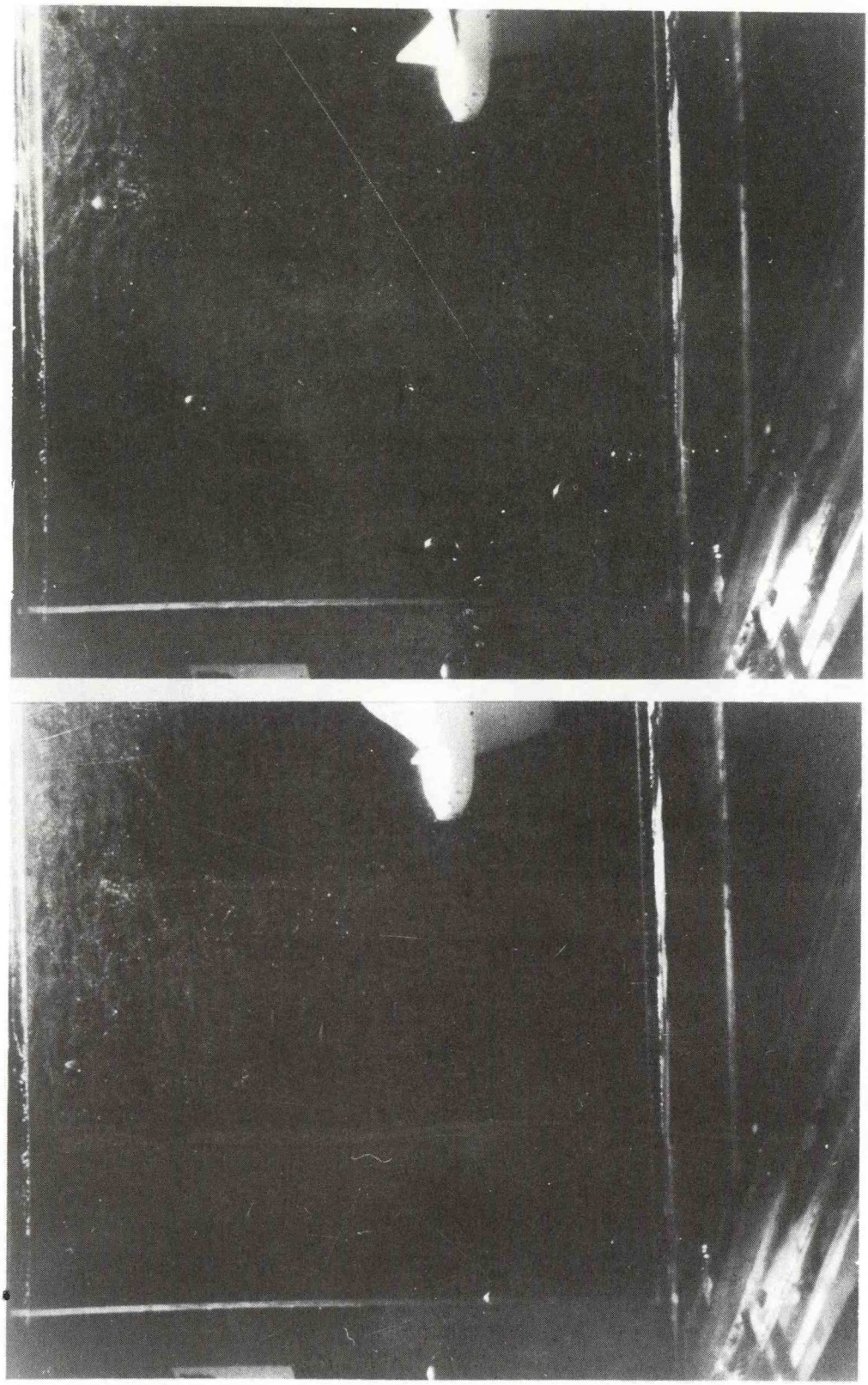

Figure 6f

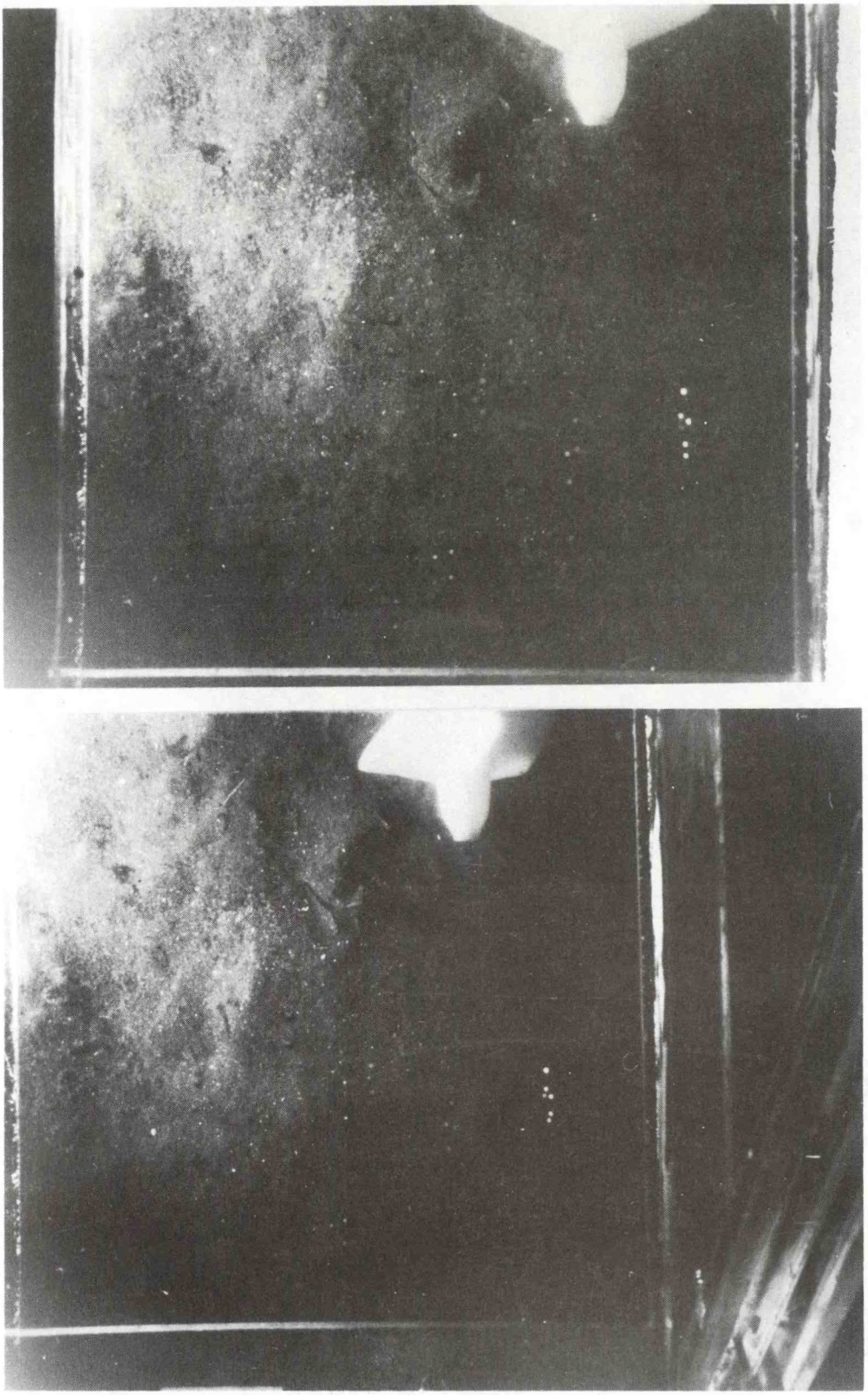

Figure 6g

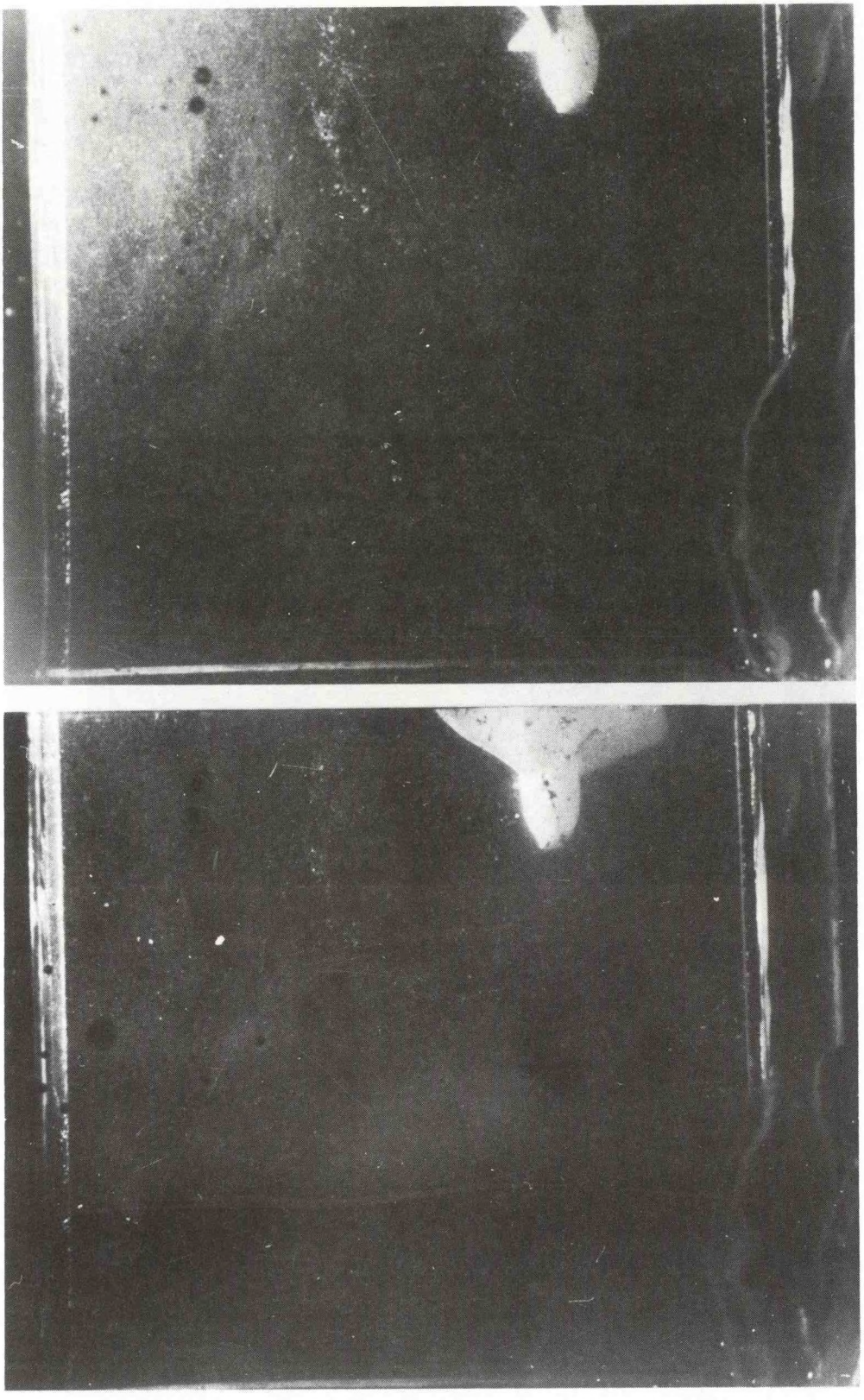

Figure 6h

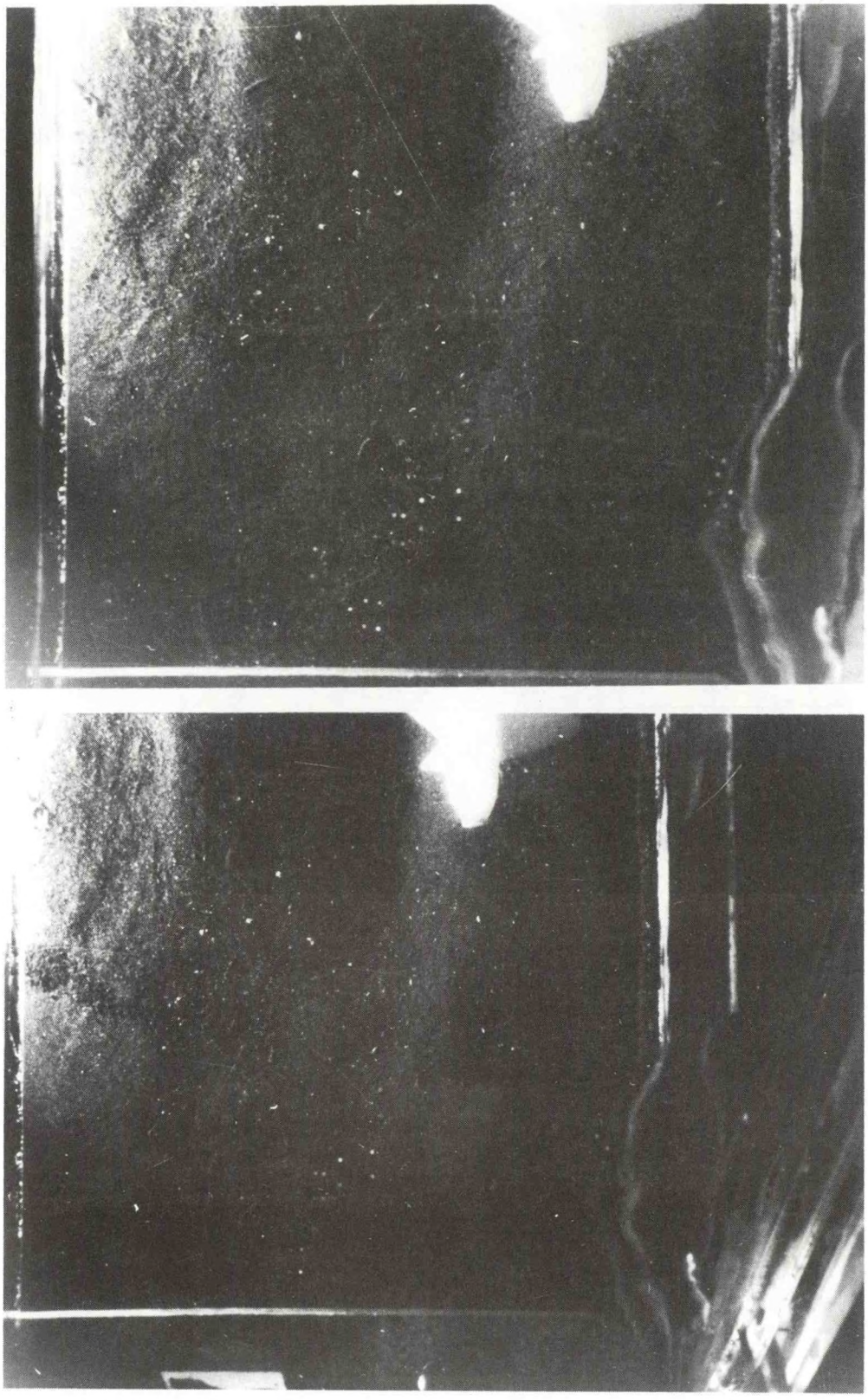

Figure 6i

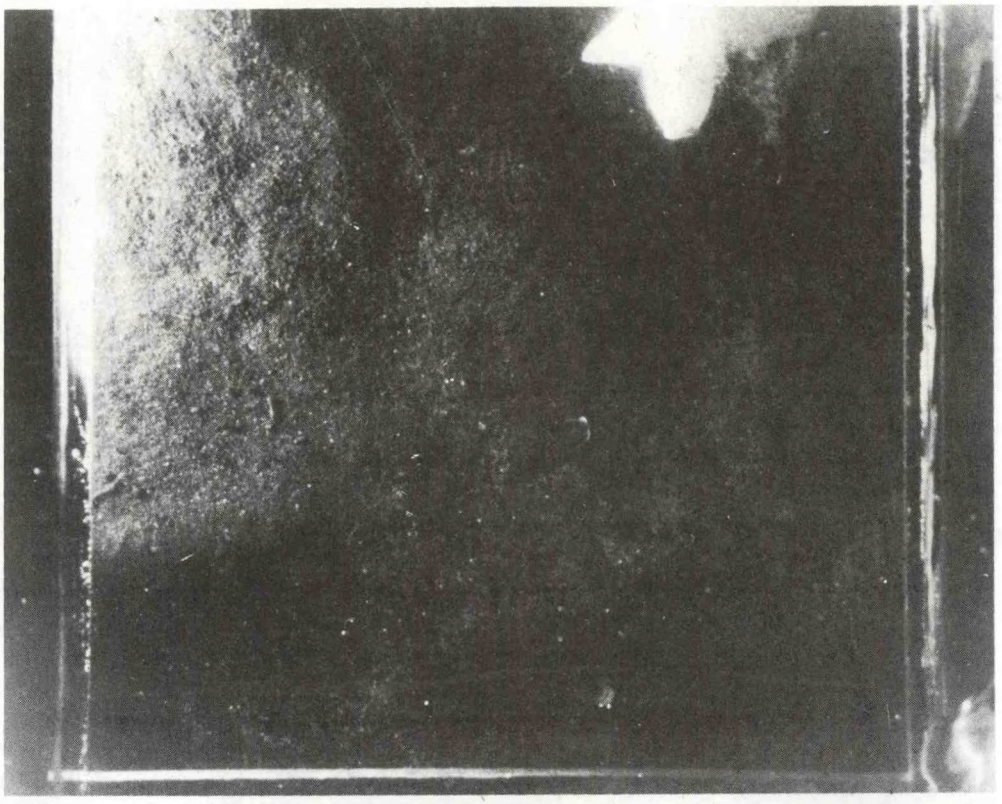

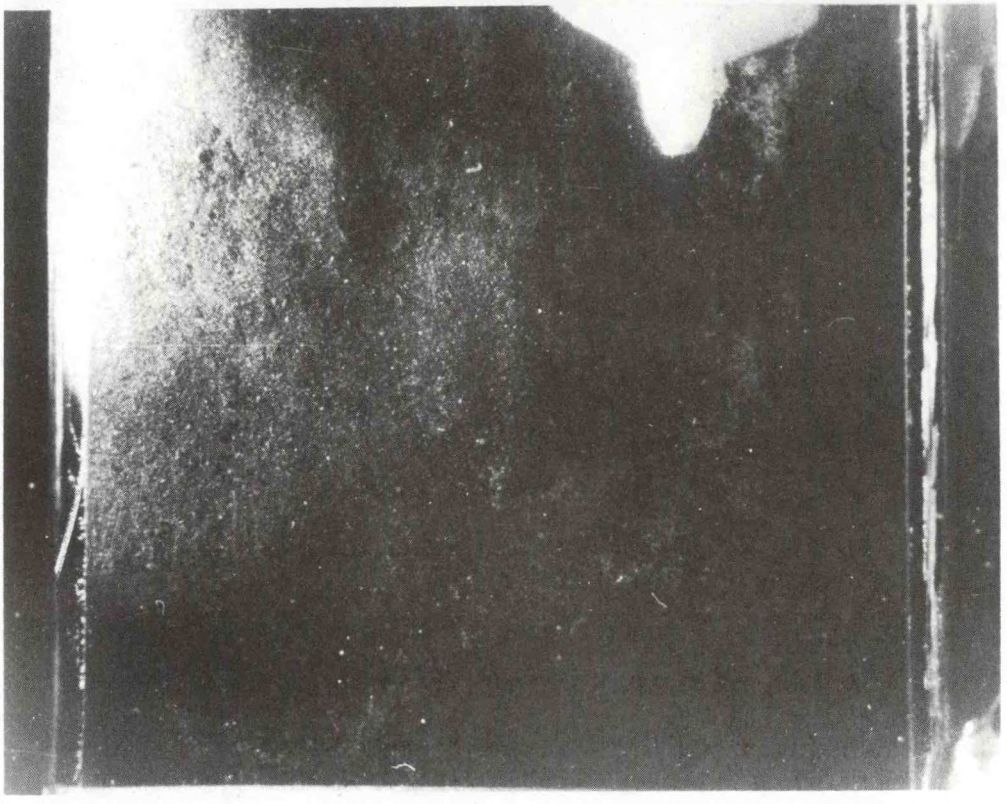

SF-15

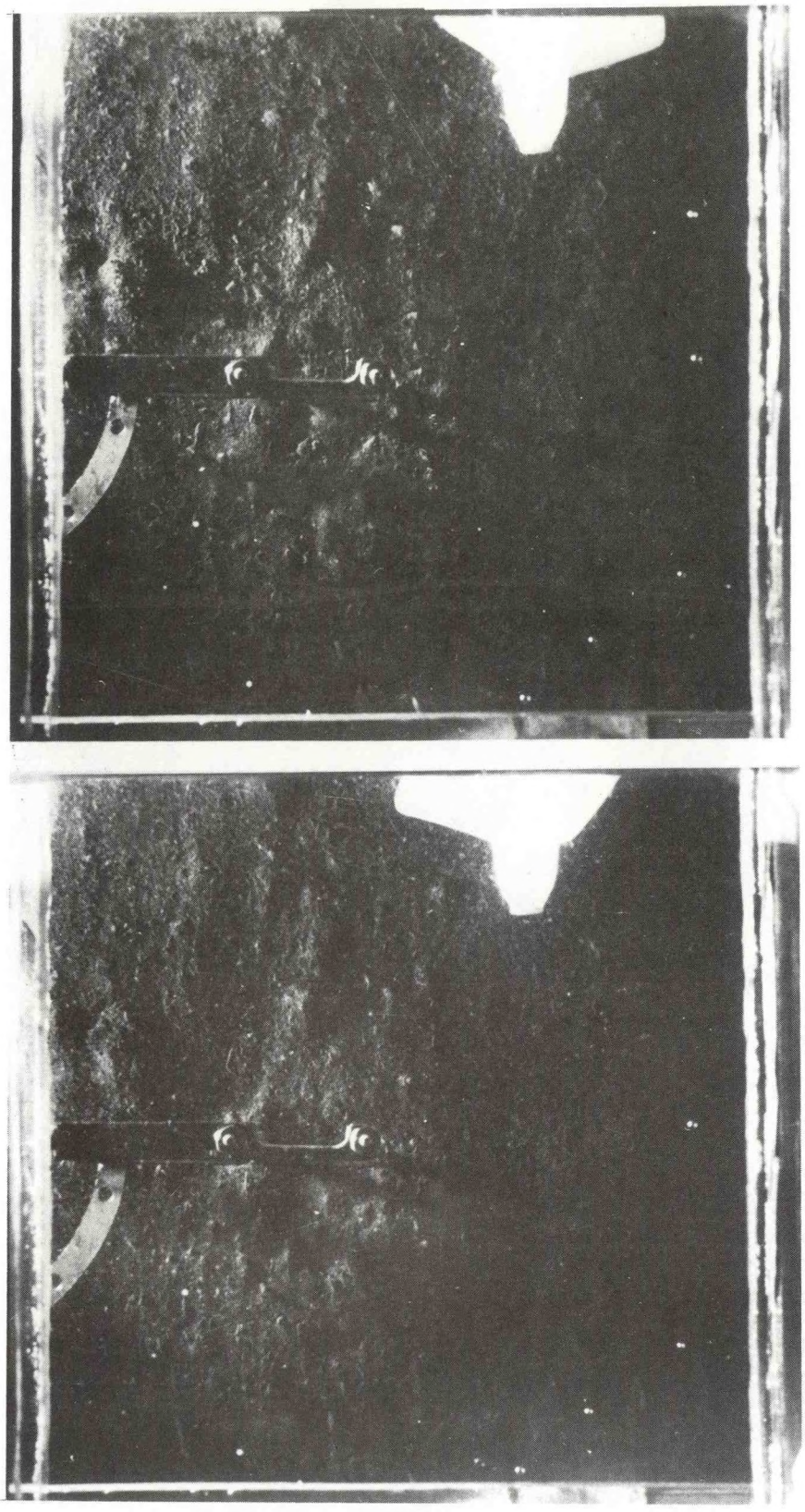

Figure 6k

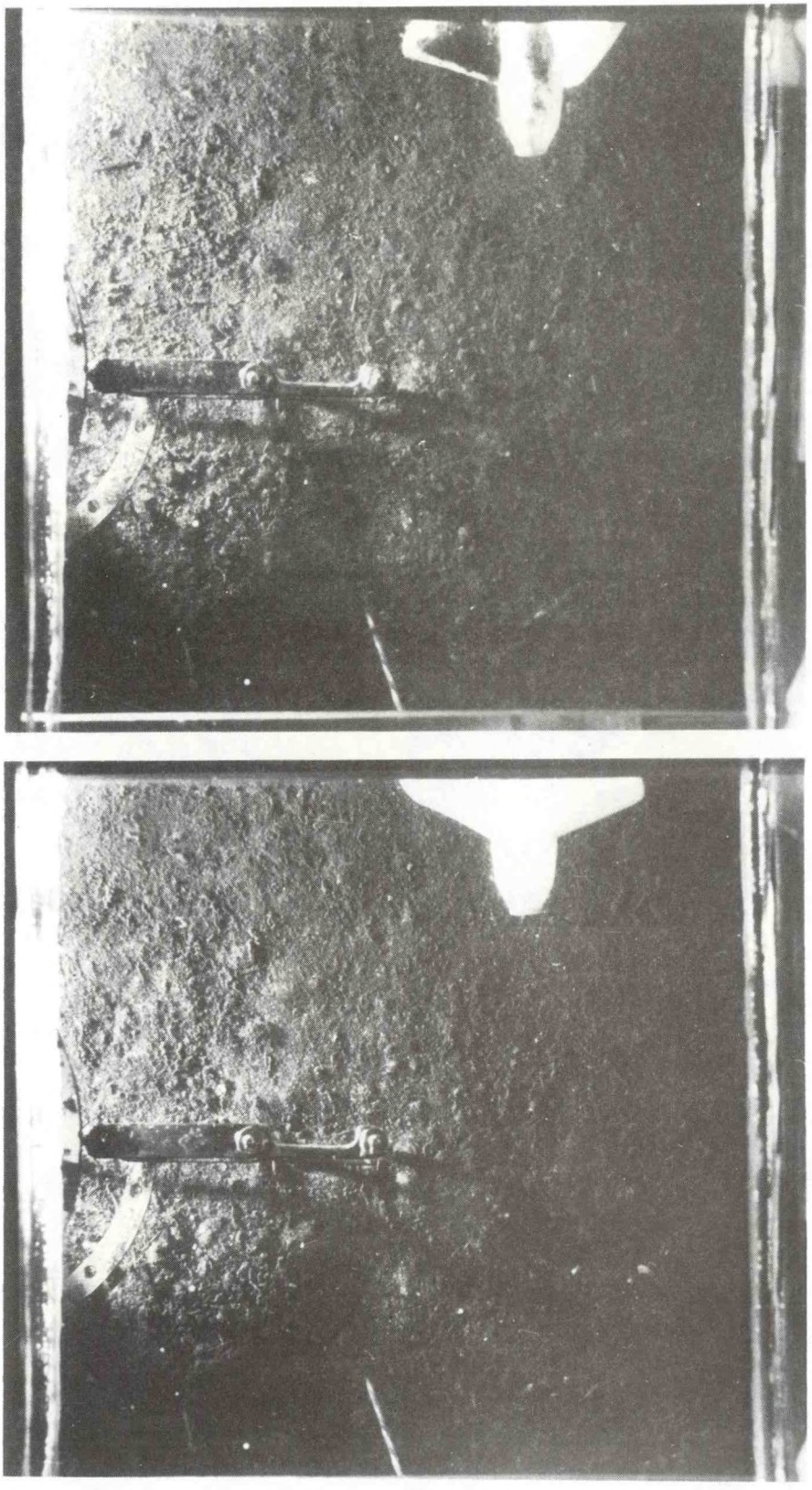

Figure 61

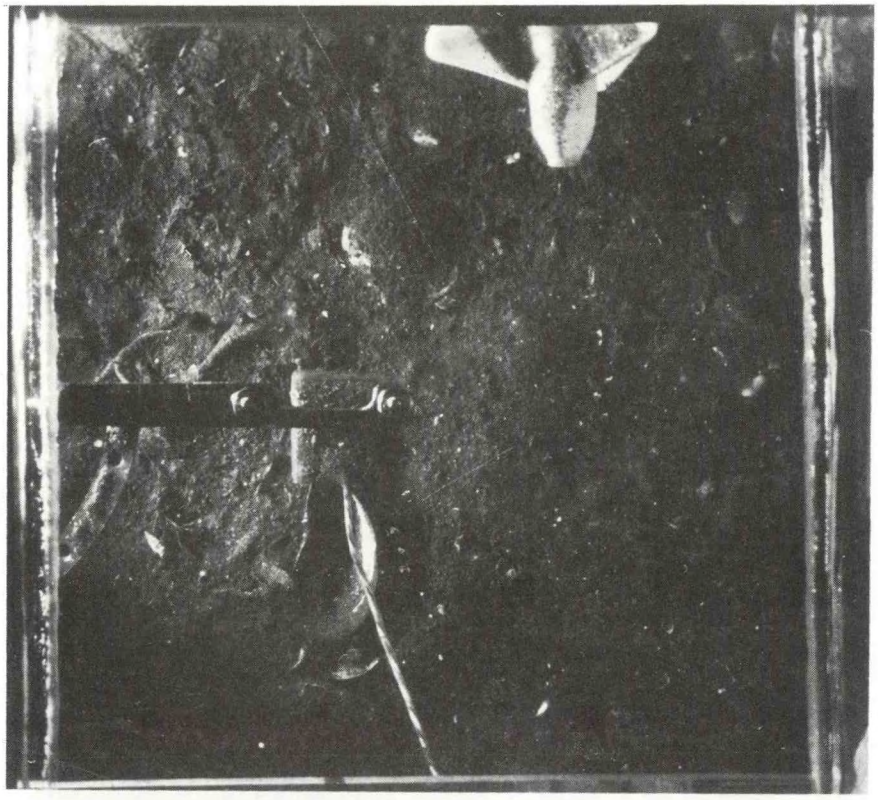

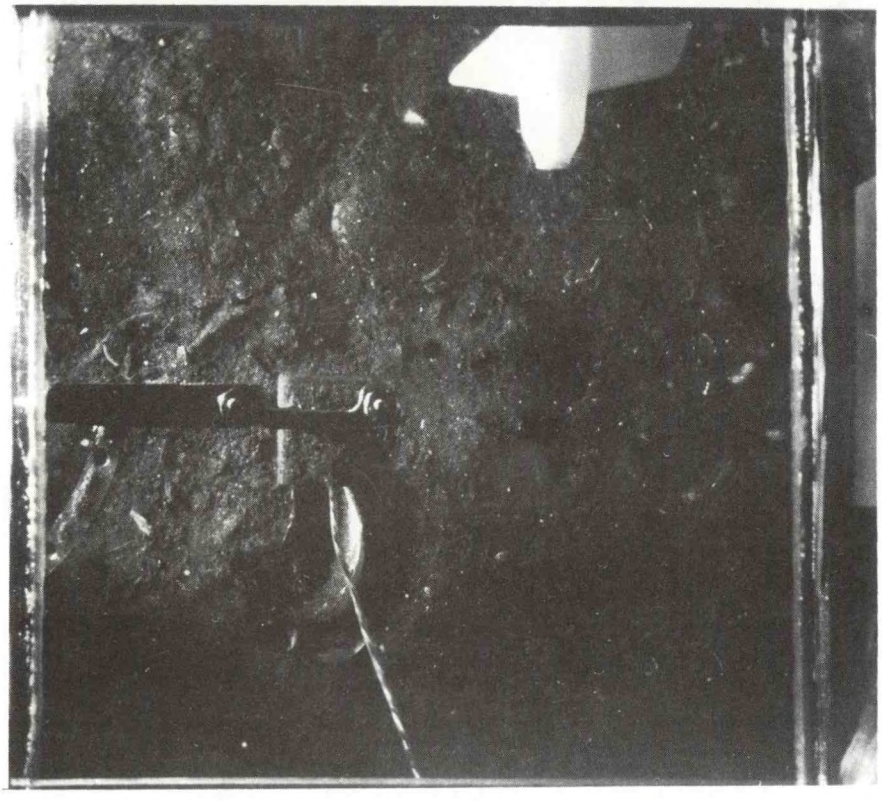

SF-18A

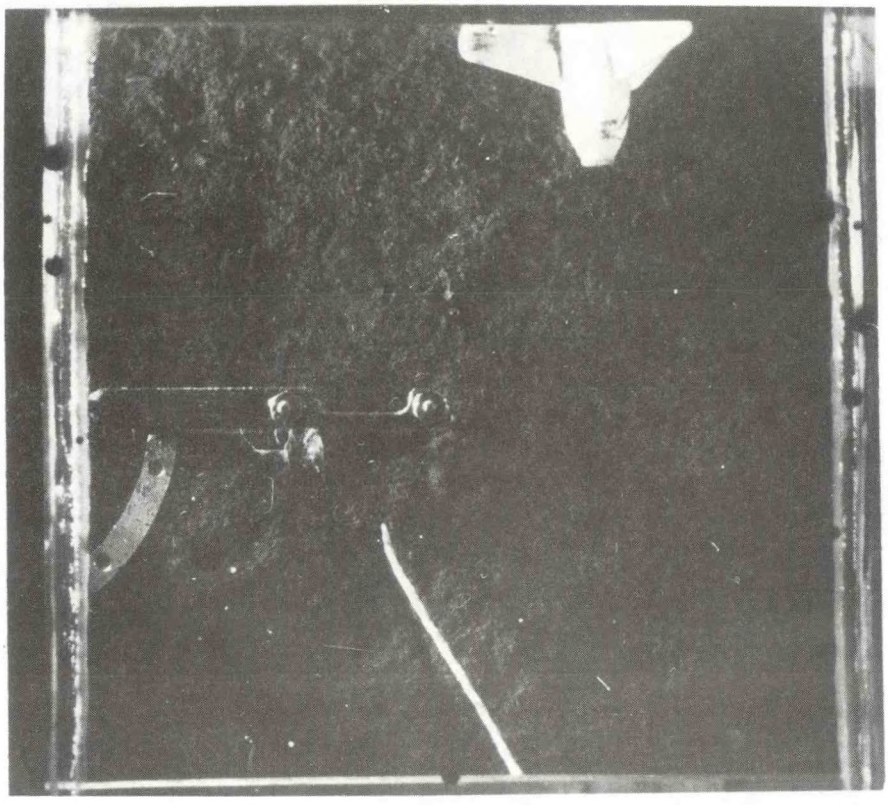

Figure 6n

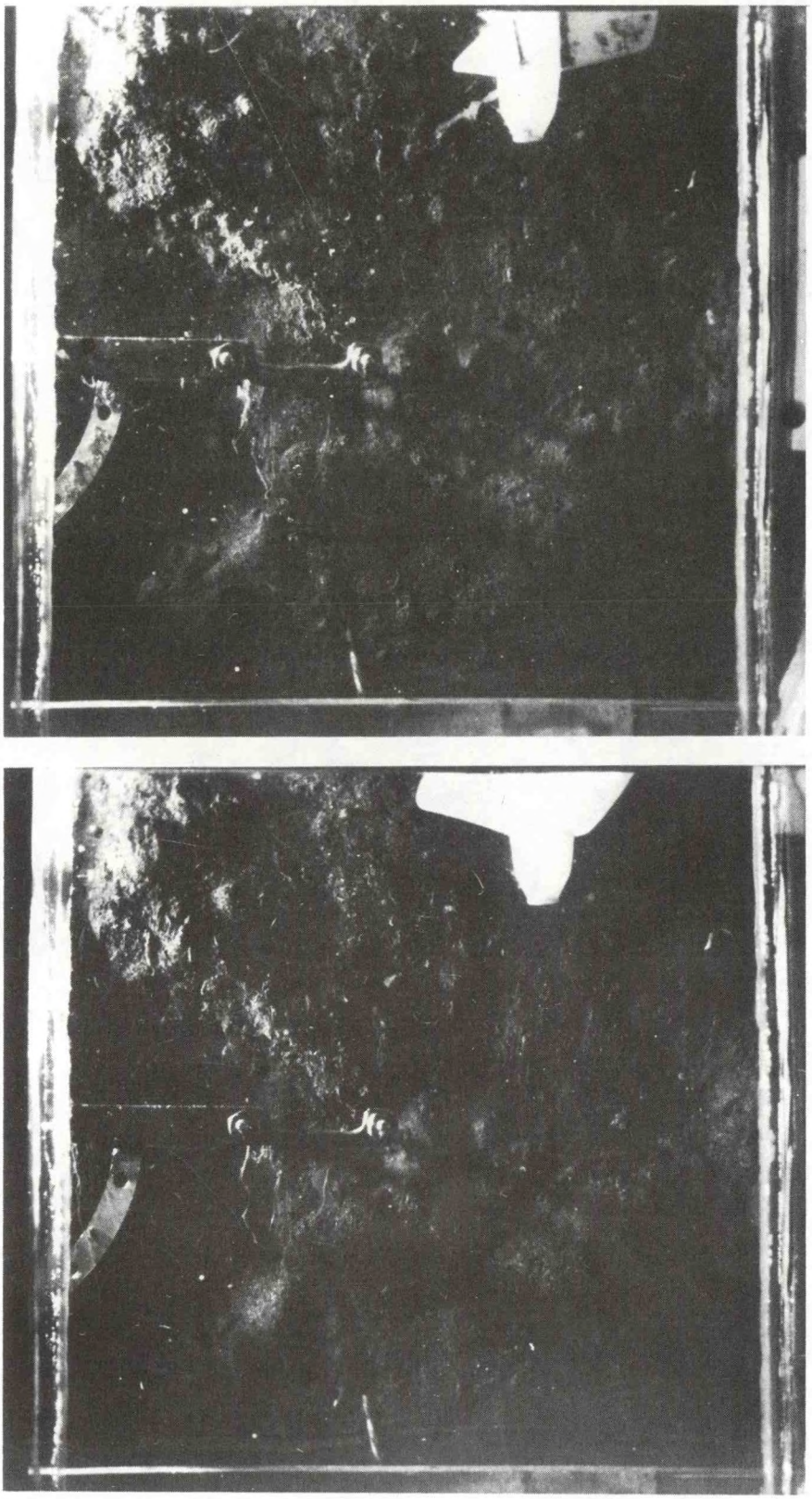

Figure 6o

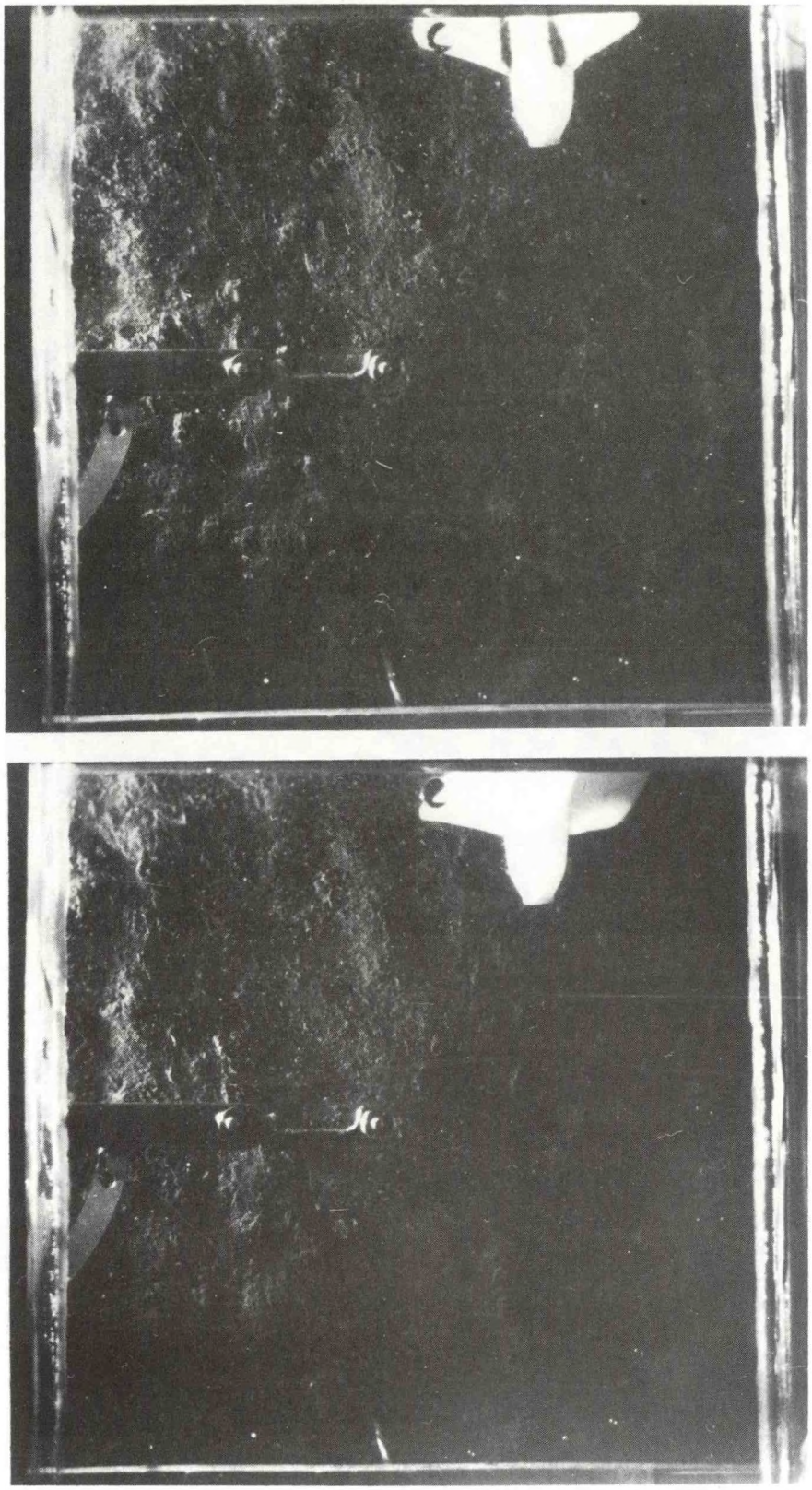

Figure 6p

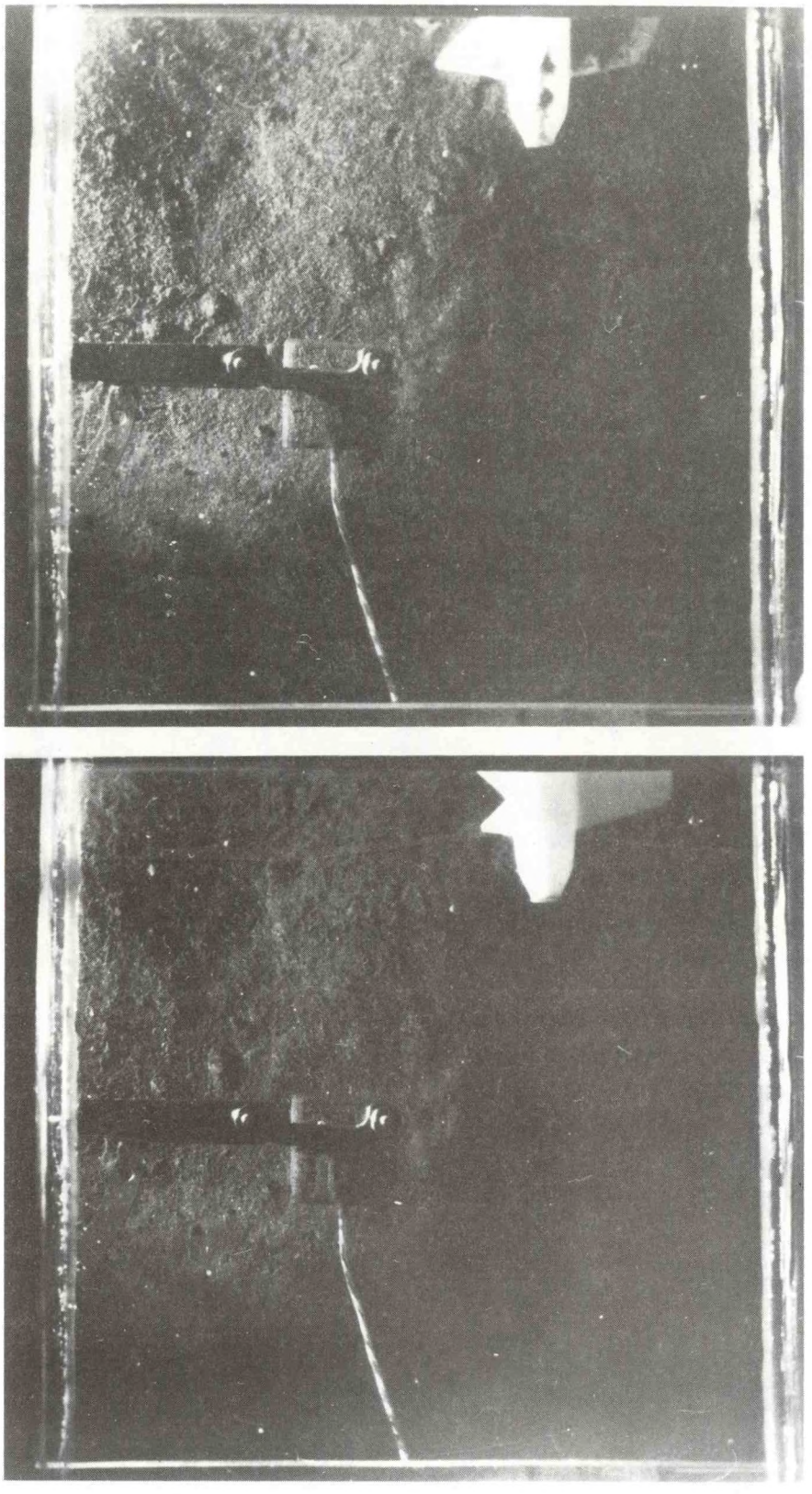

Figure 6q

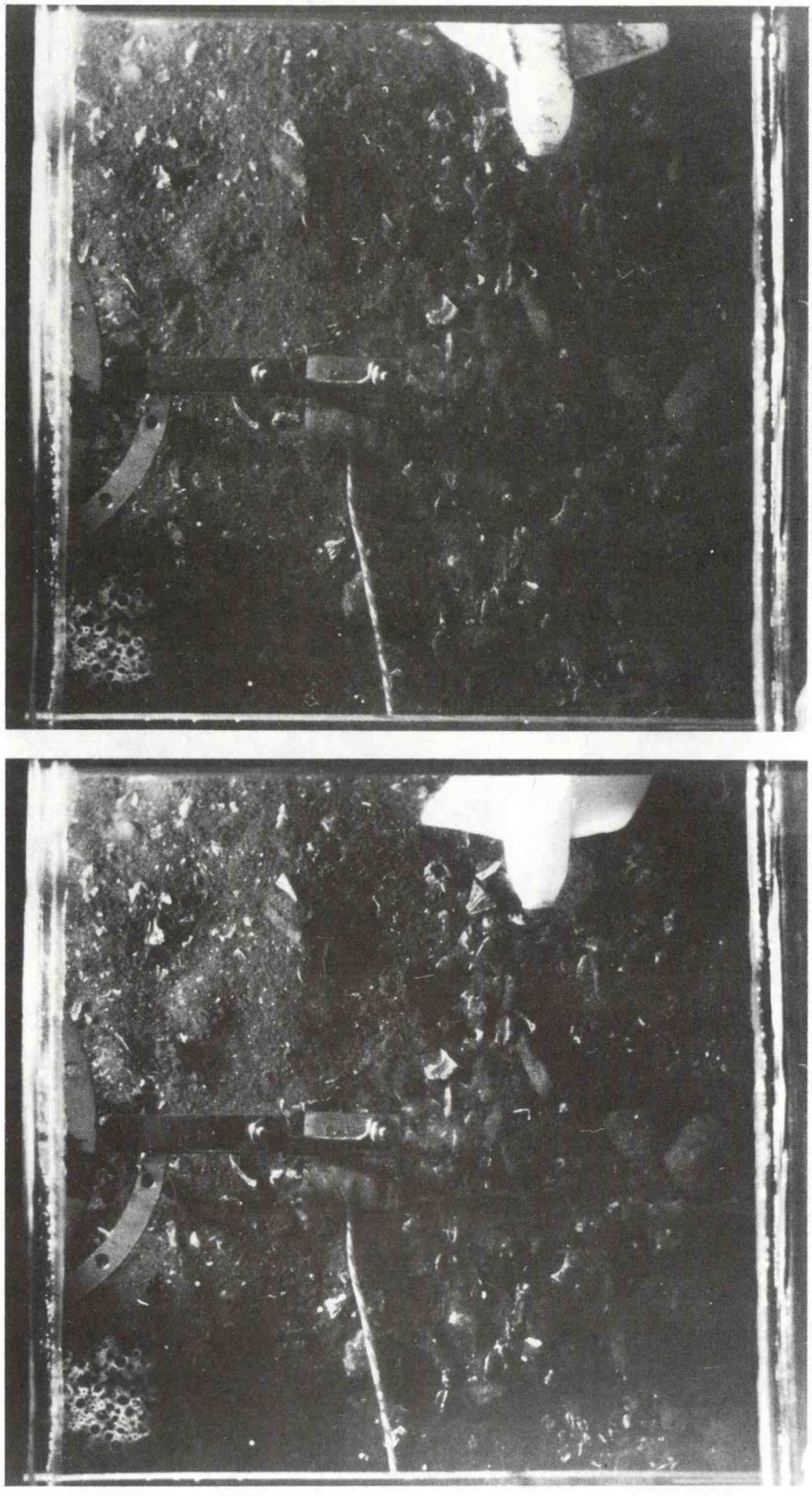

Figure 6r

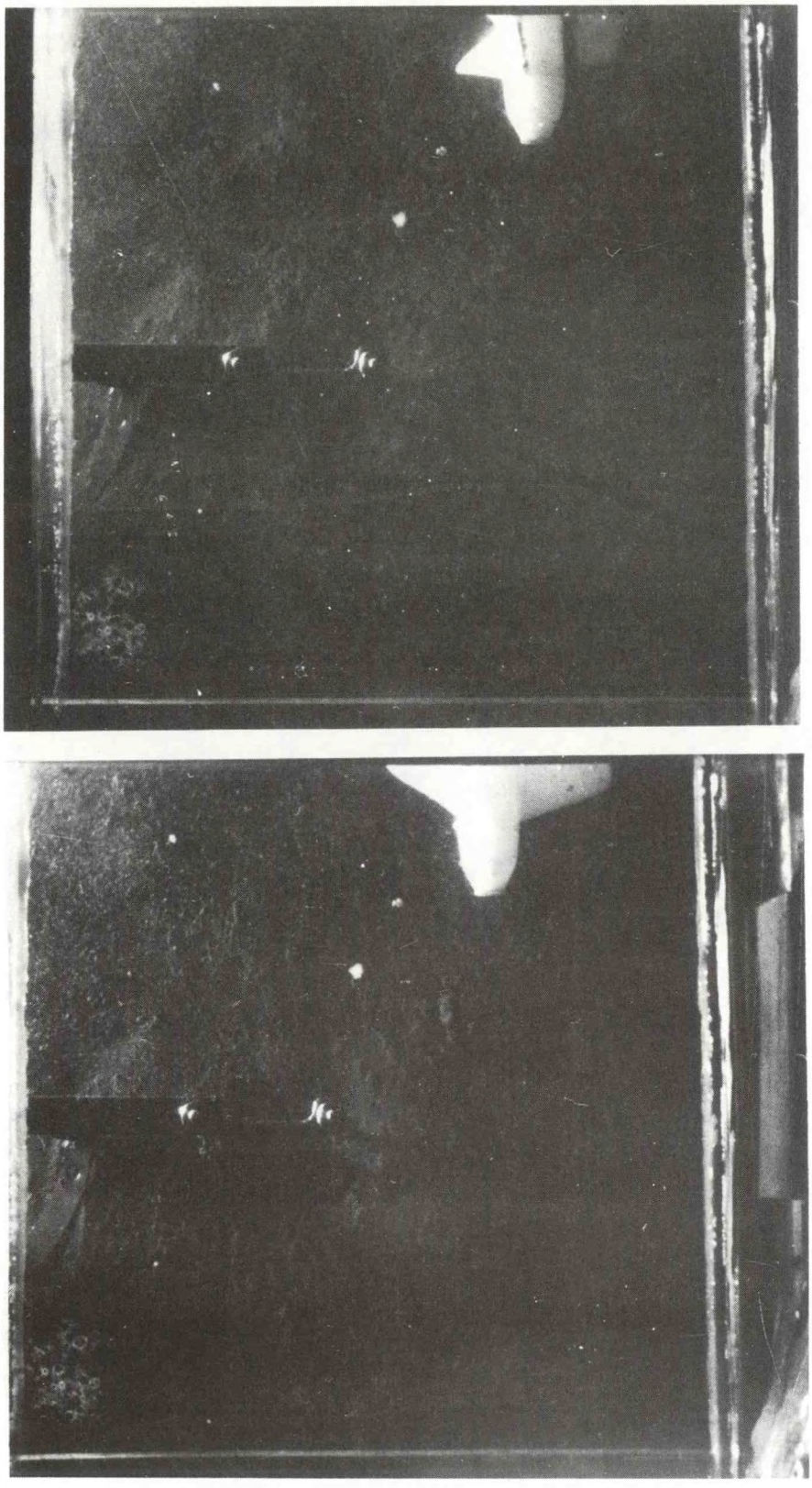

Figure 6s

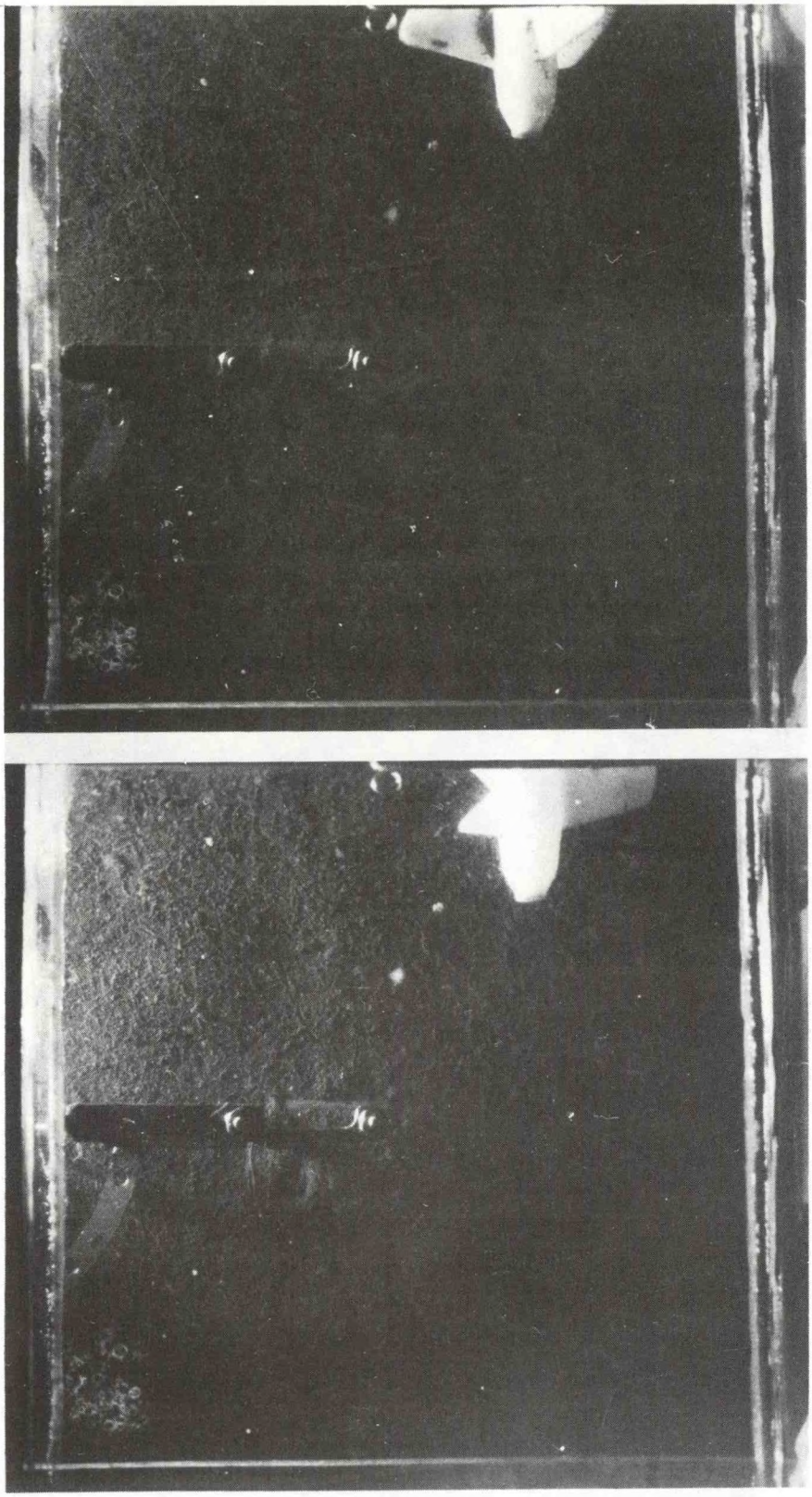

Figure 6t

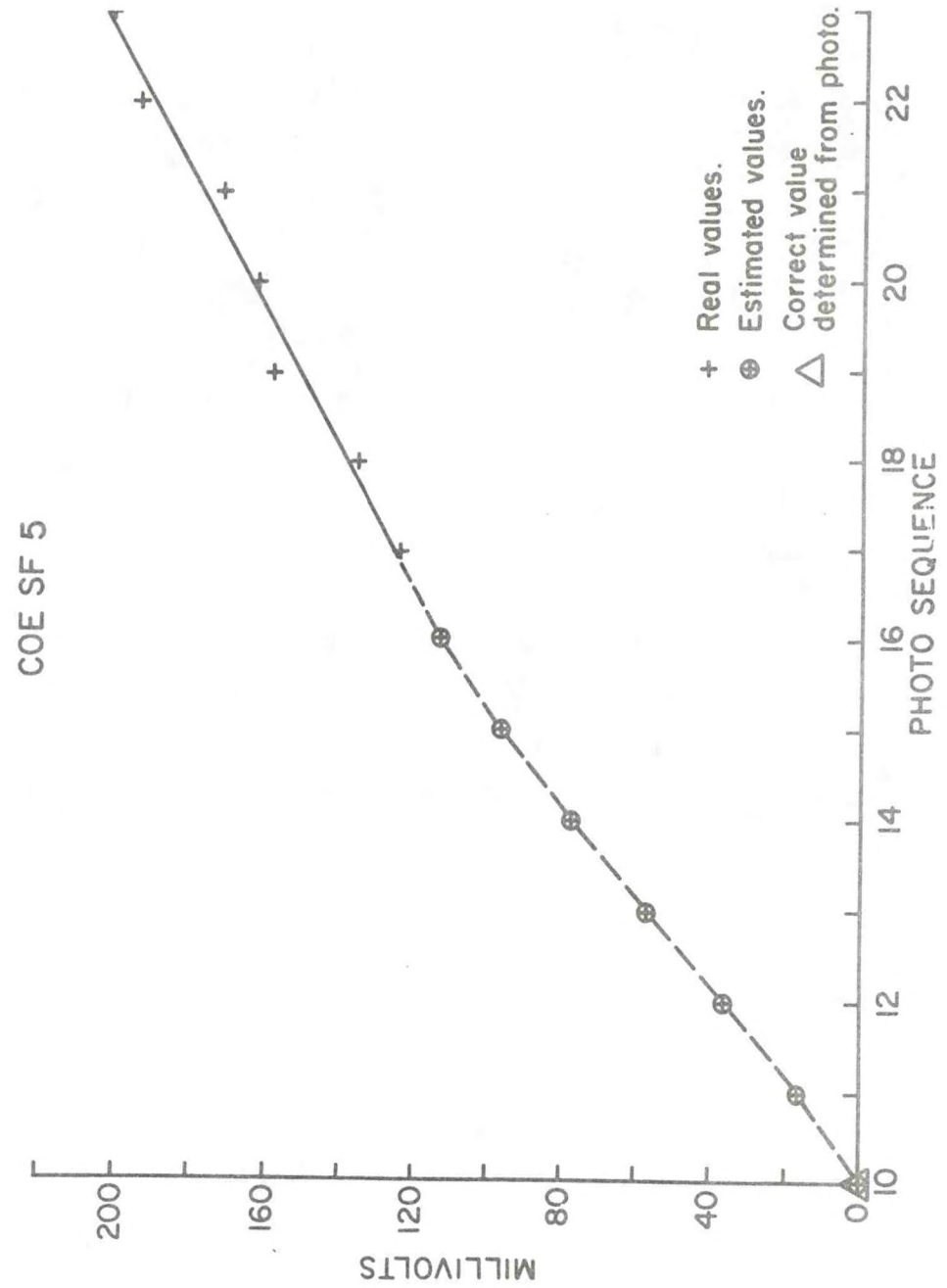

Figure 7: Plot showing velocity versus time curve developed to estimate threshold velocity for SF5.

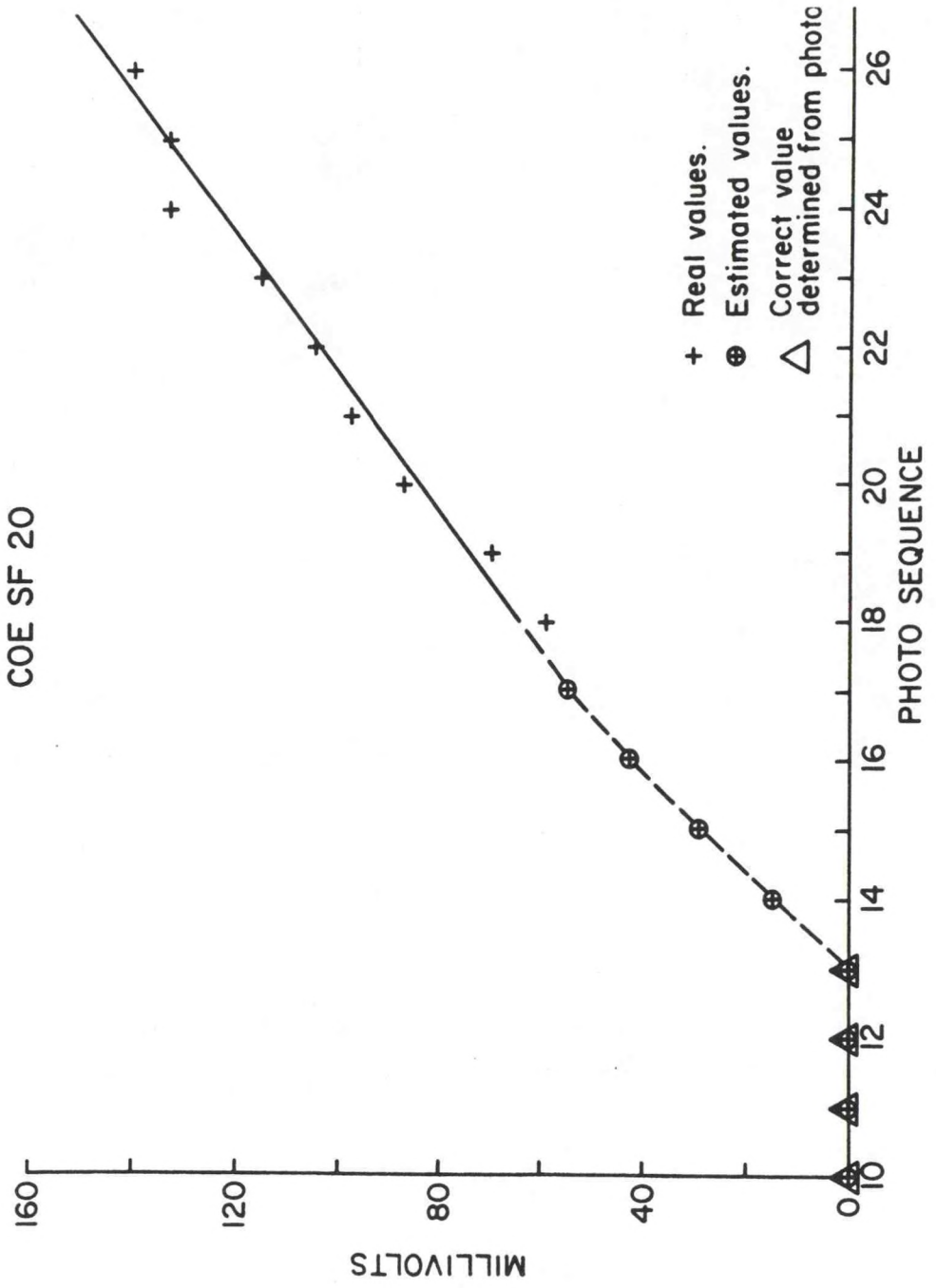

Figure 8: Plot showing velocity versus time curve developed to estimate threshold velocity for SF20.

Benthic animal trails which developed during one run (SF9; Figure 6i), were regarded as pertaining to a separate threshold criteria than for the undisturbed surrounding areas, since fresh bioturbation disturbs the sediment and affects natural erosional characteristics.

All SEAFLUME deployment positions are given in Table 1. Figure 2 shows the site of each run that provided data. Next to each site is a histogram showing percent by weight of the gravel, sand, and fine fractions of the sediment from the diver core samples. Note that SF8, SF9, and SF10 are not on this map, as they were deployed outside the perimeter of the sandcap. Also on this map are the nominal positions of the concentration-velocity (CV) probes (probes were retrieved and re-deployed at these stations about every two months for servicing). Results of CV deployments are presented in a companion report (Young, 1982, this report).

Table 2 summarizes grain size and flow data for each SEAFLUME run. SEAFLUME runs SF11, SF12, SF18(A), SF22, SF25, and SF26 were aborted runs. During SF2, the panel which regulates the flow speed became inoperative. As previously noted, threshold velocity could not be determined for SF8, SF17, and SF24. Core samples for SF8, SF9, and SF10 were lost at sea, eliminating grain size data from those runs. There were no SF13 or SF14 runs. In all, a total of 25 SEAFLUME runs were attempted. Six runs from the first cruise (SF1-SF12) and seven of the twelve runs from the second cruise (SF15-SF26) provided complete flow and sediment data.

Table 2 gives the results of the grain size analysis for each core sample taken. Included in this table are percent by weight of the gravel, sand and fines, results of the pipette analysis of the fines, and the mean phi (θ) size of the sand fraction from ARSA analysis. Phi (θ) is defined as $[(-\log_2(d)]$ where d is the diameter of the grain in millimeters. From the grain size data

Table 1: SEAFLUME deployment locations.

SEAFLUME Run Number	Latitude	Longitude
SF1	40°22.18'	73°50.01'
SF2	40°22.38'	73°50.26'
SF3	40°22.38'	73°50.26'
SF4	40°22.59'	73°50.15'
SF5	40°21.85'	73°50.79'
SF6	40°22.45'	73°50.83'
SF7	40°22.49'	73°49.93'
SF8	40°24.38'	73°51.59'
SF9	40°24.15'	73°51.80'
SF10	40°24.30'	73°48.10'
SF11	40°22.73'	73°50.56'
SF12	40°22.63'	73°50.69'
SF15	40°22.56'	73°50.39'
SF16	40°22.32'	73°50.17'
SF17	40°22.12'	73°50.09'
SF18(A)	40°21.85'	73°50.92'
SF18(B)	40°21.85'	73°50.92'
SF19	40°21.94'	73°50.77'
SF20	40°22.44'	73°50.09'
SF21	40°22.17'	73°49.90'
SF22	40°22.06'	73°50.08'
SF23	40°22.81'	73°50.79'
SF24	40°22.63'	73°50.31'
SF25	40°22.28'	73°50.91'
SF26	40°22.33'	73°50.17'

Table 2: Grain size analyses from samples taken at SEAFLUME sites.

SEAFLUME Run	% by Weight Gravel >2.0 mm	% by Weight Sand 2.0-.064 mm	% by Weight Fines < .064 mm	Pippete Analysis of Fines*				Mean Sand Diameter (ϕ/cm)
				.064-.032 mm	.032-.016 mm	.016-.004 mm	<.004 mm	
SF1	2.4	94.8	2.8	--	--	--	--	2.3/.0203
SF3	0.6	95.0	4.4	--	--	--	--	2.5/.0177
SF4	9.9	87.7	2.4	--	--	--	--	2.2/.0218
SF5	0.4	87.0	12.6	--	--	--	--	2.5/.0177
SF6	2.0	95.2	2.8	--	--	--	--	2.6/.0165
SF7	1.5	92.5	6.0	--	--	--	--	2.4/.0189
SF15	1.0	73.8	25.2	2.6	5.5	5.2	11.9	2.4/.0189
SF16	14.9	83.4	1.7	--	--	--	--	2.1/.0233
SF18(B)	4.3	94.4	1.3	--	--	--	--	1.9/.0268
SF19	.2	13.9	85.9	8.5	17.1	25.2	35.1	3.6/.0082
SF20	21.1	72.9	6.0	--	--	--	--	2.8/.0144
SF21	31.4	64.3	4.3	--	--	--	--	2.2/.0218
SF23	2.8	24.5	72.7	6.8	7.5	20.0	38.4	2.2/.0218

*(% by weight)

it is observed that the percentage of sand was generally greater for samples taken during the first cruise. Except for SF18B, sediments from the second cruise contained more fine material. Pipette analysis for the four samples (SF15, SF17, SF19, and SF23) that had relatively high percentages of fines show that most of the fines had a diameter less than .004 mm. Also noted is the generally higher percentage of gravel (> 2 mm) present in samples taken during the second cruise. Sediment samples from the second cruise also had a greater variance (1.9-3.5ϕ) than those from the first cruise (2.2-2.6ϕ).

3.1 Comparison of Hot Film and Propellor Velocities

Recalling that the hot film velocity measurements were made along the top and side walls of the flume, and at the bed surface via the drag plate, we use these measured wall velocities as estimates of U_* along these surfaces. These values are compared with U_* calculated from propellor measurements and law-of-the-wall equation (2) in Table 3.

Due to the deployment procedures and the soft "fluffy" layer of fine sediments at the bed surface, a cloud of loose surficial suspended matter was stirred up and subsequently settled on the hot wire probes. Also, in many deployments the hot film plate sank completely through the sediment-water interface despite efforts during the cruise to modify the elevator mechanism. In other cases, the hot film plate became contaminated by the resuspended matter during deployment and was only swept clear by flows exceeding threshold conditions. Particles remained attached to the velocity probes even when flow was above threshold and no data was obtained from these sensors. However, the bottom hot film sensor plate was swept clean of sediments during several runs, and no particles adhered to the hot film sensor on the flume top wall. In those cases, velocities from top and bottom plates

Table 3: Comparison between U_* measured determined by the hot film sensor on flume top wall and U_* calculated from law-of-the-wall equation (2) using propellor velocities.

SEAFLUME Run #	U_* Equation (1)	U_* Wall Sensor
15	0.68	0.89
16	0.50	0.81
18B	0.83	1.10
19	0.40	1.05
20	0.48	0.93
21	0.54	0.82
23	0.54	1.17

agreed to within ± 10%. This infers that the roughness of the flume top wall and the sediments comprising the lower flow boundary were of about the same magnitude. If their roughness had differed significantly, the flow profile would have been assymetrical and top and bottom wall velocities would not have agreed so well. The measurements show that the threshold U_*, determined by the top wall sensor, is higher than the U_* derived from the propellor flow meter under the wall law assumption.

We suspect several factors contribute to this inconsistency between hot film and propellor U_*. The first is the reasonableness of the assumption, discussed earlier, that the flume boundary layer is fully developed at the measurement section. It was estimated that the boundary layer thickness was about 6 cm. If this was not the case, and the thickness much less than 6 cm, the wall law equations used to calculate U_* do not apply, even approximately.

Turbulence spectra for SF19 using data from the top wall sensor for a six-minute interval encompassing the onset of erosion were calculated to see how far the flow in the flume might deviate from that of a fully developed turbulent flow. The results (Figure 9) are compared with a hot film velocity spectrum from a fully developed turbulent flow in a laboratory flume. Energy levels of the SEAFLUME spectra are lower at almost all frequencies than the levels in the laboratory flume, again suggesting incomplete development of the SEAFLUME boundary layer.

Other factors, discussed elsewhere, including choices of bed roughness (Z_o), and the constant in equation (2), can also lead to variation in U_* from propellor velocities. However, after checking the effect on U_* (equation (2)) of reasonable but extreme variations in these factors, it was determined that U_* values were changed by factors of only 1.05 to 1.30, not enough to explain all differences observed in Table 3.

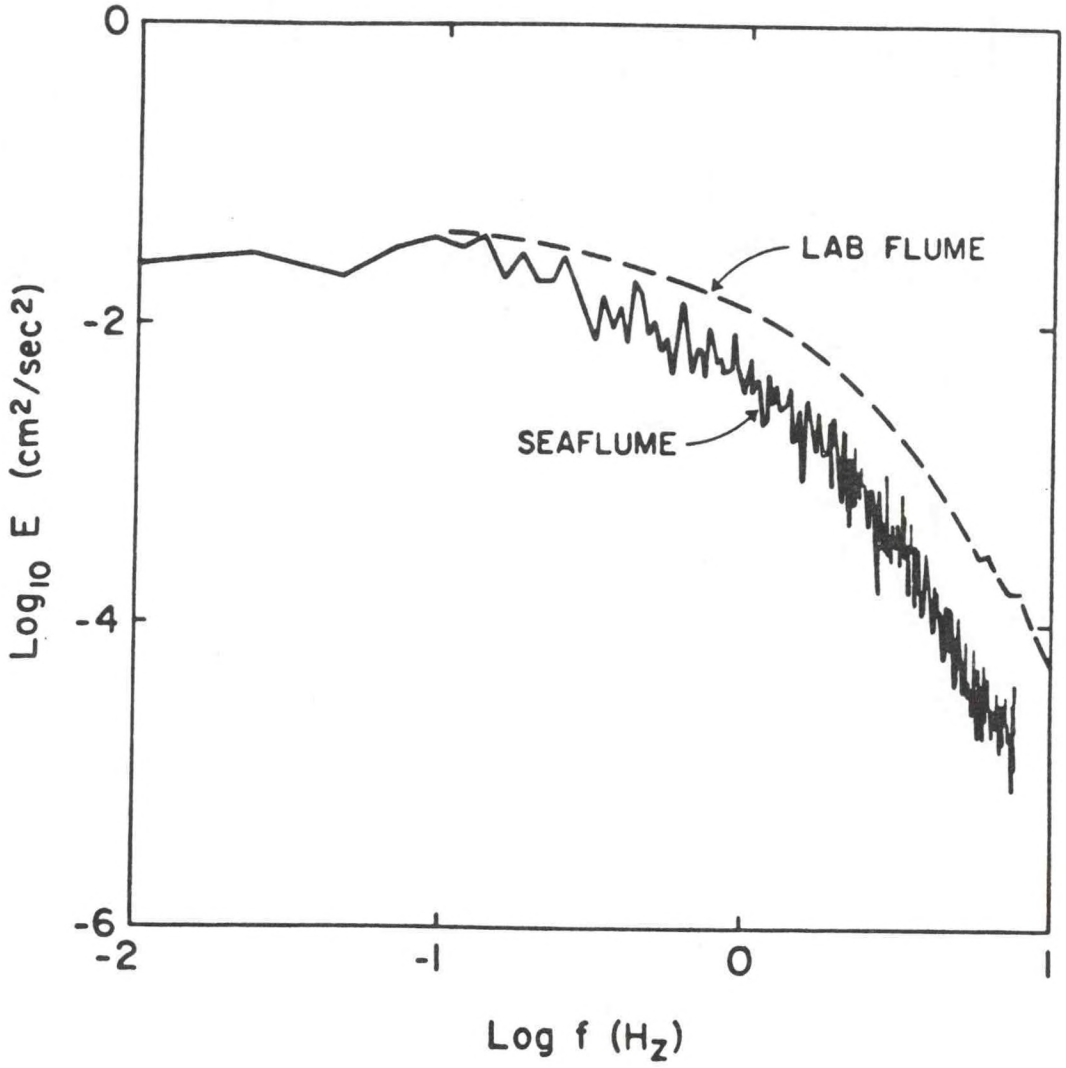

Figure 9: Turbulence spectra from run SF19 top sensor (solid line) and from a fully developed smooth turbulent boundary layer in a laboratory flume (dashed line).

We conclude that U_* from propellor measurements underestimate values of U_* from wall measurements because of incomplete boundary layer development. The November experiments (SF1-SF7) did not include hot film measurements. We, therefore, increase the calculated values of U_* for SF1-SF7 by a factor of 1.7, the average value of the ratio of hot film U_* to propellor U_* during the June experiments (SF15-23). It is felt that this procedure, although approximate, is better than accepting uncorrected data strongly suspected of containing a systematic bias.

3.2 Summary of Results

Flow velocity and threshold parameters calculated from the velocity and grain size data are summarized in Table 4. The value of U_* was found by using equation (2) for SF1-7 and multiplying by 1.7, and the hot film data from the flume top wall for SF15-23. The constants $Z_o = d_{65}/30$ and $C = 6.1$ were used in equation (2). The diameter d_{65} represents the grain size of the 65th percentile in the cumulative frequency distribution for the bed sediment, which is suggested as the most appropriate roughness parameter in poorly-sorted sediments (Einstein, 1950). The constant C is from laboratory studies of flow over regular corrugated roughness elements (Daily and Harleman, 1966), a first approximation to the bed conditions encountered here.

Also presented in Table 4 is an estimate of U_{100}, the mean-flow threshold velocity at 100 cm above bottom. U_{100} was calculated from equation (2) using an arbitrary value of $Z_o = 5.0$ cm and $C = 6.1$. The value of U_{100} is not particularly sensitive to the choice of Z_o, but is strongly affected by C. The values of $Z_o = 5.0$ cm was thought to represent the roughness felt by a geophysical scale boundary layer flow better than the grain roughness d_{65}.

Table 4: Flow velocity and threshold parameters determined by SEAFLUME measurements for various sediment types.

Run	U (cm/sec)	U_* (cm/sec)	U_{100} (cm/sec)	d_{65} (cm)	θ_T	Re_*	$\sqrt{\Xi}$
1	11	.64	13.8	.0238	.01101	1.159	11.05
3	18	1.03	22.4	.0209	.03284	1.647	9.09
4	16	.94	20.3	.0268	.02112	1.919	13.20
5	23	1.32	28.6	.0209	.05362	2.105	9.09
6	25	1.43	30.9	.0198	.06625	2.158	8.38
7	15	.87	18.8	.0230	.02107	1.523	10.50
15	15	.89	19.3	.0202	.02524	1.798	11.32
16	10	.81	17.5	.0270	.01564	2.187	17.49
18B	18	1.10	23.8	.0334	.02332	3.674	24.06
19	8	1.05	22.7	.0082	.08654	.861	2.93
20	10	.93	20.1	.0170	.03275	1.581	8.74
21	11	.82	17.8	.0209	.02071	1.714	11.91
23	16	1.30	28.2	.0259	.04200	3.367	16.43

Data plotted on Shields and Yalin diagrams (Figure 10) are in reasonable agreement with the threshold curves, considering experimental conditions and the approximations needed to derive the values of U_*, θ_T, Re, and Ξ. Data scatter seems greater on the Yalin diagram only because the Yalin curve is presented as a single-valued function. In fact, uncertainty in the Yalin curve is of the same order as expressed by the shaded area on the Shields diagram, because the Yalin curve (from Miller et al., 1980) was derived from the averaged Shields curve.

4. DISCUSSION

Sediments encountered during the SEAFLUME experiments ranged from gravelly sands, to sands, to sandy muds. Beds were sometimes smooth, but more often deformed by irregular bedforms. Consequently, the assumptions made in comparing the field results to laboratory threshold values for smooth monosized sediments were not often met. It is, therefore, not surprising that some of the data fall off the accepted threshold curves (Figure 10).

The presence of about 5% or more of mud (diameter < .0065 cm) in the sediments suggests that cohesion should be considered as an additional force resisting erosion. Data in Table 2 show that 7 of the 13 flume runs had > 5% muds; two (SF19 and SF23) had > 70% mud.

The muddy sediments plot on or reasonably close to the Shields curve (Figure 9), indicating that the sandy-muds and muddy sands behaved as noncohesive sediments characterized by the mean diameter of the sand fraction. We speculate that the muds (even for SF19 which had 86% mud) were unconsolidated and only slightly cohesive. Further, the mud fraction may have been located mostly in the sediment pore spaces between sand grains or below the sediment water interface. The diver sampling procedures tended to

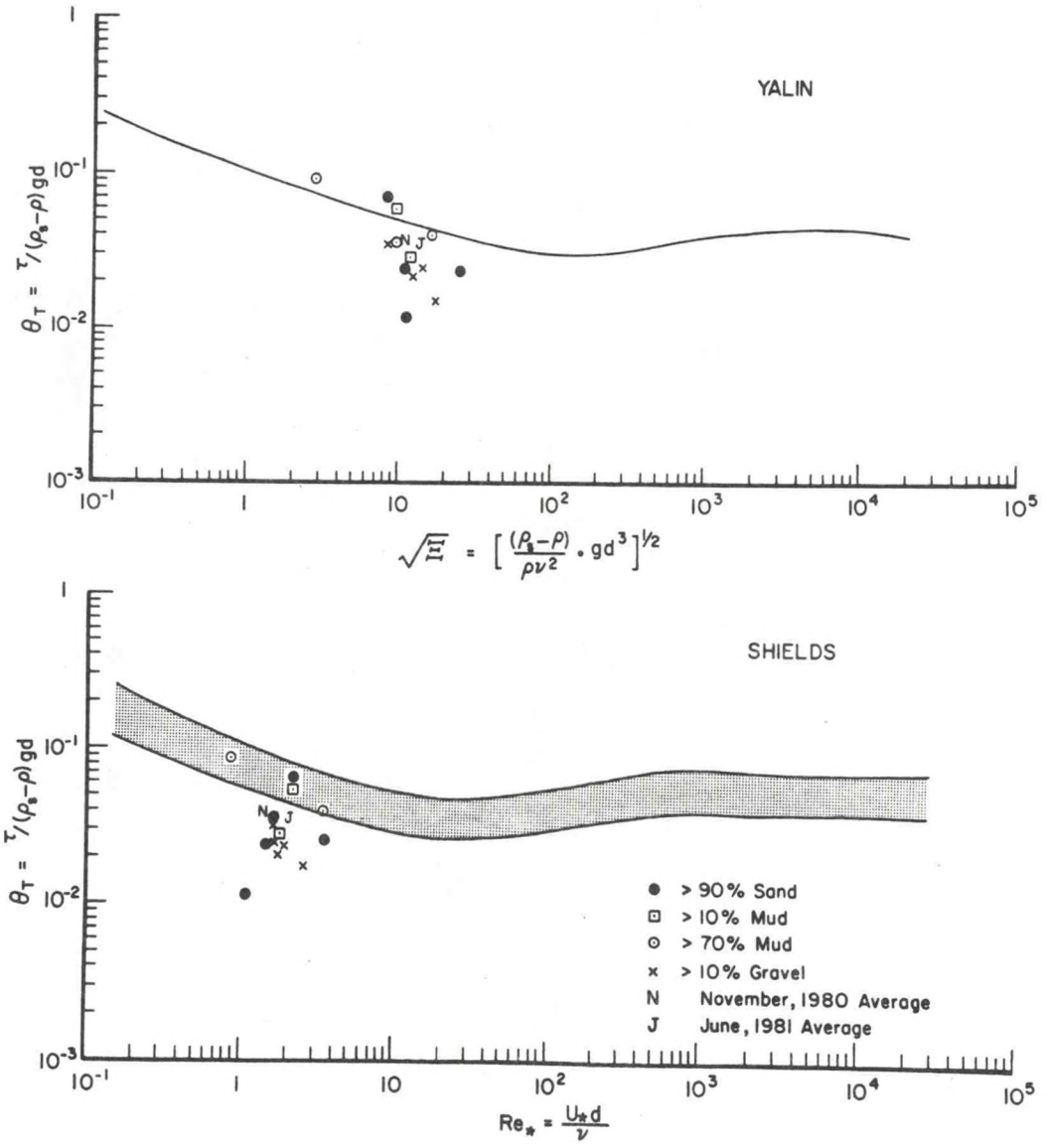

Figure 10 : Shields and Yalin diagrams with SEAFLUME data plotted for comparison with threshold curves for erosion. Curves are from Miller et al. (1977). Symbols are explained on the figure and are meant to show association of data points on the basis of sediment texture.

Table 5: Cruise averaged values of U_*, U_{100}, and threshold parameters.

Cruise	U_* (cm/sec)	U_{100} (cm/sec)	Re_*	θ_T	$\sqrt{\Xi}$
November 1980	1.04	22.5	1.75	.0034	10.2
June 1981	0.99	21.3	2.17	.0035	13.3

homogenize any layering or other stratigraphy so that the position of the mud fraction with respect to the sediment surface is not known. In any case, the muddy sediments behaved more like sands and cohesion seems to be negligible.

Gravelly sediments plot mainly below the threshold curve (Figure 10), suggesting either a lower U_* value than calculated, or a larger effective diameter. In this case, we interpret the results as indicating larger effective diameters. Evidently, the representative diameter d_{65} used to calculate θ_T, Re_* and Ξ does not adequately characterize the bed roughness. The choice of a diameter weighted by the sand plus gravel fractions would no doubt bring the data into closer agreement with the threshold curve.

For the cases where the sediments were sands with only traces of gravel and sand (Figure 10), the data exhibit reasonable scatter and so can be said to agree with the Shields and Yalin criterion for erosion.

Finally, cruise-averaged values of the threshold parameters are given in Table 5 and are also plotted on Figure 10. They are seen to plot very close to their expected positions, in very close agreement with the threshold criterion. Considering the approximations necessary to arrive at these values, the averaged values of U_* and the other parameters can be considered to adequately represent the average threshold conditions necessary to erode the sediments encountered at the sand cap site.

5. CONCLUSIONS

Erosion experiments carried out using a sea-going flume to determine threshold U_* and U_{100} for the sediments capping the Corps of Engineers dumpsite are compared with expected values of U_* derived from the threshold shields and Yalin curves. Reasonable agreement is found between the observed and expected values lending support to the assumption that the threshold U_*

values found here can be used in other calculations of transport and erosion rates. Such calculations are the subject of a separate part of this study (Young, 1982, this report).

REFERENCES

Daily, W. L., and Harleman, R. F. (1966). Fluid Dynamics. Addison-Wesley Publishing Co., Inc., Reading Mass., USA.

Einstein, H. A. (1950). The bed-load function for sediment transportation in open channel flows. U.S. Dept. Agriculture, Tech. Bull. 1026, 71 pp.

Gust, G. (1981). Tools for oceanic small-scale high frequency flows: Metal-clad hot wires. Jour. Geophys. Res., 87:447-455.

Gust, G., and Patrick, G. A. (1981). The high frequency tail of deep sea turbulence in the immediate vicinity of the sea bed (abs.). EOS, 62:899.

Miller, M. C., McCave, I. N., and Komar, P. D. (1977). Threshold of sediment motion under unidirectional currents. Sedimentology, 24: 507-527.

Nelsen, T. A. (1976). An automated rapid sediment analyser (ARSA). Sedimentology, 23: 867-872.

Schlichting, H. (1968). Boundary Layer Theory. McGraw-Hill, New York, 497 pp.

Young, R. A. (1977). SEAFLUME: A device for In-situ studies of threshold erosion velocity and erosional behavior of undisturbed marine muds. Marine Geology, 23: M11-M18.

Young, R. A., and Southard, J. B. (1978). Erosion of fine-grained marine sediments: Seafloor and laboratory experiments. Geol. Soc. Amer. Bull., 89: 663-672.

Young, R. A., and Mann, R. (1982). Erosion velocities of skeletal carbonate sands, St. Thomas, Virgin Islands. Mar. Geol. (in press).

APPENDIX A:

SEAFLUME 1-24

INCIPIENT MOTION NOTES

SF1 (14 NOV 1980)

Initial Bed Description:

The bed is fairly flat and smooth. Some depressed areas are present near the left portion of the photograph. A small amount of shell hash is present and some organic material or "fluff" covers most of the bed surface. Note the small dark area located ten centimeters from the down-stream edge and five centimeters from the left side of the photograph.

Bed Description at Threshold:

The depression noted in the initial photograph appears deeper and more defined. Shell hash is slightly more exposed and the "fluff" material is arranged in a linear pattern in the direction of flow. The small dark are noted previously is larger and has changed shape. Threshold velocity for this run is 11 cm/s.

SF2 (14 NOV 1980)

Initial Bed Description:

A large round depression is located near the left side of the photograph. The left side of this depression is bordered by a ridge of mostly shell material. The rest of the bed is flat and smooth and is covered with a small amount of shell hash and some organic "fluff". The panel on the seaflume jammed during this run. The highest velocity reached was 7 cm/s. No motion was detected over the entire sequence.

SF3 (15 NOV 1980)

Initial Bed Description

There is a small area of highly concentrated shell hash in the upper left corner of the photograph. A curving depression is located just to the right

of this shell hash and extends down to the mid-left portion of the photograph. There is a small amount of shell material scattered over the rest of the bed. Some organic "fluff" is also present.

Bed Description at Threshold:

The curving depression has been partially filled. There is a newly formed depression located 5 cm below the left side of the flow meter propeller. Some shell material has been displaced. There is indication of slight lineation patterns forming in the direction of flow. Threshold velocity for this run is 18 cm/s.

SF4 (15 NOV 1980)

Initial Bed Description:

A high concentration of shell hash borders the left side of the photograph. The rest of the bed is flat and smooth.

Bed Description at Threshold:

The shell hash is unchanged. Just to the right of the hash, near the top of the photograph, there are some small, newly-developed depressions. Threshold velocity for this run is 16 cm/s.

SF5 (16 NOV 1980)

Initial Bed Description:

The bed is characterized by several small depressed areas. A small amount of shell material is present in the top left portion of the photograph.

Bed Description at Threshold:

Bed has been smoothed. Most depressions are filled. Slightly more shell hash is present in the upper left corner. Threshold velocity for this run is 23 cm/s.

SF6 (16 NOV 1980)

Initial Bed Description:

Bed is characterized by undulatory ripples. There is a small amount of shell hash present.

Bed Description at Threshold:

The ripples are slightly more oriented in the direction of flow. The are in the upper left corner has been smoothed slightly. Changes in shadows between ripples are evident, indicating movement of surrounding sediments. Threshold velocity for this run is 25 cm/s.

SF7 (16 NOV 1980)

Initial Bed Description:

The bed is fairly flat. There is a curved ridge just to the left of the propellor. A couple of large shell pieces are sticking up out of this ridge. There is an area of relief on the left edge of the photograph about mid-way between the top and bottom. There is a small dark are located about 4 cm from the top and 4 cm from the left side.

Description of Bed at Threshold:

The small dark are noted has changed size and shape. The area of relief on the left has undergone slight change and is less defined. The large shell

piece below the propellor is more exposed and the ridge below it has slumped. Threshold velocity for this run is 15 cm/s.

SF8 (17 NOV 1980)

Initial Bed Description:

Bed is fairly flat and smooth. There is a curved line of shell hash to the left of the propellor. To the left of the lower tip of this hash is some slight relief. No motion was detected over this entire run. First and last photos of the run are presented for comparison. Velocity ranged from 0-36 cm/s.

SF9 (17 NOV 1980)

Initial Bed Description:

Bed is smooth with a large depression to the left of the propellor. A small amount of shell hash is present.

Bed Description at Threshold:

Some erosion has occurred 7.5 cm from the top on the left side of the photograph. Also, a slight ridge has formed about 4 cm down-stream from the propellor. Threshold velocity for this run is 13 cm/s. Evidence of threshold motion is noted earlier in this sequence. Note the last three photos presented for this run. The first two pictures show a trail being made by a gastropod. In the third photo (velocity = 9 cm/s) the trail is partially covered. Since this study is interested in movement of undisturbed sediment, the erosion of this freshly bioturbated sediment is not regarded as representing the threshold.

SF10 (17 NOV 1980)

Initial Bed Description:

There is a curved depression half-way between the propellor and the left edge of the photograph. Some worm tubes are located on the left side of the photograph about 10 cm from the top.

Bed Description at Threshold

There is a slight ridge forming to the left of the propellor: The worm tubes have been displaced. A piece of shell material is now present about 4 cm from the top on the left side. Threshold velocity for this run is 17 c/s.

SF11 (17 NOV 1980)

Run Aborted

SF12 (17 NOV 1980)

Run Aborted

SF15 (26 JUN 1981)

Initial Bed Description:

The bed is characterized by prominent depressions and mounds. There is a fair amount of organic "fluff" on the bottom.

Description of Bed at Threshold:

The depressions and mounds have become smoothed out slightly, especially above the drag plate arm. A slight lineation pattern is developing. Threshold velocity for this run is 15 cm/s.

SF16 (27 JUN 1981)

Initial Bed Description:

Bottom is fairly flat. There is a lot of organic "fluff" present. Several worm tubes are noticed.

Bed Description at Threshold:

Aggregates above the drag plate arm are being swept away. Threshold velocity for this run is 10 cm/s.

SF17 (27 JUN 1981)

Initial Bed Description:

The bed has some large pieces of shell scattered over it. Otherwise, it is fairly flat. This sequence was difficult to analyze. The photograph showing threshold motion could not be identified. The first and last photograph of this run are shown for comparison. Velocity ranged from 0-10 cm/s for this run.

SF18A (28 JUN 1981)

Initial Bed Description:

The bed has many small depressions and mounds. It appears to be fairly muddy. This run was aborted. No flow was ever created in the SEAFLUME.

SF18B (28 JUN 1981)

Initial Bed Description:

The bed has many prominent mounds and depressions. There is a large, deep depression to the left of the drag plate arm. Notice the small mound about 2 cm below the left side of the propellor.

Bed Description at Threshold:

Uncovering of some shell material has occurred. There is a worm tube present 5 cm from the top on the left side of the photograph. The area around the small mound noted in the initial photograph has changed slightly. There are now three small mounds present there. Threshold velocity for this run is 18 cm/s.

SF19 (28 JUNE 1981)

Initial Bed Description:

Bed had some small depressions and mounds present. Organic "fluff" covers the surface.

Description of Bed at Threshold:

Small mounds above and below the drag plate arm are gone. Bed is generally smoother. Threshold velocity for this run is 8 cm/s.

SF20 (29 JUN 1980)

Initial Bed Description:

Bed is fairly flat and smooth. There are some small mounds, probably sediment covered rocks or shell present. There is a worm tube located just above the mid portion of the drag plate arm.

Bed Description at Threshold:

The small mound that was located just above the drag plate is gone. The worm tube has been swept away. The small round mound that is just above the mid portion of the drag plate arm has changed shape slightly and a new smaller mound has formed above it. A trail has been uncovered just below the drag plate. Threshold velocity for this run is 10 cm/s.

SF21 (29 JUN 1981)

Initial Bed Description:

Bottom is covered with many large rocks and shells.

Bed Description at Threshold:

Slight uncovering of rock and shell material has occurred. This is evident in area 2-3 cm to the left of the propellor. Threshold velocity for this run in 11 cm/s.

SF22 (29 JUN 1980)

Run Aborted

SF23 (30 JUN 1981)

Initial Bed Description:

Bed is fairly flat and muddy looking. Organic fluff covers the surface. Many aggregates are present below the drag plate arm. There is a small crescent moon-shaped shadow 5 cm above the mid portion of the drag plate arm.

Bed Description at Threshold:

Aggregates are arranged in a linear pattern in direction of flow. A new shell is present just below the propellor. The cresent moon-shaped shadow has disappeared, indicating sediment motion in that area. Threshold velocity for this run is 16 cm/s.

SF24 (30 JUN 1981)

Initial Bed Description:

Bed is flat smooth and muddy looking. Organic fluff covers the surface. Threshold motion could not be identified for this sequence. The fine, low

density material or fluff, began to be removed as soon as current was induced, (second photo) exposing covered trails and worm tubes, but this probably does not represent true incipient motion. Velocity for this run ranged from 0-32 cm/s. Photos taken after velocity reached 11 c/s were disregarded due to piece of paper entering flume and causing deflection of the normal flow.

SF25 (30 JUN 1981)

Run Aborted

SF26 (30 JUN 1981)

Run Aborted

WAVE HINDCASTING FOR A SEDIMENT TRANSPORT MODEL OF CAPPED MATERIAL AT THE NEW YORK DREDGED MATERIAL DUMPSITE

by

Georges Drapeau*

National Oceanic and Atmospheric Administration
Atlantic Oceanographic and Meteorological Laboratories
4301 Rickenbacker Causeway
Miami, Florida 33149

*On sabbatical leave from: INRS-Oceanologie
Laboratoire Oceanologique de Rimouski
Rimouski, Qc
Canada G5L 3A1

1. INTRODUCTION

1.1 Wave Hindcasting and Forecasting

Wave hindcasting and forecasting has evolved since World War II from Sverdrup-Munk (1947) Bretschneider (1957) method and the Pierson-Neuman-James (1955) method to the Pierson-Moskowitz (1964) spectral method. More recent developments have resulted from the Joint North Sea Wave Project (JONSWAP, Hasselmann et al., 1973) and experiments by Liu and Ross (1980) in Lake Michigan integrating stable and unstable atmospheric conditions.

Two basic concepts can be used for wave hindcasting: the wave spectral model and the wave parametric model. The first one is based on the integration of the wave energy balance equation and the second one assums an approximate invariance (Hasselmann et al., 1976) of the normalized wave spectral shape with fetch; the latter is easier to use as wave heights and frequencies are calculated directly on the basis of wind intensity, fetch and duration.

1.2 Seasonal and Infrequent Events

As the ultimate objective of this study is to contribute data to evaluate the probability of breaching as well as the ultimate life span of a sediment cap, it is important to consider both the seasonality of the wave climate at the dumpsite site, but also the infrequent events not well represented by monthly-averaged regional wave data.

2. SETTING OF THE NEW YORK BIGHT DUMPSITE

2.1 Location of Depth

The dumpsite for the dredged material (mud) in the New York Bight Apex is located 9.8 km due South of Ambrose Lightship, at a depth of 27 to 30 m (Figure 1).

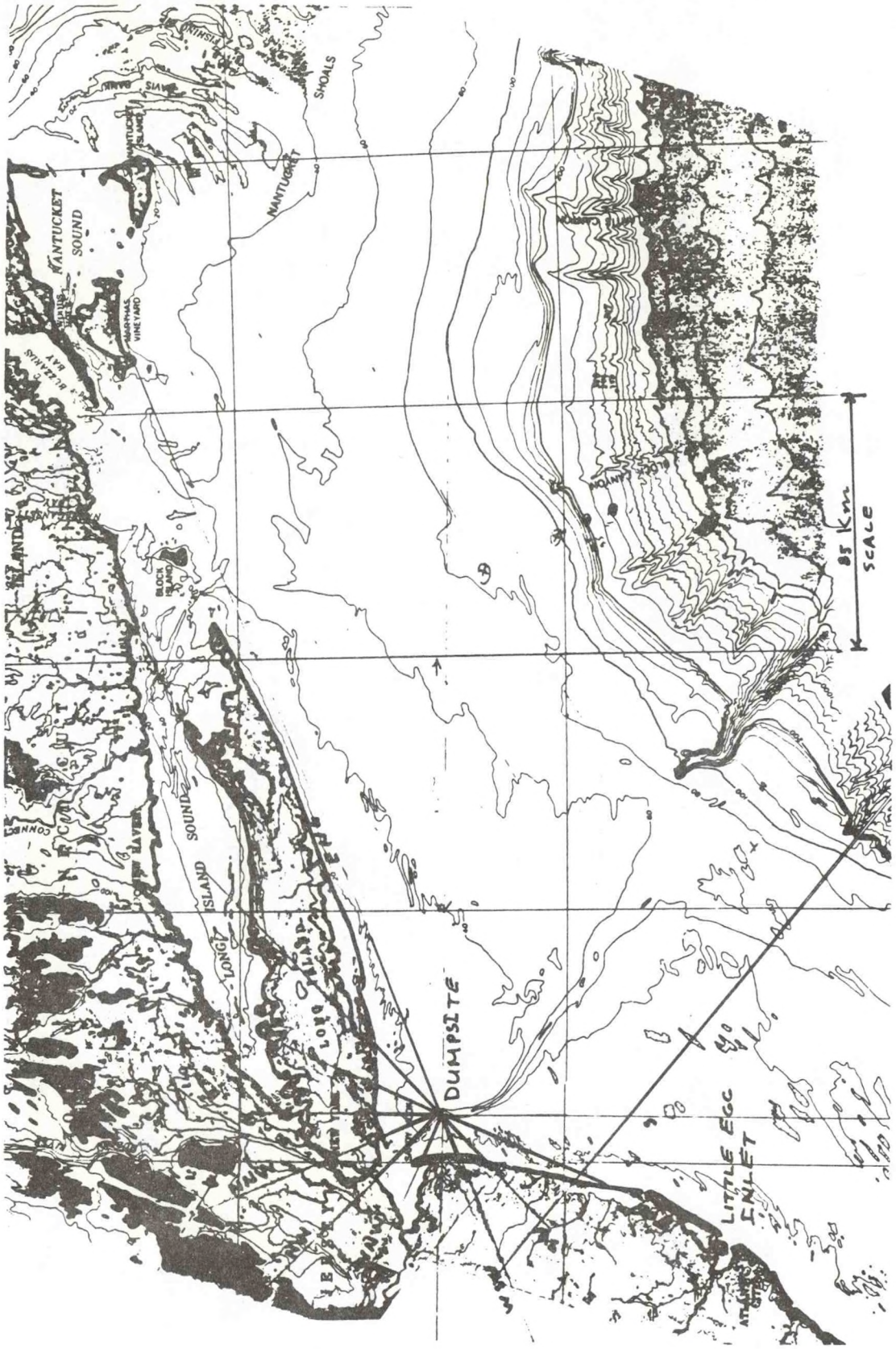

Figure 1. Location map. Fetches from Ambrose Lightship are outlined. The dumpsite is located five nautical miles south of the Ambrose Lightship station. The location of EG&G survey at Little Egg Inlet is also shown on the figure.

2.2 Types of Sediments

Approximately 900,000 cubic yards of muddy sediments that had failed the ocean dumping pollution criteria had to be capped. Approximately 500,000 cubic yards of sediments finer than sand and 1,500,000 cubic yards of sandy sediments were emplaced in two layers between July and November 1980.

3. DATA BASE

3.1 Ambrose Lightship (ALS)

The data available for this study are Ship's Weather Observations log sheets on microfiches. The microfiches available cover the period from November 1956 to December 1980. According to the Index of Surface Weather Records (National Climatic Center) the data were recorded at a height of 18 feet (from a lightship) until 1966 and at a height of 94 feet from a tower since 1967. The data recorded are in accordance with the International Weather Ship Weather Code: date, time, sky condition, present weather, visibility, wind: speed and direction; state of the sea: height and period; sea water temperature, air temperature, and barometric pressure.

3.2 Public Service Electric and Gas Company of New Jersey (PSEG)

The Public Service Electric and Gas Company of New Jersey was engaged in an environmental site assessment off Little Egg Inlet, New Jersey to evaluate the site proposed for the nuclear powered Atlantic Generating Station. EG&G environmental consultants carried out a wave observation program in September, October and November 1974. During the three-month observation period, a Datawell Waverider Wave Measurement System was deployed at the proposed site for the generating station along with three Clinet CI-25 Wind Recorders at a height of 10 m in the vicinity of the station. Air and sea temperatures were also recorded during the same interval. This survey provided an excellent set

of data of four records per day for wave height and period, wind velocity and direction, and air and sea temperatures during these three months. Although these data are recorded 75 km south of the dumpsite, they are useful to analyse waves coming from offshore.

4. OBJECTIVES OF THE STUDY

(1) The immediate objective of this study is to examine the visual wave observations recorded at the Ambrose Lightship to determine how they can be used as input for the sediment transport model.

(2) Winds and waves recorded at Ambrose Lightship are correlated in order to verify existing models and to assess the best relationships for that location.

(3) Winds from the John F. Kennedy Airport are correlated with those of Ambrose Lightship. Wind data from John F. Kennedy Airport can then be used to extend the investigations at the dumpsite.

(4) Generation of waves in the Atlantic Ocean outside the study area is analysed for the period November 1980 to June 1981.

5. DATA ANALYSIS

5.1 Ambrose Lightship (ALS)

5.1.1 Summary of Data

Records from microfiches were transferred to a computer file. Four records per day at 6-hour interval were copied: month, date, hour, wind direction (16 points of compass), wind velocity (knots), state of the sea: height (feet), period (seconds); sea water temperature (°F), air temperature (°F), and barometric pressure (inches Hg) for a total of 1464 records.

Data from ALS for the year 1980 are summarized on Figure 2. The first column on the figure indicates the mid-point value of the corresponding cell on the histogram; the second column, the cell fraction, and the third column the number of observations for each cell of the histogram.

Wind direction: (degrees true north) The histogram shows that the wind is blowing predominantly from the quadrant northwest-northeast and also from the southwest.

Wind velocity: (meters per second) The maximum velocity recorded is 23.2 m/s and the mean value is 5.4 m/s. The histogram shows that the events that reach an intensity of 14 m/s or more are rare; 96.3% of the time the wind intensity is below that level.

Wave height: (meters) The highest wave height recorded is 3.7 m and the mean wave height is 0.60 m. The first row outlines the zero-height records, that is 284 records of calm. The histogram shows a break between 1.66 an 2.00 meter wave heights, as indicated by the number of observations for each cell.

Wave period: (seconds) The maximum wave period recorded is nine seconds and the mean period is 1.91 seconds. In some instances visual observers have a tendency to overestimate wave periods (Schneider and Weggel, 1981) and in other cases to underestimate it (Quayle and Changery, 1982). At the Ambrose Lightship the observations seem to be biased in the latter direction.

5.1.2 Fetches

The fetches for the 16 points of the wind rose from Ambrose Lightship are shown on Figure 1. It shows in particular that the dumpsite location is quite protected and that unlimited fetches are restricted to winds from the quadrant east to south.

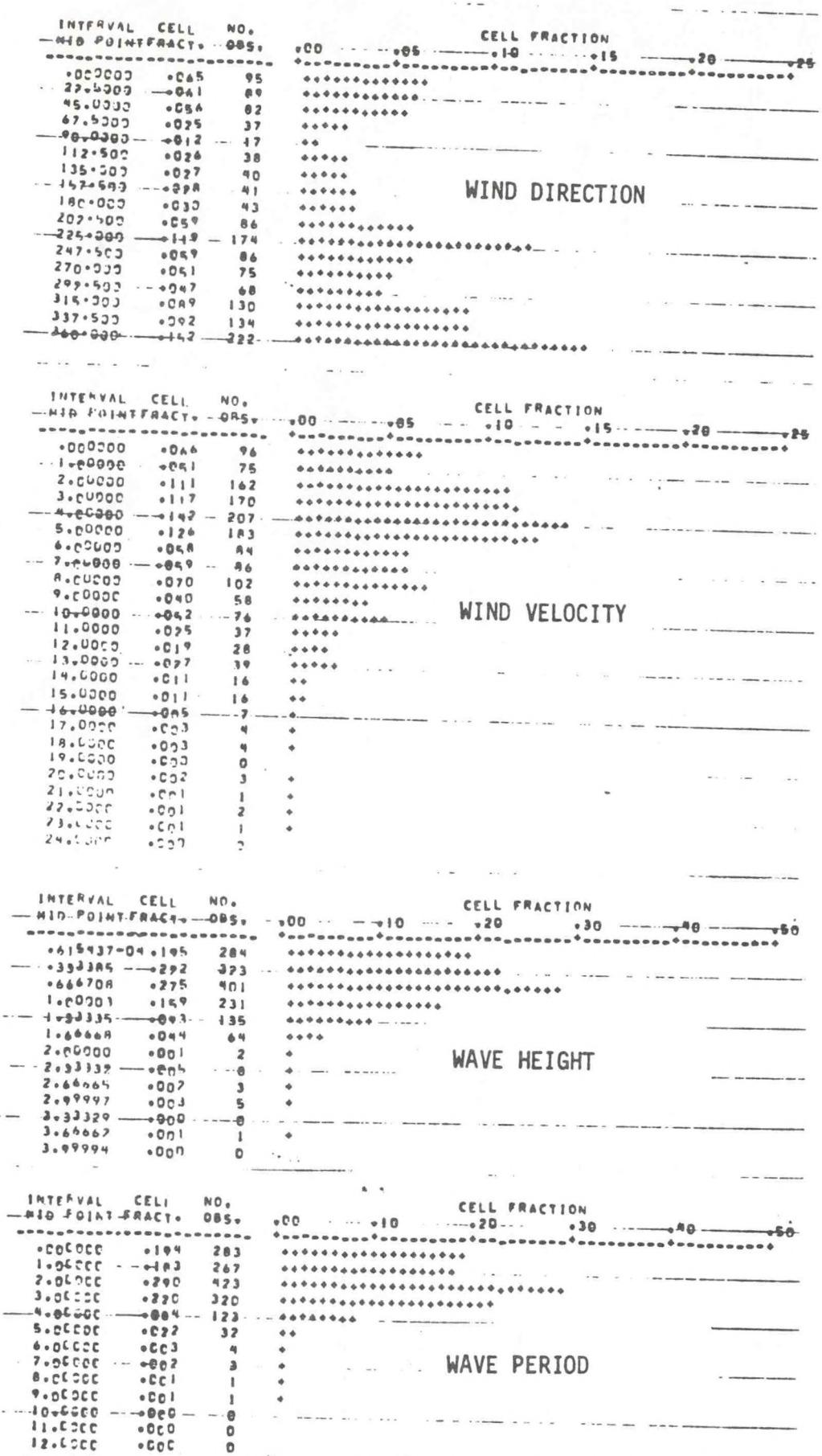

Figure 2. Histograms of Ambrose Lightship data for 1980. The first column on the figure indicates the mid-point value of the corresponding cell (first = zero values); the second column, the cell fraction; and the third column, the number of observations for each cell of the histogram.

5.2 Public Service Electric and Gas Company of New Jersey (PSEG)

The wind data recorded at PSEG were vector averaged from hourly averages of three wind sensors 10 km apart that provided accurate identification of the local wind. Wave records of 20 minutes duration from the wave rider buoy were made four times a day, every six hours. The wave height and period were determined from energy spectrum analyses, the period (peak spectral period T_s) corresponding to the frequency band containing the most energy and the wave height (significant wave height H_s) being four times the standard deviation of a wave record.

6. CORRELATION OF WINDS AND WAVES

The development of generalized concepts related to wind generated waves is summarized by Sylvester (1974). Four dimensionless parameters can relate the energy source to the energy sink all linked by the important variable of wind velocity in a dimensionless form:

Source	Fetch gF/U^2
	Duration gt/U
Sink	Wave height gH/U^2
	Wave period $gT/2\pi U$

g: gravitational acceleration
F: fetch
U: wind velocity
t: wind duration
T: wave period
H: wave weight

6.1 Limited Fetch

It has been pointed out by Kitaigorodskii (1962) that fetch-limited wave parameters, when non-dimensionalized in term of U and g, should be functions only of the single non-dimensional variable $X = gF/U^2$ identified as the non-dimensional fetch parameter. Similarly the non-dimensional peak-energy frequency is defined as $V = U_{10}f_m/g$ and the non-dimensional total energy is defined as $e = Eg^2/U_{10}^4$. These parameters are related, but the functional forms vary among different studies. For instance, Hasselmann et al. (1976) have developed the following equations for the non-dimensional peak-energy frequency (V) and the non-dimensional total energy (e).

$$V = 3.5\ X^{-0.33} \tag{6.1}$$

$$e = 1.6 \times 10^{-2} X \tag{6.2}$$

where for a given wave-energy density spectrum S(f), f_m is the peak-energy frequency and $E = S(f)df$ is the measure of total energy per unit surface area with the constant factor ρg left out. The significant wave height is defined as $H_s = 4\sqrt{E}$.

Measurements during variable atmospheric conditions led Liu and Ross (1980) to define distinct relationships for stable and unstable atmospheric conditions:

Stable conditions

$$V = 2.05\ X^{-0.27} \tag{6.3}$$

$$e = 6.8 \times 10^{-8}\ X^{1.1} \tag{6.4}$$

Unstable conditions

$$V = 1.9\ X^{-0.27} \tag{6.5}$$

$$e = 1.2 \times 10^{-7}\ X^{1.1} \tag{6.6}$$

6.2 The Effect of Wind Stability

It is a recognized fact that waves on the ocean develop more rapidly and reach greater heights when the air temperature is lower than the water temperature. The effect of atmospheric stability has been analysed by Cardone (1969). This author developed an algorithm to calculate wind friction velocity (U_*) using wind velocity (U), air temperature (T_a), sea temperature (T_s) and height of measurements (Z) above the sea as inputs. Cardone's model is based on different sets of assumptions. Cardone proposes (p. 39) that "at least for situations in which the high frequency part of the wave spectrum is a reflection of the local wind (a condition common to active wave generating situations), the roughness parameter can be expressed in terms of physical constants and U_* only".

$$Z_o = A_1/U_* + A_2\, U_*^2 + A_3 \tag{6.7}$$

so that the drag coefficient, referred at 10 m, C_{10} is minimum at U_{10} = 6 m/s. Then

$$Z_o = 0.684/U_* + 4.28 \times 10^{-5}\, U_*^2 - 4.43 \times 10^{-2}. \tag{6.8}$$

Cardone also explains that a universal relation should exist between the non-dimensionalized wind shear and temperature gradient

$$\phi_u = \frac{Kz}{U_*}\frac{\partial u}{\partial z} \tag{6.9}$$

$$\phi_t = \frac{Z}{T_*}\frac{\partial \theta}{\partial Z} \tag{6.10}$$

If velocities and temperatures were measured at more than one elevation the problem could be solved readily. In most cases however wind velocity and air temperature are measured at one height only.

The gradient of potential temperature can be defined as

$$\frac{\partial\theta}{\partial z} = \frac{\phi_u\,(Z_a/L') - (\theta_a - \theta_s)}{Z[\ln(Z_a/Z_o) - \psi(Z_a/L')]} \tag{6.11}$$

where

θ_a = air temperature

Z_a = height at which θ_a is measured

θ_s = sea temperature

Z_o = roughness parameter (see equation 6.8)

U_* = friction velocity (shear velocity)

Then

$$\phi_u(Z/L') = \frac{Kz}{U_*}\,\frac{\partial U}{\partial Z} \tag{6.12}$$

$$\psi(Z/L') = 1 - \phi_u - 3\ln\phi_u + 2\ln\left(\frac{1+\phi_u}{2}\right) + 2\tan^{-1}\phi_u - \frac{\pi}{2} + \ell n\left(\frac{1+\phi_u^2}{2}\right) \tag{6.13}$$

$$L' = \frac{U_*^2\,\bar{\theta}\,[\ln(Z_a/Z_o) - \psi(Z_a/L')}{K^2 g(\theta_a - \theta_s)} \tag{6.14}$$

$$U_* = \frac{K\,Um}{[\ln(Zm/Zo) - \psi(Zm/L')]} \tag{6.15}$$

K = Cte = 0.4

The problem is solved by iteration:

1. An initial value for L' is calculated assuming $\psi = 0$ and $U_* = 0.04$ Um.

2. This first estimate of L' is used to solve equation (6.15) iteratively calculating ψ from equation (6.13), ϕ_u being solved implicitly by $\phi^4 - 18(Za/L')\phi^3 - 1 = 0$ and U_* is computed.
3. U_* is used to recompute the stability length from equation (6.14) iteratively.
4. A convergence criterion is set for $L'(n) - L'(n-1) \leq \epsilon$.

Liu and Ross (1980) have conducted experiments over Lake Michigan under different atmospheric stability conditions. They concluded that the discrepancy between stable and unstable atmospheric conditions could be accounted for by using Cardone's model to determine the wind friction velocity that integrates the atmospheric conditions. By analogy with the equations developed previously, a single equation is developed to account for stable and unstable atmospheric conditions:

$$e_* = 3.5 \times 10^{-5} X_*^{1.1} \qquad (6.16)$$

where the friction velocity U_* replaces the wind velocity at 10 m, $X_* = gF/U_*^2$ and $e_* = Eg^2/U_*^4$.

6.3 Unlimited Fetch

For the conditions of unlimited fetches, the wave height depends solely on wind velocity. Silvester (1974) summarizes the formulas obtained by different workers:

$H_{1/3} = 0.0268\ U_{10\text{-}12}^2$ Sverdrup and Munk, 1947; Bretschneider, 1957.

$H_{1/3} = 0.0510\ U_{7.5}^{5/2}$ Pierson, Neumann and James, 1955.

$H_{1/3} = 0.0133\ U_{grad}^2$ Darbyshire, 1959.

$$H_{1/3} = 0.0213\, U^2_{19.5}$$ Pierson and Moskowitz, 1964.

$H_{1/3}$: wave height in meters of the highest 1/3 of waves and taken as the equivalent of the significant wave height H_s.

U: wind velocity in meters per second at the height above sea level indicated by the subscript.

6.4 Differentiation Between Sea and Swell

JONSWAP (Hasselmann et al., 1976) has provided a substantial base to evaluate the nature of different types of waves. The e (non-dimensional energy) vs V (non-dimensional peak-energy frequency) relationship can be used as a model for prediction of equilibrium state for growing waves under uniform wind field (Hasselmann, 1978). The relation between e and V is defined by Hasselmann et al. (1976) as:

$$e = 5.1 \times 10^{-6}\, v^{-10/3} \tag{6.17}$$

and by Liu and Ross (1980) as:

Stable conditions $$e = 1.26 \times 10^{-6}\, V^{-4.07} \tag{6.18}$$

Unstable conditions $$e = 1.64 \times 10^{-6}\, v^{-4.07}. \tag{6.19}$$

It is assumed that wave growth patterns may start off-equilibrium and grow towards equilibrium until fully developed conditions are reached when V reaches a lower value of 0.13 to 0.15. Values of V lower than 0.13 are indicative of swell conditions as schematized on Figure 3. This criterion is used to distinguish sea from swell waves in the study area.

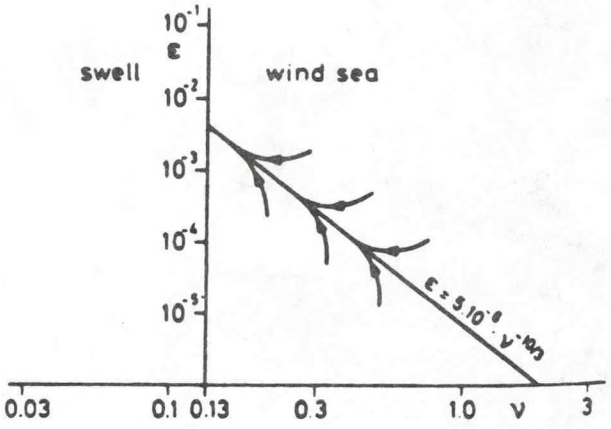

Figure 3. Wave growth shown in relation with non-dimensional total energy (e) and non-dimensional peak-energy frequency (V). After Hasselmann, 1976.

7. EVALUATION OF AMBROSE LIGHTSHIP WAVE HEIGHT AND WAVE PERIOD DATA

The first objective of this study is to provide wave heights and periods as input for the sediment transport model. For that purpose, the quality of data recorded at Ambrose Lightship is compared with those of PSEG.

7.1 Unlimited Fetch

7.1.1 Comparison of records from ALS and PSEG

To compare measurements recorded at ALS and FSEG both records were examined and those records corresponding to winds from unlimited fetches occurring simultaneously at both stations were retained (Table 1). Comparison of wind velocity, wave height and wave period is shown on Figure 4.

Wind velocity: The upper diagram of Figure 4 shows that wind velocities recorded at the two stations are essentially the same. The sharp peaks of some of ALS data probably result from the fact that wind velocity were read from an anemometer and represent instantaneous measurements while the records from PSEG are hourly averages from three anemometers.

Wave heights: Wave heights from both stations are reasonably well correlated although waves observed at ALS are often lower. This difference can be explained by the location of ALS further inside the apex of the New York Bight.

Wave period: No definite explanation is found to account for the marked discrepancy between computed wave periods at PSEG and the visual observations made at ALS. Evaluation of the accuracy of visually observed wave data indicates that visual observers may be biased and either overestimate (Schneider and Weggel, 1981) or underestimate (Quayle and Changery, 1982) wave measurements. The good agreement between wave heights as well as wind velocities make unlikely the probability that the wave periods at the two locations are as different as the records show.

Table 1

PSEG								ALS					
Mo	Da	Hr	Dir	Wv	Hs	Tm	ΔT	Hr	Dir	Wv	Hv	Tv	ΔT
9	8	21	150.00	4.00	.71	8.10	-7.00	19	180.00	4.63	.30	1.00	-2.78
9	12	9	105.00	.50	.71	9.30	-3.80	13	180.00	5.15	.30	3.00	2.22
9	12	15	150.00	3.00	.85	13.00	-3.80	16	180.00	8.24	.91	4.00	2.78
9	17	9	150.00	3.00	.44	8.10	-2.00	7	180.00	2.57	.00	.00	-1.67
9	18	15	180.00	3.50	.59	9.30	-2.00	19	180.00	7.21	.30	3.00	- .56
9	19	15	140.00	5.00	.62	9.30	-3.00	16	180.00	5.66	.30	3.00	1.67
9	19	21	140.00	5.00	.72	8.10	-3.00	22	180.00	7.21	.61	3.00	.00
9	20	9	90.00	.50	.68	8.10	-4.00	13	180.00	5.15	.00	.00	.56
9	21	15	185.00	10.00	1.43	4.60	-3.50	16	180.00	15.44	1.83	4.00	1.11
9	25	9	145.00	5.00	1.36	9.30	-8.00	7	135.00	10.30	.91	5.00	-4.44
9	25	15	180.00	5.50	1.22	9.30	-8.00	16	180.00	11.33	1.52	5.00	-2.78
9	27	15	170.00	6.00	.77	8.10	-4.00	16	180.00	9.27	.61	2.00	1.67
9	28	3	140.00	6.00	.77	10.80	-2.50	4	180.00	6.18	.30	3.00	.00
9	28	9	145.00	7.00	.57	9.30	-2.50	10	180.00	9.27	.30	3.00	1.11
9	28	15	140.00	7.00	.87	9.30	-2.50	16	158.00	7.21	.30	1.00	1.11
9	28	21	150.00	11.00	1.31	10.80	-2.50	22	180.00	15.44	1.22	4.00	.56
10	5	15	200.00	9.00	.69	9.30	-4.00	16	180.00	4.12	.30	3.00	5.56
10	11	21	135.00	5.00	.57	9.30	- .50	22	180.00	7.21	.30	1.00	-1.11
10	13	16	54.00	9.30	1.44	5.40	1.00	16	158.00	6.69	.61	2.00	-1.67
10	13	21	75.00	8.40	1.33	6.60	1.00	22	135.00	5.15	.61	1.00	-3.89
10	14	3	90.00	9.00	1.27	5.90	.00	4	135.00	9.27	.61	3.00	-2.22
10	14	9	120.00	9.50	1.32	5.40	.00	7	135.00	9.27	.91	3.00	-1.67
10	14	15	135.00	6.00	.85	5.00	.00	13	180.00	7.21	.61	3.00	.56
10	14	21	180.00	8.50	.92	4.10	.00	19	180.00	9.27	.91	3.00	1.67
10	24	21	150.00	4.50	.98	13.00	-2.00	19	180.00	5.15	.30	4.00	-1.67
10	28	9	90.00	5.00	.64	5.00	1.00	12	112.00	5.15	.61	4.00	-1.67
10	28	16	90.00	4.00	.62	5.40	1.00	15	112.00	5.15	.61	4.00	-1.11
10	28	22	140.00	4.00	.48	9.30	1.00	21	158.00	6.18	.30	4.00	-1.67
10	29	4	135.00	4.50	.44	9.30	1.50	3	180.00	7.21	.30	4.00	-3.33
10	29	10	150.00	4.50	.58	4.30	1.50	6	135.00	2.06	.00	.00	-1.11
10	29	16	175.00	5.00	.54	4.60	1.50	15	180.00	7.21	.61	4.00	1.11
10	30	10	165.00	5.00	.50	9.30	1.50	9	180.00	4.12	.00	.00	- .56
11	11	16	75.00	5.00	.88	10.80	-4.50	15	180.00	2.06	.30	3.00	-2.22
11	11	22	108.00	7.00	.94	10.80	-4.50	21	135.00	8.24	.30	4.00	-5.00
11	12	4	100.00	3.50	1.00	8.10	.00	3	112.00	5.15	.61	3.00	-3.33
11	12	10	100.00	7.00	1.06	5.40	.00	9	90.00	10.30	.61	4.00	-2.22
11	12	16	125.00	9.00	1.19	5.00	.00	15	135.00	9.27	.30	3.00	- .56
11	12	22	145.00	10.00	1.48	5.00	.00	21	135.00	13.38	.91	3.00	.00
11	19	16	195.00	5.00	.38	9.30	-2.70	15	180.00	4.12	.00	.00	.56
11	20	10	190.00	6.50	1.05	5.00	.00	9	180.00	7.72	.61	4.00	-1.67
11	20	16	200.00	8.00	1.11	5.40	.00	15	180.00	8.24	.61	4.00	1.11
11	23	16	215.00	5.00	.64	10.80	-7.00	15	180.00	4.12	.00	.00	-5.56
11	24	16	200.00	9.00	1.25	5.40	-2.50	15	180.00	10.30	.91	4.00	2.22

Mo = month, Da = day, Dir = wind direction, Wv = wind velocity, Hs = significant wave height, Tm = period of peak frequency, Hv = visual wave height, Tv = visual period, ΔT = sea-air temperature difference

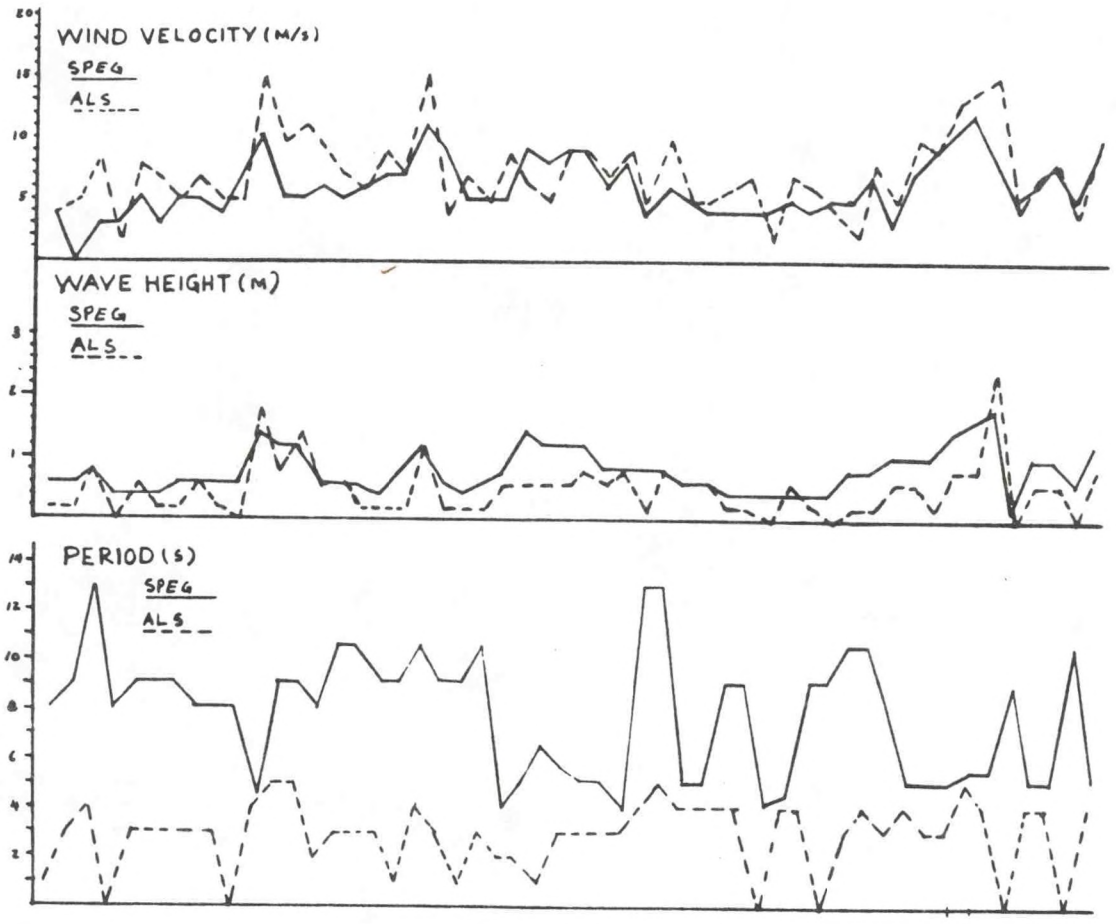

Figure 4. Comparison between the Public Service Electric and Gas of New Jersey (PSEG) data off Little Egg Inlet and the Ambrose Lightship data.

7.1.2 Alternative to determine wave period for ALS data (unlimited fetch)

To investigate further the discrepancy between wave periods at ALS and PSEG, we advance the hypothesis that the spectrum of waves at ALS is normal. In other words, it is assumed that the "shape invariance of wind-sea spectra" concept developed by Hasselmann et al. (1976) is valid in the New York Bight Apex. Based on the Pierson-Moskowitz (1964) spectra Hasselmann et al. propose:

$$f_m = \left(\frac{0.74}{1.25}\right)^{1/4} g/(2HU_{12.5}) = 0.14g/U_{19.5} \qquad (7.1)$$

where $U_{19.5}$ is the wind velocity in m/s at 19.5 m. At ALS the wind is measured at 28.7 m (94 ft). A wind velocity reduction of 4 percent (Silvester, 1974, Fig. 3-8) is used to transform the wind measured at a height of 28.7 m to a height of 19.5 m.

The distribution of wave periods corresponding to frequencies containing maximum wave energy at PSEG and wave periods observed visually at ALS are shown on Figure 5, as well as the computed wave period on the basis of wind speed, as discussed above. Figure 5 reproduces the lower portion of Figure 4 and outlines with more detail the discrepancy between the wave periods recorded at PSEG and those observed at ALS. The figure also shows that a better estimate of wave periods at ALS could be obtained using the relation: $T = 0.7289\ U_{19.5}$ than using visual observations. The value of the coefficient is related to height at which the wind velocity is measured. The following simplified correlation is used:

$U_{28.8}$	$U_{19.5}$	U_{10}
1.04	1.00	0.93
1.00	0.96	0.90

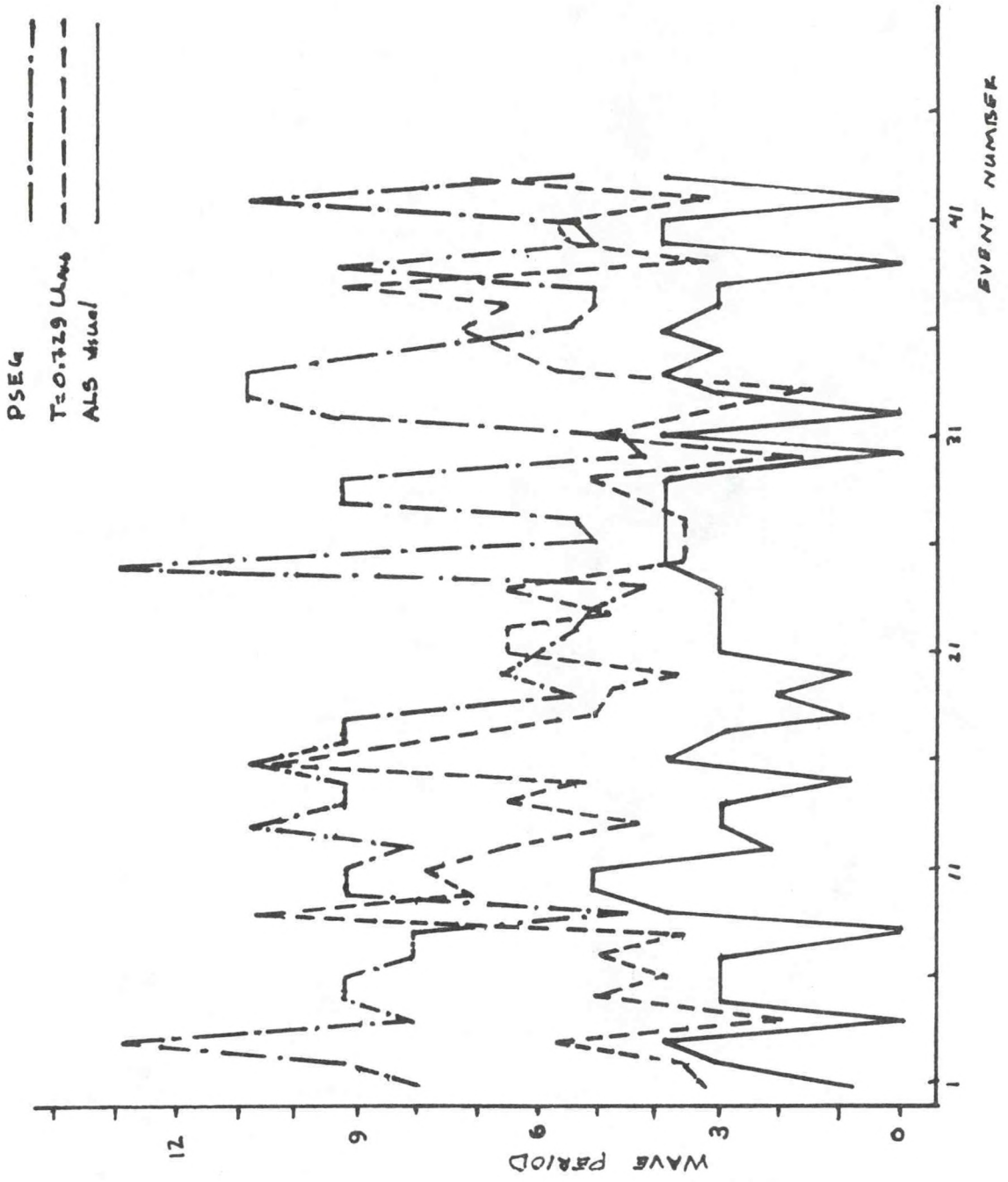

Figure 5. Comparison of wave periods for 43 concomitant events at Little Egg Inlet (PSEG) and the dumpsite. For the dumpsite, visual observations are plotted as well as wave periods calculated on the basis of wind velocity.

7.2 Limited Fetch

Limited fetches comparisons between ALS and PSEG are not possible. The correlation between wind generated waves and visual observations at ALS are discussed in the next chapter.

8. CORRELATION OF WIND AND WAVE RECORDS AT AMBROSE LIGHTSHIP

The second objective of this study is to determine the best equations to described the wave climate at Ambrose Lightship on the basis of wind conditions. The basic concepts elaborated in Chapter 6 are used for that purpose.

8.1 Limited Fetch

8.1.1 Wave Height

The Liu and Ross (1980) model is used to determine wave height and wave period. As discussed previously, these authors propose the following relationship:

$$e_* = 3.5 \times 10^{-5} X_*^{1.1} \qquad (8.1)$$

where

$e_* = Eg^2/U_*^4$ F: fetch

$X = gF/U_*^2$ E: total energy

$H_s = 4\sqrt{E}$ H_s: significant wave height

U_*: friction velocity (Cardone)

Figure 1 shows the fetches for the 16 points of the wind rose. The length of some of the fetches, the ENE fetch for example, could vary considerably. To gain some insight on the effective fetches versus the measured distance to the seashore, linear regressions were computed for visually observed wave heights versus computed wave heights for different

fetches and the results are tabulated on Table 2. Figure 6 also shows one example of linear regression. As the figure shows, as well as the data from Table 2, there are "residual" waves at zero wind velocity that are interpreted as reflecting the contribution of the swell.

8.1.2 Wave Period

For the computation of wave period, corresponding to the peak energy frequency, two equations are used depending on atmospheric stability as discussed previously (Liu and Ross, 1980):

For stable conditions $$V = 2.05\ X^{-0.27} \tag{8.2}$$

$$V = U_{10} f_m / g$$

$$X = gF/U_{10}^2$$

For unstable conditions $$V = 1.90\ X^{-0.27} \tag{8.3}$$

It reduces to

Stable conditions $$T_m = 0.09211\ F^{0.27}\ U_{10}^{0.46} \tag{8.4}$$

Unstable conditions $$T_m = 0.0995\ F^{0.27}\ U_{10}^{0.46} \tag{8.5}$$

These relationships are for winds measured at 10 m above sea level. The winds at ALS are measured at 28.8 m. A correction factor of 0.9 is applied to convert wind at 28.8 m to their equivalent at 10 m.

8.2 Unlimited Fetch

As mentioned previously, under unlimited fetch conditions the wave heights are a function solely of the square of the wind velocity and the wave periods are directly related to the wind velocity.

Table 2

	Measured Fetch = Distance to seashore				Effective Fetch = Adjusted to water depth and generate waveheights			
Direction	F(km)	a	b	R	F	a	b	R
NNE (22.5°)	24	0.24	.90	.710	24	.24	.90	.710
NE 45.	31	0.20	.61	.565	25	.21	.67	.554
ENE 67.5	55+	0.35	.28	.473	30	.37	.35	.432
E 90.0	UN							
ESE 112.5	UN							
SE 135.0	UN							
SSE 152.5	UN							
S 180.0	UN							
SSW 202.5	63	0.31	0.42	.571	25	.32	.64	.537
SW 225.0	24	0.42	0.68	.581	18	.43	.80	.583
WSW 247.5	14	0.38	0.64	.407	13	.38	.65	.401
W 270.0	13	0.24	1.12	.626	12	.24	1.15	.619
WNW 292.5	16	0.26	1.02	.672	16	.26	1.02	.672
NW 315.0	25	0.26	1.02	.748	25	.26	1.02	.748
NNW 337.5	19	0.23	0.76	.684	18	.23	.76	.684
N 360.0	22	0.11	1.15	.768	22	.11	1.15	.768

Basic Equation: $H_{visual} = a + bH_{computed}$

R: Correlation Coefficient for the linear regression equation

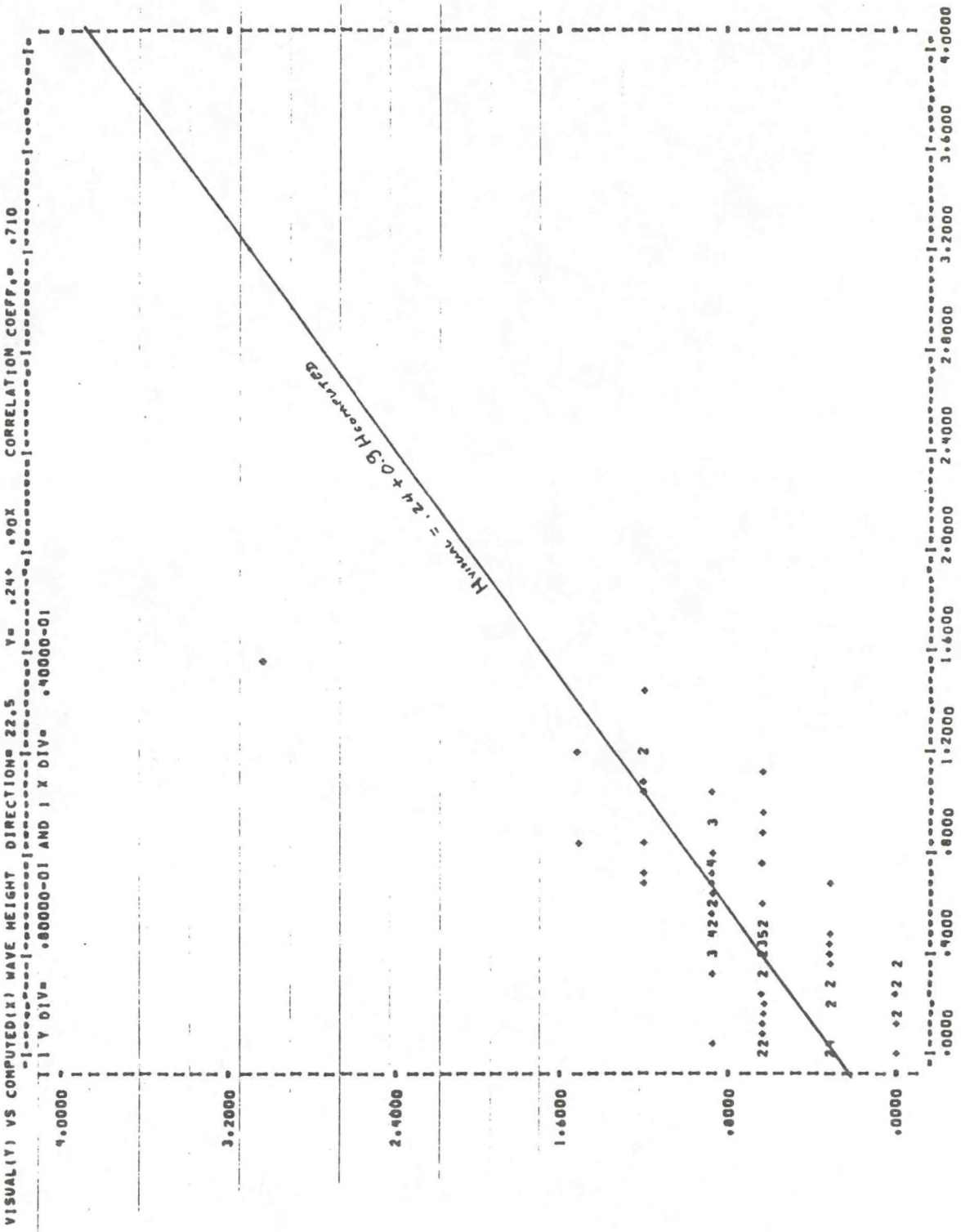

Figure 6. Regression of visual versus computed wave height for the ENE fetch.

It is informative to compare the characteristics of records from ALS and PSEG with those from other experiments. The parameters $V = f_m U/g$ (non-dimensional frequency) and $e = Eg^2/U^4$ (non-dimensional total energy) are often used for that purpose to produce plots of these two parameters in the form shown on Figure 3. Data from ALS for unlimited fetch using parameters e and V are shown on Figure 7. On the same figure are plotted the equations for Ross' stable and unstable conditions and also the JONSWAP equation. The shifting of the data towards the right confirms the observation made previously that the observed wave periods are shorter than expected (V being directly related to the wave frequency). However, the overall slope of the plotted data is in good agreement with Ross equations.

8.2.1 Wave Period

The analysis of wave period has already been discussed when comparing unlimited fetch records from ALS and PSEG in Section 7.1.1 and on Figures 4 and 5. We have come to the conclusion that depending on the height of wind velocity measurements

$$T_s = 0.7289\, U_{19.5} \tag{8.6}$$

$$T_s = 0.7009\, U_{28.8} \tag{8.7}$$

$$T_s = 0.7838\, U_{10} \tag{8.8}$$

8.2.2 Wave Height

Attempts were made to determine the relationship of the wave height to the square of the wind velocity on the basis of the recorded data. The first step to take is to distinguish wind waves from swell. As discussed previously, the parameter V can be used for that purpose. Liu and Ross (1980) indicate that wind waves are present when $V > 0.13$. The value $V = 0.13$ is

identified on Figure 7 and shows the repartition of wind-waves and swell for unlimited fetch records.

The relationship between the significant wave height and the wind velocity should have the form:

$$H_s = C\,U^2 \tag{8.9}$$

and we want to determine the constant C from actual records. For that purpose we assume that the data recorded at PSEG are more accurate than the visual observations from ALS because of the bias introduced in the observation of wave periods.

All the records from PSEG for unlimited fetches and for which $V \geq 0.13$ are used for calibration. A least-square routine is used for that purpose and the results are:

$$H_s = 0.01467\,U_{10}^2. \tag{8.10}$$

The values of the coefficient for the 95 percent confidence limits are 0.01339 and 0.01596 respectively. Figure 8 shows the distribution of the data used for calibration as well as the least square regression curve.

The value of the coefficient C is lower than those obtained from other studies. As mentioned previously the Pierson-Moskowitz equation as well as the JONSWAP results give

$$H_s = 0.0246\,U_{10}^2 \tag{8.11}$$

for $U_{10} - 0.93\,U_{19.5}$.

However, Figure 8 shows that the least square curve is already high for larger values of U and an increase of that coefficient would accentuate that tendency. There remains the possibility that some of the PSEG data for unlimited fetch are duration limited.

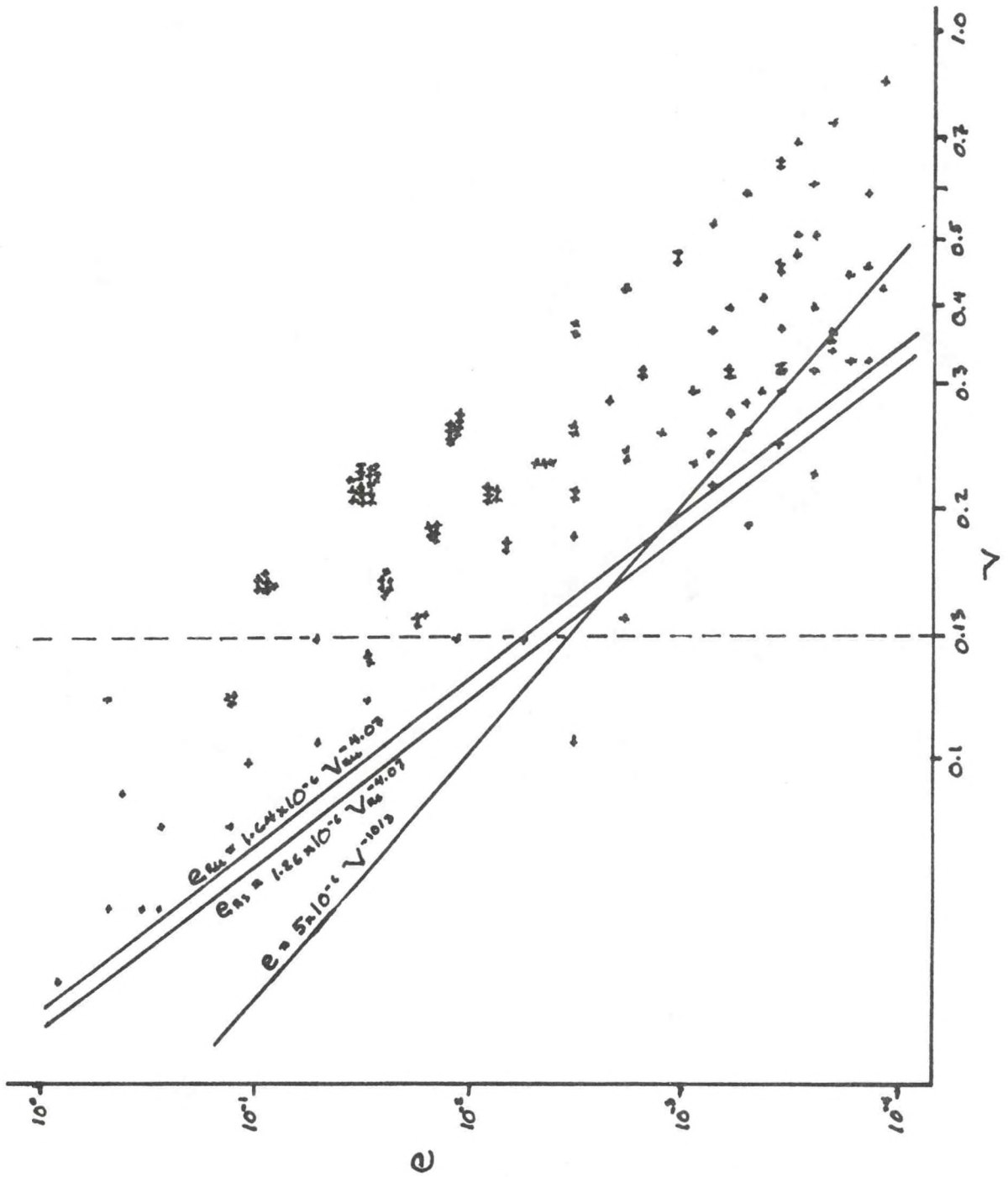

Figure 7. Plot of non-dimensional total energy (e) versus non-dimensional peak-energy frequency (V) for ALS data showing also linear regressions for JONSWAP as well as Ross stable and unstable equations.

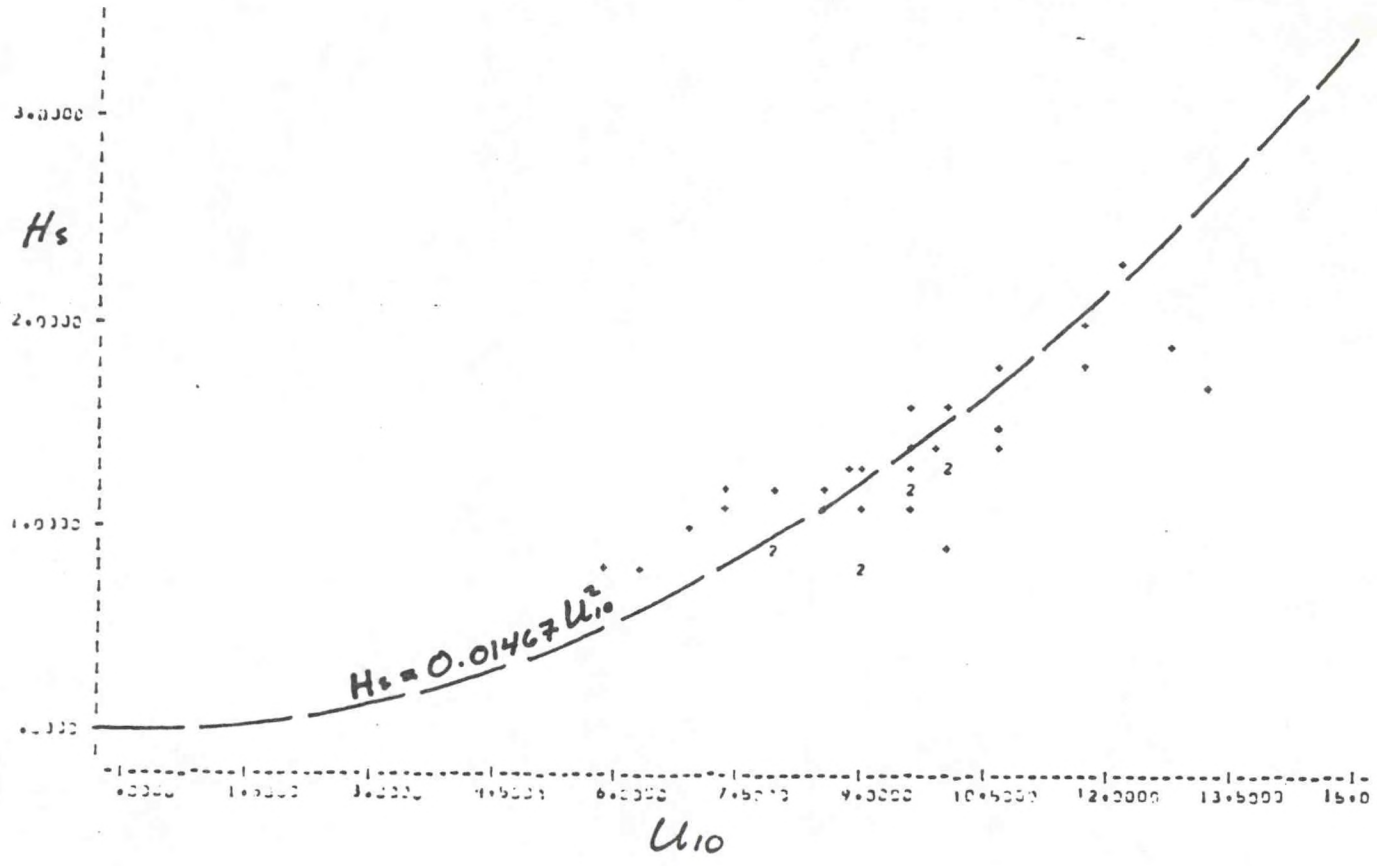

Figure 8. Correlation between significant wave height (Hs) and wind velocity (U_{10}) for unlimited fetches. Second degree best fit curve is also shown.

8.3 Wind Duration

The wind duration in the process of generation of waves is a parameter difficult to assess. For instance, Carter (1982), when summarizing JONSWAP results, notices that the identification of a duration equivalent to a given fetch is ambiguous and can vary by as much as 30% depending which relationship is used. In the present study, the fact that in some instances the generation of waves may be duration-limited is dealt with implicitly. Figure 9 shows graphs of significant wave height (H_s) vs wind speed (U_{10}). Graph 1 is obtained from PSEG wave data (Fig. 8) and Graph 2 is based on JONSWAP after Carter (1982). The lower constant obtained for PSEG data can be interpreted by comparing JONSWAP equations (Carter, 1982) with the results obtained in this study.

For duration-limited growing seas the JONSWAP parametric equation for significant wave height can be written as:

$$H_s = 0.0146\, D^{5/7} U^{9/7} \tag{8.12}$$

for which D is the duration in hours and U the wind speed in m/s at 10 m above the sea surface. For fully developed sea, the JONSWAP relation would be

$$H_s = 0.0240\, U^2. \tag{8.13}$$

Equations 8.12 and 8.13 are equated to determine the value of D as a function of U. It yields

$$D = 2.01\, U. \tag{8.14}$$

If the same procedure is followed using results from this study, that is, substituting Equation 8.10 for Equation 8.13, we obtain

$$D = 1.00\, U. \tag{8.15}$$

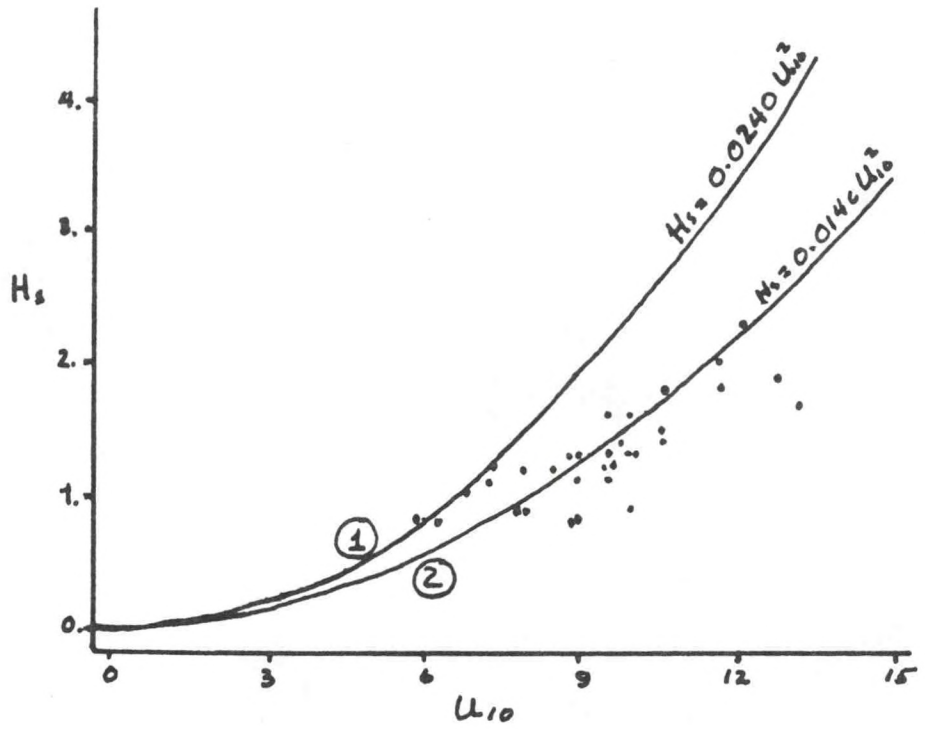

Figure 9. Comparison of the JONSWAP equation Hs = 0.0240 U_{10}^2 and the one used in this study Hs = 0.0146 U_{10}^2.

It means that when we use Equation 8.10 to calculate wave heights from unlimited fetches, we implicitly set that the generation of waves by the wind becomes duration-limited at the threshold D = 1.00 U, a lower limit than the JONSWAP one: D = 2.01 U.

This lower duration threshold for winds of this study is in agreement with the geographical location of the New York Bight Apex, where the unlimited fetch is restricted to the east to south quadrant. It is not a quadrant from which winds are prevailing (12.3 percent) as the upper histogram of Figure 2 shows. Those winds coming from east to south are likely to result from transitory weather patterns whose duration is limited.

8.4 Model Summary

In summary, the prediction of wave height and period at ALS based on wind speed (U), wind direction (D), and air-sea temperature difference DT ($DT = T_a - T_s$) is as follows:

Limited fetch $\qquad 0 \leq D < 90 \quad \text{or} \quad 180 < D \leq 360$

Significant wave height:

Use Cardone's friction velocity (U_*) which integrates height of wind measurement and air stability (DT)

$$e_* = 3.5 \times 10^{-5} X^{1.1}$$

$$H_{1/3} = (3.5 \times 10^{-5} (gF/U_*^2)^{1.1} 16 \times U_*^4/g^2)^{0.5}$$

Wave period (period of maximum wave energy)

$DT > 0 \Longrightarrow$

$$T_m = 0.0921 F^{0.27} U_{10}^{0.46}$$

$DT < 0 \Longrightarrow$

$$T_m = 0.0995\ F^{0.27} U_{10}^{0.46}$$

Unlimited fetch $\qquad 90 \leq D \leq 180$

$$H_{1/3} = 0.01467\ U_{10}^2$$

$$T_m = 0.7838\ U_{10}$$

9. CORRELATION OF WAVE HINDCASTING AND CV PROBE MEASUREMENTS

9.1 Transfer of Surface Wave Energy to the Bottom

Theories to describe water waves have been described extensively and their domains of application well defined. The depth (h) of the CV probe at the dumpsite is 30 m. The linear wave theory applies when $H/h \ll 1$ which is the case at the dumpsite and also $S = HL^2/2h^3 \ll \frac{16H}{3}$ where H is the wave height, L the wave length and h the water depth. However, the linear wave theory does not apply whenever $S > 8$. When the linear wave theory is applicable, the maximum orbital velocity (U_b) and orbital diameter (d_o) at the bottom are defined by:

$$U_b = \frac{H}{T \sinh\left(\frac{2Hh}{L}\right)} \tag{9.1}$$

$$d_o = \frac{H}{\sinh\left(\frac{2Hh}{L}\right)} \tag{9.2}$$

in which $L = 1.56\ T^2$ for $h/L > 0.5$; and for $h/L < 0.5$ L is approximated using:

$$L = L_\infty \left[\tanh\left(\frac{2Hh}{L_\infty}\right)\right]^{1/2}. \tag{9.3}$$

Among the parameters that determine U_b, the hyperbolic sine is the most limiting. This function increases exponentially and U_b becomes very small for $2\ Hh \gg L$. It means that at the depth of 30 meters waves have to be high, and more importantly have to have a long period to induce significant oscillations

on the bottom. The following examples demonstrate how the bottom orbital velocity varies as a function of wave period at a depth of 30 m:

$H_{1/3}$	T_m	U_b
1.0	5.0	1.00 cm/s
1.0	6.5	5.50
1.0	8.0	97.5

For all practical purposes, at a depth of 30 m, waves having a period shorter than 6 seconds have little effect on the bottom.

9.2 Comparison of CV probe and Wave Hindcasting Measurements

9.2.1 CV probe data

Measurements from the CV probe were recorded at 60-minute intervals. These data were averaged over 6-hour periods to produce four records per day directly comparable with the wave hindcasting data. Measurements of the north-south and east-west bottom current components were added vectorially. These data are shown on Figure 10 for the period November 19 to December 31, 1980. Figure 10a shows the water transparency which varies between 50 and 70 percent, the diminution of the transparency being directly related to the stirring of the bottom sediments. The measure of wave energy (Figure 10b) shows a strong correlation with the reduction of water transparency. The wave period (Figure 10c) does not show any apparent correlation with the wave energy, neither does the bottom current velocity (Figure 10d). The hourly records of bottom current velocities show better than this one the contribution of the semi-diurnal tidal currents to the bottom current field.

9.2.2 Comparison of data

The boxed section of Diagrams A and B in Figure 10 is shown with more detail on Figure 11. The hourly records of CV probe measurements of water

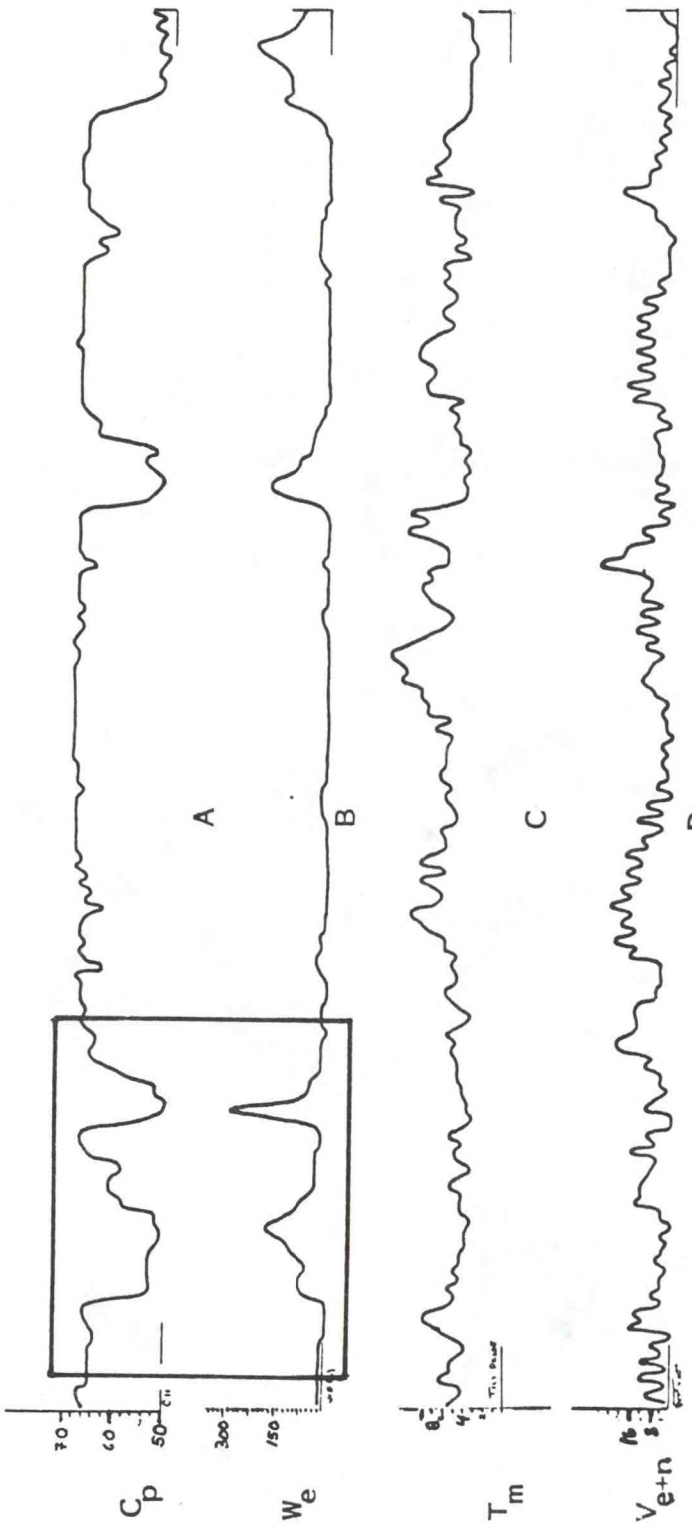

Figure 10. CV-probe measurements between November 19 and December 31, 1980. A: water transparency, B: wave energy, C: wave period, D: bottom current velocity.

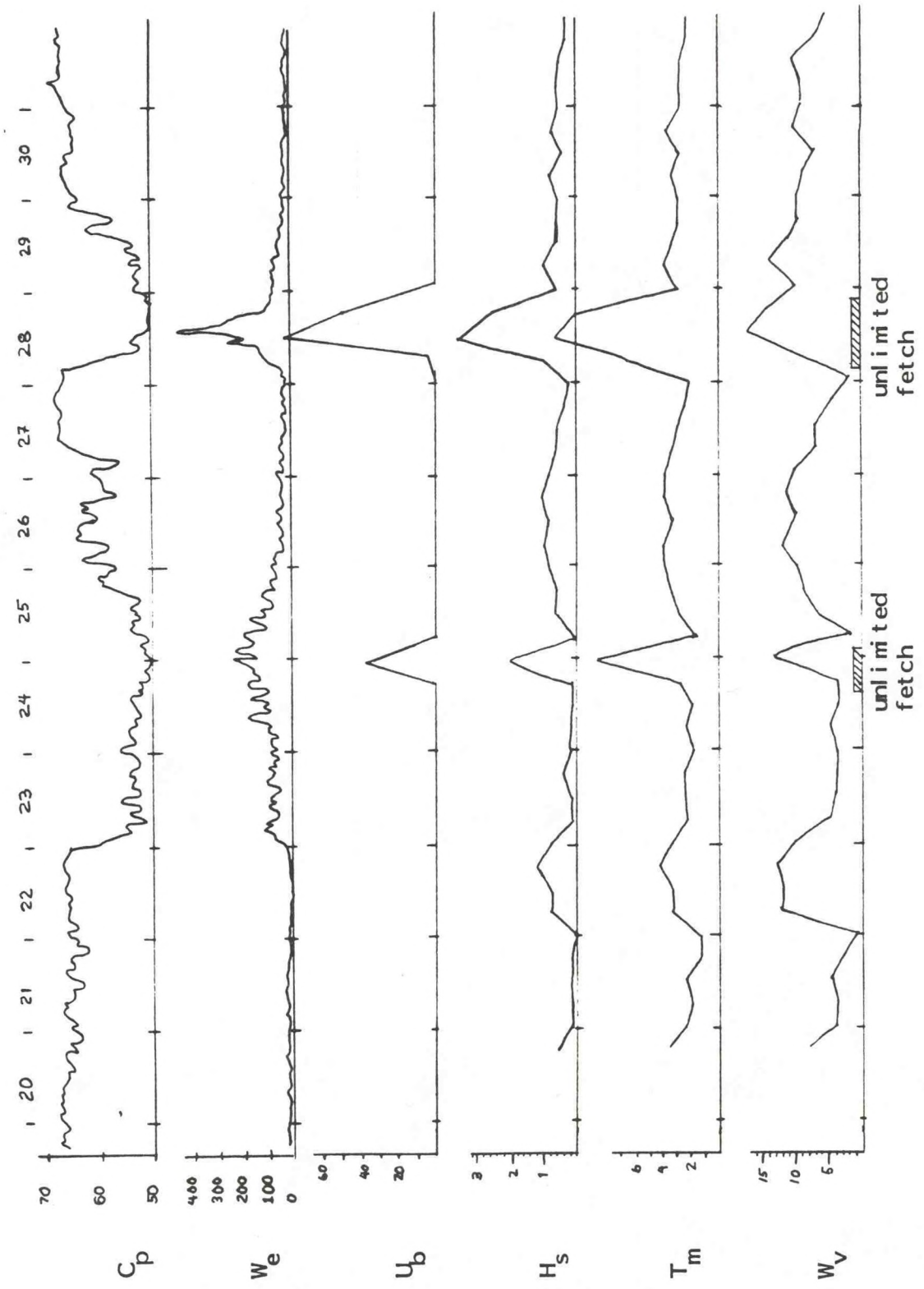

Figure 11. Details of measurements for the period 20 to 30 November 1980. Hourly records of water transparency (Cp) in percentage, wave energy (We) measured in cm^2/s^2, maximum bottom orbital velocity (Ub) in cm/s computed from surface waves, period of peak-energy frequency (Tm) and wind velocity (Wv) in m/s with indication of unlimited fetch intervals.

transparency (C_p) and wave energy (W_e) are transcribed directly for the period November 20 to 30, 1980. The two diagrams concur to outline two events: one of lesser magnitude and longer duration from November 23 to 25, and a shorter more intensive event on November 28. At the bottom of the figure is shown the wind velocity (W_v) recorded at Ambrose Lightship for the same period. Also shown on that same diagram are the two intervals during which the wind was blowing from offshore (unlimited fetch). Above this diagram of wind velocity are plotted the hindcasted wave periods (T_m) corresponding to peak energy frequency, and significant wave heights (H_s). More intense waves are naturally hindcasted when winds are blowing from offshore. Orbital bottom velocities (U_b) were computed using hindcasted wave heights and periods. The depth of water of 30 m considerably dampens the energy of surface waves, as discussed previously, and only the larger waves propagate to the bottom. This phenomenon is well outlined by the diagram U_b showing that orbital velocities on the bottom are significant during only two intervals, those during which higher wave energy was recorded by the CV probe. It confirms the adequacy of the wind hindcasting model.

Figure 12 compares wave energy recorded from the CV probe with hindcasted data for the whole period of deployment (November 19 - December 31). The wave energy as recorded by the CV probe is shown on diagram W_e of Figure 12. The other four diagrams are related to the surface wave hindcasting and outline the following: maximum bottom orbital velocity U_b, significant wave height (H_s), wave period (T_m), and wind velocity and direction (W). Not all the sequences of higher wave energy recorded by the CV probe have their counterpart in terms of wave bottom orbital velocities. Event 3, for instance, recorded by the CV probe, does not correspond to significant bottom orbital velocities generated by surface waves. Event 4 has a much stronger

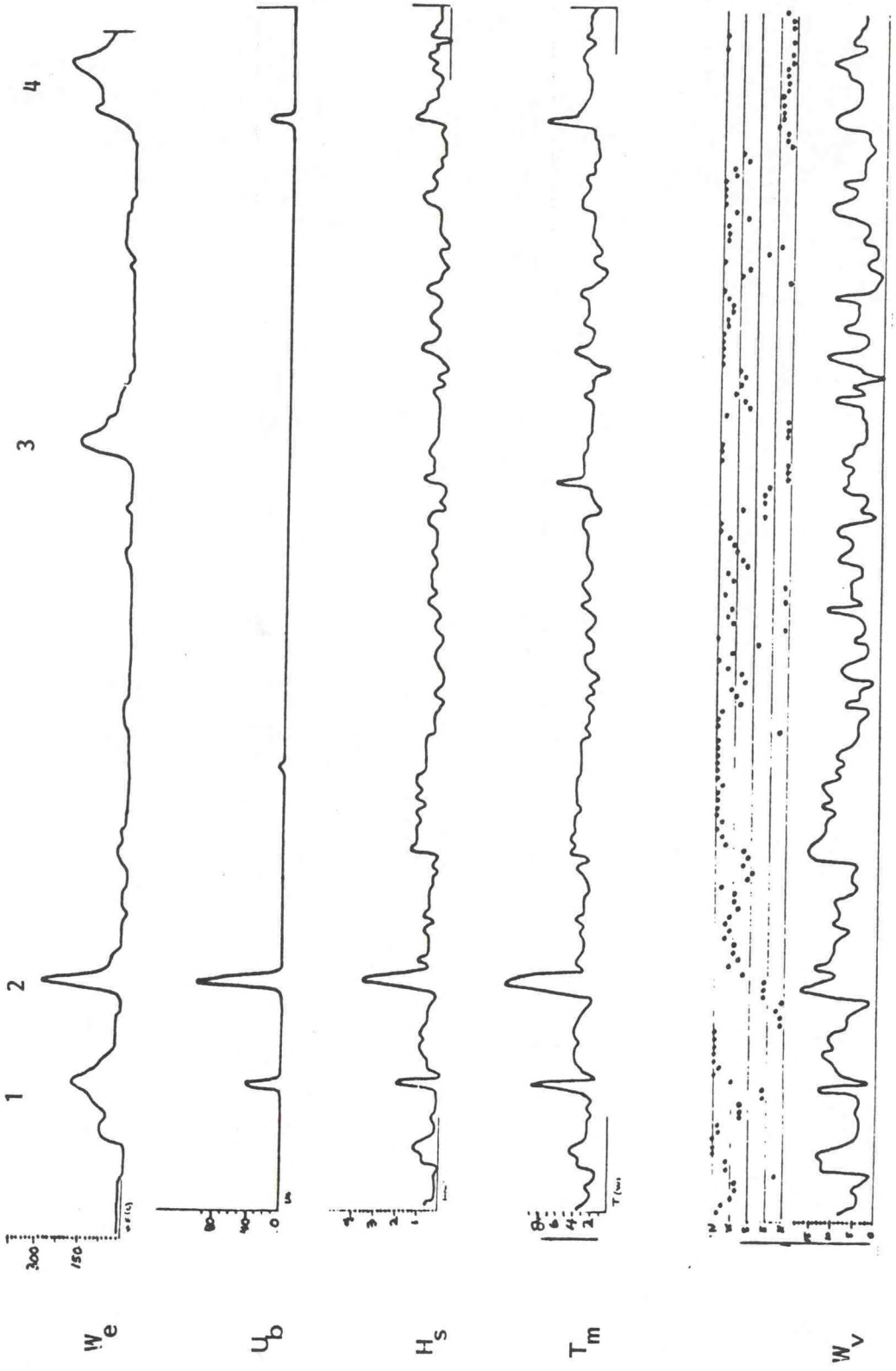

Figure 12. Same parameters as Figure 11 covering the period November 19 to December 31, 1980. The four major events for that period are labeled. The wind direction is also indicated.

show on the CV probe records than on those of bottom orbital velocities. To conclude, these data outline that wave hindcasting adequately outlines the impact of surface waves climate on bottom sediments, but it shows as well that not all the wave energy recorded on the bottom is generated locally and that swell waves also contribute to the transport of bottom sediments.

10. USE OF JOHN F. KENNEDY AIRPORT WIND DATA FOR WAVE HINDCASTING AT THE DUMPSITE

The immediate interest of using John F. Kennedy Airport (JFK) wind data is to extend the correlation between locally generated wind waves and CV probe measurements. The data available from Ambrose Lightship station end on December 31, 1980 and the CV-probe survey covers the period November 19, 1980 to June 23, 1981. The JFK data are used to extend this study to the end of the CV probe deployment. It is also an opportunity to evaluate the reliability of land stations for coastal wave hindcasting.

10.1 Calibration Procedure

10.1.1 Wind direction

The winds from JFK were found to be systematically lagging those from Ambrose Lightship (ALS). This lag is in agreement with the Ekman spiral effect: because of air friction, being greater on land than at sea, wind direction at the height of measurement departs more from the gradient wind at JFK than at ALS. Figure 13 shows the lag in wind direction between the two stations. As expected, the deflection is lesser for winds blowing from offshore.

10.1.2 Wind velocity

The wind velocity is higher at ALS than JFK. For November and December 1980 the average velocity for winds from all directions is:

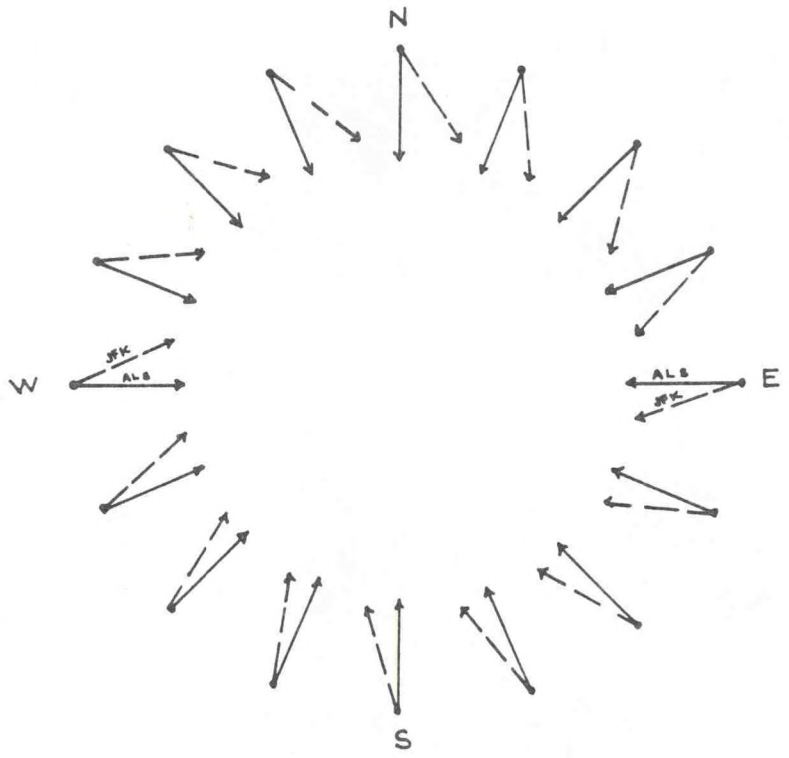

Figure 13. Differences in orientation between wind directions at Ambrose Lightship (full arrows) and John F. Kennedy Airport (dashed arrows).

JFK 6.68 m/s

ALS 8.34 m/s

The correlation between wind velocities at the two stations is not as systematic as for the direction. Winds were divided into two categories: onshore and offshore. For offshore winds no systematic trend is discernable and a constant value of 1.66 m/s was added to JFK wind velocities. For onshore winds, different regression equations were tested to correlate velocities from the two stations. The simplest and best fit is obtained with a linear regression:

$$W_{als} = 0.912 + 1.56\, W_{jfk} \qquad (10.1)$$

for which the correlation coefficient is R = 0.83.

10.2 Wave Hindcasting Using JFK Wind Data

A flow chart (Figure 14) summarizes the steps followed to compute wave heights and periods and maximum bottom orbital velocity and maximum bottom excursion using wind data from JFK Airport. The steps followed are described in this report and the numbers in parenthesis on the flow chart diagram are those identifying the equations used in the report.

10.3 Verification of Wave Hindcasting from JFK Airport Wind Data

The accuracy of the wave hindcasting based on JFK wind data can be verified by comparing the results with those recorded on the bottom at the dumpsite by the CV probe. As the CV probe measures the wave energy at the bottom, based on the variation of current velocities, the best criterion for comparison is to use the bottom orbital velocities computed from hindcasted wave heights and periods. The results are outlined as time series on Figure 15. The figure shows that the bottom orbital velocities hindcasted from JFK

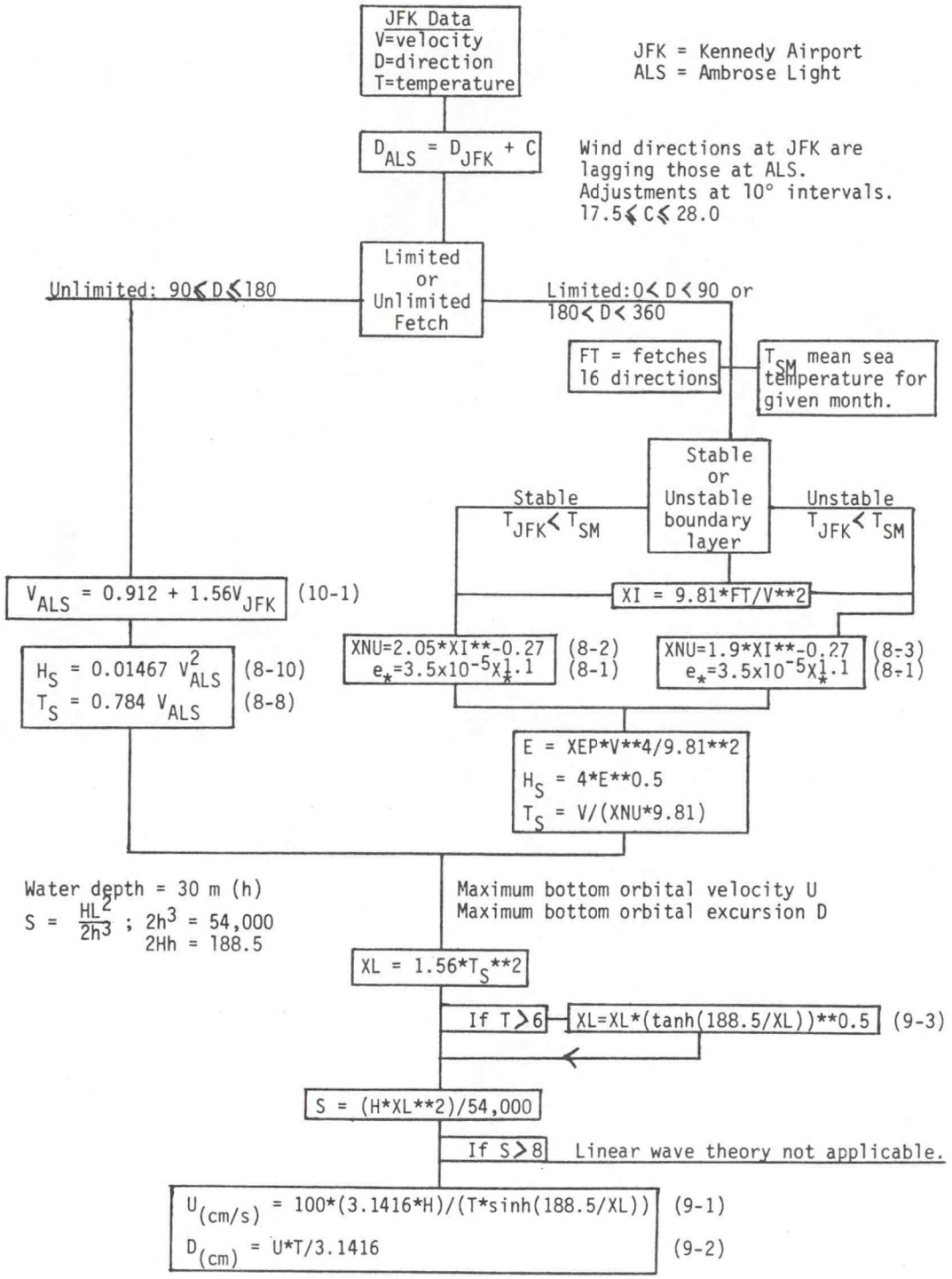

Figure 14. Flow chart for computation of maximum bottom orbital velocities using wind data from John F. Kennedy airport.

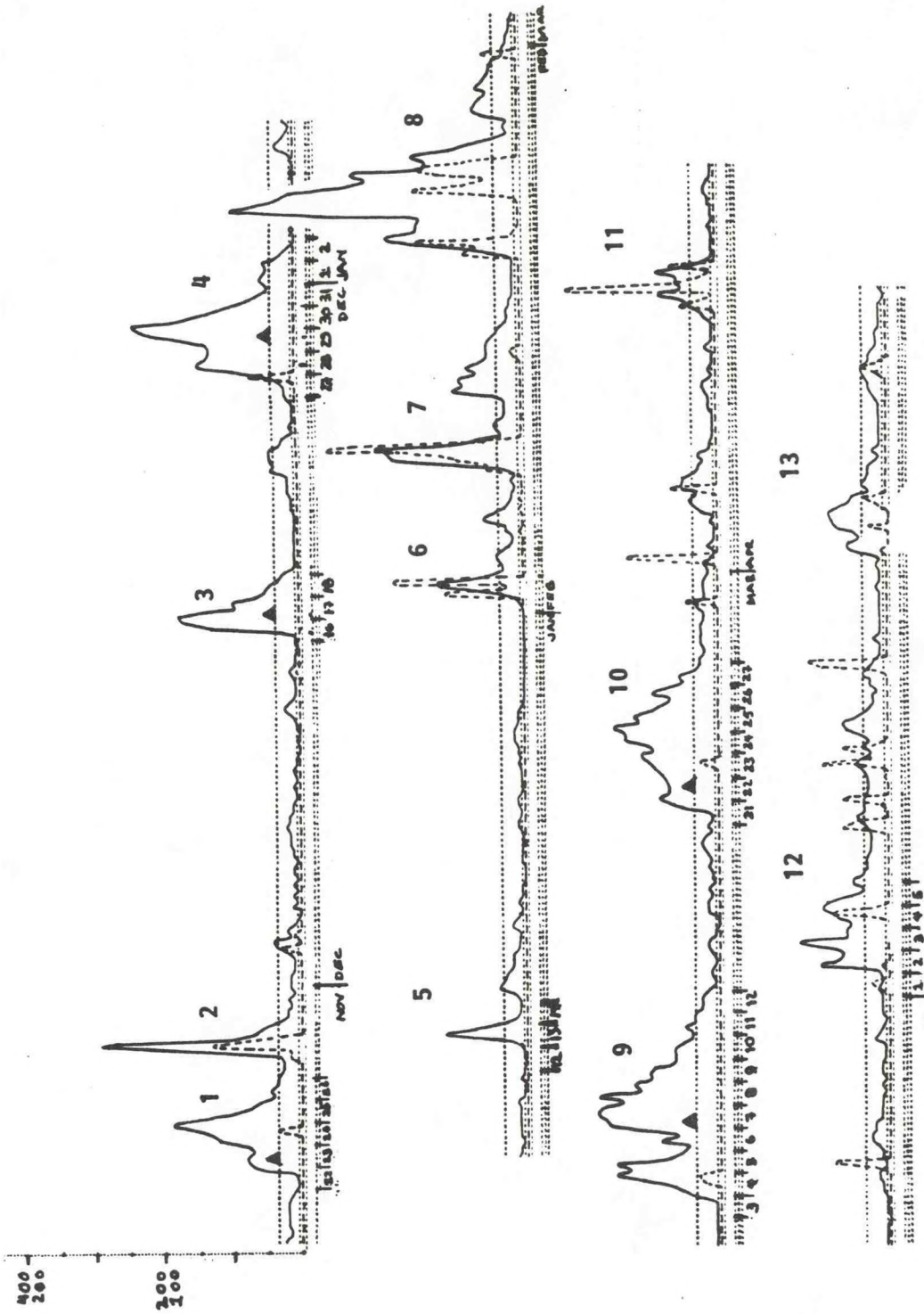

Figure 15. Time series of bottom wave energy (full lines, scale 0-400 cm^2/s^2) and computed maximum bottom orbital velocities (dashed line, scale 0-200 cm/s).

wind data are factual and correlate very well with the episodes measured by the CV probe on the bottom. The figure shows also that not all the events recorded by the CV probe are related to sea waves generated in the New York Bight. Swell waves have then to be examined.

11. WAVES GENERATED OUTSIDE THE NEW YORK BIGHT

Wave energy on the bottom was recorded at the dumpsite by the CV probe system during the period from November 19, 1980 to June 23, 1981. The continuous record of wave energy measured on the bottom is shown on Figure 15. The level of wave energy is shown by a solid line on that figure at a scale of 0-400 cm^2/sec^2. The dotted line on the same figure is a plot of the maximum bottom orbital velocity derived from wave hindcasts from wind records from JFK. As explained previously, the wind measurements at JFK are corrected for the study area and used to compute the heights and periods of waves generated at the dumpsite. These wave parameters are used to calculate the maximum bottom orbital velocities at the dumpsite. The results are plotted as a dotted line at the scale 0-200 cm/sec. The time series of wave energy measured by the CV probe outlines 13 more important events. The records for the month of June are not reproduced because no event of interest occurred during that last month of survey.

The time series for the maximum bottom orbital velocities (dotted line) shows a marked coincidence with many of the CV probe events, but not all. As the plot of maximum bottom orbital velocities is derived directly from wind conditions prevailing at the dumpsite, it implies that in some cases the wave energy recorded on the bottom at the dumpsite resulted from waves generated outside the New York Bight. The events on Figure 15 labeled 1, 3, 4, 5, 9 and 10 are specific cases when the waves generated by the winds prevailing at the

dumpsite did not have the dimension necessary to generate the wave energy recorded on the bottom. These six events are investigated to determine whether or not these records of high wave-energy intensity resulted from swell formed elsewhere on the Atlantic Coast and propagating in to the New York Bight.

The approach used is that suggested by Ross (1979), a refinement of Ross (1976), which presents a simple approach to hindcasting waves generated by hurricanes. Although originally intended only for use in circular hurricane wind fields, experience has shown its validity when applied to extra-tropical lows (Ross, personal communication). Adjusted geostrophic winds are used to specify the sea-surface wind in the parametric equations of Ross which are used to calculate the wave energy spectrum.

11.1 Methodology

Geostrophic wind (Silvester, 1974):

$$U_{sg}/g = (0.52/\sin\theta)\ \Delta P/\Delta n$$

θ = latitude in degrees

ΔP = pressure differential in millibars

Δn = spacing of isobars in degrees (latitude)

U_{sg} = geostrophic wind in dimensions commensurate with g (gravity).

Basic wave parameters (Ross, 1979):

$$\upsilon = f_m\ U_{10}/g$$

$$Er = \tau g/U_{10}^2$$

$$\epsilon = Eg^2/U_{10}^4$$

$$\upsilon = 0.97\ Er^{-0.21}$$

$$\epsilon = 2.25 \times 10^{-5}\ Er^{0.45}$$

$\gamma = 4.7\ Er^{-.13}$

$\alpha = 0.035\ \upsilon^{0.82}$

f_m = spectral peak frequency

U_{10} = wind velocity at 10 m = $0.7\ U_{sg}$

r = distance from center of depression to point of interest

E = total energy

Hs = $4\ \sqrt{E}$ · significant wave height.

Wave energy spectrum (Hasselmann et al., 1976):

$$E(f) = \alpha g^2 (2H)^{-4} f^{-5} \exp \left\{ -\frac{5}{4} \left(\frac{f_m}{f}\right)^4 + \ln \gamma \exp \left(-\frac{(f - f_m)^2}{2p^2 f_m^2} \right) \right\}$$

where $r = \begin{cases} \sigma_a, & f \geq f_m \\ \sigma_b, & f \leq f_m \end{cases}$

In the present case, $\sigma_a = \sigma_b = 0.1$.

11.2 Meteorological Conditions

The meteorological conditions prevailing on the Atlantic Coast when Events 1, 3, 4, 5, 9 and 10 were recorded are shown on Figure 16. The six maps show the weather patterns at 0700 EST for the dates specified.

It is assumed that the generation of swell waves that reached the New York Bight is associated with the offshore passage of well-defined barometric low pressure systems. The regions of wave formation with the proper orientation to reach the New York Bight are shown on each map. The horizontal pressure gradient in the generation area is used to calculate the geostrophic wind. The length of the radius from the generation region to the center of the depression and the distance to the New York Bight Apex are also determined from these maps. The input data for each event analysed are listed on Table 3.

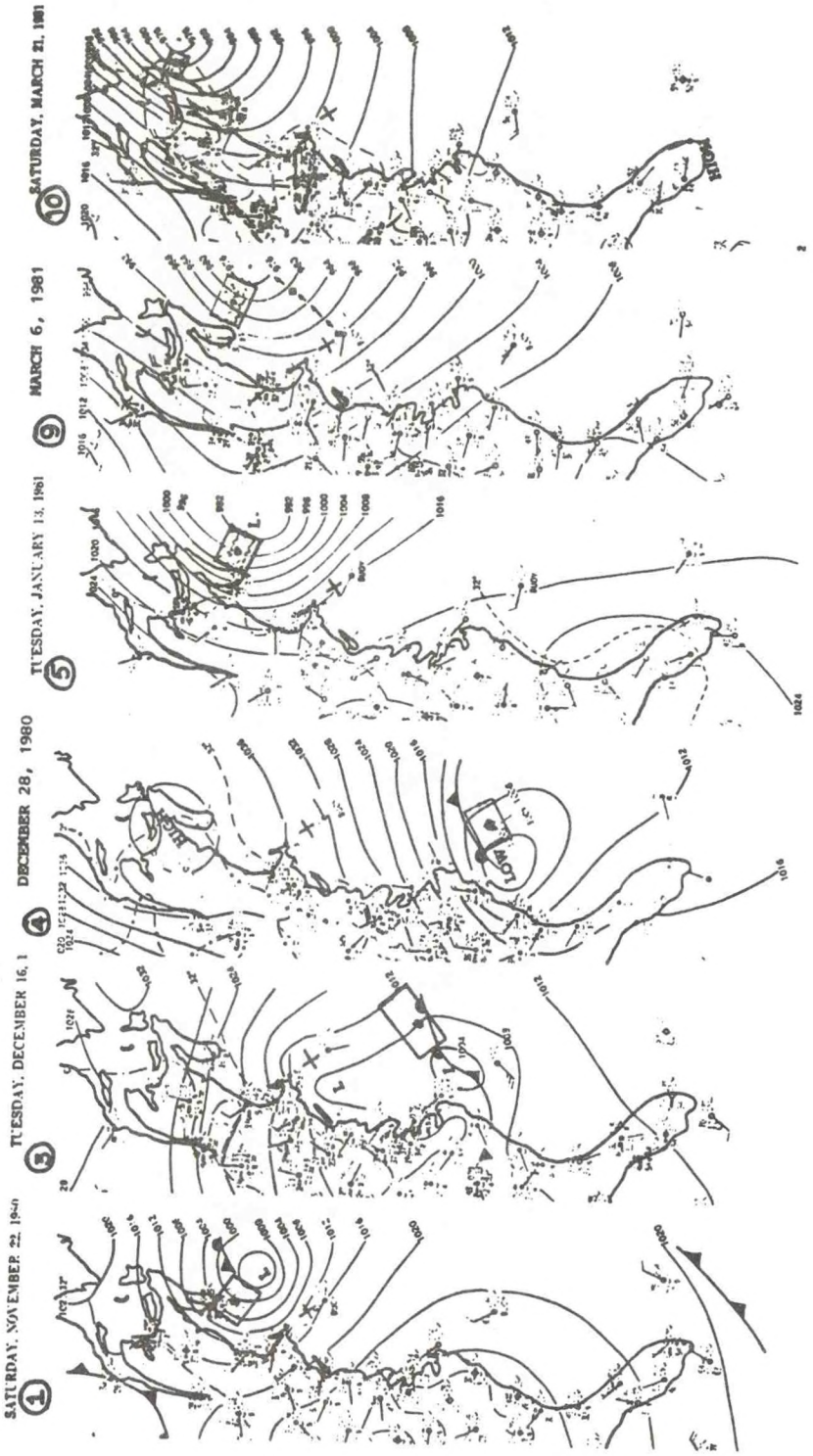

Figure 16. Weather patterns at 0700 EST for the dates specified on each map.

Table 3

Event	Date	dP	dL	Lat	Radius	Distance
1	22/11/80	8.0	1.7	43.5	195	650
3	16/12/80	4.0	1.5	35.0	296	600
4	28/12/80	4.0	1.5	32.5	203	950
5	13/01/81	8.0	1.8	43.5	222	850
9	06/03	12.0	2.4	43.6	205	888
10	21/03/81	8.0	1.25	45.0	138	1165

11.3 Wave Energy Spectra

Energy spectra of waves in the generation area are computed for each event. The results are tabulated on Table 4. The following parameters appear on the table: (1) reduced geostrophic wind velocity (U_{gs}) in m/s; (2) Philips parameter alpha (α); (3) gamma (γ); (4) nu (υ); (5) total energy (E); (6) peak energy frequency (f_m), and (7) significant wave height (H_s). Then for each 0.01 increment, for frequencies from 0.05 to 0.17, the level of energy and the time in hours (arrival) needed for waves of that frequency to reach the New York Bight Apex are calculated. The time of arrival of the peak energy frequency is also indicated by a black triangle on Figure 15.

The wave energy spectra are drawn on Figure 17. Examination of these wave energy spectra in relation with Figures 15 and 16 shows that the path of propagation of the different wave trains also plays an important role. For instance, even if Events 3 and 4 are less intense, the waves generated were facing the New York Bight Apex more directly than those coming from offshore Nova Scotia.

11.4 Discussion

The results presented in this chapter are interesting because they confirm that all the events recorded by the CV probe are related to wave activity, the waves being generated in the New York Bight itself or outside. However, the results presented in this chapter are only qualitative; bottom orbital velocities cannot be calculated at the present stage of investigation. To quantify the results, the wind velocity would have to be evaluated with more precision using gradient wind considering the translations of low pressure systems, and taking into account atmospheric conditions of stability or instability. Also the propagation of the waves from the generation area to

Table 4

Event 1 22/11/80	Event 3 16/12/80	Event 4 28/12/80	Event 5 13/01/81	Event 9 06/03/81	Event 10 21/03/81
W(m/s) = 24.4	W(m/s) = 16.6	W(m/s) = 17.7	W(m/s) = 23.0	W(m/s) = 25.8	W(m/s) = 32.3
Alpha = 0.0084	Alpha = 0.0069	Alpha = 0.0075	Alpha = 0.0081	Alpha = 0.0085	Alpha = 0.0099
Gamma = 1.645	Gamma = 1.409	Gamma = 1.505	Gamma = 1.593	Gamma = 1.659	Gamma = 1.851
NU = 0.177	NU = 0.138	NU = 0.154	NU = 0.169	NU = 0.180	NU = 0.215
TOT.E = 3.141	TOT.E = 1.147	TOT.E = 1.185	TOT.E = 2.789	TOT.E = 3.855	TOT.E = 6.417
FM = 0.071	FM = 0.081	FM = 0.085	FM = 0.071	FM = 0.068	FM = 0.065
HS(m) = 7.089	HS(m) = 4.284	HS(m) = 4.355	HS(m) = 6.680	HS(m) = 7.854	HS(m) = 10.133
Freq = 0.050	Freq = 0.050	Freq = 0.050	Freq = 0.050	Freq = 0.050	Freq = 0.050
Energy = 8.992	Energy = 0.165	Energy = 0.035	Energy = 7.599	Energy = 21.576	Energy = 53.035
Arrival = 11.574	Arrival = 10.683	Arrival = 16.915	Arrival = 15.135	Arrival = 15.811	Arrival = 20.744
Freq = 0.060	Freq = 0.060	Freq = 0.060	Freq = 0.060	Freq = 0.060	Freq = 0.060
Energy = 61.917	Energy = 7.170	Energy = 3.565	Energy = 54.857	Energy = 104.811	Energy = 210.667
Arrival = 13.888	Arrival = 12.820	Arrival = 20.299	Arrival = 18.162	Arrival = 18.974	Arrival = 24.893
Freq = 0.070	Freq = 0.070	Freq = 0.070	Freq = 0.070	Freq = 0.070	Freq = 0.070
Energy = 130.035	Energy = 27.388	Energy = 18.870	Energy = 116.256	Energy = 165.435	Energy = 227.831
Arrival = 16.203	Arrival = 14.957	Arrival = 23.682	Arrival = 21.189	Arrival = 22.136	Arrival = 29.042
Freq = 0.080	Freq = 0.080	Freq = 0.080	Freq = 0.080	Freq = 0.080	Freq = 0.080
Energy = 92.230	Energy = 46.026	Energy = 39.280	Energy = 86.978	Energy = 93.700	Energy = 112.792
Arrival = 18.518	Arrival = 17.094	Arrival = 27.065	Arrival = 24.216	Arrival = 25.299	Arrival = 33.190
Freq = 0.090	Freq = 0.090	Freq = 0.090	Freq = 0.090	Freq = 0.090	Freq = 0.090
Energy = 54.944	Energy = 37.916	Energy = 40.885	Energy = 52.179	Energy = 59.452	Energy = 73.423
Arrival = 20.833	Arrival = 19.230	Arrival = 30.448	Arrival = 27.243	Arrival = 28.461	Arrival = 37.339
Freq = 0.100	Freq = 0.100	Freq = 0.100	Freq = 0.100	Freq = 0.100	Freq = 0.100
Energy = 37.843	Energy = 25.089	Energy = 26.399	Energy = 36.005	Energy = 40.382	Energy = 48.838
Arrival = 23.148	Arrival = 21.367	Arrival = 33.831	Arrival = 30.270	Arrival = 31.623	Arrival = 41.488
Freq = 0.110	Freq = 0.110	Freq = 0.110	Freq = 0.110	Freq = 0.110	Freq = 0.110
Energy = 26.061	Energy = 18.087	Energy = 18.522	Energy = 24.855	Energy = 27.346	Energy = 32.599
Arrival = 25.462	Arrival = 23.504	Arrival = 37.215	Arrival = 33.297	Arrival = 34.786	Arrival = 45.637
Freq = 0.120	Freq = 0.120	Freq = 0.120	Freq = 0.120	Freq = 0.120	Freq = 0.120
Energy = 18.012	Energy = 13.096	Energy = 13.613	Energy = 17.206	Energy = 18.699	Energy = 22.087
Arrival = 27.777	Arrival = 25.641	Arrival = 40.598	Arrival = 36.324	Arrival = 37.948	Arrival = 49.786
Freq = 0.130	Freq = 0.130	Freq = 0.130	Freq = 0.130	Freq = 0.130	Freq = 0.130
Energy = 12.605	Energy = 9.455	Energy = 9.960	Energy = 12.053	Energy = 12.993	Energy = 15.255
Arrival = 30.092	Arrival = 27.777	Arrival = 43.981	Arrival = 39.351	Arrival = 41.111	Arrival = 53.935

cont.

Table 4

Event 1 22/11/80	Event 3 16/12/80	Event 4 28/12/80	Event 5 13/01/81	Event 9 06/03/81	Event 10 21/03/81
Freq = 0.140	Freq = 0.140	Freq = 0.140	Freq = 0.140	Freq = 0.140	Freq = 0.140
Energy = 8.961	Energy = 6.867	Energy = 7.299	Energy = 8.575	Energy = 9.193	Energy = 10.750
Arrival = 32.407	Arrival = 29.914	Arrival = 47.364	Arrival = 42.378	Arrival = 44.273	Arrival = 58.084
Freq = 0.150	Freq = 0.150	Freq = 0.150	Freq = 0.150	Freq = 0.150	Freq = 0.150
Energy = 6.478	Energy = 5.038	Energy = 5.390	Energy = 6.202	Energy = 6.624	Energy = 7.723
Arrival = 34.722	Arrival = 32.051	Arrival = 50.747	Arrival = 45.405	Arrival = 47.435	Arrival = 62.232
Freq = 0.160	Freq = 0.160	Freq = 0.160	Freq = 0.160	Freq = 0.160	Freq = 0.160
Energy = 4.761	Energy = 3.742	Energy = 4.022	Energy = 4.560	Energy = 4.856	Energy = 5.650
Arrival = 37.037	Arrival = 34.188	Arrival = 54.131	Arrival = 48.433	Arrival = 50.598	Arrival = 66.381
Freq = 0.170	Freq = 0.170	Freq = 0.170	Freq = 0.170	Freq = 0.170	Freq = 0.170
Energy = 3.554	Energy = 2.815	Energy = 3.035	Energy = 3.404	Energy = 3.619	Energy = 4.204
Arrival = 39.351	Arrival = 36.324	Arrival = 57.514	Arrival = 51.460	Arrival = 53.760	Arrival = 70.530

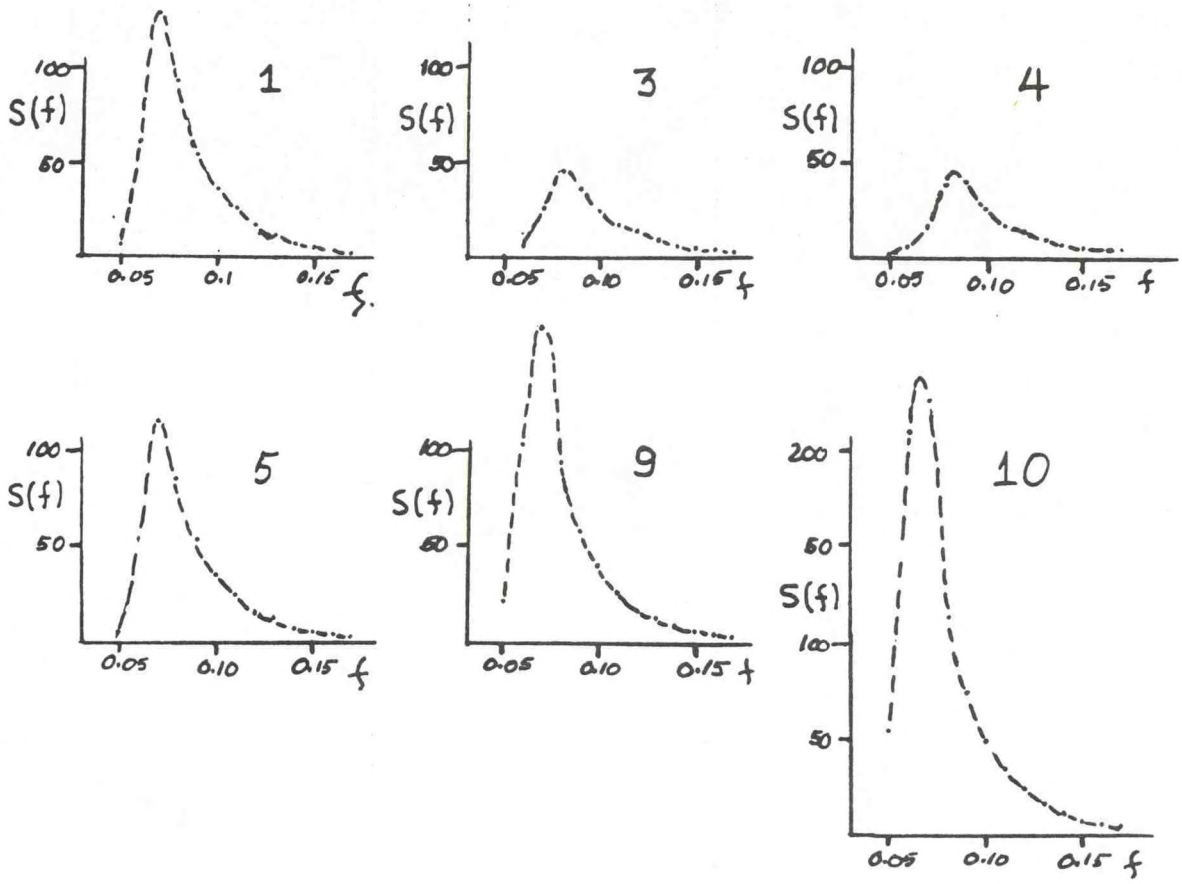

Figure 17. Energy spectra of waves (m^2-s) versus frequency (Hz) for the six events discussed in the text.

the point of interest would have to be examined for refraction and potential attenuation by winds and currents.

12. INFREQUENT EVENTS

The data available from Ambrose Lightship extend back to November 1956. It is possible to verify the impact of infrequent events, that is, storms of different intensities, suceptible to have affected the dumpsite area. Storm surges in the New York Bight have been described by Pore and Barrientos (1976). The events examined are listed as follows:

Table 5

Event	Days/Mo/Yr	Type	Name
1	08-09/03/57	E	
2	30-31/07/60	T	Brenda
3	09-13/09/60	H	Donna
4	14-15/09/61	T	Esther
5	06-07/03/63	E	
6	23-24/01/66	E	
7	27-28/08/71	T	Doria
8	18-20/02/72	E	
9	21-23/06/72	T	Agnes
10	09-10/08/76	H	Belle

H = Hurricane

T = Tropical storm

E = Extra-tropical storm

12.1 Sea Waves

Wave heights and periods, bottom orbital velocities, and bottom orbital diameters were computed using wind measurements at Ambrose Lightship. In the case of Hurricane Belle, the ALS station was evacuated and winds from John F. Kennedy Airport were used instead. The results are summarized on Figures 18 to 27. On most figures the increase and then decrease of wind velocity depict the passage of the storm. In many cases the wind direction is such that onshore winds are not a major constituent of the storm. The more important events are discussed separately.

Event 3 (Donna): 15-foot high and 7-second waves were reported at ALS for that hurricane.

Event 6: Fairly intense bottom orbital velocities (88 to 94 cm/sec) are hindcast because of the presence of onshore winds during that extra-tropical storm.

Event 7 (Doria): The most intense bottom orbital velocities (206 cm/s) of all events hindcasted. These high orbital velocities are associated with strong onshore winds (26 m/s) recorded at ALS.

Event 8: The second in intensity after Event 7 as bottom orbital velocities of 146 cm/s are hindcasted.

Event 9 (Agnes): Characterized not by the intensity of the event, but by the longer duration of significant bottom orbital velocities.

Event 10 (Belle): Below expectations because winds are blowing from north-east and the hindcasting model does not generate high waves locally.

12.2 Swell Waves

The spatial generation of waves by hurricanes has been analysed by Ross and Cardone (1978). Different models were explored and applied to the

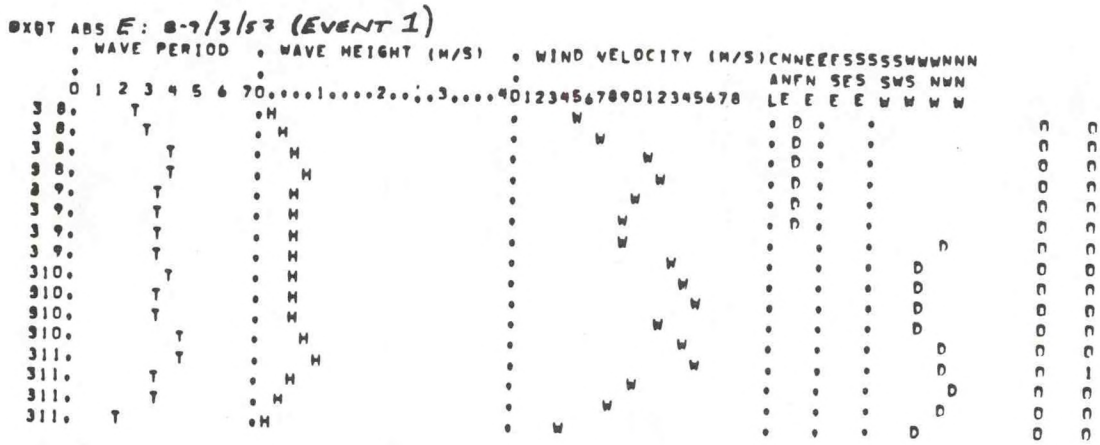

Figure 18

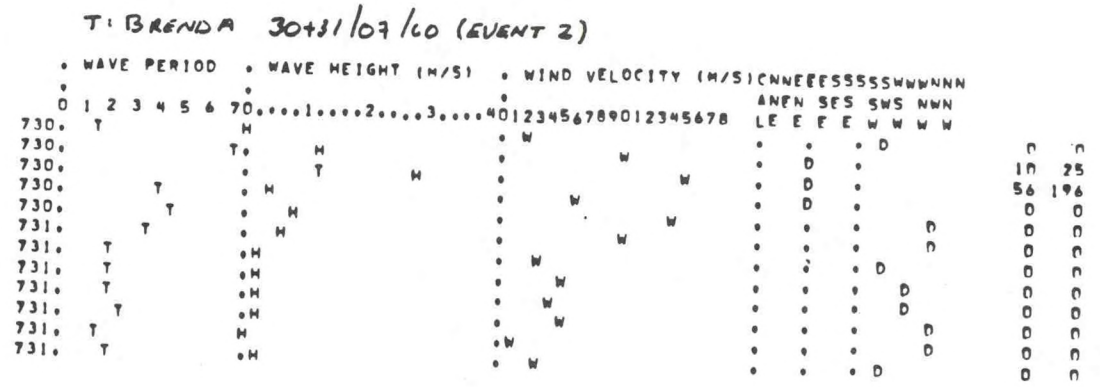

Figure 19

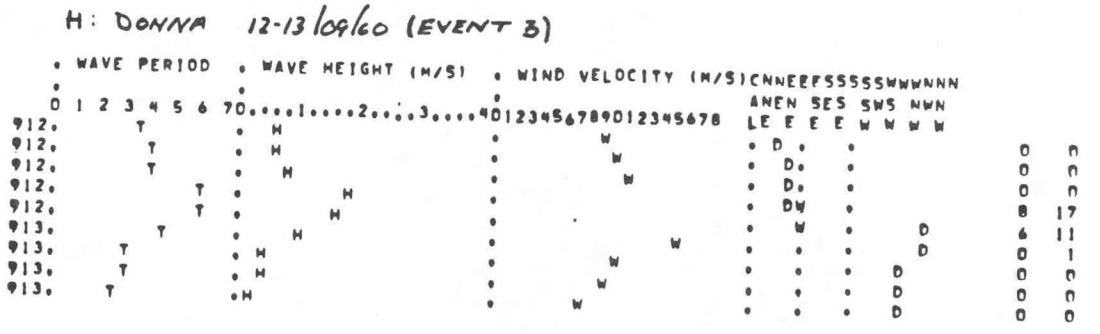

Figure 20

Figure 18-27. The four parameters shown are the computed wave period (T) in seconds and wave height (H) in meters, the wind velocity (W) in m/s and the wind direction (D). The scale is reproduced at the top of each figure. At the far left, the month and date are indicated and repeated for each record of the same day (ex: 730 means July 30). The two columns at the far right indicate: the first one the maximum bottom orbital velocity (cm/s) and the second one the maximum bottom excursion (cm).

T: 14-15/09/61 (EVENT 4)

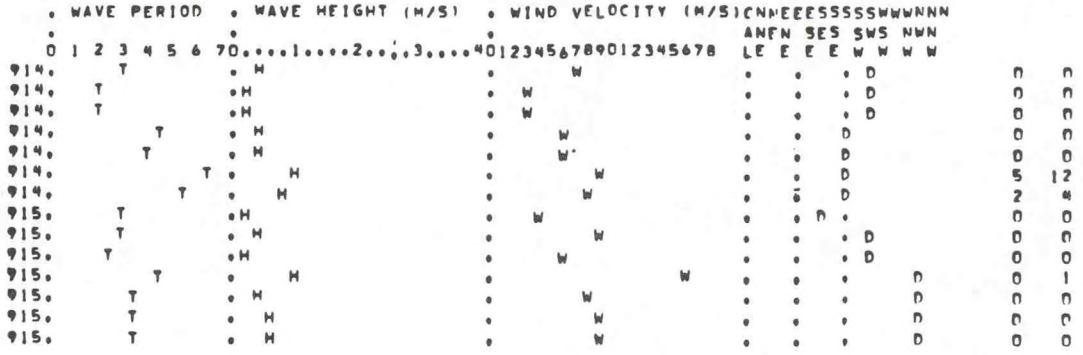

Figure 21

E: 6-7/03/63 (EVENT 5)

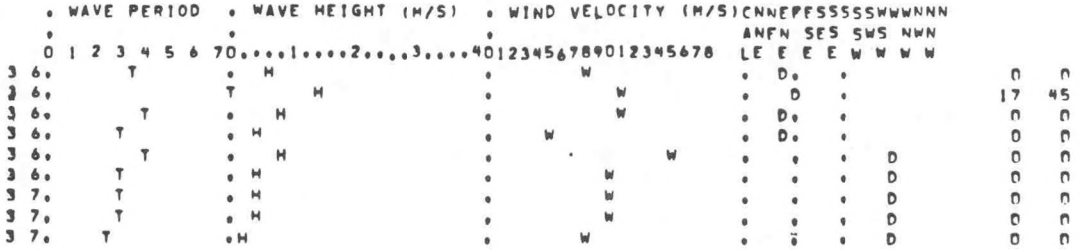

Figure 22

E: 23-24/01/66 (EVENT C)

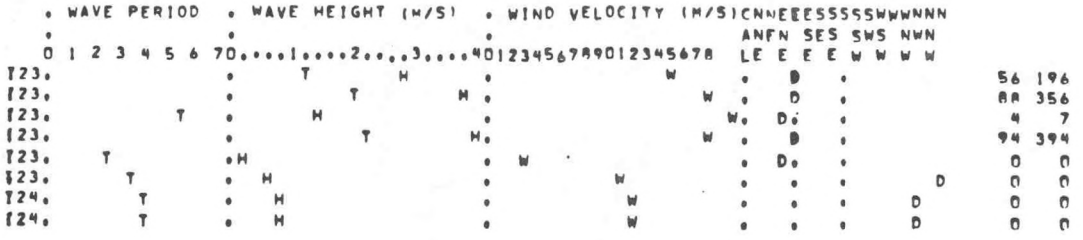

Figure 23

T: DORIA 27-28/08/71 (EVENT 7)

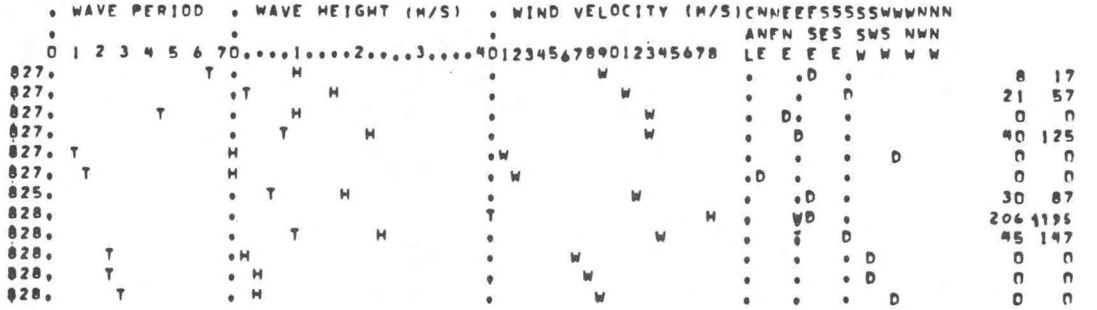

Figure 24

E: 18-21/02/72 (EVENT 8)

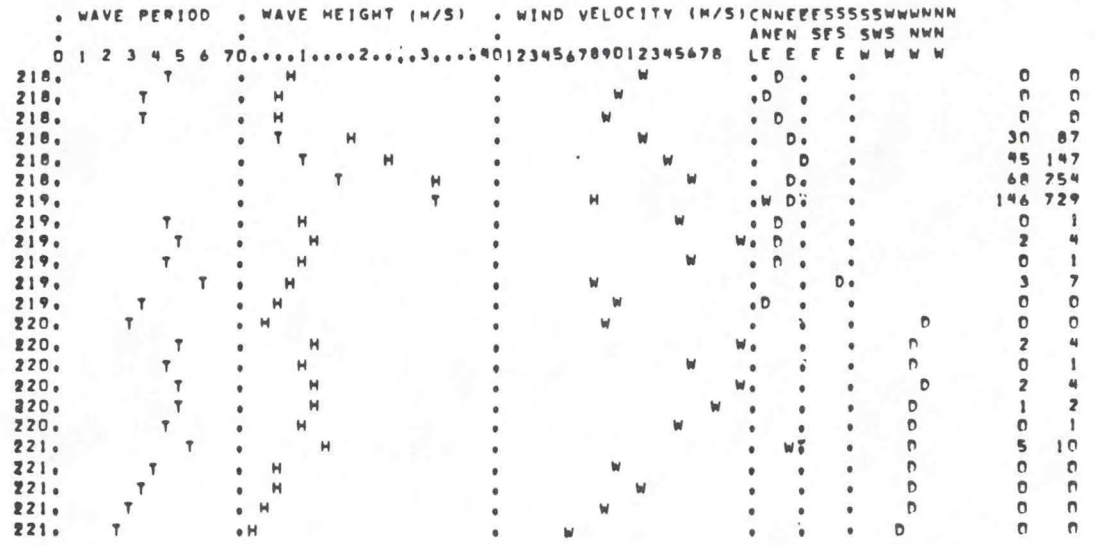

Figure 25

T: AGNES 21-23/10/72 (EVENT 9)

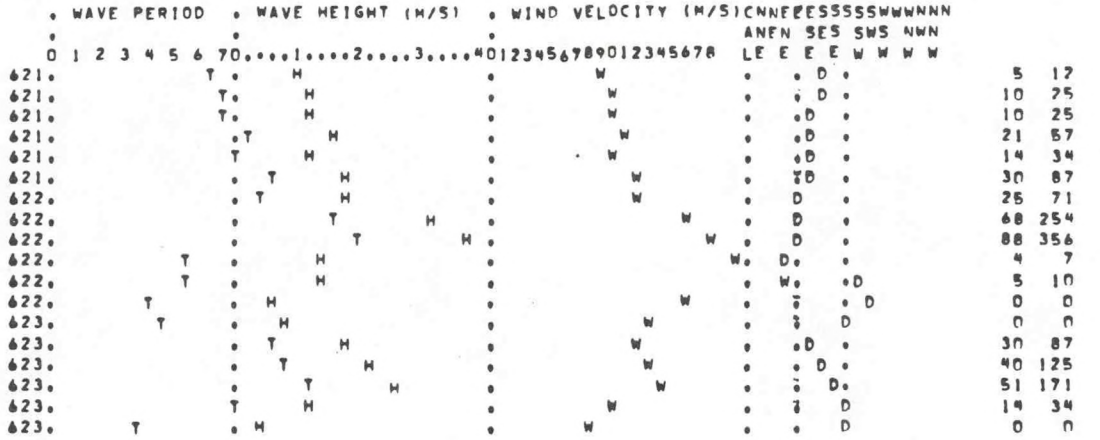

Figure 26

H: BELLE 9-10/8/76 (EVENT 10)

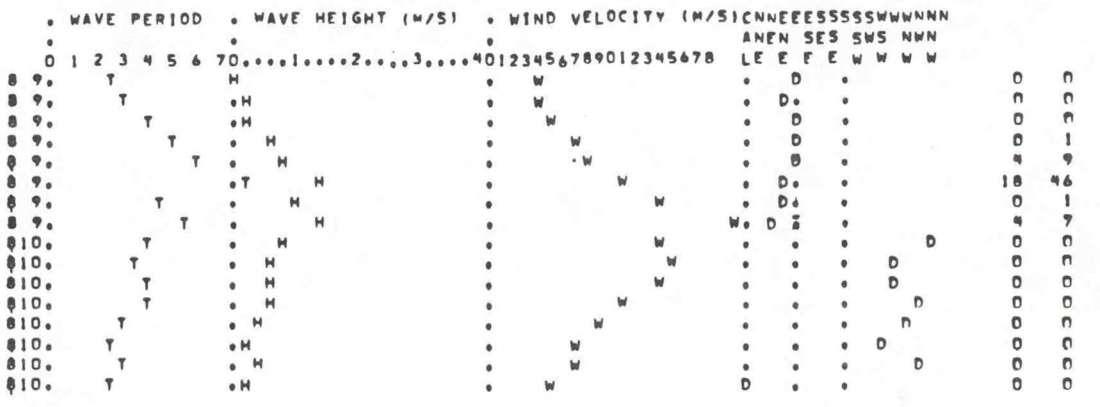

Figure 27

Atlantic Coast offshore the New York Bight. The results are reproduced on Figure 28. These outlines the potential of hurricanes to generate, under different conditions, swell waves in the New York Bight.

The National Hurricane Center has compiled a comprehensive analysis of all storms on the Atlantic Coast since 1886, including the maximum significant waves heights generated by each storm as it progressed along its course. With respect to the New York Bight, it is assumed that the maximum impact from a storm would be felt when the storm center reaches latitude 40°N because the waves formed in front of the storm center would then be propagating towards the New York Bight. The storm characteristics at latitude 40°N, or nearby, compiled by NHC are listed on Table 6. These data, when used in conjunction with Figure 28, permit a qualitative estimate of the swell waves reaching the New York Bight during major storms.

On the basis of these records, it appears that the most severe storm is the ill-fated 1938 hurricane, in which case the computed significant wave height reaches 13.5 meters. It is interesting to notice that "Gladys" (1975) produced 13.1 meter waves, but its center was farther seaward (67.0°W) longitude versus 73.0°W for the 1938 storm).

In summary, storms generating waves higher than 10 m [1938, 1959, 1975 (Gladys) and 1978 (Ella)] are not numerous enough to warrant probability analyses. We can only notice that the two extreme events: the 1938 storm (H_s = 13.5 m) and Gladys (H_s = 13.1 m) are 37 years apart.

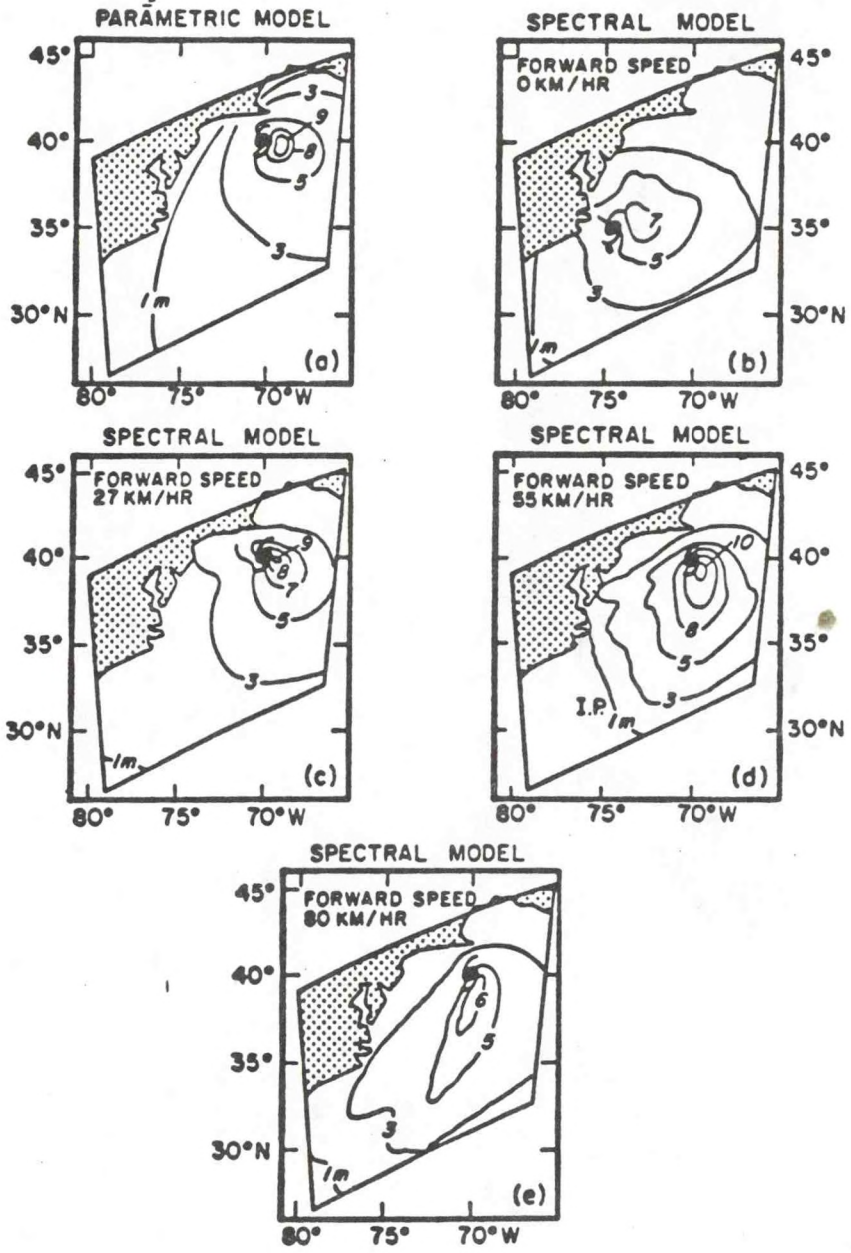

Figure 28. Contour diagrams of the significant wave height for storms of the U.S. Atlantic Coast (from Ross and Cardone, 1978).

Table 6

Year	Date	HR	Lat	Lon	Hs	Year	Date	Hr	Lat	Lon	Hs	
1886	08/26	00	39.9	67.8	6.7	1943	09/08	18	38.8	64.6	5.7	
1887	08/22	00	38.7	70.1	6.9	1944	07/19	06	38.6	62.0	5.3	
1887	08/26	06	39.9	63.2	8.8	1944	08/03	12	39.8	72.8	2.2	
1888	10/12	06	38.4	73.3	4.0	1944	09/15	00	39.9	73.2	7.5	
1888	11/27	06	39.8	70.3	6.4	1945	06/27	06	40.0	70.1	3.8	
1891	09/07	18	39.5	68.0	8.8	1946	07/09	06	39.6	61.6	4.3	
1891	10/05	18	39.9	67.8	7.5	1946	09/15	00	38.7	67.5	6.2	
1891	10/13	18	39.5	71.5	6.3	1948	09/01	06	39.0	65.1	6.4	
1891	10/19	12	39.0	63.9	7.4	1948	09/24	18	39.8	62.3	7.5	
1892	08/21	12	40.0	63.0	7.1	1948	10/15	18	38.5	47.9	2.4	
1893	06/18	06	39.8	70.2	5.8	1949	08/25	18	38.5	59.8	7.0	
1893	08/21	18	39.5	68.6	9.9	1950	08/21	00	39.4	69.5	8.1	ABLE
1893	08/24	06	39.4	73.9	7.6	1950	09/12	00	39.3	70.6	5.2	FOX
1893	08/16	18	38.4	66.1	4.8	1951	05/24	12	39.5	60.0	2.9	ABLE
1894	09/30	18	39.8	72.3	1.3	1951	10/06	12	39.5	65.7	6.2	HOW
1894	10/10	12	39.4	74.0	5.3	1952	09/07	12	39.0	64.0	6.7	BAKER
1894	10/27	00	37.8	66.2	9.1	1952	09/28	18	40.0	56.9	6.9	CHARLIE
1896	09/10	06	40.0	69.2	7.6	1953	08/15	00	39.3	72.3	6.2	BARBARA
1896	09/24	12	38.9	62.7	7.6	1953	09/07	06	38.6	70.3	7.2	CAROL
1896	10/13	12	40.0	67.2	6.5	1954	08/31	12	40.2	72.9	8.6	CAROL
1903	07/26	06	39.8	53.5	4.8	1954	09/11	12	38.0	73.0	8.3	EDNA
1903	09/15	06	39.1	75.0	6.8	1955	09/21	00	39.4	67.8	7.5	IONE
1906	09/10	18	39.8	58.1	7.5	1956	08/18	00	39.5	66.4	5.5	CLEO
1908	08/01	18	39.1	71.0	7.1	1956	08/29	12	39.8	70.8	7.9	DAISY
1908	09/17	12	39.6	64.1	6.1	1958	09/29	00	39.0	65.9	9.8	HELENE
1912	11/24	00	39.1	69.0	5.3	1958	10/11	12	39.3	56.0	7.1	JANICE
1916	07/21	06	39.9	71.4	6.2	1959	06/19	12	38.4	65.3	11.7	
1923	09/09	00	39.2	58.5	5.3	1959	07/11	06	39.5	72.4	3.5	CINDY
1923	10/01	06	39.1	61.9	9.6	1960	09/12	18	40.0	73.1	9.0	DONNA
1924	08/26	18	40.6	70.3	9.1	1961	10/08	06	39.2	64.7	8.0	FRANCES
1924	09/04	06	38.6	66.0	6.9	1962	09/02	00	39.7	65.0	2.9	ALMA
1926	08/07	18	39.6	65.6	6.9	1962	10/07	06	39.1	65.4	7.9	DAISY
1926	09/21	12	40.0	60.0	4.9	1962	10/22	00	39.5	59.7	6.5	ELLA
1926	10/24	00	39.2	50.1	6.3	1963	10/29	06	37.8	68.8	8.4	GINNY
1927	08/24	12	38.0	72.4	8.5	1964	09/04	00	38.7	56.9	7.9	CLEO
1932	09/09	06	39.5	67.7	7.4	1964	09/14	12	38.0	71.5	4.4	DORA
1933	09/17	12	38.9	72.1	5.1	1964	09/24	00	39.2	69.0	7.1	GLADYS
1933	10/07	18	39.4	65.9	9.5	1966	06/14	00	39.2	72.1	2.4	ALMA
1934	09/08	18	38.7	73.8	6.0	1966	07/21	06	39.5	63.2	5.9	CELIA
1935	08/24	18	39.7	57.6	7.7	1966	09/03	18	39.7	51.1	8.6	FAITH
1935	09/07	00	39.7	65.4	9.6	1968	10/21	00	38.6	68.3	6.8	GLADYS
1935	10/01	12	38.8	62.0	7.6	1969	08/12	00	38.6	68.0	8.0	BLANCHE
1936	09/19	00	38.6	74.0	7.1	1969	09/09	18	40.1	69.9	8.2	GERDA
1936	09/24	12	38.6	68.6	6.9	1969	10/17	12	39.6	60.2	6.6	KARA
1937	09/25	18	38.5	61.2	7.9	1971	08/15	12	39.7	67.2	7.1	BETH
1938	09/21	18	39.0	73.0	13.5	1975	07/28	00	39.3	67.2	6.6	BLANCHE
1940	09/02	06	39.8	70.3	6.1	1975	10/02	18	37.8	67.0	13.1	GLADYS
1940	09/16	12	39.7	67.6	6.1	1976	08/10	00	38.8	73.8	7.7	BELLE
1941	09/25	06	39.7	67.5	2.0	1977	10/15	00	39.2	63.3	6.2	EVELYN
1941	10/14	12	39.5	45.0	2.9	1978	09/04	12	40.0	63.0	10.4	ELLA

REFERENCES

Bretschneider, C. L., 1957. Revisions in wave forecasting deep and shallow water. Proceedings, Sixth Conference on Coastal Engineering, p. 30-67.

Cardone, V. J., 1969. Specification of the wind distribution in the marine boundary layer for wave forecasting. New York Univ., Rept. TR-69-1, Contract No. NONR-285(57) (NTIS AD-702490), 131 pp.

Carter, D. J. T., 1982. Prediction of wave height and period for a constant wind velocity using the JONSWAP results. Ocean Engng., Vol. 9, No. 1, p. 17-33.

Darbyshire, J., 1959. A further investigation of wind-generated waves. Deutsche Hydrographische Zutschrift, Vol. 12, p. 1-13.

Hasselmann, K., et al., 1973. Measurements of wind-wave growth and swell decay during the Joint North Sea Wave Project (JONSWAP). Deutsche Hydrographische Zutschrift, Reich A (8).

Hasselmann, K., D. B. Ross, P. Muller, and W. Sell, 1976. A parametric wave prediction model. Jour. Phys. Oceanogr., Vol. 6, No. 2, p. 200-228.

Kitaigorodskii, S. A., 1962. Application of the theory of similarity to the analysis of wind-generated wave-motion, I. Geophys. Ser. Acad. Sci., USSR, Vol. 1, p. 105-117.

Liu, P. C., and D. B. Ross, 1980. Airborne measurements of wave growth for stable and unstable atmospheres in Lake Michigan. Jour. Phys. Oceanogr., Vol. 10, p. 1842-1853.

Pierson, W. J., G. Neumann, and R. W. James, 1955. Practical methods for observing and forecasting ocean waves. U.S. Hydrographic Office Publ. No. 603, 284 pp.

Pierson, W. J., and L. Moskowitz, 1964. A proposed spectral form for fully developed wind seas based on the similarity theory of S. A. Kitaigorodskii. Jour. Geophys. Res., Vol. 69, p. 5181-5190.

Pore, N. A., and S. Barrientos, 1976. Storm Surges. MESA New York Bight Atlas Monograph 6, New York Sea Grant Institute, Albany, NY.

Quayle, R. G., and M. J. Changery, 1982. Preliminary height and period adjustments for visual wave data. Mar. Weather Log., Vol. 26, p. 2-3.

Ross, D. B., 1976. A simplified model for forecasting hurricane-generated waves. Bull. Amer. Meteor. Soc., p. 113.

Ross, D. B., 1979. Observing and predicting hurricane wind and wave conditions. Ocean Products and IGOSS Data Processing Services System (IDPSS), Moscow, USSR, 2-11 April 1979, 15 pp.

Ross, D. B., and V. J. Cardone, 1978. A comparison of parametric and spectral hurricane wave prediction products. In: A. Faure and K. Hasselmann (eds.), Turblent Fluxes through the Sea Surface, Wave Dynamics, and Prediction, Plenum Press, p. 647-665.

Schneider, C., and J. R. Weggel, 1981. Visually observed wave data at Pt. Magu, California. Proceedings, Seventeenth Coastal Engineering Conference, Vol. 1, p. 381-393.

Silvester, R. R., 1974. Coastal Engineering, Vols. 1 and 2. Elsevier Scientific Publ., 438 pp.

Sverdrup, H. V., and W. H. Munk, 1947. Wind, sea and swell theory of relations for forecasting. U.S. Hydrographic Office Publ. No. 601.

ESTIMATES OF SEDIMENT TRANSPORT FROM LONG-TERM FLOW AND TURBIDITY MEASUREMENTS, DREDGED MATERIAL DUMP SITE, NEW YORK BIGHT APEX

Robert A. Young

National Oceanic and Atmospheric Administration
Atlantic Oceanographic and Meteorological Laboratories
4301 Rickenbacker Causeway
Miami, Florida 33149

INTRODUCTION

This report covers the long-term, near-bottom flow and turbidity observations taken from November 1980 to June 1981 at the southeast quadrant of the New York dredged material dumpsite (Figure 1) as part of the study of a sediment cap placed on dredged material dumped there in 1980. Included in this report is an estimate of long-term erosion and deposition rates.

Goals of the Study

Observations of flow and turbidity were made to gain insight into the sediment transport conditions at the dumpsite over a significant portion of a year. Statistics from the observations were used in a quantitative model of near-bottom sediment transport to estimate the frequency and magnitude of transport events and were compared to field observations to assess the effectiveness of the modeling approach. Statistics from the modeled transport were then used to develop an estimate of the long-term rate of erosion (or deposition) at the dumpsite.

Environmental Background

Water circulation in this region is complex. A general flow to the southwest has been reported (Mayer et al., 1979). Superimposed on this flow is a secondary flow described as a clockwise gyre centered over the bank east of Christiaensen Basin; the western, northward-flowing arm of the gyre is thought to extend over the study area (Charnell and Hansen, 1974). Reversal of the southwest shelf flow, interactions with the nearby Hudson estuary, and shearing between surface and bottom flows induced by opposing flow directions, all act at various times to obviate simple explanations of flow. Present and past flow measurements in the New York Bight apex indicate that semi-diurnal tides and aperiodic storms are the principle sources of flow energy. Average

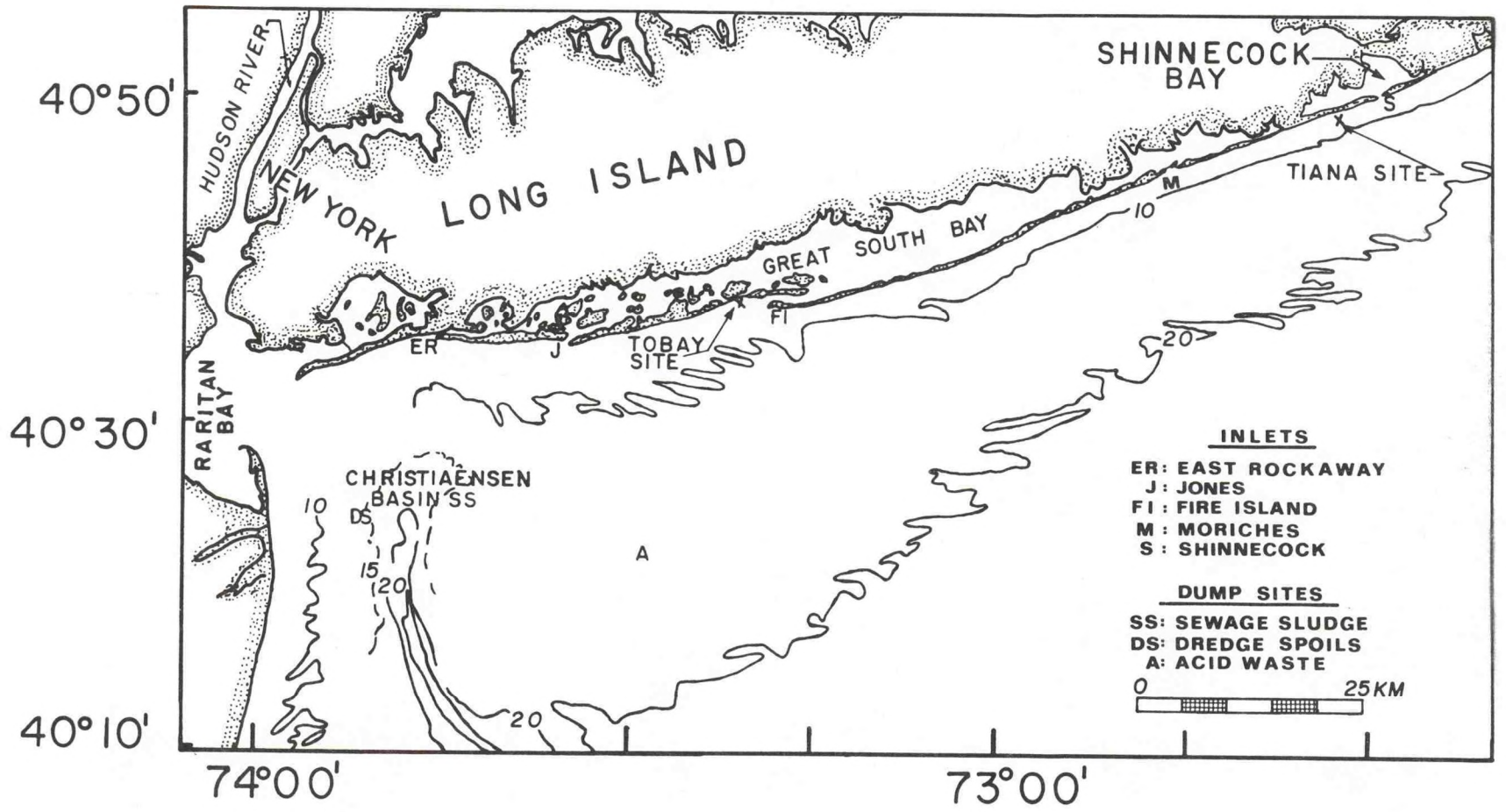

Figure 1. A portion of the New York Bight showing the Christiaensen Basin, the upper portion of the Hudson Shelf Valley (depression south of the Christiaensen Basin), and Bight apex dumpsites.

flow speeds can range from ≤ 5 cm/sec for tidal flows to > 50 cm/sec in response to storms. Mean flow speeds observed during the present study never exceeded 30 cm/sec.

Since depths at the dumpsite are ≃ 30 m, only large surface waves are expected to induce significant orbital velocities near the seafloor. Past work (Grant and Madsen, 1978; Butman et al., 1979) indicates that at these depths waves do induce and/or enhance sediment transport.

Model Background

Several different models have been merged to perform the transport calculations. Although some of these models have been tested extensively in the laboratory, none has had adequately tested in the field. Therefore, transport calculations presented here must be conservatively viewed as order-of-magnitude estimates.

Since flow conditions in the study area may vary among quasi-steady tidal currents, wind-driven storm flows with little wave influence, and wave-dominated combined wave-current flows, the approach taken in calculating transport must also vary. This is because no single model exists which takes into account all of the above conditions. Further, extensive and detailed flow observations far surpassing funding and time allotted this project would be required to satisfy simultaneously the data requirements for models describing all of the above flow conditions. Our approach has been to use first-order approximations for some of the data requirements where the qualitative results are negligibly affected. For example, transport direction is a more important variable than the rate or magnitude of transport. Consequently, greater effort was spent acquiring data to assess direction than magnitude of transport.

For the steady flow case two models of bedload transport have been investigated. The first is due to Bagnold (1973) and relates the amount of sediment being transported in a steady current to the fluid power in excess of a threshold value. This leads to an expression relating the volumetric rate of transport q_B (all transport rates have units of volume of sediment/bed surface area/time) to fluid velocity cubed, u^3. In this model transport direction is the direction of the mean flow.

The other steady flow model investigated is based on the principle that the flow must exceed a threshold shear stress to initiate motion. After motion is initiated the mean flow seems to transport the sediment. This concept is supported by a large body of experimental data (Yalin, 1972; see Graf, 1971, for a more complete discussion) and is the basis for the pioneering approach of Shields (1936). By grouping together all important flow and sediment parameters into two dimensionless variables describing bed shear stress at erosion and sediment grain size, Shields (1936) was able to show that a smooth curve resulted, separating the transporting and non-transporting conditions for flat beds of uniform sediments. Many subsequent investigators have verified and amplified Shields results, but arguments have also been made that some transport occurs even at sub-threshold conditions due to the natural variability of bed shear stress in a turbulent boundary layer (Einstein, 1950). However, transport rates under sub-threshold conditions will likely be relevant only to problems having geologic rather than human time-scales. Consequently, we will limit ourselves to models which require a threshold for initiation of sediment motion.

Transport due to waves at the study area may be important, but due to the 30 m water depth, wave-induced transport is probably significant only during major storms. In a companion investigation of wind-wave models appropriate

for the study area, Drapeau (section C, this report) suggested that only long waves having periods equal to or greater than six seconds generate significant oscillatory currents near the bottom. As will be shown later, long-term, near-bottom flow measurements at the study area tend to support this hypothesis.

When both waves and currents are present, their boundary layers interact non-linearly; determination of the resulting bed shear stress must take these factors into account. In a series of papers, Madsen and Grant (1976), Smith (1976), and Grant and Madsen (1978, 1979) have presented models of boundary layer flow incorporating wave-current interactions in order to calculate sediment transport. The Grant and Madsen (1979) model solves the dynamics of the wave-current interaction through the concept of a linearized, combined, wave-current friction factor determined by the apparent bottom roughness. The apparent roughness depends on both the physical bottom roughness (grain size, small bedforms) and wave characteristics. The apparent roughness is always equal to or larger than the physical roughness. This results in the current experiencing a larger bottom resistance due to the presence of the wave. The mathematical form of this model is best developed in Grant and Madsen (1978) and is described briefly later in this report.

Near-bottom velocity in wave-current flows, combined with the appropriate wave-current friction factor, can be used to find the threshold erosional stress, following the results of Madsen and Grant (1976). Madsen and Grant and others (Komar and Miller, 1973; Sleath, 1978) suggest that the curve for threshold stress under oscillatory flows parallels but does not coincide with the curve Shields (1936) found for steady currents (Figure 2).

Transport rates under combined flows are not well studied empirically or theoretically. Only a few empirical studies exist (Inman and Bowen, 1962;

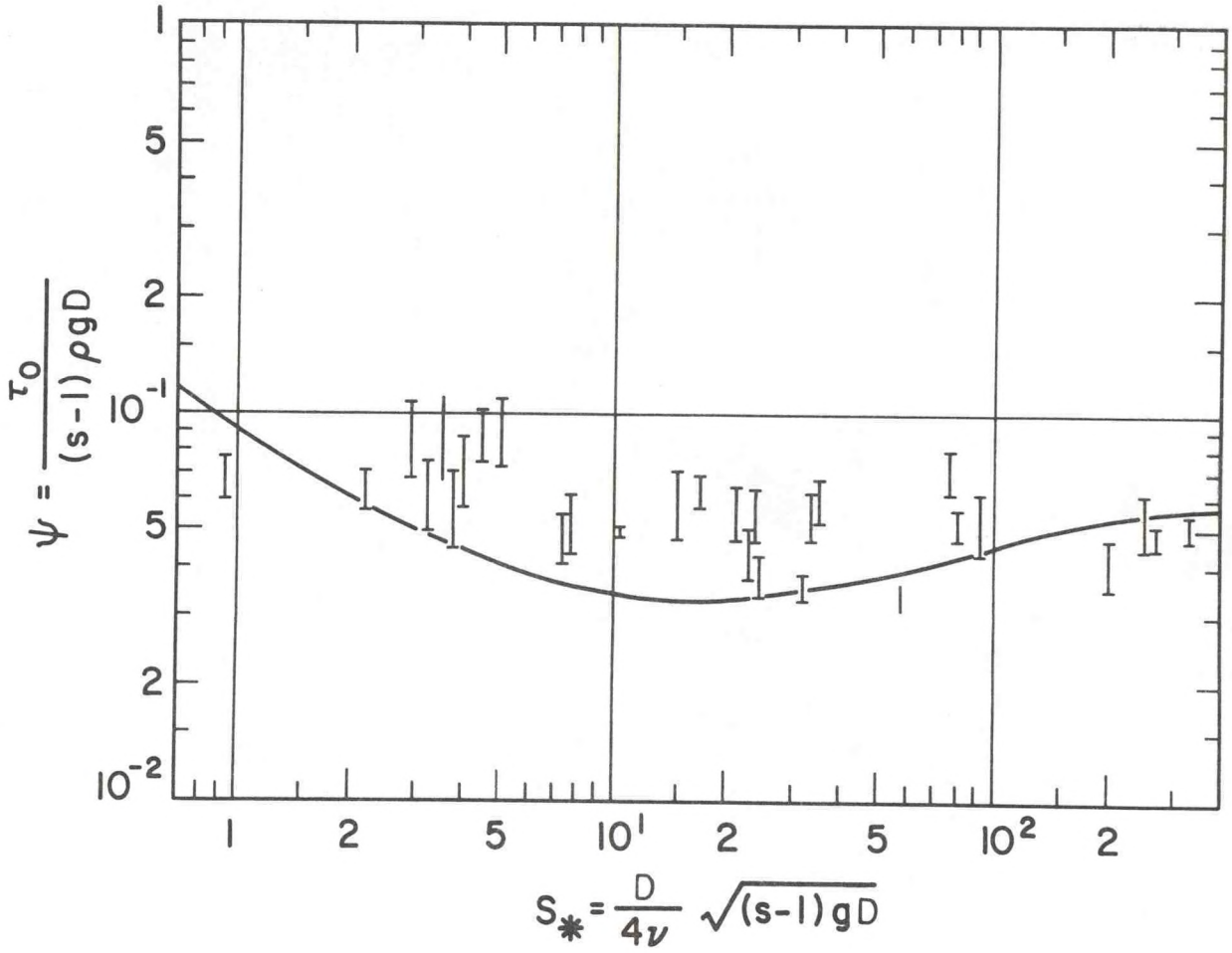

Figure 2. Shields curve for oscillatory flows (from Madsen and Grant, 1976).

Bliven et al., 1977; Hammond and Collins, 1979), while a much larger body of data and theory exist for transport under waves alone. Vincent et al. (1981) reinterpreted the data used by Madsen and Grant (1976) to calculate bedload transport rates, q, under combined flows. The approach suggested by Madsen had q proportional to bed shear stress τ cubed, or $q \propto \tau^3$. Since τ is proportional to velocity squared (u^2), Madsen and Grant's approach has $q \propto u^6$. Vincent et al. (1981) point out that most other investigators (e.g., Einstein, 1950; Bagnold, 1973) have assumed the volume of sediment transported is proportional to the product of τ and the transport velocity, yielding $q \propto u^3$. Using this approach and laboratory data for calibration, Vincent et al. (1981) derived a time-dependent combined-flow transport function which depends on the excess shear stress during each wave cycle to resuspend the sediment when it is then advected by the mean flow. This function was used in the present study when flow conditions were appropriate. Transport using the combined flow model can be orders of magnitude larger than for steady flow models when waves are present (Vincent et al., 1982a).

Important assumptions made in development of all the above transport models are that sediments are uniform in size and the sediment beds smooth and flat. This is rarely the case in natural ocean sediments and can lead to spurious results. The problem of non-uniform grain size distributions was also discussed by Einstein (1950). Einstein suggested that on poorly-sorted flat beds the larger grains protrude farther into the flow and partially shield the smaller ones. He recommends using a grain diameter representing the mode of the larger grains. Following Einstein, we use the 65th percentile of the distribution (65% of the grains are finer then d_{65}) as the representative size of bed sediments in the present study because of the poor sorting of the sediments in the sand cap.

METHODS

Field deployments of the CV probes (see below) to obtain flow and transport data were made at the stations shown on Figure 3. Station location data and deployment statistics are given in Table 1 and Figure 4. Data recovery was about 98% for CV1, 48% for CV2 and 86% for CV3. CV1, CV2 and CV3 were all located on the sand cap, and were placed on a north-south longitudinal transect to observe any deviations in flow pattern due to topography, gradients in transport due to erosion or deposition, and as insurance against loss of data due to failure or premature removal of the current meters.

The possibility of significant data loss was realized during all three deployments of CV2 because of battery failure, and during its final deployment when the probe was dragged up by a fishing vessel.

Instrument Systems

The concentration-velocity (CV) probes used in this study consist of microprocessor-controlled electromagnetic current meters (Marsh McBirney 585), coupled with an optical transmissometer (Sea Tech 100) for turbidity measurements, mounted together on a tripod (Figure 5). The current meter was specially programmed to control and power the transmissometer and record its output. The electromagnetic current meter calibration was checked before deployment, but not subsequent to it. Internal calibration checks on gain show no changes occurred during the deployment, but yield no information on zero drift. However, our past experience with these instruments suggests that zero drift is probably negligible. Zero drift and gain changes in the transmissometers were checked before and after deployments and found to be negligible. The pressure transducer was calibrated in the laboratory by applying known loads to the transducer.

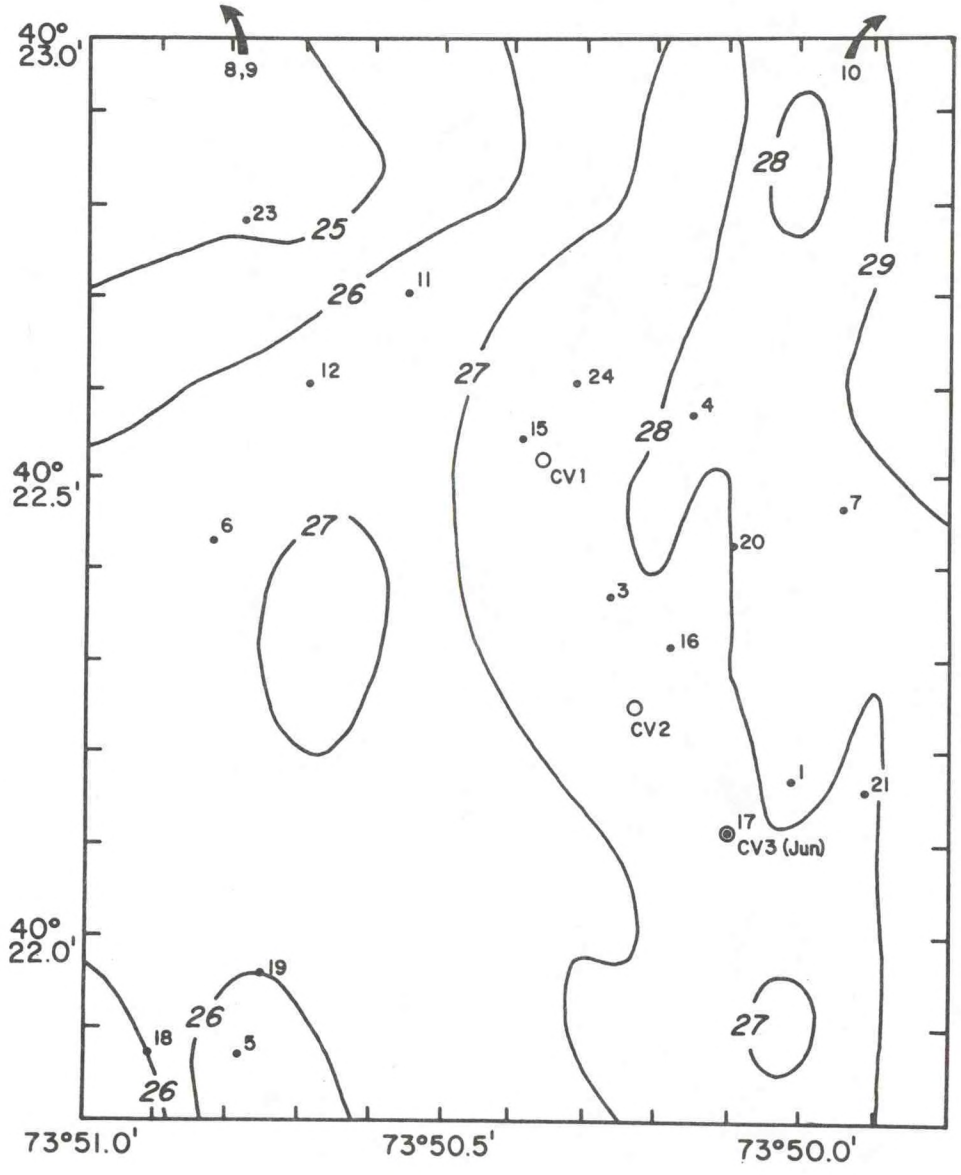

Figure 3. Study area in the southeast quadrant of the dredged materials dumpsite. CV probe stations are open circles. See Table 1 and Figure 4 for dates and location data. Stations marked by small solid dots are Seaflume locations (section B, this report). Depth in meters.

Table 1: Location Data for CV Probe Deployments.

CV1:	40°22.52'N 73°50.36'W	19 November 1980 - 26 June 1981
CV2:	40°22.25'N 73°50.23'W	19 November 1980 - 29 April 1981
	40°28.41'N 73°45.52'W	30 April - 3 May 1981 (dragged up)
CV3:	40°22.12'N 73°50.10'W	7 February - 26 June 1981

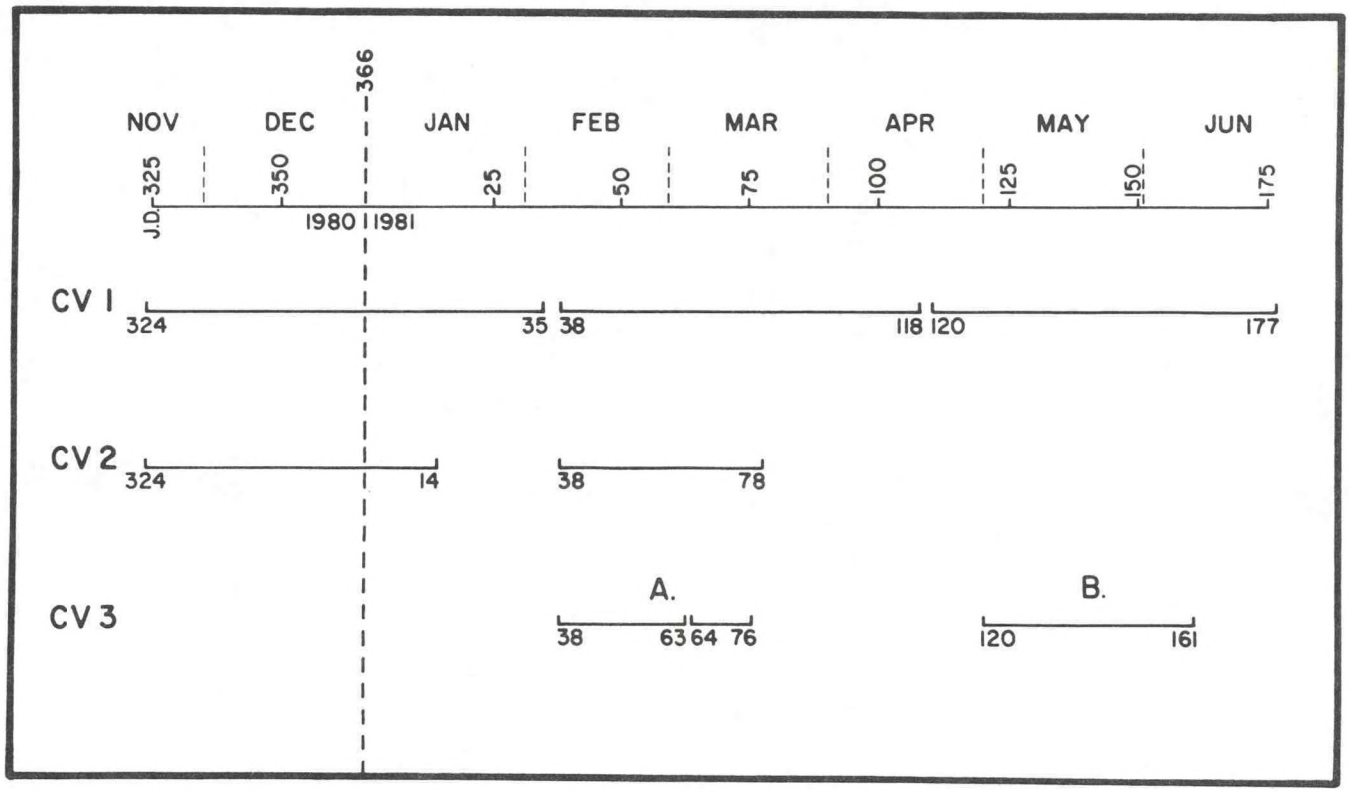

Figure 4. Deployment durations yielding useful data are indicated by the solid bars. Numbers are Julian days (JD) of each year.

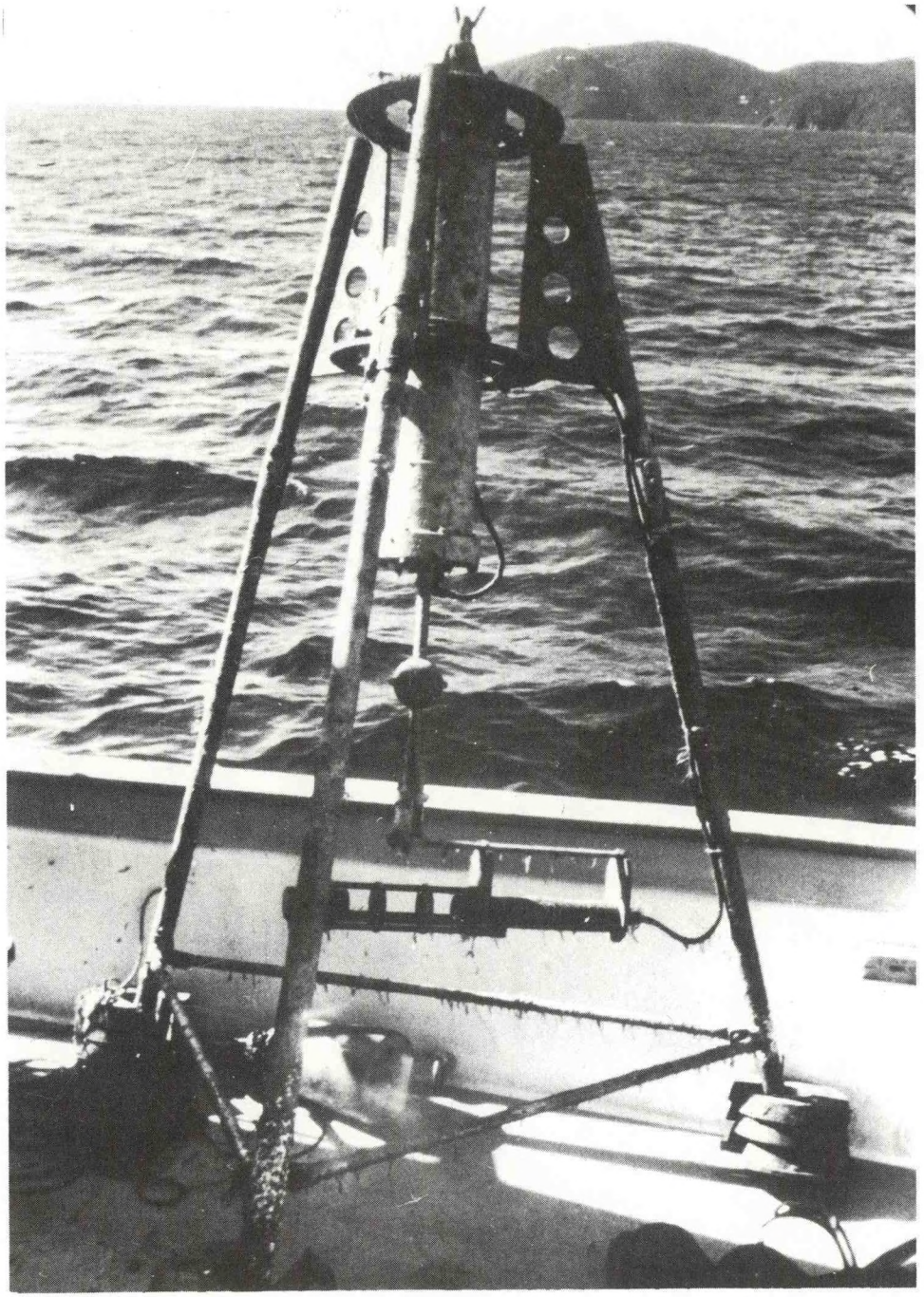

Figure 5. CV probe used for flow and transport measurements. Rubber sphere with protruding electrodes for current measurement is underneath pressure housing for electronics. Sphere is 1 m off bottom. Transmissometer with horizontal light-beam path is under sphere. Not shown are subsurface float, acoustic release, and rope basket which are attached to top of probe when in place.

The current meter sensor was mounted one meter above the tripod base. The transmissometer was mounted below the current meter at about 50 cm above the tripod base. This arrangement minimized flow interference between the two sensors (Figure 5).

Flow velocity at 100 cm ($\vec{U}_{100}$) and percent transmission (Tr) were sampled once per second during measurement periods of three or four minutes. Averaged values of ($\vec{U}_{100}$, Tr) and ($\vec{U}^2_{100}$, Tr^2) were determined by the microprocessor and recorded for each burst. Arrow overbars indicate vector quantities. Intervals between measurements were one hour during the first deployment period from November 1980 to February 1981, and two hours in the following deployments. A pressure sensor on the current meter was used to determine average pressure P during each measurement period.

An attempt was made to use the $\vec{U}^2$, Tr^2, and P^2 values to demean the velocity, transmission, and pressure measurements in order to estimate their statistical variance. The pressure and velocity variance can also be used to estimate wave energy reaching the seafloor (Silvester, 1974). However, during the multiplication process roundoff errors accumulate in the microprocessor due to the limited bit size of the data words. These errors bias the calculation in an unpredictable way and attempts to calculate variance produced random results. This could be corrected by reprogramming of the microprocessor to increase the size of the data words, but the problem was recognized too late in the project schedule to effect this change.

The tripods were deployed with acoustic recall systems to prevent accidental fouling by surface vessels. The acoustic recall systems consisted of a release mechanism and bouyed rope basket holding sufficient rope to reach the surface and retrieve the tripods. These systems worked fairly well. Only one release failure occurred during eight deployments; an acoustic pinger on the tripod was used to locate and retrieve it by bottom dragging.

Instrument Calibrations and Computer Processing

Cassette tapes from the current meters were processed by standard programs on the laboratory computer. Data was first passed through a program which screens the data for easily identified bad data points. After initial editing and hand selection of the first good data record on the bottom, the data is converted from integer to engineering units.

The data were then computer plotted as times series to analyze relationships between flow and suspended sediment (Tr) and to identifiy spurious data points. Spurious data points were edited from the computer data files by hand. The resulting data set is the longest near-continuous record of near-bottom flow and suspended sediment obtained in the New York Bight apex.

Transmissometer Measurements

No attempt has been made to calibrate the Tr values in terms of suspended sediment concentrations. Percent transmission is highly dependent on size and composition (index of refraction) of suspended particles. These properties change with time even at the same site because of variation in contributions from aperiodic biological productivity, resuspension from local sources, and advection of suspended matter from outside the study area.

Bulk suspended matter concentrations near the seafloor are typically 1-10 mg/ℓ during tranquil periods and may reach much larger values during storms (Nelsen, 1979; Young et al., 1981). However, during tranquil periods suspended particles are probably silt and clay-sized with a large proportion of organic detritus due to dredged material dumping immediately north and west of the cap site, and sewage sludge dumping to the east. Both of these activities continued all during the probe deployments. The fine particle load in the Bight, except during the extreme wintertime, consist largely of algae and plankton. During resuspension events, coarser inorganic sediments are

resuspended but the grain sizes and compositions of resuspended particles at the 50 cm height of the sensor are not known or easily predicted. Thus, results of our transmissometer measurements are reported as simply percent transmission over a 0.25 m light path.

These relative values could easily be converted to optical attenuation units through the equation

$$I_R/I_S = \exp(-Cr) \qquad (1)$$

where I_R/I_S is the ratio of light intensity measured at the receiver to the source intensity, r is the optical path length, and C is the attenuation coefficient. The ratio $(I_R/I_S) \times 100$ is identified as the percent transmission reported in the present study. While others have reported reasonable correlations between Tr and suspended matter concentrations in other parts of the water column (Drake, 1971; Meade et al., 1975), variability in size and composition of near-bottom suspensions, as discussed above, prevented similar calibration attempts in the present study.

RESULTS

Presentation of the results will be separated into two main sections, the first describing the characteristics and overall flow statistics of the mean flow. The second section will discuss estimates of sediment transport based on the observed flows and the waves generated by a wind-wave model developed for this study (Drapeau, section C, this report).

Mean Flow

Time-series plots showing relationships among plots of flow velocity $\vec{U}$, wave energy (WE) and percent transmission (Tr) are presented in Figures 6

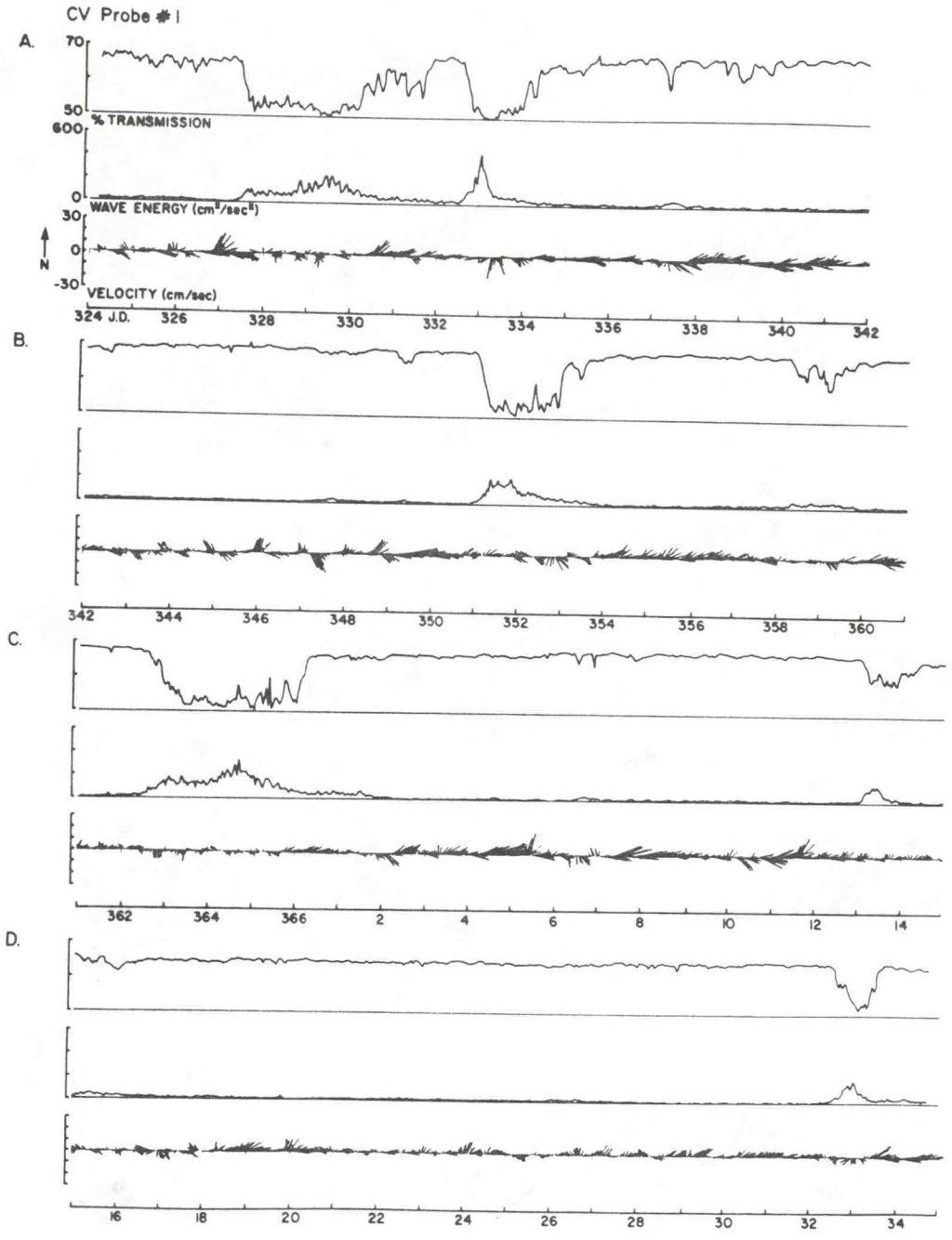

Figure 6a. Time-series plots of velocity and percent transmission data from CV1. Numbers beneath each graph set are Julian days in 1980 and 1981. Velocity plots are stick diagrams showing direction (north up, east to right, etc.) and speed (length of stick; scale at left).

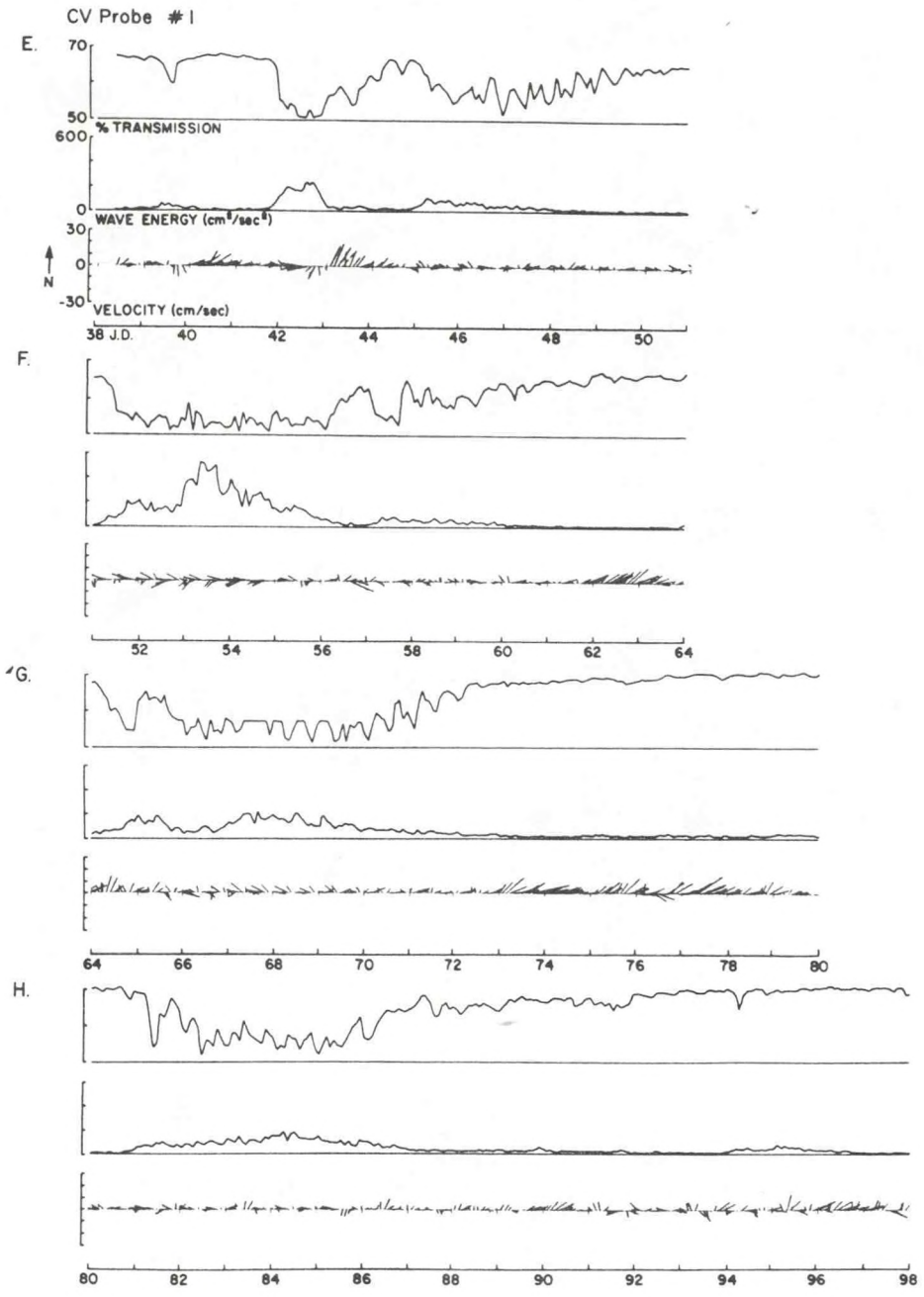

Figure 6b. Same as for Figure 6a.

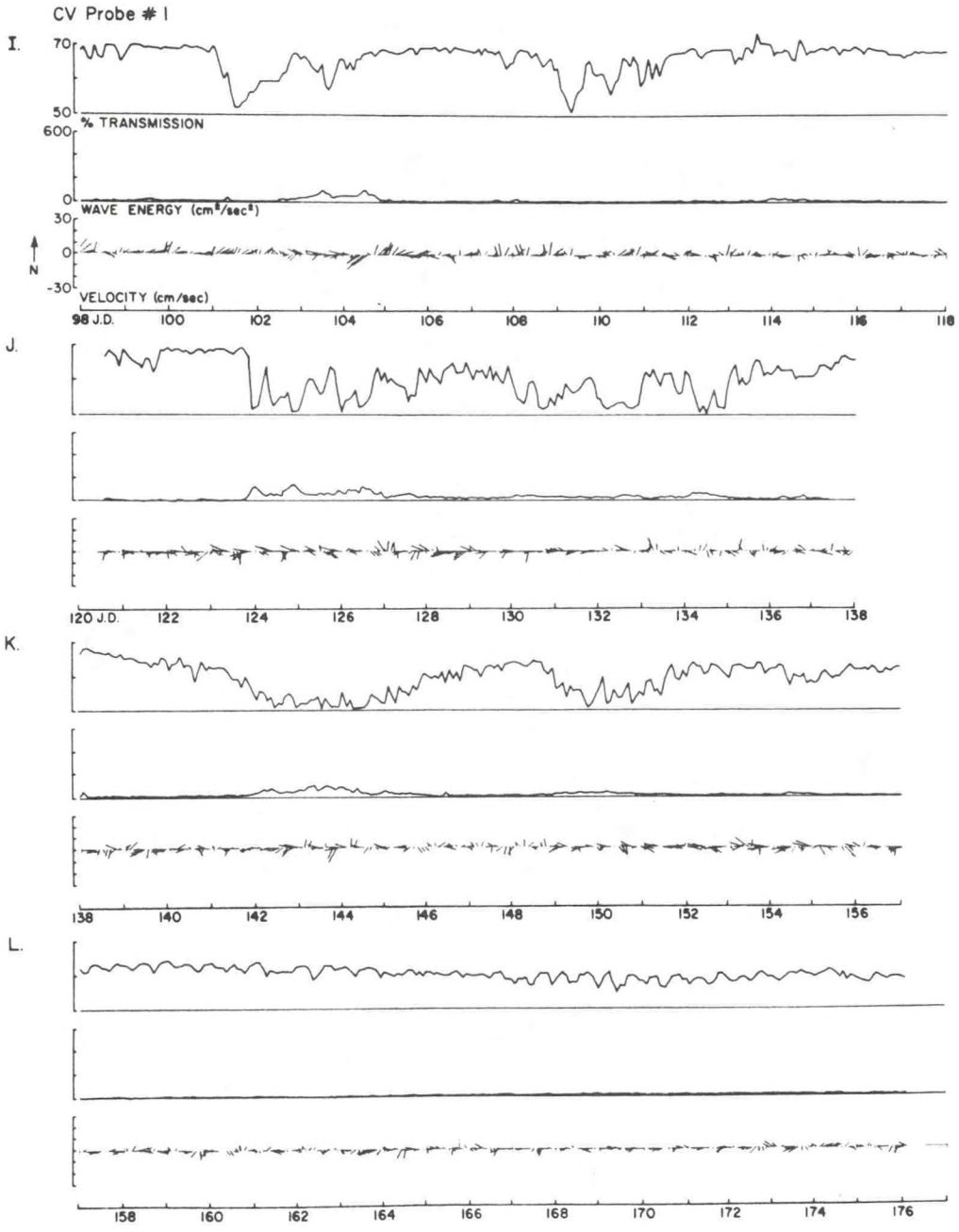

Figure 6c. Same as for Figure 6a.

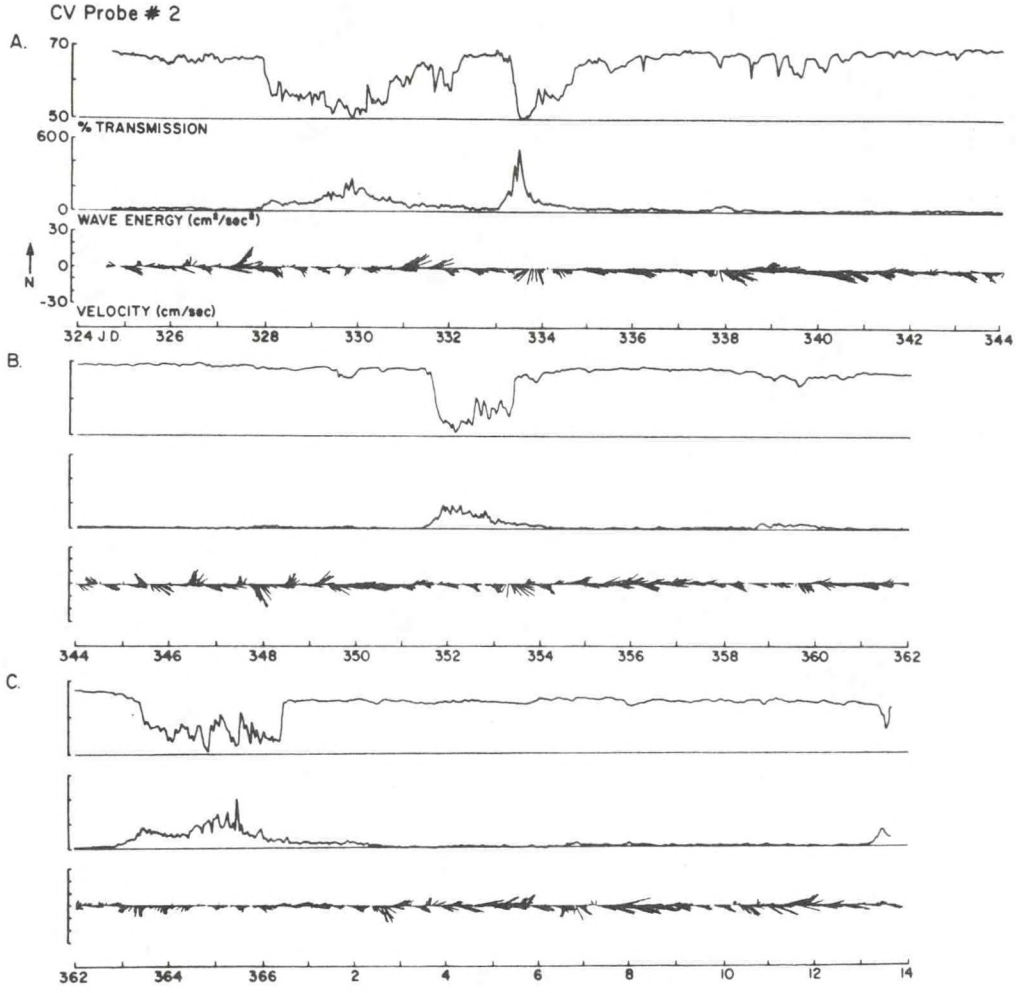

Figure 7a. Time-series plots of $\vec{U}$, WE and Tr data from CV2.

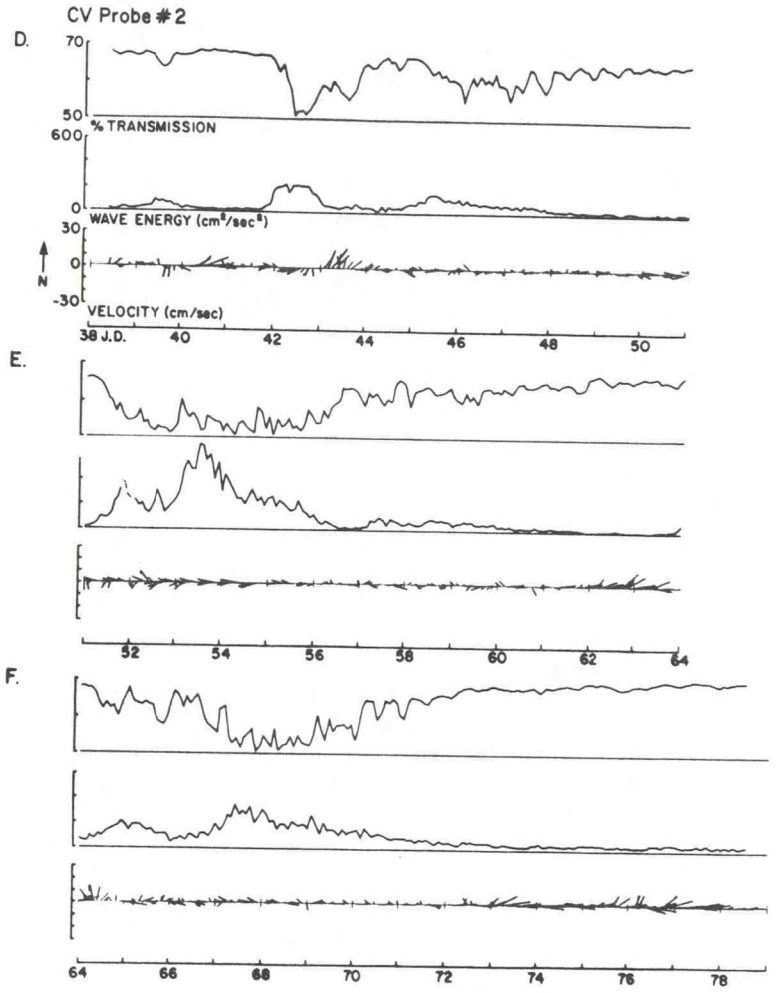

Figure 7b. Same as for Figure 7a.

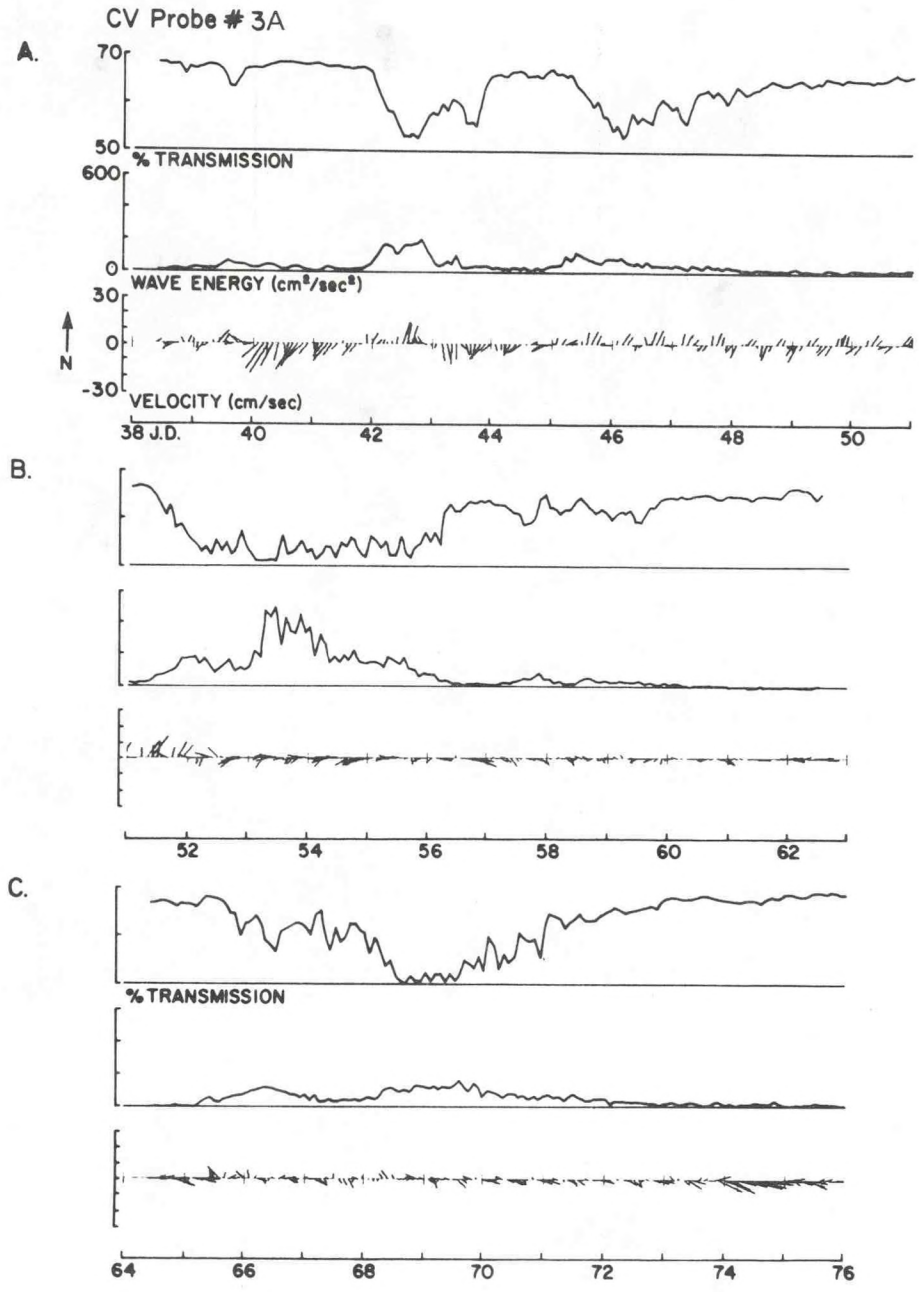

Figure 8. Time series plots of $\vec{U}$, WE and Tr data from CV3A.

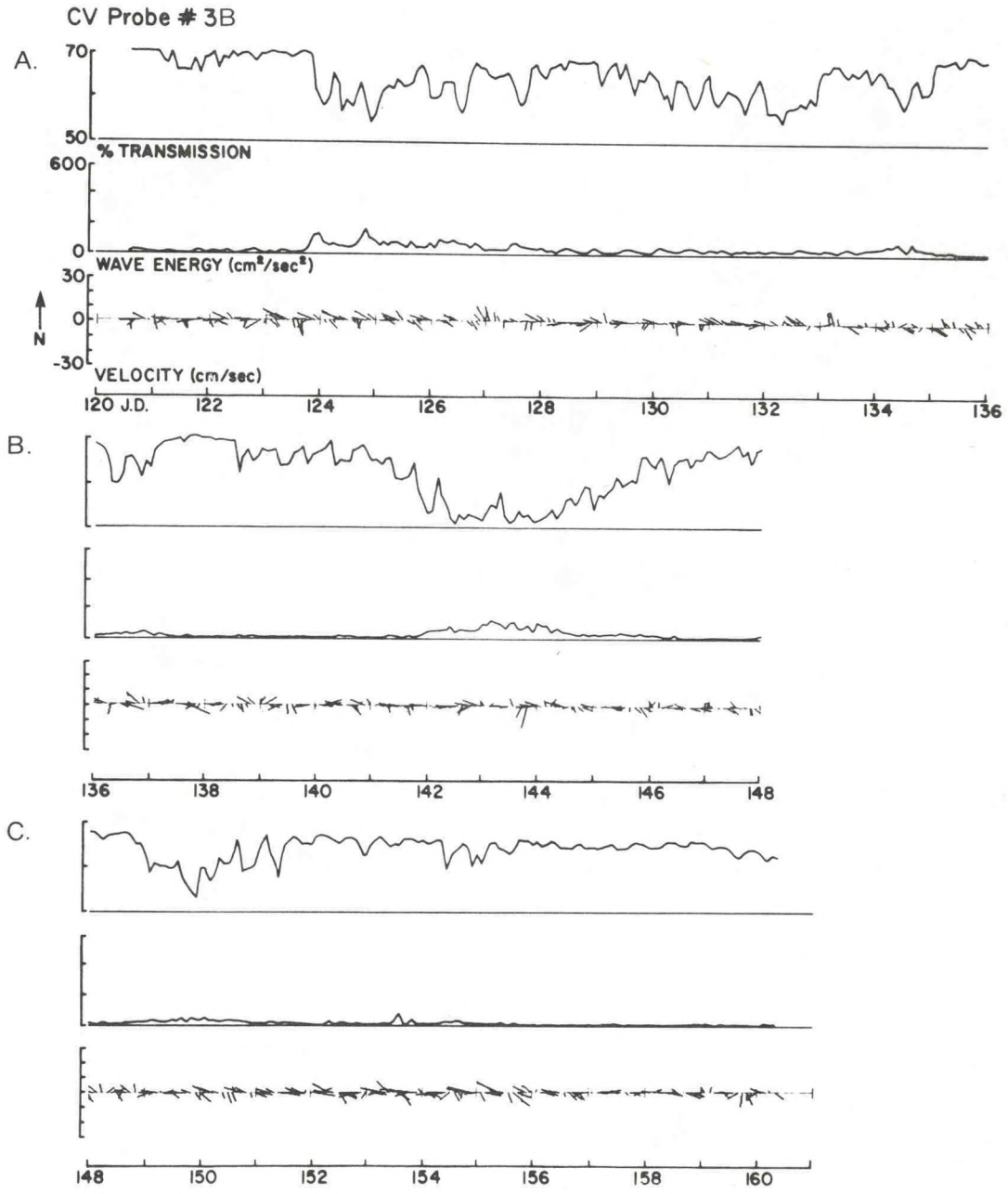

Figure 9. Time-series plots of $\vec{U}$, WE and Tr data from CV3B.

to 9. Visual comparisons of WE, and Tr immediately indicate the apparent importance of waves to resuspension at this site. There are few instances (e.g., Figure 6c, plot I, JD 101-102 and 109-111) where Tr decreases (turbidity increase) without a concurrent increase in WE. It must be emphasized that changes in Tr are likely to best reflect changes in fine (< 62 μm) suspended matter concentrations and therefore may not always indicate transport of coarser or heavier particles nearer than 50 cm to the bed. However, wave-induced bedload transport is closely tied to suspended load through release of the fine material in bed sediments by wave stirring of the slightly muddy bottom sediments (Young et al., 1981; Clarke et al., in press). Waves may also enhance vertical mixing of resuspended sediments of all sizes through an increase in the vertical eddy diffusivity over that due to a steady current alone (Vincent et al., 1982a).

Mean currents at 100 cm above bottom were generally on the order of 6 to 7 cm/sec during the deployments (Figure 10). Histograms representing all speed and direction observations from CV1 (Figure 10) are representative of CV1, CV2 and CV3 data.

Since high wind conditions usually result in both wave generation and advective forcing of the flow, it is not surprising that WE varies with U_{100}. However, high U_{100} values not associated with tides can be caused by forcing outside the local area. In those cases, high U_{100} values need not be accompanied by waves. This apparently did not occur during the present study.

Another case, high WE with average U_{100}, did occur during several periods (e.g., Figure 6a, plot C, JD 363-366; Figure 6b, plot E, JD 42-43; plot G, JD 67-70; plot H, JD 82-86). We shall show later that high WE during these events may have been from either long period swell or other turbulent flow mechanisms because local winds were insufficient to produce surface waves capable of stirring the bottom sediments.

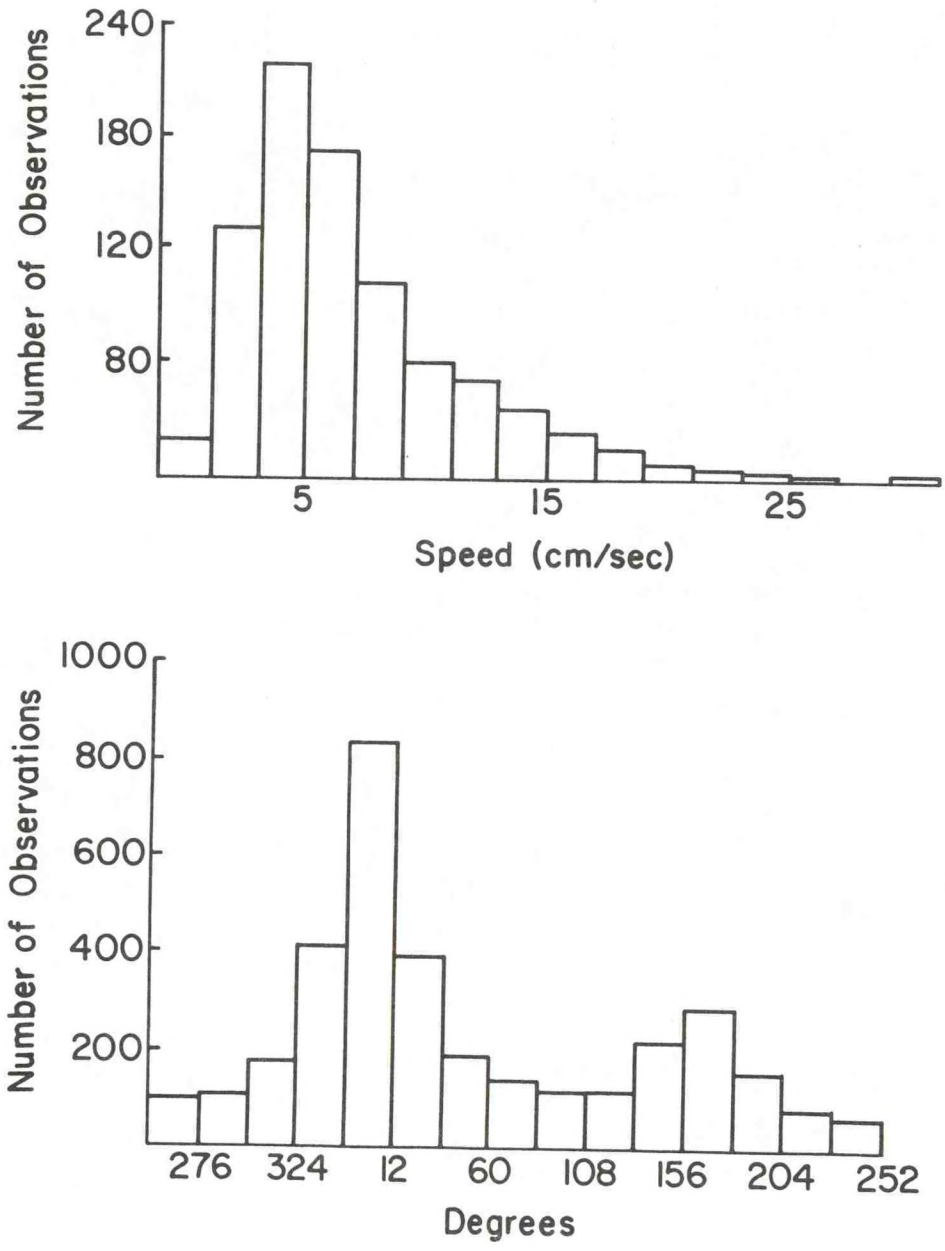

Figure 10. Histograms of mean flow speed and direction from probe CV1.

The net direction of suspended fine particle flux can be estimated qualitatively by plotting the north versus east components of the product of the vector velocity $\vec{U}$ and Tr, or $\vec{U} \cdot Tr$ for $Tr < 60\%$. The resulting scatter plot (Figure 11) indicates net flux to the south (177° true) We shall show later that calculated and observed fluxes are in generally good agreement.

Wave-Current Model Calculation

Before presenting results of the combined flow and mean flow transport calculations, a description is given of the theory and models.

Boundary Layer and Sediment Transport Theory: The interactions between the mean current and wave boundary layers are non-linear. This results in a turbulent shear velocity for the combined flow, U_{*cw}, defined by (Grant and Madsen, 1978)

$$U_{*wc} = \frac{1}{2} (f_{wc}\ \alpha)^{1/2}\ |\vec{U}_b| \tag{2}$$

$$\alpha = 1 + \left(\frac{|\vec{U}_a|}{|\vec{U}_b|}\right)^2 + 2\ \frac{|\vec{U}_a|}{|\vec{U}_b|}\ \cos \phi_c \tag{3}$$

where f_{wc} is a combined wave-current friction factor, $\vec{U}_b$ is the maximum wave-orbital current velocity in the potential flow region just outside the thin wave boundary layer, as determined by measurement or linear wave theory (Grant and Madsen, 1978; Vincent et al., 1982a), and ϕ_c is the angle between $\vec{U}_a$ and $\vec{U}_b$. The reference velocity $\vec{U}_a$ is not defined explicitly by Grant and Madsen but is assumed to take into account the affects of the waves on the mean flow. The same problem exists for definition of ϕ_c; $\vec{U}_a$ and ϕ_c are usually determined as part of an iterative procedure used to determine the value of other wave boundary layer variables. As Vincent et al. (1982a) note,

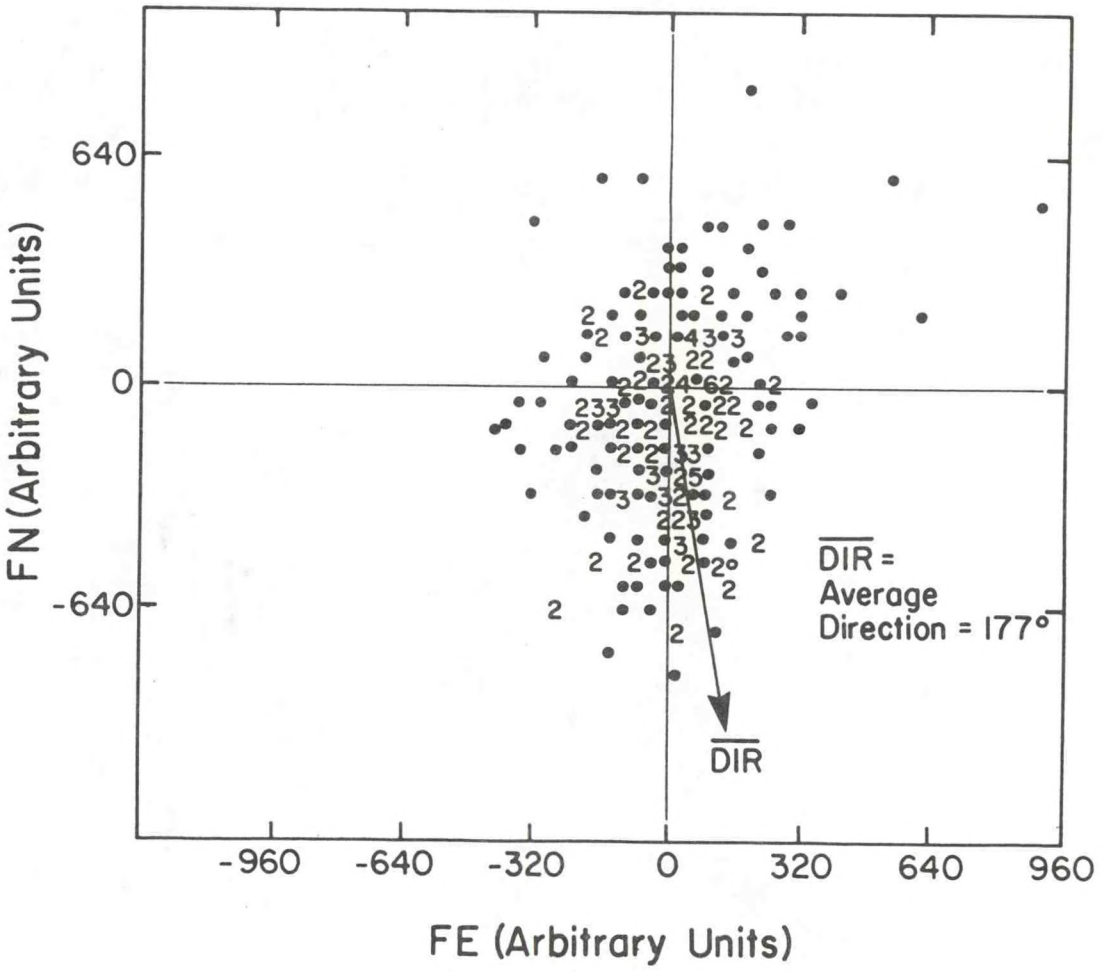

Figure 11. Plot of the CV1 north (FN) versus east (FE) flux components when Tr < 60%. Numbers indicate number of observations and symbol ● indicates ten or more observations.

determination of $\vec{U}_a$ and ϕ_c are critical to the calculation of transport rates since they may differ considerably from the speed and direction of the flow as taken directly from the CV probes or similar sensors.

The steady flow velocity at height z ($\vec{U}_z$) inside the rough turbulent wave boundary layer is related to physical boundary roughness K_b by

$$\vec{U}_z = \frac{\vec{U}_{*c}}{\kappa} \left(\frac{U_{*c}}{U_{*wc}} \right) \ell n \frac{30\ z}{K_b} \ . \tag{4}$$

Outside the wave boundary layer U_z is related to the combined flow boundary roughness K_{wc} by

$$|\vec{U}_z| = \frac{U_{*c}}{\kappa} \ell n \frac{30\ z}{K_{wc}} \ . \tag{5}$$

The combined-flow roughness K_{wc} is an apparent roughness due to the presence of the wave which accounts for the grain roughness and the wave motion. The ratio K_c/K_{wc} is always greater than one and is defined by

$$\frac{K_{bc}}{K_b} = 24 \left(\frac{U_{*wc}}{|\vec{U}_b|} \cdot \frac{A_b}{K_b} \right) \left(1 - \frac{U_{*c}}{U_{*wc}} \right) \tag{6}$$

where U_{*c} is the mean flow friction velocity, A_b is the amplitude of the near-bottom orbited motion, and the bed roughness K_b is defined as the sediment grain diameter.

Few laboratory studies are known to the author on transport rates under waves or combined flows (Manohar, 1955; Inman and Bowen, 1962; Kalkanis, 1964; Abou-Seida, 1965; Bliven et al., 1977; Sleath, 1978). Of these, only the Inman and Bowen and Bliven et al. studies include combined flows. No field studies of wave or combined flow transport rates appear to be available in the literature.

Threshold under waves or combined flows seems to follow laws similar to those proposed for threshold conditions under steady currents. Several laboratory studies of wave threshold (Komar and Miller, 1973; Madsen and Grant, 1976; Dingler, 1979; Hammond and Collins, 1979) indicate that the threshold condition for uniform sediments under waves may be expressed by the wave Shields number, ψ_{TH}, a dimensionless shear stress, or

$$\psi_{TH} = \frac{0.5\ \rho\ f_{wc}\ |\vec{U}_w + \vec{U}_a|^2_{CRIT}}{(\rho_s - \rho)\ gD} \cdot \tag{7a}$$

Substituting (2) into (7a) yields

$$\psi_{TH} = \frac{0.5\ \rho\ f_{wc}\ |\vec{U}_w + \vec{U}_a|^2_{CRIT}}{(\rho_s - \rho)\ gD} = \frac{\rho |U^2_{*wc}|_{CRIT}}{(\rho_s - \rho)\ gD} \cdot \tag{7b}$$

Here ρ and ρ_s are water and sediment density, respectively, g is the gravitational constant, D is sediment grain size, and $\vec{U}_{CRIT} = \vec{U}_w + \vec{U}_a$ represents the combined wave and steady current velocity at threshold.

Instantaneous volumetric bedload transport rates q are given variously as (Madsen and Grant, 1976)

$$q_{MG} = 40\ WD\ \psi^3\ \frac{\vec{U}}{|\vec{U}|} \qquad (\psi \geq \psi_{TH}) \tag{8}$$

$$q_{MG} = 0 \quad (\psi < \psi_{TH}) \tag{9}$$

and (Vincent et al., 1981)

$$q_v = \vec{U}\ C^* = 0.09\ (\psi - \psi_{TH})\ \ \vec{U} \quad (\psi \geq \psi_{TH}) \tag{10}$$

$$q_v = 0 \quad (\psi < \psi_{TH}) \tag{11}$$

where C* is the volumetric concentration of sediments per unit area of bed surface with units of length. The transport rate is perhaps better related to the product of the excess shear stress required to lift the sediment into suspension and the mean flow required to transport it. This yields $q \propto \breve{U}^3$, a form more in agreement with the results of Bagnold (1973) than those of Madsen and Grant (1976). Differences in calculated transport rates from field studies are discussed in Vincent et al. (1982a) and indicate best agreement between q_{MG} and q_v at "moderate" rates of transport. At high rates q_v is in better agreement with the results of laboratory transport experiments than q_{MG}; at low rates q_v tends to underpredict while q_{MG} gives good agreement with laboratory results (Vincent et al., 1981). The consequence of using one or the other of equations (8) or (10) in the present study are described below.

An alternate procedure has also been used to find ψ_{TH}. Sleath (1978) has reconsidered the results of several previous investigations of wave threshold and has suggested a revised wave-Shields diagram (Figure 12) which has ψ_{TH} as a function of the non-dimensional grain size

$$D_* = \left[\frac{(\rho_s - \rho)}{\rho} \frac{g}{\nu^2}\right]^{1/3} D \tag{12}$$

where ν is kinematic fluid viscosity. Comparisons are given below between transport rates calculated using equation (7) and the ψ_{TH} values from in Figure 12.

Transport rates in the above equations are instantaneous values with time intervals scaled by typical wave-time scales (e.g., wave period T). The flow data collected for the present study include only vector-averaged velocities

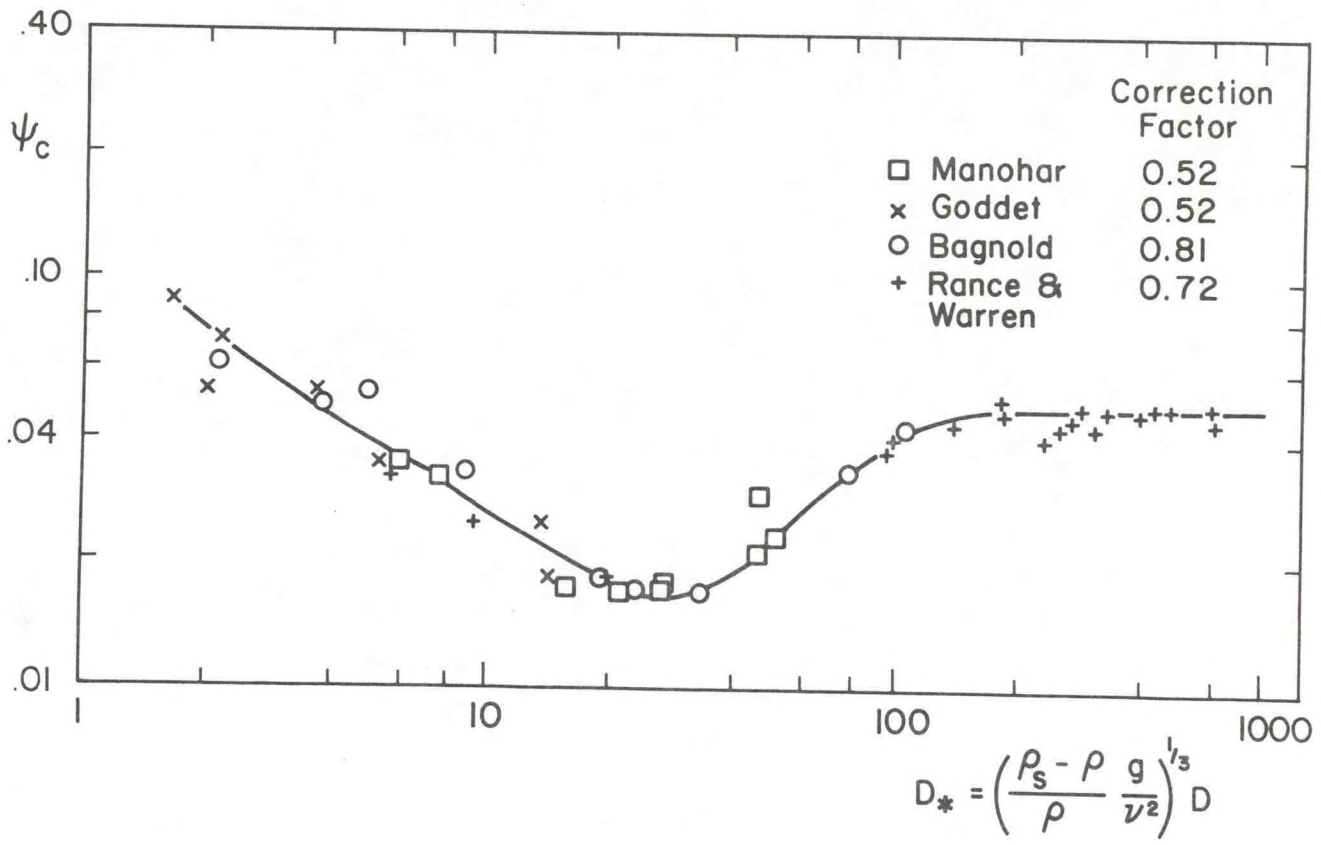

Figure 12. Shields curve for oscillatory flow as modified by Sleath (1978).

$\langle\vec{U}\rangle$ from the CV probes in the form of north (V_N) and east (V_E) velocity components sampled at 1 Hz and averaged over periods of three to five minutes every one or two hours. Thus, the current measurements include the effect of oscillatory and mean flows, and the oscillatory components cannot be extracted. Instrumental procedures for extracting the variance (waves) from the mean flow, described in the previous section on instrument systems, were not successful.

At the depths of the study area (25-30 m) we can expect the oscillatory currents due to waves to be nearly symmetrical. Hence, the vector averaging procedure for V_N and V_E should tend to minimize the oscillatory contribution to $\langle\vec{U}\rangle$. However, other residual unsteady flow components will not be averaged out and will introduce errors into the value of $\langle\vec{U}\rangle$ which are difficult to estimate. If the flow were stationary (invariant in time) and steady, the instantaneous turbulent fluctuations, U', in $\vec{U}$ would conform to

$$U' = \langle\vec{U}\rangle - \vec{U} \tag{13}$$

and would tend to sum to zero over suitable averaging periods. Information on the variability of $\vec{U}$ when wave currents exceed mean flow currents, based on data from combined flows at other locations in the New York Bight, indicates it is small in frequency ranges corresponding to the averaging period for $\vec{U}$ compared with wave-induced variability (Lavelle et al., 1978; Vincent et al., 1982b; Clarke et al., in press). Hence, we infer that errors in $\langle\vec{U}\rangle$ for mean flow are small for the purposes of this study. However, for purposes of sediment transport calculations we must somehow account for the wave-current interactions to avoid violating the assumptions of the transport theories.

Several approximations must be made to apply the bedload theories for combined flows to the CV probe data. First, average values for $\vec{U}_a$ and $\vec{U}_b$ must be chosen for equations (2) and (3). Grant and Madsen (1978) indicate an iterative procedure to find $\vec{U}_a/\vec{U}_b$. In the present study the reference velocity $\vec{U}_a$ was approximated by $\vec{U}_{100}/2$ based on results of Vincent et al. (1982a). This is a first order approximation at best, but it will be shown below that this and other approximations of the parameters required to estimate transport have a reasonably small effect on the results.

Grant and Madsen (1978) emphasize that the direction and magnitude of the combined-flow bottom stress is not a simple vector sum of the wave and current. However, for purposes of our study there is no alternative but to define ϕ_c as the reference direction of U_a, the direction given by the vector sum of the current plus wave.

The wave-current friction factor f_{wc} is also found by approximation. First, the wave friction factor f_w is found as a function of A_b/D using an iterative procedure based on the results of Jonnson (1966). This is combined with the estimated current friction factor f_c as

$$f_{wc} = \frac{|\vec{U}_a|\, f_c + |\vec{U}_b|\, f_w}{(|\vec{U}_a| + |\vec{U}_b|)} . \qquad (14)$$

Current friction factors depend also on grain size and bedforms present. A value of $f_c = 2\ U_{*c}^2/U_a^2$ (Sternberg, 1972) was used at first to estimate f_c, but proved unstable because of imprecision in estimating U_{*c} and U_a. A constant value of $f_c = .005$ was chosen for the present study in the mid-range of expected values for the bedforms and sediment types encountered (Sternberg, 1972).

The value of $\vec{U}_b$, the near-bottom wave orbital velocity, was derived from a wind-wave generation model developed for this study (Drapeau, section C, this report). Surface significant wave heights H_s and periods T_s were determined as a function of wind speed at nearby Kennedy Airport after correction for distance from the site. These waves, representing the averages of the highest 1/3 of the waves generated locally during the periods of current measurement, were used to find maximum values of $|\vec{U}_b|$ and $|A_b|$ through linear wave theory (Silvester, 1974). This value of $\vec{U}_b$ and the values of f_{wc} and α are used in equation (2) to find U_{*wc} which is used in equation (7b) to find ψ_{TH}.

The effects of selective attenuation with depth of the high-frequency portion of the surface wave spectrum are well known. An empirical correction

$$\frac{H_s}{H_b} = \frac{1}{0.16 + \cosh kh} \tag{15}$$

where h is depth, k is wave number and H_b the apparent wave height associated with depth h has been suggested by Draper (1957). This correction was used in this study.

Transport is then found by calculating the value of

$$q = \int_0^{2\pi} f(\psi)\, d\beta \tag{16}$$

where β is phase angle of the wave. In practice, the calculations are done at increments of $\beta = 2\pi/36$. When $\psi > \psi_c$, $f(\psi)$ is found according to equations (8) or (10).

Bedload under steady currents was calculated using the empirical equation first given by Bagnold (1973) and later modified by Gadd et al. (1978). This relationship

$$q_B = 4.48 \times 10^{-5} \, |(|\vec{U}| - U_{TH})|^3 \qquad (17)$$

was suggested by Gadd et al. to be the form best fitting most laboratory results. Direction is from the mean flow reference velocity, $\vec{U}_{100}$.

Another steady flow model, more closely fitting the hypothesis that excess shear stress is responsible for suspension while the mean flow is responsible for advection, is

$$q_{EXC} = 9.3 \times 10^{-7} \, |(\vec{U}_{100} - U_{TH})|^2 \, \vec{U}_{100}. \qquad (18)$$

Direction here is also given by the mean flow reference velocity.

Resuspension of fine sediments follows the ideas suggested by Clarke et al. (in press). In a bed of mixed sands and muds the fines are released during transport of the sands. However, because of their low settling velocities, the fines are mixed relatively far above the bed and tend to form uniform suspensions. The concentration of resuspended fines depends on the percent of fine sediments in the bed and on the depth of erosion which is a function of the rate of coarse bedload transport, or

$$q_F = \vec{U}C$$

$$C = \frac{MC^* \rho_s}{B} \qquad (19)$$

where M is the percentage of mud in the bottom sediments, and B is the scale thickness of the layer of uniform suspension.

Operationally, the calculation proceeds by first comparing $\vec{U}_{100}$ with orbital wave velocity $\vec{U}_w$. If $\vec{U}_{100} >> \vec{U}_w$ and $\vec{U}_{100} > U_{TH}$, then $q = (q_B, q_{EXC})$. If $\vec{U}_w > \vec{U}_{100}$ and $\vec{U}_w > U_{TH}$, then $q = (q_{MG}, q_v)$.

Before presenting the results of transport calculations from the CV probe measurements, comparison is made between the methods described above using average waves and currents with methods presented by Grant and Madsen (1978) and Vincent et al. (1982a) which take into account each wave separately. The data used were obtained from field measurements of waves and currents on the inner shelf off Long Island, New York (Vincent et al., 1982a). The data include velocity profiles (three points) within 1.0 m of the bed, and bottom pressure, both sampled at 1 Hz for five minutes every four hours. These data were used to calculate q_v using average waves and currents, and q_v on a wave-by-wave basis. Comparison of the results (Figure 13) indicates good agreement between the two methods. Linear regression indicates that $r^2 = 0.89$ and the slope of the best fitting line is 1.08. This lends support to use of the approximations described above in applying the averaged version of the Grant and Madsen (1978) model to the present data set.

Transport Calculations and Discussion: Bedload transport rates were calculated according to the equations given above for q_{MG}, q_v, and q_{EXC}. Vincent et al. (1981) showed that measured transport rates under waves are under-predicted by q_{MG} at low rates while q_v tends to over-predict by about the same amount. At high transport rates q_v agrees well with the independent transport measurements while q_{MG} tends to over-predict. Thus, choice of the best bedload transport model for the present study must be somewhat subjective since the only independent transport measurements obtained by which calculated rates can be judged were semi-quantitative estimates of suspended load flux from the CV probe measurements. The CV probe measurements give only indirect information on the actual bedload transport rates.

Flow data from CV1 and wind waves from wind speeds measured at J. F. Kennedy Airport (Drapeau, section C, this report) were used in the bedload

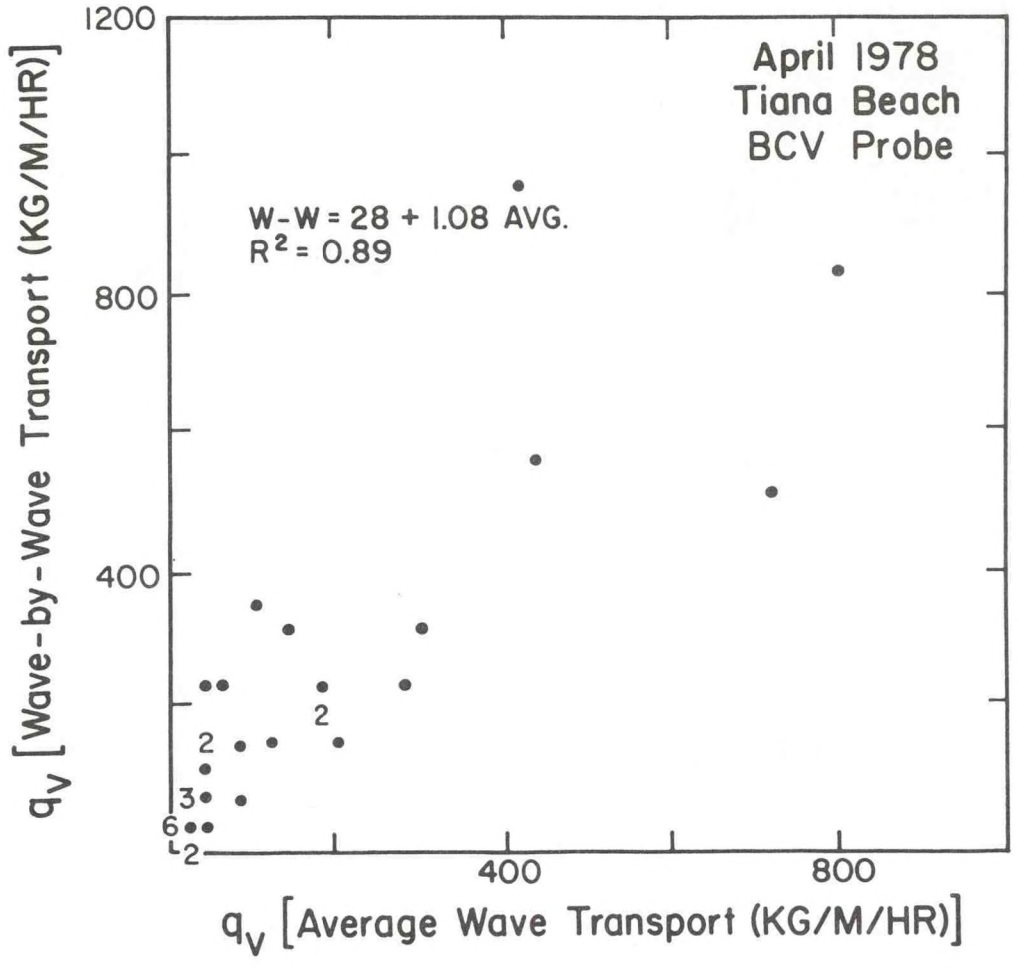

Figure 13. Comparison between values of q_v calculated using averaged wave and current values and q_v using wave-by-wave analysis.

equations and the resulting time series are plotted along with the series of Tr and WE (Figure 14).

Qualitative agreement among the various bedload estimates, Tr, and WE is reasonably good. Major events are well correlated, but several lesser WE and Tr events are not reflected in the bedload estimates. Recalling that bedload depends mainly on wave-current interactions, we investigated the possibility that swell waves, not predicted by local conditions, may be responsible for some of the resuspension events. A model developed by Ross (1979) was used by Drapeau to predict swell due to wind gradients generated by large-scale low pressure systems centered at various locations on the eastern seaboard of North America during ten WE events. Arrival times of the swell waves in the study area and other wave characteristics consistent with those required to resuspend sediments were in good agreement for six of the ten events supporting the hypothesis that these resuspension events may have been generated by swell waves. However, the effects of swell are not generally considered in the bedload calculations because the estimated precision of swell wave heights and directions is low.

Progressive vector plots of q_V and q_{MG} (Figure 15) indicate good agreement in average directions but a factor of two differences in rates. Few events produced transport during the study period. Transport evidently occurred during only about 5% (44 of 849) of the deployment measurements. Two of these transport events account for over 50% of total transport during the deployment.

The most intense transport event during the deployment occurred during March (JD 51-56; Figure 6b, plot F; Figure 7b, plot E). Mean speeds were not particularly high during this event compared to other periods (e.g., JD 73-79; Figure 6b, plot G), the major difference being the presence of waves. Highest

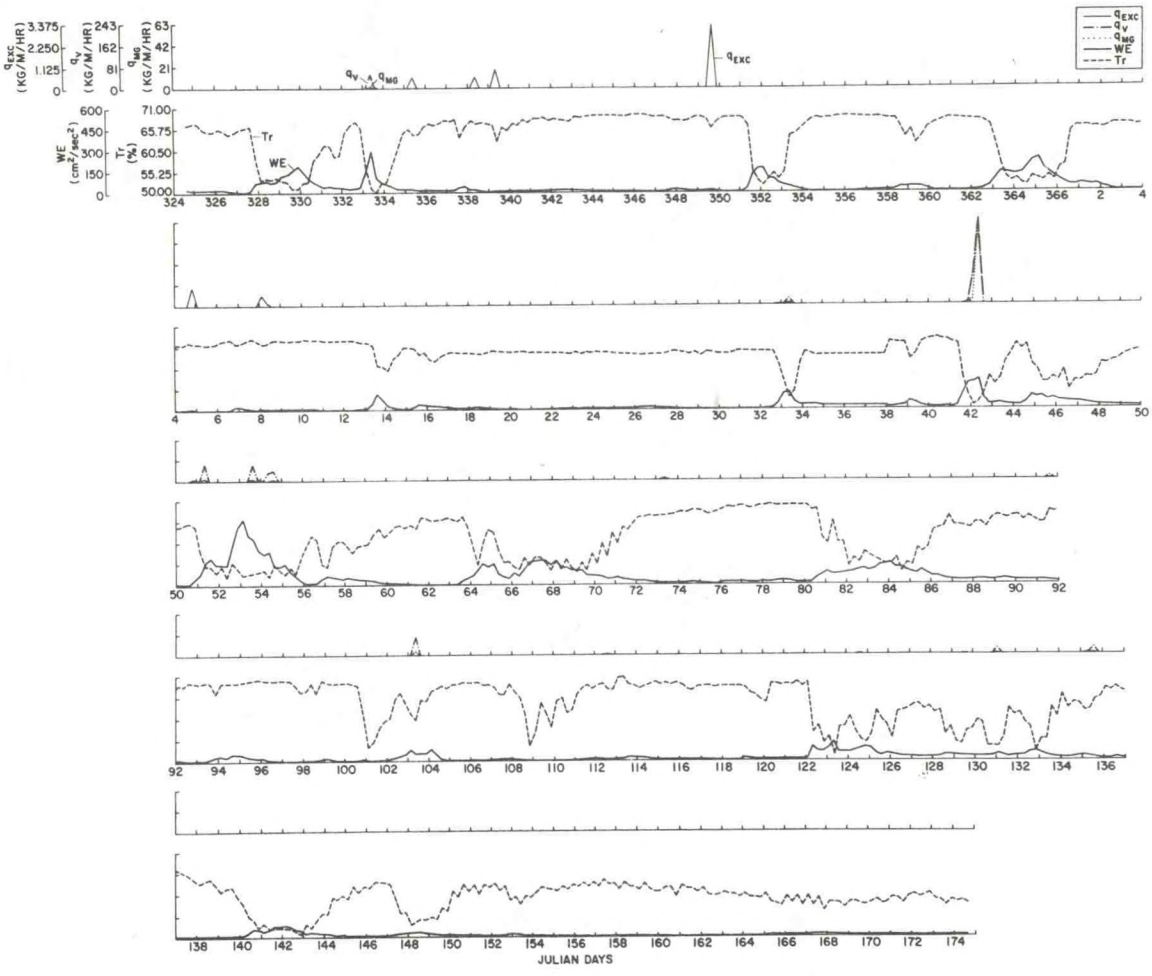

Figure 14. Time-series of calculated bedload transport rates based on CV1 and wind-wave model data compared with bottom wave energy (WE) and suspended sediment (Tr) from CV1.

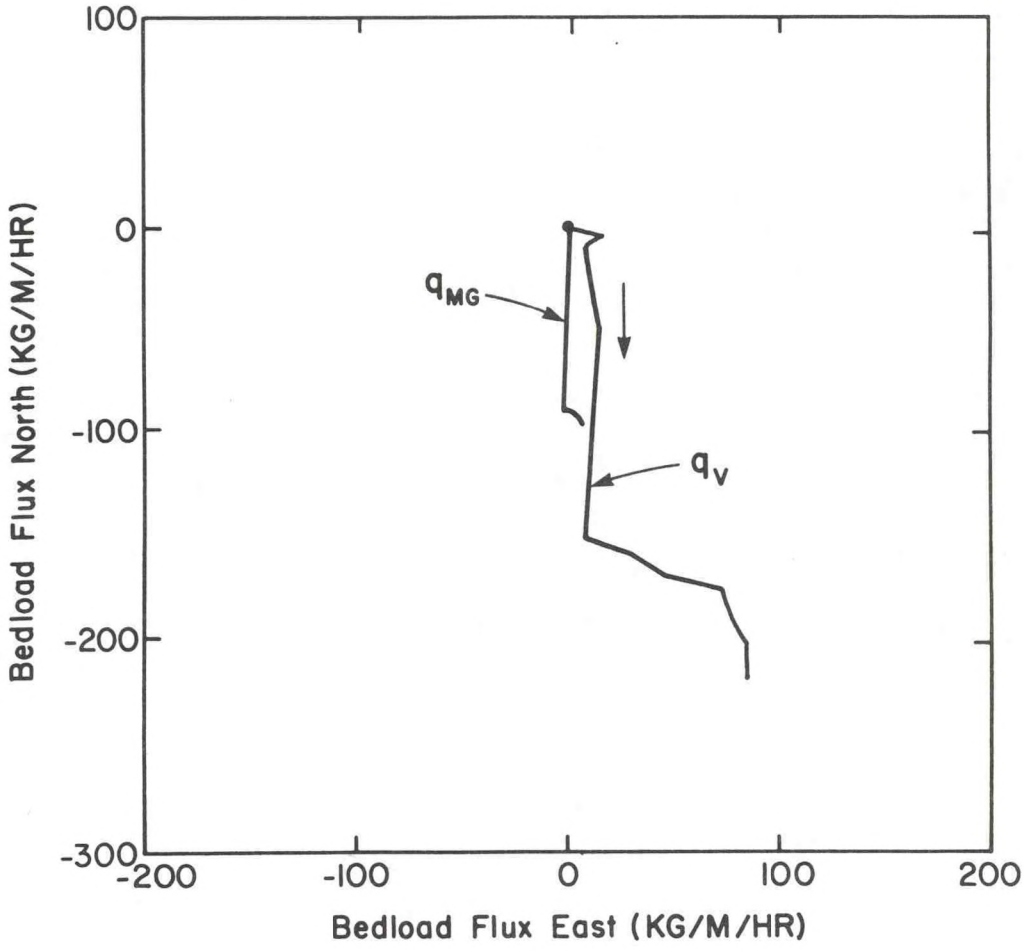

Figure 15. Progressive vector plots comparing q_V and q_{MG} for CV1. Period covered is from November 1980 through June 1981.

mean flow speeds often occurred during periods of lowest wave energy. Han and Mayer (1981) report highest correlations between wind forcing and bottom currents occur when water column stratification is weakest. Thus, before stratification strengthens in April or May, we should expect strong winds to be most strongly coupled to mean flows in addition to generating surface waves.

Several contradictory examples can be cited from the data in Figures 6 to 9. These lend no positive support to the hypothesis described above. Thus, while winds may generate waves capable of transporting the bottom sediments, wind stress magnitude and direction may be just as important as parameters in developing response in the mean flow and hence significant bedload transport. Similar ideas concerning wind-current coupling have been suggested elsewhere (Nelsen et al., 1978; Mayer et al., 1979, Han and Mayer, 1981).

In Vincent et al. (1981, 1982b) the threshold Shields number for transport ψ_{TH} was found from the steady flow curve presented by Miller et al. (1977). Designating this threshold Shields number by ψ_M and the one suggested by Sleath (1978) for waves by ψ_S, the value of q_v can be calculated both ways for comparison.

Values of q_v using ψ_M produce much larger transport rates than ψ_S (Figure 16). This is because, for the sediments at the CV1 site, $\psi_S > \psi_M$ (.04/.03), and q_v is highly dependent on $\psi-\psi_{TH}$ (equation (10)). Net transports calculated using the three wave-current methods are shown in Figure 17. While rates vary, as expected, the directions are similar. Nearly coincidental directions of q_v and q_{MG} are the result of the similar approximations made in determining the wave and current directions used in calculation of both rates.

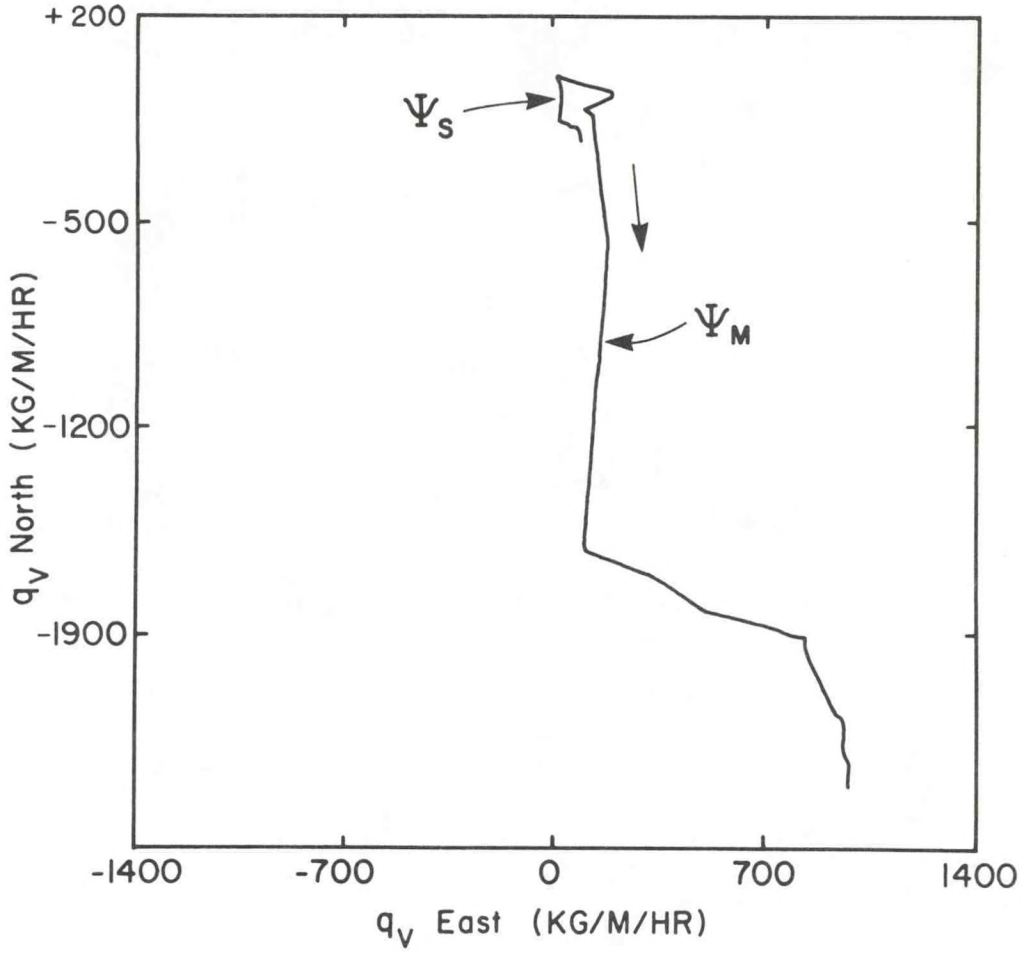

Figure 16. Comparison of q_v for CV1 using the Shields parameter ψ_s for waves (Sleath, 1978) with ψ_M, the one for steady flows (Miller et al., 1977).

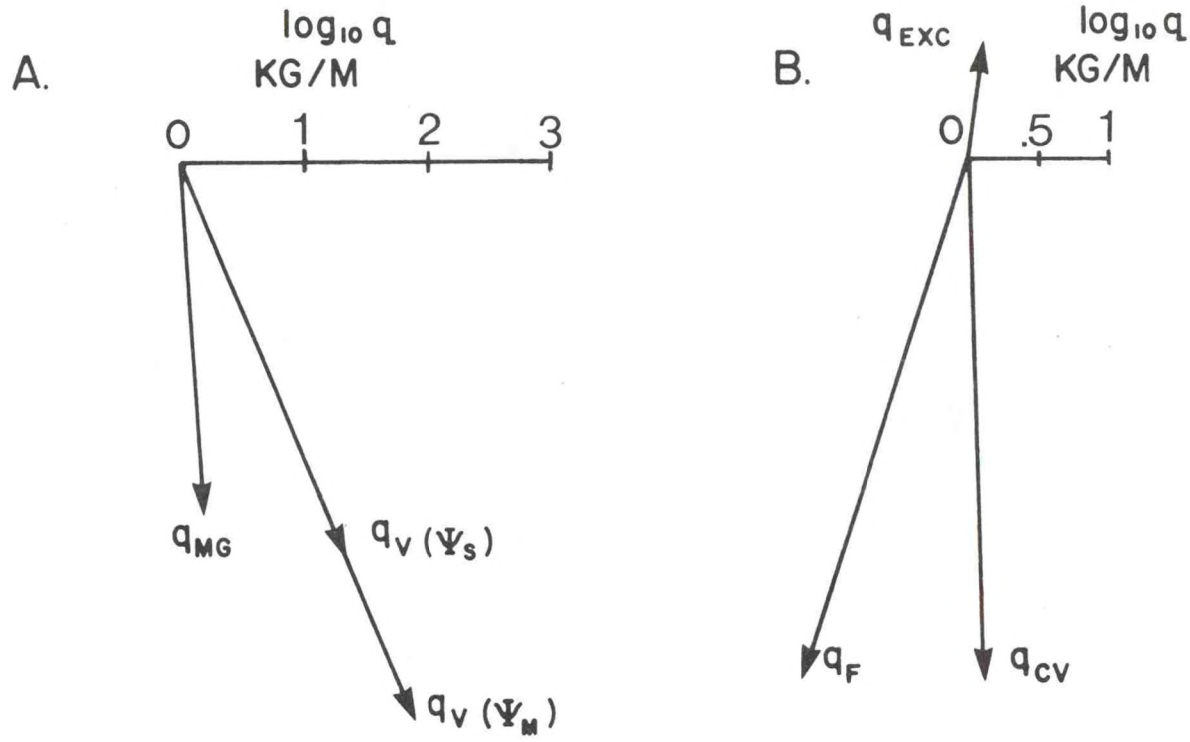

Figure 17. A: Net transports using the three wave-current methods: q_{MG} and q_V using ψ_M and ψ_S. B: Net fine sediment transport from equation 19 (q_F) versus from CV probe measurements (q_{CV}).

Flux directions and rates from CV1 measurements during the 214-day deployment are thought to best represent fine suspended matter transport (Figure 18). Fluxes were calculated as $(F_N, F_E) = \vec{V}_{N,E} \cdot Tr$: units are therefore arbitrary. Net fine sediment transport direction calculated by equation (19) is reasonably close to the direction of net flux from the CV probe measurements (q_{CV} on Figure 17) and from bedload transport rates. However, had only steady flow threshold and transport equations been considered (either equations (17) or (18)), net transport direction (Figure 17) would have been opposite to the wave-current bedload (q_V, q_{MG}) and CV probe flux directions (q_{CV}). This observation emphasizes the importance of waves to sediment transport on the continental shelf.

CONCLUSIONS

The goal of this study has been to estimate the transport rates and directions of sediments capping a dredged material deposit in the inner New York Bight. Various models were used to obtain these estimates and the resulting transport directions were found to be in excellent agreement with each other and with the direction of suspended sediment flux from the CV probe measurements.

A lesser degree of confidence can be attributed to the transport rate estimates. First, the calculation of U_{*wc}, and hence excess ψ, assumes that the mean flow boundary layer is fully described by equation (5). The mean flow shear velocity U_{*c} is normally determined in the field by measurement of velocity at three or more points along a normal to the bottom. Thus, the assumption of the semi-logarithmic mean velocity profile was not testable from the CV probe measurements which included only one velocity measurement. Likewise, no data were obtained from the thin (~ 1-5 cm thick) wave-boundary layer.

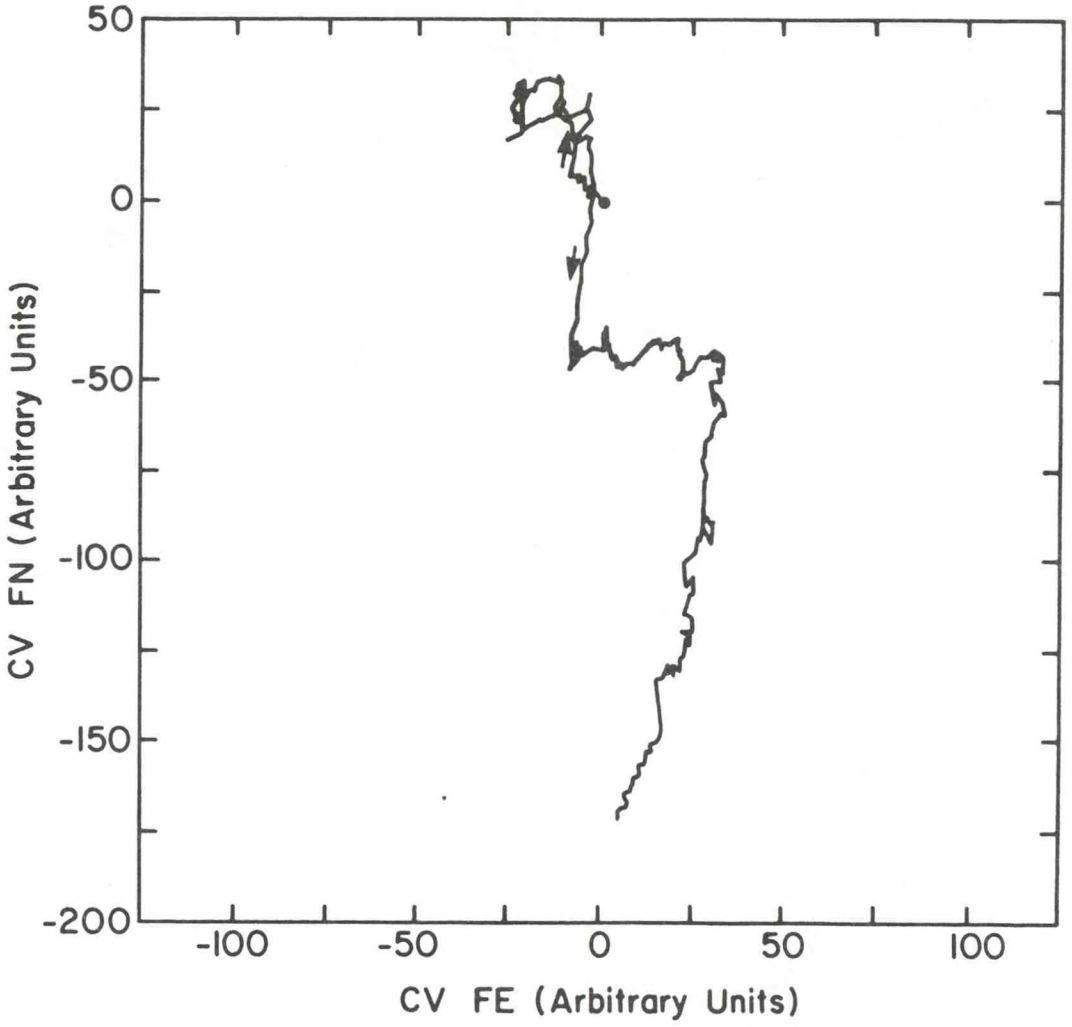

Figure 18. Progressive vector plot of CV probe flux. The labels CV FN and CV FE are north and east flux components. Total deployment duration of 214 days is shown.

Secondly, the transport rates in equations (8) and (10) are based only on laboratory experiments; no field verification of transport rates under waves or combined flows are available. It is, therefore, not surprising that q_V and q_{MG}, for example, should vary by a factor of two, but no rational process is suggested for choosing between these two values of q.

Comparison of wave-current transport rates with steady flow rates indicates that steady flow velocities seldom exceeded threshold and these events did not coincide with periods when waves were effectively stirring the bottom. Moderate waves combined with relatively mild currents proved sufficient to produce transport events which would not have occurred under the waves or currents alone. Steady-flow transport rates are at least an order of magnitude less than wave-current rates. While no great confidence is given to their exact values, it is felt that the relationships among the rates is a reasonable reflection of transport actually taking place at the dumpsite.

Transport rates on shallower and deeper portions of the dumpsite were calculated assuming similar mean flows, but with appropriate changes in wave characteristics due to depth variations. Rates at 21 m (shallowest portion of the dumpsite) were about 20% greater than at the CV probe site (23 m). Rates at 30 m were about 20% less than at 23 m.

In a companion study, Clarke (section E, this report) suggests that under long-term averaged waves and currents little change in cap thickness occurs after 100 moderately energetic transport events and that transport directions are along a north-south axis. It appears that the weight of all results of the dumpsite studies infer that little or no change will occur to the sediment cap over many years. Further south, along the Virginia coast, aperiodic extreme events, such as the "once in a hundred years" Ash Wednesday storm of 1962 (Moody, 1964) have been responsible for transport of extremely large sand

volumes. In the case cited by Moody, the crest of a sand ridge ten meters in height was transported about one kilometer from its previous location. Water depths in the Moody study area were somewhat shallower than at the dredged material dumpsite, and sediment grain size was coarser and much better sorted. If such an extreme event were to occur over the dredge material dumpsite studied here, considerable transport could be expected, but not as much as occurred at Moody's site.

REFERENCES

Abou-Seida, M. M. (1965). Bedload function due to wave action. Rept. HEL-2-11, Hydraulic Engineering Lab., Univ. of California, Berkeley, CA.

Bagnold, R. A. (1973). The nature of saltation and "bedload" transport in water. Proc. Royal Soc. London A, 332:473-504.

Bliven, L., Huang, N. E., and Janowitz, G. S. (1977). An experimental investigation of some combined flow sediment transport phenomena. Rept. 77-3, UNC-SG-77-04, Univ. of North Carolina, Raleigh, NC, 140 pp.

Butman, B., Noble, M., and Folger, D. W. (1979). Long-term observations of bottom current and bottom sediment movement on the mid-Atlantic continental shelf. Jour. Geophys. Res., 84:1187-1205.

Charnell, R. L., and Hansen, D. V. (1974). Summary and analysis of physical oceanography data collected in the New York Bight apex during 1969-1970. MESA Rept. 74-3, NOAA, Boulder, CO, 47 pp.

Clarke, T. L., Lesht, B., Young, R. A., Swift, D. J. P., and Freeland, G. L. (in press). Sediment resuspension by surface-wave action: An examination of possible mechanisms. Mar. Geol.

Dingler, J. R. (1979). The threshold of grain motion under oscillatory flow in a laboratory wave channel. Jour. Sed. Petrol., 49:287-294.

Drake, D. E. (1971). Suspended sediment and thermal stratification in Santa Barbara Channel, California. Deep-Sea Res., 18:763-769.

Draper, L. (1957). Attenuation of sea waves with depth. La Houille Blanche, No. 6, 926-931.

Einstein, H. A. (1950). The bed-load function for sediment transportation in open channel flows. U.S. Dept. of Agriculture, Tech. Bull. 1026, 71 pp.

Gadd, P. E., Lavelle, J. W., and Swift, D. J. P. (1978). Estimates of sand transport on the New York shelf using near-bottom current meter observations. Jour. Sed. Petrol., 48:239-252.

Graf, W. H. (1971). Hydraulics of Sediment Transport. McGraw-Hill, New York, 513 pp.

Grant, W. D., and Madsen, O. S. (1978). Bottom friction under waves in the presence of a weak current. NOAA Tech. Memo., ERL MESA-29, NOAA, Boulder, CO, 131 pp.

Grant, W. D., and Madsen, O. S. (1979). Combined wave and current interaction with a rough bottom. Jour. Geophys. Res., 84:1797-1807.

Hammond, T. M., and Collins, M. B. (1979). On the threshold of transport of sand-sized sediments under the combined influence of unidirectional and oscillatory flow. Sedimentology, 26:795-812.

Han, G. C., and Mayer, D. A. (1981). Current structure on the Long Island inner shelf. Jour. Geophys. Res., 86:4205-4214.

Inman, D. L., and Bowen, A. J. (1962). Flume experiments on sand transport by waves and currents. Proceedings, Eighth Conference on Coastal Engineering, Mexico, pp. 137-150.

Jonnson, I. G. (1966). Wave boundary layers and friction factors. In: Proc., Tenth Int. Conf. Coastal Engineering, Amer. Soc. Civil Engineers, New York, pp. 127-148.

Kalkanis, G. (1964). Transportation of bed material due to wave action. Tech. Memo. 2, U.S. Army Corps of Engineers, Washington, D.C.

Komar, P. D., and Miller, M. C. (1973). The threshold of sediment movement under oscillatory waves. Jour. Sed. Petrol., 43:1101-1110.

Lavelle, J. W., Young, R. A., Swift, D. J. P., and Clarke, T. L. (1978). Near-bottom sediment concentration and fluid velocity measurements on the inner continental shelf, New York. Jour. Geophys. Res., 83:6052-6062.

Madsen, O. S., and Grant, W. D. (1976). Sediment transport in the coastal environment. R. M. Parsons Laboratory for Water Resources and Hydrodynamics, Mass. Inst. Tech. Rept. 209, 105 pp.

Manohar, M. (1955). Mechanics of bottom sediment movement due to wave action. Tech. Memo. 75, Beach Erosion Board, U.S. Army Corps of Engineers, Washington, D.C.

Mayer, D. A., Hansen, D. V., and Ortman, D. A. (1979). Long-term current and temperature observations on the middle Atlantic shelf. Jour. Geophys. Res., 84:1776-1792.

Meade, R. H., Sach, P. L., Mannheim, F. T., Hathaway, J. C, and Spencer, D. W. (1975). Sources of suspended matter in waters of the middle Atlantic Bight. Jour. Sed. Petrol., 45:171-188.

Miller, M. C., McCave, I. N., and Komar, P. D. (1977). Threshold of sediment motion under unidirectional currents. Sedimentology, 24:507-527.

Moody, D. W. (1964). Coastal morphology and processes in relation to the development of submarine sand ridges off Bethany Beach, Delaware. Unpublished Ph.D. thesis, The Johns Hopkins Univ., Baltimore, MD, 160 pp.

Nelsen, T. A. (1979). Suspended particulate matter in the New York Bight apex: Observations from April 1974 through January 1975. NOAA Tech. Memo. ERL MESA-42, NOAA, Boulder, CO, 78 pp.

Nelsen, T. A., Gadd, P. E., and Clarke, T. L. (1978). Wind-induced current flow in the upper Hudson Shelf Valley. Jour. Geophys. Res., 83:6073-6082.

Ross, D. B., 1979. Observing and predicting hurricane wind and wave conditions. Ocean Products and IGOSS Data Processing Services System (IDPSS), Moscow, USSR, 2-11 April, 1979, 15 pp.

Shields, A. (1936). Application of similarity principles and turbulence research to bed-load movement (in German), Mitteilungen der Preussiche Versuchsanstalt fur Wasserbau und Schiffbau, Berlin, No. 26.

Silvester, R. (1974). Coastal Engineering. Elsevier, New York, 457 pp.

Sleath, J. F. A. (1978). Measurements of bed-load in oscillatory flow. Jour. Waterway, Port, Coastal Ocean Div., Proc., Amer. Soc. Civil Engineers, 104 (WW4):291-307.

Smith, J. D. (1976). Modelling of sediment transport on continental shelves. In: E. D. Goldberg, I. N. McCave, J. J. O'brien, and J. H. Steele (eds.), The Sea, Vol. 6, John Wiley and Sons, Inc., New York.

Sternberg, R. W. (1972). Predicting intitial motion and bed-load transport of sediment particles in the shallow marine environment. In: D. J. P. Swift, D. B. Duane, and O. H. Pilkey (eds.), Shelf Sediment Transport: Process and Pattern. Dowden, Hutchinson and Ross, Stroudsburg, PA, 61-82.

Vincent, C. E., Young, R. A., and Swift, D. J. P. (1981). Bed-load transport under waves and currents. Mar. Geol., 39:71-80.

Vincent, C. E., Young, R. A., and Swift, D. J. P. (1982a). On the relationship between bedload and suspended sand transport on the inner shelf, Long Island, New York. Jour. Geophys. Res., 87:4163-4170.

Vincent, C. E., Young, R. A., and Swift, D. J. P. (1982b). Sediment transport on the Long Island shoreface, North American Atlantic shelf: Role of waves and currents in shoreface maintenance. (submitted to Continental Shelf Research).

Yalin, M. S. (1972). Mechanics of Sediment Transport. Pergamon Press, New York, 416 pp.

Young, R. A., Clarke, T. L., Mann, R., and Swift, D. J. P. (1981). Temporal variability of suspended particlate concentration in the New York Bight. Jour. Sed. Petrol., 51:293-306.

SIMULATION OF SEDIMENT TRANSPORT AT THE DREDGE MATERIAL DUMPSITE USING COMBINED WAVE AND CURRENT STATISTICS

Thomas L. Clarke

National Oceanic and Atmospheric Administration
Atlantic Oceanographic and Meteorological Laboratories
4301 Rickenbacker Causeway
Miami, Florida 33149

INTRODUCTION

The sand cap at the dredge material dumpsite can be regarded as a mound of sandy material on the ocean floor. Two questions of major importance concerning the cap are: (1) What is the expected life of the cap? and, (2) What would be the consequences of cap breaching? These two questions will be answered based on computer models of the combined near bottom wave orbital velocity and mean current flow, and of the effects of these flows on bottom material.

The first question is addressed by means of a Monte-Carlo simulation of storm events. Combined wave and mean current events with statistics matching observations of flow at the dredge material dumpsite were randomly generated. After including the production by the sand cap bathymetric perturbation of both wave shoaling and mean flow veering, the erosion caused by the simulated storms was calculated. After integrating events for three years the predicted erosion was only a few centimeters so that cap life should be centuries.

The effects of breaching were addressed by using a model developed for modeling fine sediment transport in the New York Bight as a whole. This model assumes that fine grained sediment undergoes a random walk whose statistics are determined by wave driven resuspension and mean flow determined advection. If the cap should be breached then the fine sediment underlying the cap would be exposed to resuspension events and after a few years the surface layer of exposed sediment would reach equilibrium within the Bight Apex.

SAND TRANSPORT (Cap Life)

Given the problem of predicting the future evolution of a hill of sandy material on the ocean floor, the most straightforward method is to time integrate the rate of change of depth with time. Symbolically, the depth at time T, D(T), is given by

$$D(T) = \int_{T_o}^{T} \frac{dD}{dt}\, dt + D(T_o) \qquad (1)$$

The rate of change of depth dD/dt can be calculated using the continuity equation from the divergence of the bed-load transport $\vec{Q}(t)$. The quantities D, $\vec{Q}$ and dD/dt are functions of spatial position.

Assuming that sand is transported only as bed-load, dD/dt is given by

$$\frac{dD}{dt} = \nabla \cdot \vec{Q} \qquad (2)$$

There are many methods for calculating the bed-load transport $\vec{Q}$ from observed flow quantities and sand parameters. The simplest formulations such as the Bagnold (Gadd et al., 1978) relation which depend only on the mean flow speed will not be adequate in the wave dominated environment of an open continental shelf. The two most widely accepted methods for calculating Q in a combined wave and mean flow regime are those due to Madsen and Grant (1976) and Vincent et al. (1981). The Vincent approach will be used here as it is simpler and is more suitable for incorporation in a simulation where $\vec{Q}$ will have to be calculated at many spatial points and many time steps in order to evaluate the rate of change as given by equation 2, and then to integrate using equation 1 to find the change in water depth.

The Vincent method is based on the concept of traction carpet depth or C*. The depth of the traction carpet is empirically related to the wave orbital velocity at the bottom through use of the Shield's parameter (Vincent et al., 1981) which is a non-dimensionalized form of the bottom shear stress. C* is found to be a linear function of the wave Shield's parameter above a threshold, ψ_T. The sand contained within the traction carpet is then advected by the mean flow, so that $\vec{Q}$ is proportional to the mean flow velocity and the excess Shields parameter. Thus, given the mean flow, the wave orbital velocity at the bottom, and the sediment parameters (grain size, and density), the Vincent relation gives an unambiguous value for the discharge $\vec{Q} = .09\ (\psi - \psi_T)\vec{u}$.

In order to estimate the mean flow velocity, and the wave orbital velocity at the spatial and temporal scales necessary to evaluate equations 1 and 2, a statistical approach has been used. As a result of other modeling efforts a large body of current meter data has been processed into summary statistical form (Clarke et al., in review). In addition, a large body of wave height, direction and period measurements is available from the MESA project (Lettau et al., 1976). In order to use numerical methods to calculate change of bottom depth from equation 2, the discharge $\vec{Q}$ must be calculated on a fairly regular grid with spacing small enough to resolve the flow features of interest. This in turn requires that mean flow and wave velocities be known on the same grid. For the case of the COE dump site this spacing might be on the order of 200 meters.

In order to provide the most realistic simulation practical, the Monte-Carlo method was used. The mean and variance of the historical velocity data was extracted, and used in conjunction with a random number generator to generate Gaussian psuedo-random variables with the same statistics as the

observed currents. The time scale needed in equation 1 was estimated by the use of correlation times to measure the duration of typical resuspension events as explained in Clarke et al. (1982). The necessary Gaussian psuedo-random variables are four-dimensional because there are two components of mean flow and two components of wave orbital velocity. The covariance matrix $\sum$ is thus four by four, but it can be decomposed conceptually into four two-by-two matrices

$$\sum = \begin{bmatrix} \sum_u & \sum_{wu} \\ \sum_{uw} & \sum_w \end{bmatrix} \tag{3}$$

The submatrix $\sum_u$ represents the covariance (variances and cross-correlation of the individual velocity components) of the mean flow and was extracted directly from the summary statistical data. Similarly, the submatrix $\sum_w$ involves only the wave orbital velocity and can be estimated from historical wave data. The remaining two submatrices are transposes of each other, $\sum_{uw} = \sum_{wu}^T$, and are the most difficult to estimate, since they involve the cross correlation of mean flow and wave orbital velocity. Fortunately, the data provided by the November 1980 to June 1981 deployments of the CV probes provided measurements of both mean flow and wave orbital velocity so that these matrices could be estimated by computing the correlation between the mean flow and the mean square wave orbital velocity during the deployments.

In order to further refine the simulation, the wave orbital velocity component of the random Gaussian vector was corrected for shoaling affects over bottom topographic variations. In addition, the mean flow component was used as a boundary condition (flow at infinity) for a potential flow solution over a Guassian bottom depth perturbation. This potential flow was then extrapolated to the bottom by use of a friction factor of .005.

The potential flow solution was obtained by Fourier transforming the bottom bathymetry; note that a Gaussian bump has a Gaussian transform. If D* (m, n) is the transform of the bathymetry D(x, y), then the flow over D can be expressed as

$$\vec{u} = \vec{u}_\infty + \int dm \int dn\ D^*(m, n)\ \Delta\vec{u}(m, n) \tag{4}$$

where $\Delta\vec{u}(m, n)$ is the flow over a sinusoidally corregated bottom with wavenumbers m and n. This works because the potential flow equations are linear. Convenient basic solutions over corrugated bottoms are provided by the shallow water linear wave theory. Shallow water theory is used because the Froude number is assumed small, and the acceleration of gravity is adjusted so that the linear wave solutions are stationary in the presence of the mean flow. This implies that the relation between the depth of the corrugations and the flow perturbation is given by

$$|\Delta\vec{u}(m, n)| = |\vec{u}_\infty|\ D^*(m, n)/D_\infty \tag{5}$$

This can be substituted into the inverse Fourier relation to give an expression for the total flow perturbation. This integral is still a little complicated, but after a stationary phase asymptotic evaluation is done, the total flow perturbation is given by

$$\Delta u_x = \frac{\Delta D}{D} \left[\frac{x}{x^2 + \sigma_x^4\, y^2/\sigma_y^4}\right] \left[x u_x + y u_y\ (\sigma_x^2/\sigma_y^2)\right] \tag{6a}$$

$$\Delta u_y = \frac{\Delta D}{D} \left[\frac{y}{y^2 + \sigma_y^4\, x^2/\sigma_x^4}\right] \left[y u_y + x u_x\ (\sigma_y^2/\sigma_x^2)\right] \tag{6b}$$

where σ_x and σ_y are characteristic widths of the Gaussian bathymetry perturbation. The typical shape of the streamlines for this potential flow solution is shown in Figure 1 for flow over a symmetrical Gaussian bump with height 70% of the water depth. Because of the large height of this bump (contours of depth are dotted) the flow streamline curvatures are much exagerated over what can be expected for bathymetric perturbations in the open ocean.

Use of depth corrections to wave orbital velocity and also the use of a perturbation solution to the mean flow as given by equations 6, allows the use of only a regional value for the psuedo-random mean flow and wave orbital velocity. Without these corrections the gradient in equation 2 is identically zero so that no change in depth occurs. The inclusion of the effects of wave shoaling and mean flow perturbation produce a non-zero change and hence a change in bathymetry.

Given a Gaussian bathymetry perturbation, its change over time can then be estimated by generating psuedo-random values for flow parameters in order to simulate transport events. The covariance matrix $\sum$ derived from observation is used to generate these simulated flows. The wave orbital velocity is corrected for shoaling, and the mean flow is corrected for the effect of the bathymetry perturbation at each point on a spatial grid. Figure 2 shows the triangulated grid used in this simulation; it is 15 by 15 cells in size. The cell size was either 400 meters or 100 meters, depending on whether the dump site as a whole or just the capped area was being simulated. The Vincent bedload transport formulation is then used to calculate a discharge $\vec{Q}$ at each of the grid cells so that the finite difference form of the divergence operator can be used to evaluate equation 2 to find the rate of change of depth in a grid cell. Finally, the time integral in equation 1 is

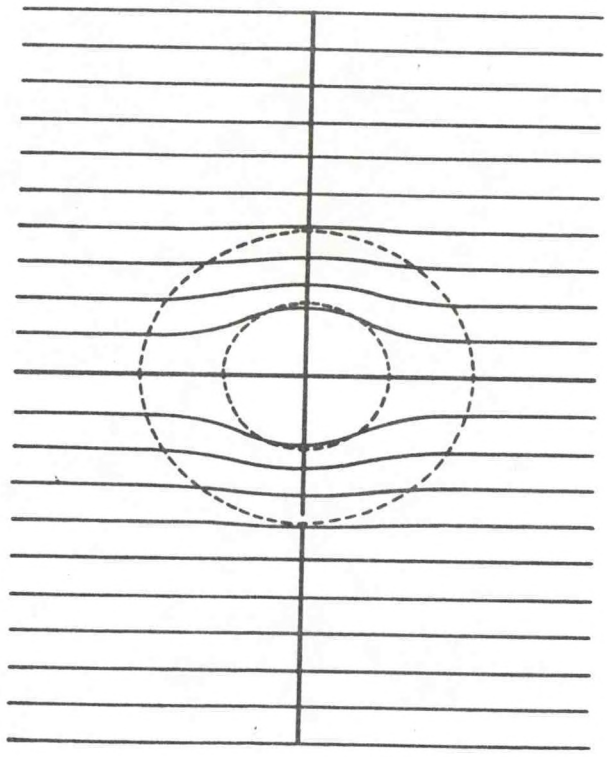

Figure 1. Steamlines of flow over symmetrical Gaussian bottom perturbation.

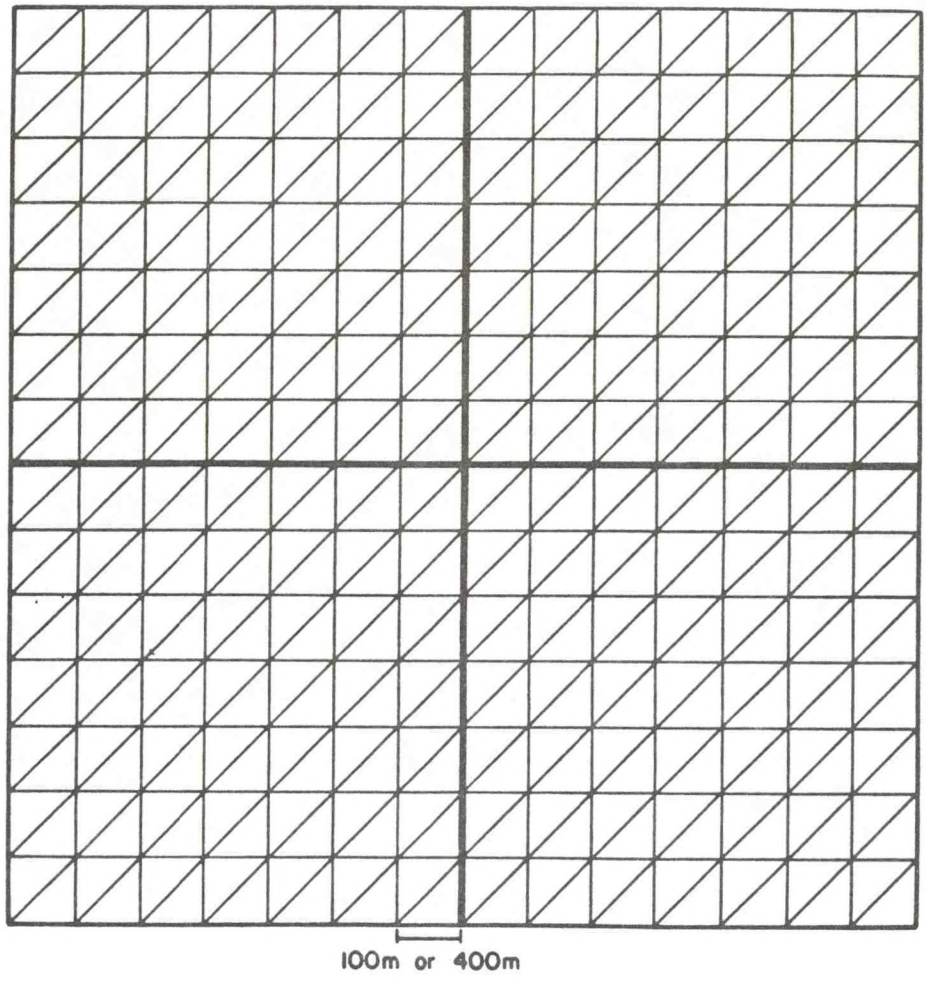

Figure 2. Grid used in sediment transport simulations.

implemented by summing over a number of these simulated events. Because of computer time limitations, only 100 events could be used in each simulation run. At the event frequency reported in Clarke et al. (1982) , this corresponds to about three years. Note however, that because only summary statistics are used in the simulation, events of greater intensity than actually observed will be produced by the psuedo-random generator.

RESULTS OF SIMULATION

There are two ways that bathymetry-induced transport gradients could cause the erosion and breaching of the sand cap. First, the regional bathymetry of the dump site as a whole could induce a transport gradient that would tend to erode the sand cap. Since the sand cap is located to the southeast of the main dumping area, this would require that the southeast portion of a large scale bottom perturbation would be primarily erosive in the observed flow climate at the dump site. Second, the bathymetry perturbation of the sand cap itself might be subject to erosion. In this case a smaller scale perturbation would have to be primarily subject to erosion in the flow climate at the dump site.

To examine these two possibilities simulations were carried out for a symmetrical bottom perturbation as shown in Figure 3. The contour units are in meters, and a latitude/longitude scale has been added so that the center of the perturbation is located at the center of the dump site as a whole. Results of the simulation are shown in Figure 4 as contours of net change after 100 flow events in centimeters. The contours in Figure 4 have been subject to smoothing to remove statistical noise produced by the limited number of events simulated. The small size of the net change (less than 10 cm) reflects the small size of the flow perturbations caused by the

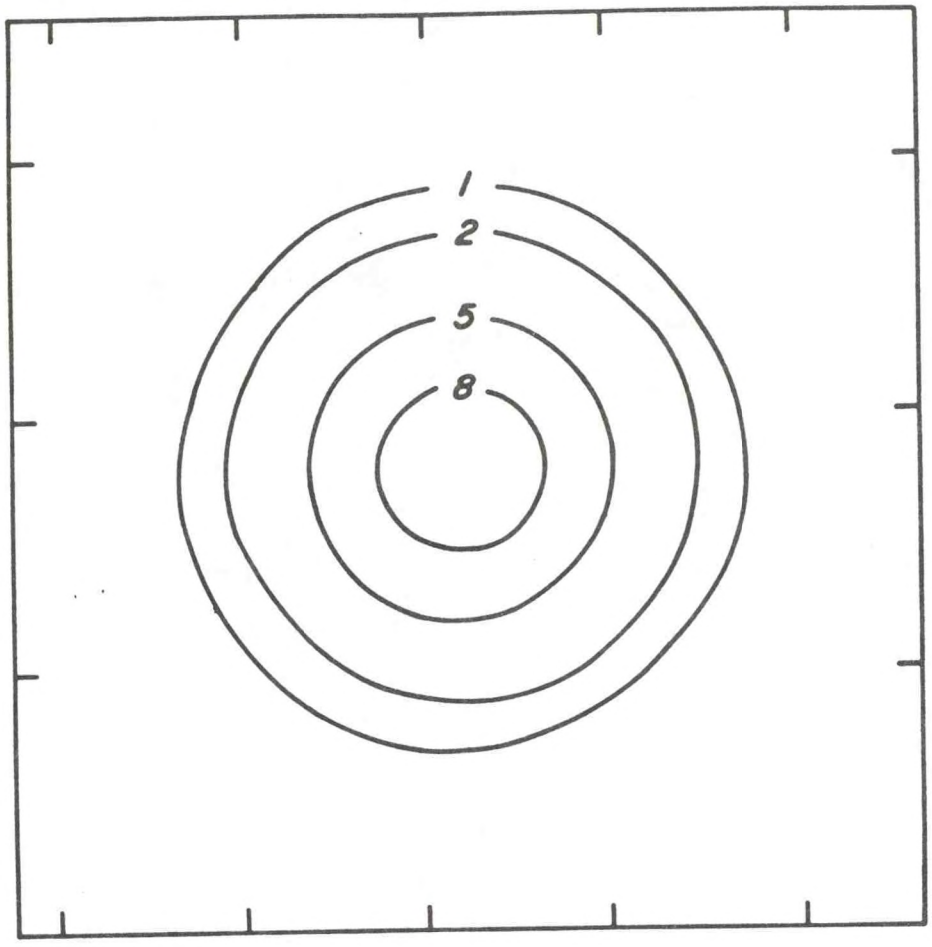

Figure 3. Bottom bathymetry perturbation used to simulate overall dump site in meters. Scale marks along the edges are in units of one minute of latitude and longitude, respectively, at the dumpsite latitude.

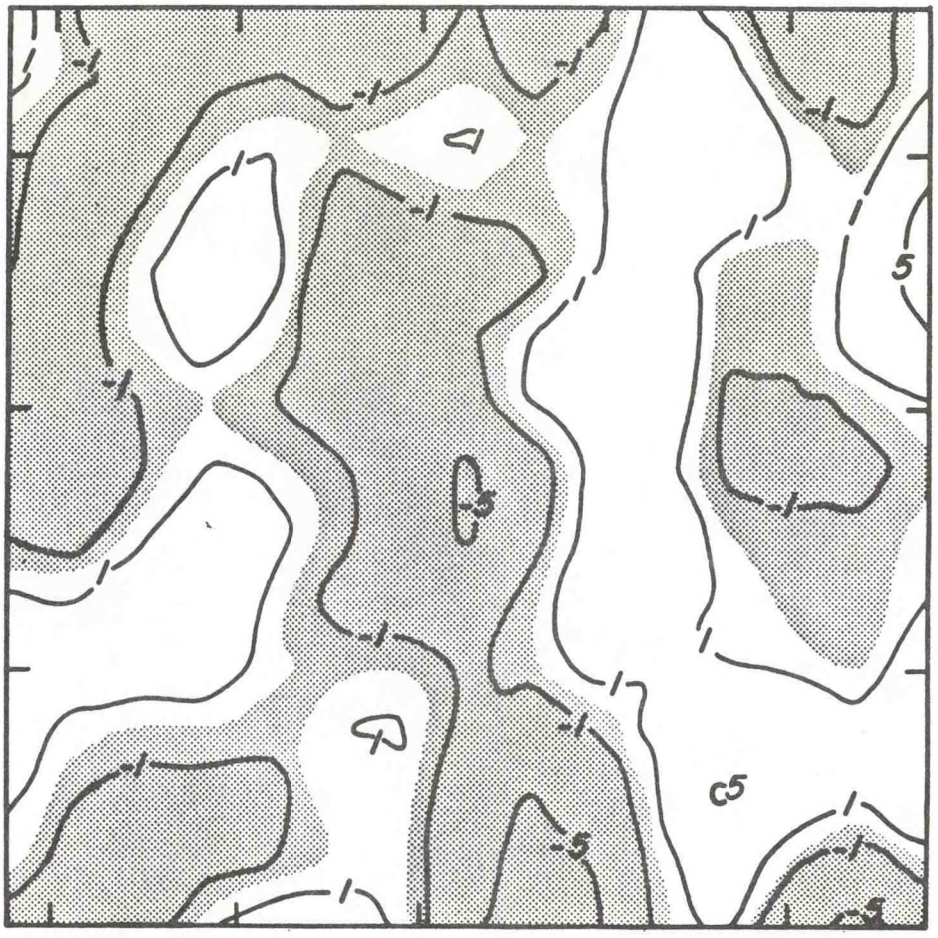

Figure 4. Simulated net change in overall dumpsite bathymetry in centimeters. Stippled area underwent erosion. Scale is the same as in Figure 3.

bathymetric perturbations. Despite the bump in the bottom the combined wave orbital velocity and mean flow field remains nearly homogenous so that the divergence in equation 2 is nearly zero.

One can discern a pattern in the contours of Figure 4, nonetheless. There is a primarily North-South trending pattern, almost a ridge and swale pattern to the change. This is consistent with other theories of bottom perturbation growth (e.g. Huthnance, 1982) which predict growth of linear features at an angle to the flow. It is extremely interesting that the present simulation, which includes the effects of surface waves as well as mean flow, produces much the same prediction as the Huthance theory which only takes into account mean flow. The patterns predicted are much the same: ridge like features at an angle to the mean flow, which here is nearly North-South. The quantitative prediction of wavelength is similar also; both predict that the ridge-like perturbations will have a scale of several kilometers.

The effect of the transport gradients produced by the overall dumpsite bathymetric perturbations on the sand cap should be small. If the sand cap lies in the southeast corner of the circle at about the 2 m contour (Fig. 3), these would be between -1 and +2 cm change. Since these changes produced during the three year simulation study are only a fraction of a meter, the effect on cap life would be negligible.

Figure 5 shows the symmetrical bottom perturbation used to examine erosion at the cap site. Latitude and longitude lines have been added as if the perturbation was at the cap site. Smoothed contours of the net change calculated from simulation of 100 flow events are shown in Figure 6. The contour units are again centimeters so that the change over the three year simulation is only a fraction of a meter. At the peak of the bathymetric

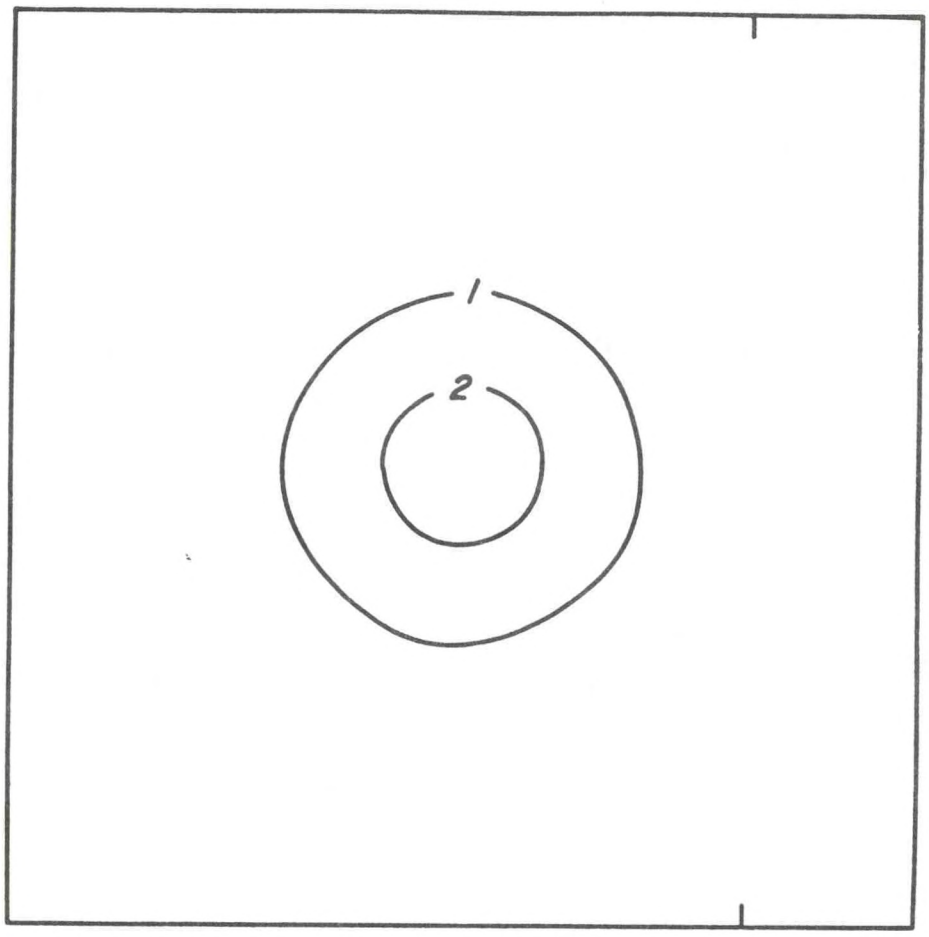

Figure 5. Bottom bathymetry perturbation used in simulation of sand cap. Height in meters. Scale: top and bottom lines are one minute of latitude (one nautical mile) apart; distance between tick marks and left margin is one minute of longitude at the latitude of the cap site.

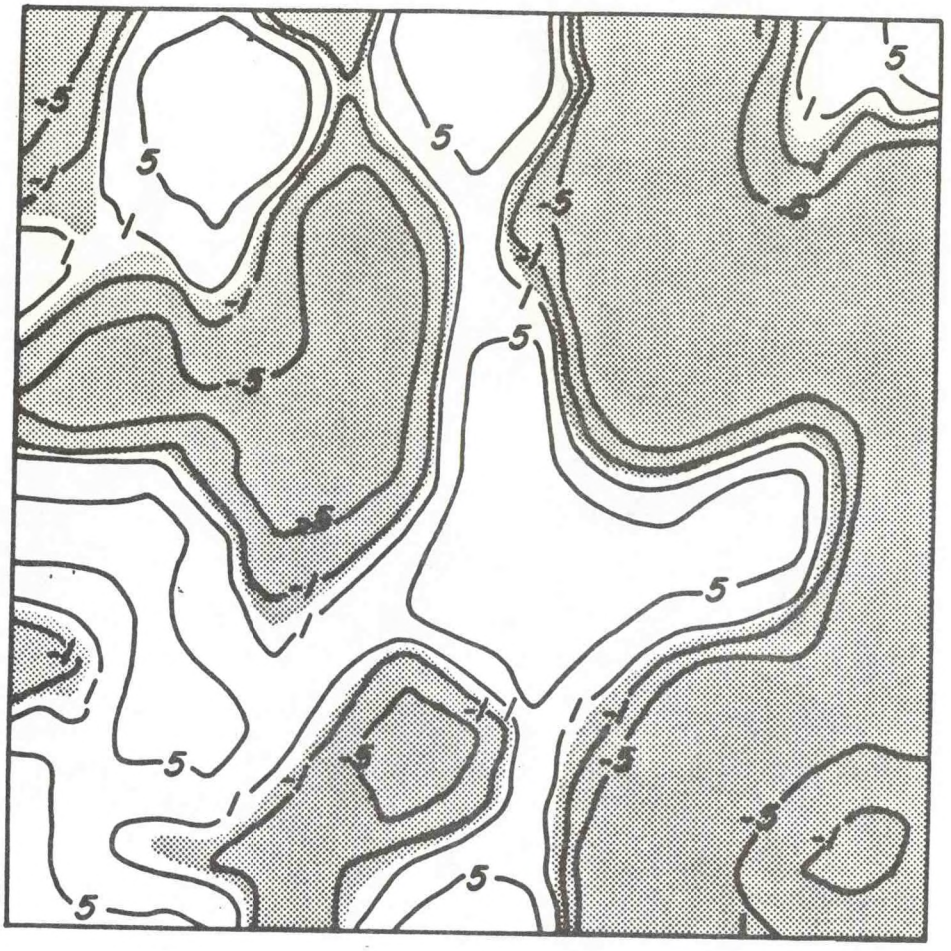

Figure 6. Simulated change in bathymetry of sand cap in centimeters. Stippled area underwent erosion. Scale is the same as Figure 5.

perturbation the change is positive so the perturbation grows, but immediately to the northwest it is negative, so that it is difficult to judge whether the net change is positive or negative. The change is very small however, so that the cap life should be very long.

Note that the characteristic separation of positive and negative features in Figure 6 is on the order of a kilometer. This is also consistent with the Huthnance theory which predicts that shorter features will grow but with a larger angle to the flow. If the contours in Figure 6 are interpreted as a ridge and swale topography, the alignment is much more nearly east-west and so make a larger angle with the mean flow.

In conclusion, erosion/deposition by the mechanism examined here will have little influence on the life of the sand cap. The flow perturbations induced by bathymetric variations are not large enough to produce significant gradients in transport.

CONSEQUENCES OF CAP BREACHING

If for some reason, anthropogenic or natural (unlikely), the sand cap should be breached, it would be of interest to predict the resulting dispersal of fine-grained contaminant-bearing sediment. The diffusion model developed by Clarke et al. (1982) is capable of answering this question. Figure 7 shows the New York Bight region with subregions used in the diffusion model outlined.

The numerical model of fine sediment transport assumes that the movement of this material on the continental shelf results from a series of statistically independent movements of the individual sediment particles. Each particle is thus undergoing a random walk and the mathematical theory of random walks can be used to solve the sediment transport problem. The

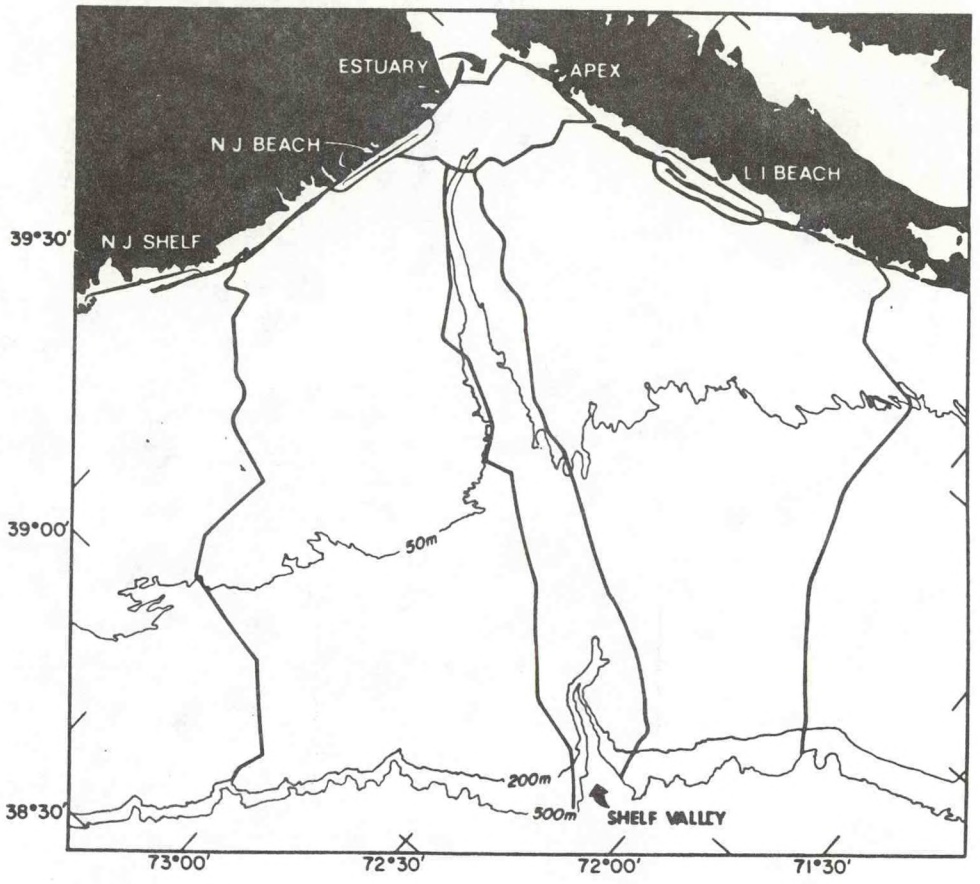

Figure 7. Bathymetric map of the New York Bight region with subregions used in this study outlined.

independent movements are assumed to be produced by resuspension due to surface wave activity and transport by mean flows. Even if periods of high surface waves are correlated with respect to the mean water motions, the effect is to produce additional advection so that the resulting sediment distribution obeys a diffusion-advection equation.

The results of running the model are shown in Figures 8 and 9 as a contour map of percent fine sediment in the upper centimeter of the bed at one year and 100 years after a perturbation (dump) at the dredge material dump site covering a model grid cell to a depth of 1 cm with fine sediment. At first, advection dominates and sediment is swept rapidly to the New Jersey shore. Later, diffusion dominates and the sediment spreads into a bilobate dispersion pattern centered around the Hudson Shelf Valley. Diffusion into the valley is lower there because of the lower magnitude of the diffusion coefficients. The maximum concentration of the sediment cloud has shifted away from the original site to the corner of the Bight. This is a consequence of the geometry of the Bight and is characteristic of dumps made in the apex region. Dispersion is slightly faster to the south partly because of the mean advection term is biased to the southwest and partly because of the regions of higher average diffusivity off the New Jersey coast.

In Figure 10 is shown the percentage of the initial perturbation that arrives at various regions within the New York Bight versus time. These regions, which are outlined in Figure 7, were chosen to be representative of environmentally sensitive regions. The percentages increase as a function of time as the cloud of sediment increases in size and begins to impinge upon the regions. Later the amount decreases as the total amount of sediment in the Bight decreases as it leaks over the shelf edge. This pattern of the amount of sediment arriving at shore areas versus time is typical for dumps in the apex region.

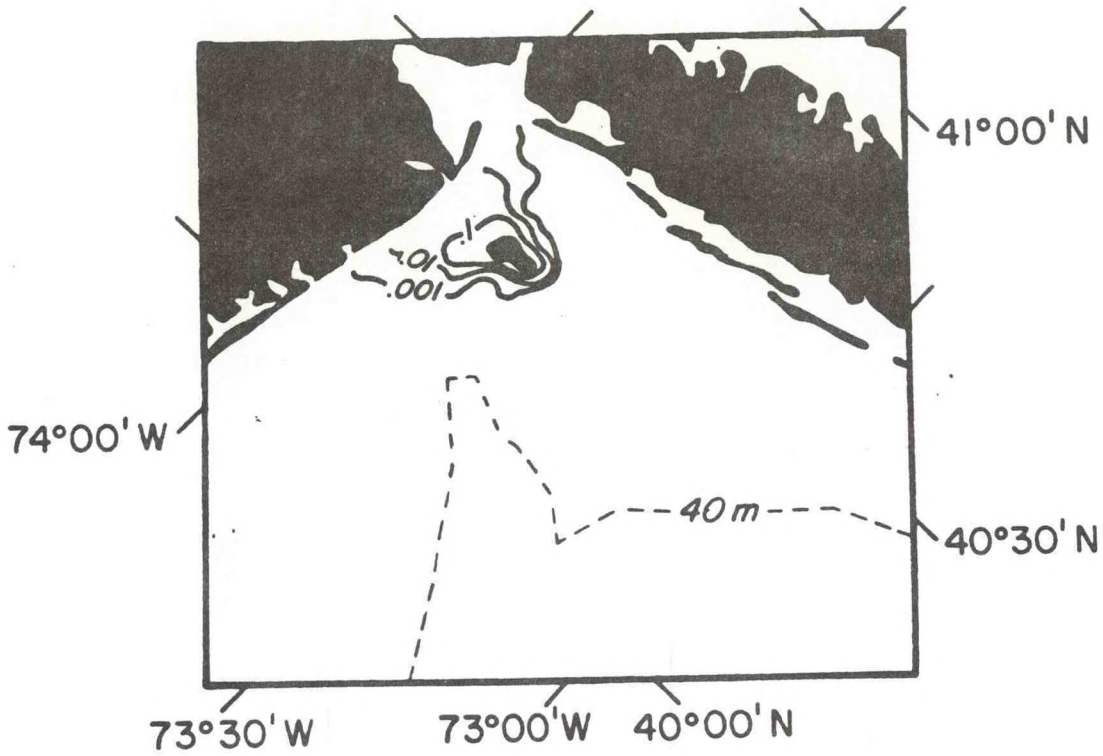

Figure 8. Contour map of sediment distribution one year after a dump at dredge spoil dump site. Units are percent fine sediment in surficial sands by weight.

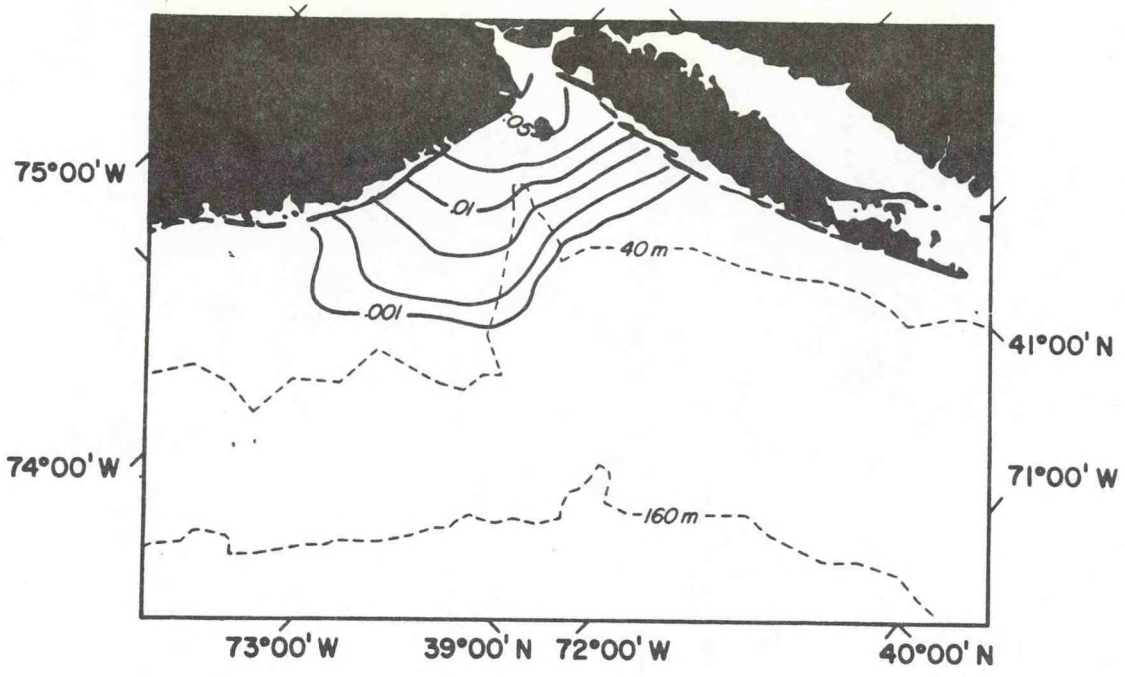

Figure 9. Contour map of sediment distribution 100 years after a dump at dredge spoil dumpsite. Units are percent fine sediment in surficial sands by weight.

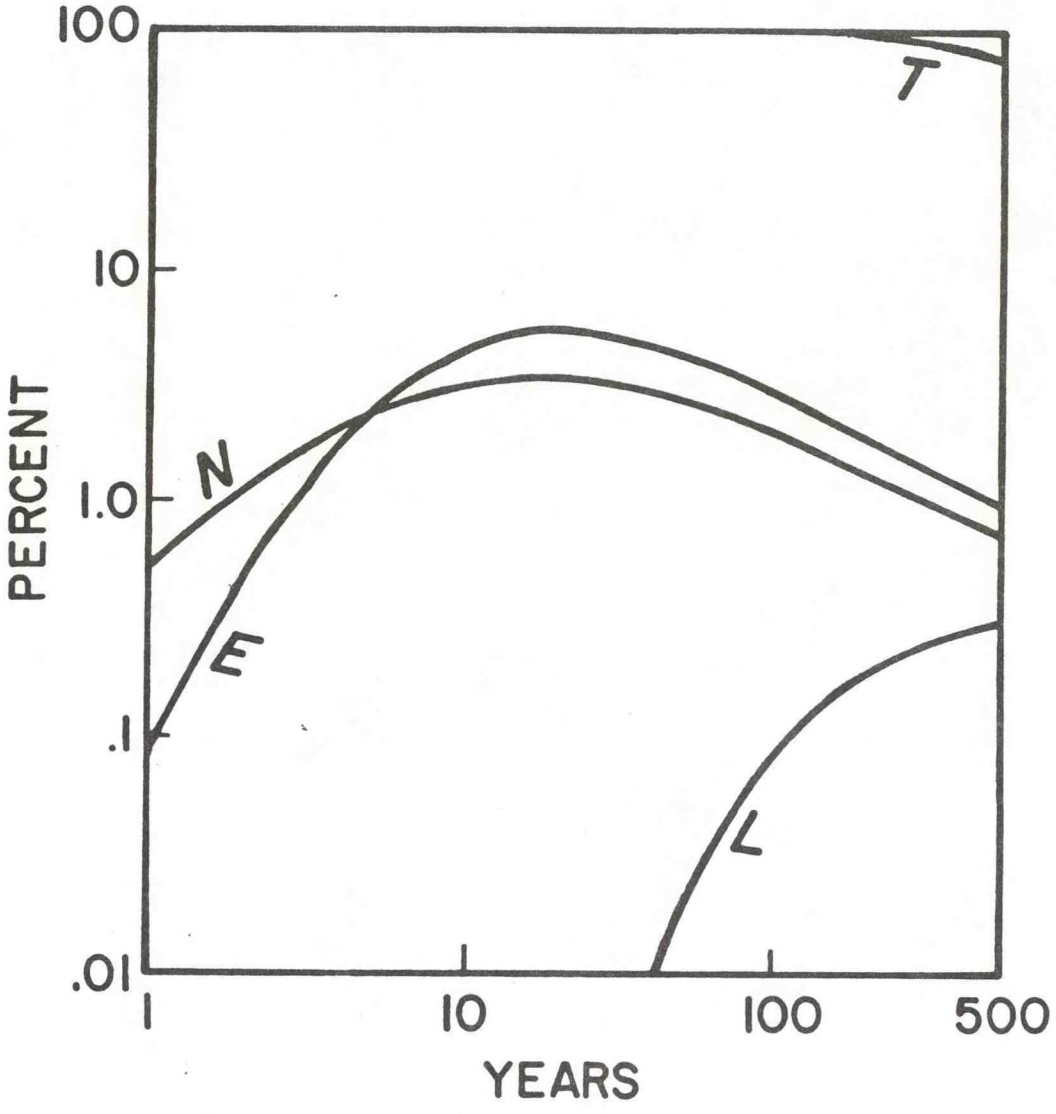

Figure 10. Percentage of initial perturbation at dredge spoil dump site arriving at selected regions of the New York Bight versus time. T = total, N = New Jersey Beach, L = Long Island Beach and E = estuary.

Clarke, T. L., D. J. P. Swift, and R. A. Young, 1982, A numerical model of fine sediment transport on the continental shelf. Environ. Geol., 4, 74-86.

Gadd, P. E., J. W. Lavelle, and D. J. P. Swift, 1978, Calculations of sand transport on the New York shelf using near-bottom current meter observations. J. Sed. Petrol., 48, 239-252.

Huthnance, J. M., 1982, On one mechanism forming linear sand banks. East Coastal and Shelf Science, 14, 79-99.

Lettau, B., W. A. Brower, and R. G. Quayle, 1976, Marine Climatology: MESA New York Bight Atlas Monograph 7, NOAA-ERL, Boulder, CO.

Madsen, O. A. and W. D. Grant, 1976, Sediment Rransport in the Coastal Environment. Rept. No. 209, Ralph M. Parsons Laboratory, Mass. Inst. Tech., Dept. Civ. Engineering, 105 pp.

Vincent, C. E., R. A. Young, and D. J. P. Swift, 1981, Bed load transport under waves and currents. Mar. Geol., 39, 71-80.

F. SUMMARY

New York harbor dredgings considered unsuitable under the the ocean dumping pollution criteria were dumped in the southeast quadrant of the New York dredged material dumpsite and subsequently capped by clean mud and then clean sand.

A five-part study was undertaken by NOAA to determine (a) what, if any, changes to the cap took place over the winter of 1980-1981, (b) the bottom current velocities necessary to initiate resuspension and erosion of cap sediment, (c) the long-term probability of erosion by wind-generated waves, (d) bottom currents and sediment transport which occurred during the 1980-1981 winter, and (e) the mathematical probability of sediment transport due to waves and bottom currents.

A. Surfical Sediments

Sediment data taken in November 1980 and June 1981 indicate:

(1) A generally smooth central area covered with 80% cap sand. The area of high sand content was somewhat reduced during the period by an influx of mud.

(2) Along the northern edge of the cap, patches of rough bottom consisted of up to 30 to 50% mud and 30% gravel in November. By June, some of the rough areas were smoothed out, gravel content was reduced to less than 5%, and areas of 30 to 50% mud content enlarged. Most of the gravel along the eastern edge of the dumpsite was construction rubble fringing the cellar dirt dumpsite immediately to the east. On other portions of the cap, gravel-sized particles were mostly rock and shell fragments.

(3) Along the eastern edge of the cap were extensive areas of rough bottom which moved slightly westward during the period. Gravel content remained high (10 to 50%), and encroached slightly westward. Mud content increased more, with expanded areas of over 30% mud.

(4) Mean grain size of the sand-sized fraction remained about the same in the central cap area, and became finer along the northern, eastern, and southern edges.

Bathymetric changes mapped by COE indicate a slight amount of erosion, less than the margin of survey error. The net effect is a slight removal of sand with some replacement by mud.

B. Threshold Erosion Velocities

Field experiments were carried out during both November 1980 and June 1981 cruises to determine the threshold current velocity needed to initiate bottom sediment resuspension on the cap. These were done using the SEAFLUME, a three-sided, open-bottom channel which forces water along the bottom at increasing speeds. Sediments at the 13 sites averaged 7.1% gravel, 75.3% sand, and 17.5% mud, and had an average mean sand diameter of 2.4 ϕ (fine sand). Threshold shear velocities at the seabed interface (U_*) ranged between 0.6 to 1.4 cm/sec, with erosional current velocities 100 cm above the seabed (U_{100}) from 14 to 31 cm/sec. Values of U_* and U_{100} averaged 1.04 and 23 cm/sec respectively, for the November cruise, and 1.00 and 21 cm/sec for the June cruise.

C. Wave Hindcasting

Wave data from Ambrose Light from November 1956 to December 1980, and from wave recorders off Little Egg Inlet, New Jersey, 75 km south of the

dumpsite, during September through November 1974, were compared with wind data from Kennedy Airport and Ambrose Light. Mathematical correlations were made, taking into account fetch, wind stability, and differences between sea and swell. Predictive formulas for wave height and period at Ambrose Light were then made. Using formulas for transfer of surface wave energy to the bottom, a comparison was made between measurements (of bottom current and water transparency) taken by the CV probes during the deployment period November 1980 to June 1981 and bottom energy predicted by hindcasting.

The results show that the wave hindcasting technique correlated very well with bottom measurements, but that at least one bottom transport event corresponded with a time of sea swell, not locally generated wind waves. In addition, bottom current data correspond well with wave hindcasting using Kennedy Airport wind data.

The last part of this section studied effects of infrequent, intense offshore storms in generating swell. The results show up to 200 cm/s bottom orbital velocity with a transport excursion of 120 m during six hours, but with a duration time of only one measurement period (six hours). Furthermore, although the build-up period during which bottom currents exceeded transport threshold velocities may be up to 36 hours, after the peak passed, velocities immediately dropped to well below threshold.

D. Sediment Transport Estimated from Bottom Flow and Turbidity Measurements

Data were collected on the sediment cap from CV probes which measure current speed and direction 100 cm above the bottom and water turbidity 50 cm above the bottom. One probe collected data during the whole study period, November 1980 to June 1981, a second probe from November 1980 to April 1981, and a third from February through June 1981. Calculations for transport rate and directions were made using several models incorporating average wave and

current data, and wave data only, the former giving slightly better results. Three wave-current methods were then compared.

The results of all methods used agree that net transport direction is to the south. However, transport calculations vary according to method used: bedload transport was from 100 to 2500 kg/m, and net fine sediment transport was from 4 to 650 kg/m during the 214-day deployment period. These variations are due to using transport rates, in the formulation of transport equations, which were based on laboratory experiments only; no field verification of rates under waves or combined wave and current flows are available. The data indicate that steady-flow transport rates are at least an order of magnitude less than wave-current transport rates; steady-flow velocities seldom exceeded threshold values and were out of phase with wave-generated bottom transport events. Moderate waves combined with mild currents did produce transport events which would not have occurred with waves or currents alone. Transport rates were also calculated at varying depths assuming similar mean flows: rates at 21 m (the shallowest dumpsite depth) were 20% greater than at 23 m, and 20% less at 30 m than at 23 m.

E. Sediment Transport Simulation

Mathematical simulations were made of transport at the cap site using combined wave and current data with two assumptions: (a) that the cap site was a portion of a larger, circular, bathymetyric bottom perturbation (the dredged material dumpsite as a whole 2.2 n. mi. across and 8+ m high; and (b) the bottom perturbation of a circular sand cap 0.4 n. mi. across and 2+ m high. Monte-Carlo simulations of bed-load transport for each were made for 100 flow events of random strength over a three year-period. Summary statistical data for wave height, direction and period taken in the New York Bight were used to calculate the mean and variance for flow and wave orbital

velocities. These were compared with these same parameters taken from the cap site CV probe deployments from November 1980 to June 1981.

The results for the whole dumpsite simulation indicate that the net change of the circular mound is a maximum erosion of 5 cm over a small area of the crest. One to five cm of erosion occurs as three irregular north-south-trending areas over the 4 n. mi. square. The cap site, at this scale, would have net changes from -1 cm (erosion) to +2 cm (deposition).

The separate calculation for the cap shows large areas of both -5 cm and +5 cm with sharp gradients between them. The crest of the mound shows deposition which extends east of the mound, but the northwest corner is eroded (-5 cm). The changes are still small.

There is a tendency in both cases to form an irregular ridge and swale topography. For the whole dumpsite, the orientation is north-south with crest spacing of about 3 km. For the cap, the orientation is northeast-southwest with a spacing of about 1 km.

Examination of the direction of dispersal of fine sediment was also made using a diffusion-advection equation. Results of eroding a bed of fine sediment 1 cm thick and 100 m square (1 m^3) show initial transport westward towards the New Jersey shore with 0.01% to 0.1% fine sediment concentrations in the surficial sediment after one year; after 100 years, diffusion has spread the sediment so that the highest concentration is 0.05% around the New York harbor mouth, decreasing to 0.001% half-way down the Long Island and New Jersey coasts, with a considerable seaward excursion.

Conclusion

Evidence from in-situ, experimental, and mathematical data indicate relatively small amounts of erosion at the cap site on an annual basis assuming "normal" yearly conditions. The 2 to 5 cm erosion over three years

from mathematical modelling translates into 0.02 and 0.05 ft/yr, or 45.7 and 18.3 yrs/ft of erosion. Thus the cap, which is four to eight feet thick, appears to be safe for the time being. However, the severe effects of a "hundred year" storm could very likely be an order of magnitude or more larger so that portions of the cap might be breached from that storm alone. Bear in mind that the cap material is fine sand, the most easily eroded material.

For a margin of safety, it is recommended that additional cap material be placed over the present cap. This should be sediment consisting of clean sand as coarse as is reasonably possible with grain size larger than 0.25 mm.